UNIVERSITÀ
DEGLI STUDI
DI PADOVA

Head Office: University of Padova

Department of Information Engineering

Ph.D. COURSE IN: Information Engineering
CURRICULUM: Information and Communication Technologies (I.C.T.)
30th SERIES

Characterization and modelling of organic devices for simultaneous stimulation and recording of cellular electrical activity with Reference-Less Electrolyte-Gated Organic Field-Effect Transistors

Coordinator: Andrea Neviani
Supervisor: Prof. Andrea Cester

Ph.D. Student: Nicolò Lago

Contents

Abstract

The study of neuronal and neurodegenerative diseases requires the development of new tools and technologies to create functional neuroelectronics allowing both stimulation and recording of cellular electrical activity. In the last decade organic electronics is digging its way in the field of bioelectronics and researchers started to develop neural interfaces based on organic semiconductors. The interest in such technologies arise from the intrinsic properties of organic materials such as low cost, transparency, softness and flexibility, as well the biocompatibility and the suitability in realizing all organic printed systems. In particular, organic field-effect transistor (OFET) -based biosensors integrate the sensing and signal amplification in a single device, paving the way to new implantable neural interfaces for *in vivo* applications.

To master the sensing and amplification properties of the OFET-based sensors, it is mandatory to gain an intimate knowledge of the single transistors (without any analytes or cells) that cannot be limited to basic characterizations or to general models. Moreover, organic transistors are characterized by different working principles and properties as respect to their inorganic counterpart. We performed pulsed and transient characterization on different OFETs (both p-type and n-type) showing that, even though the transistors can switch on and off very fast, the accumulation and/or the depletion of the conductive channel continues for times as long as ten seconds. Such phenomenon must be carefully considered in the realization of a biosensor and in its applications, since the DC operative point of the device can drift during the recording of the cellular signals, thus altering the collected data. We further investigate such phenomenon by performing characterizations at different temperatures and by applying the deep level transient spectroscopy technique. We showed that the slow channel accumulation (and depletion) is due to the semiconductor density-of-states that must be occupied in order to bring the Fermi energy level close to the conduction band. This is a phenomenon that can takes several seconds and we described it by introducing a time-depend mobility. We also proposed a technique to estimate the behavior, in time, of the position of the Fermi energy level as respect to the conduction band.

To understand the electrochemical transduction processes between living cell and organic biosensor, we realized two-electrodes structure (STACKs) where a drop of saline solution is put directly in contact with the organic semiconductor. On these devices, we performed electrochemical impedance spectroscopy at different DC polarizations and we developed an equivalent circuit model for the metal-organic semiconductor-solution structures that are typically used as transducers in biosensor devices. Our approach was extending the standard range of the bias voltages applied for devices that operate in water. This particular characterization protocol allowed to distinguish and investigate the different mechanisms that occur at the different layers and interfaces: adsorption of ions in the semiconductor; accumulation and charge exchange of carriers at the semiconductor/electrolyte interface; percolation of the ionic species through the organic semiconductor; ion diffusion across the electrolyte; ion adsorption and charge exchange at the platinum interface. We highlighted the presence of ion percolation through the organic semiconductor layer, which is described in the equivalent circuit model by means of a de Levie impedance. The presence of percolation has been demonstrated by environmental scanning electron microscopy and profilometry analysis. Although percolation is much more evident at high negative bias values, it is still present even at low bias conditions. In addition, we analyze two case studies of devices featuring NaCl (concentration of 0.1M) and MilliQ water as solution, showing that both cases can be considered as a particular case of the general model presented in this manuscript.

The very good agreement between the model and the experimental data makes the model a valid tool for studying the transducing mechanisms between organic films and the physiological environment. Hence this model could be a useful tool not only for the characterization and failure analysis of electronic devices, such as water-gated transistors, electrophysiological interfaces, fuel cells, and others electrochemical systems, but also this model might be used in other applications, in which a solution is in intimate contact with another material to determine and quantify, if undesired mechanisms such as percolation and/or redox corrosive processes occur.

Lastly, the knowledge gain on OFETs and STACKs were put together to realize electrolyte-gated field effect transistors (EGOFETs). We then developed a model to describes EGOFETs as neural interfaces. We showed that our model can be successfully applied to understand the behaviour of a more general class of devices, including both organic and inorganic transistors. We introduced the reference-less (RL-) EGOFET and we showed that it might be successfully used as a low cost and flexible neural interface for extracellular recording *in vivo* without the need of a reference electrode, making the implant less invasive and easier to use. The working principle underlying RL-EGOFETs involves self-polarization and back-gate stimulation, which we show experimentally to be feasible by means of a custom low-voltage high-speed acquisition board that was designed to emulate a real-time neuron response. Our results open the door to using and optimizing EGOFETs and RL-EGOFETs for neural interfaces.

1. Introduction

Organic electronics, in spite of being more recent with respect to conventional electronics, dates back to the fifties. Indeed, many organic substances had been shown to have semiconducting[Eley53] as well as photoconductive[Akamatu52] properties, thus stimulating the interest of the physics and chemistry communities[Brophy61].

In 1963, Bolto et al. reported the first example of high conductive polymer on polypyrrole with a conductivity up to 1 $S \cdot cm^{-1}$[McNeil63]. The same group also showed that polypyrrole can behave as an intrinsic or extrinsic semiconductor with n- or p-type characteristic[Bolto63].

Later in 1968, Berets et al. investigated the electrical properties of linear polyacetylene showing that its conductivity depends on the extent of the sample oxidation[Berets68].

In 1977, the Nobel Prizes Alan J. Heeger, Hideki Shirakawa, and Alan G. MacDiarmid found that doped polyacetylene features controlled semiconducting properties with a conductivity that can be varied over a range of eleven orders of magnitude depending of the doping type and concentration[Chiang77].

Since then, the interest of the scientific community in organic electronics has seen a dramatic increase, and, in the last 40 years, there have been a lot of technological improvements and findings. An example is the first organic electroluminescence diode, in 1970, that was originally based on a single layer of anthracene[Williams70]. Then, in 1987, the structure was improved using two different layers to enhance the injection of both electrons and holes[Tang87], hence developing what is considered the first OLED. Few years later, in 1990, the use of conjugated polymer to realize more robust structures[Burroughes90] opened the way to the development of today's OLED displays.

Aside the OLED technology, organic electronics covers a wide interdisciplinary research area that includes organic solar cells (from the first heterojunction solar cell[Tang86], to the high efficient perovskite-based DSC[Shin17]), thin film transistors (from the first all-organic TFT[Garnier90], to the light-emitting field-effect transistor[Hepp03]), and organic sensors for both chemical and biological sensors[Lin12], leading to embedded, flexible, and wearable circuits[An17].

Among these applications, in the last decade organic electronics is digging its way in the field of bioelectronics and researcher started to develop neural interfaces based on organic semiconductors. The interest in such technologies arise from the intrinsic properties of organic materials such as their flexibility[Gustafsson92] and the suitability in realizing all organic printed systems[Sirringhaus00]. Moreover, there are many other interesting properties that make organic platform so appealing[Berggren07], including i) the transparency of the thin-film materials that allow optical investigation of the tissue in direct contact with the sensor; ii) polymers and molecules can be tuned to meet the desired specifications in different kind of sensors; iii) organic semiconductors are soft material that can be self-assembled and self-organized mimicking the biological structures; iv) organic compounds can be modified by means of bio-molecular groups thus promoting cell viability[Tengvall98]; and v) organic electronics devices and biosensors can be fabricated using natural, cheap, bio-degradable, and bio-resorbable materials[Głowacki13, Kim10].

Despite these remarkable properties, organic neural interfaces have not yet reached the market because organic transistors and sensors still show poor electrochemical stability when exposed to light, air, and water environments[Sirringhaus09]. In addition, organic transistor-based sensors typically feature much smaller mobilities and, consequently, lower performance with respect to their inorganic counterpart.

However, these limits are mainly ascribable to the relatively novelty of the technology. In fact, organic field-effect transistors featuring high air[Huang17], thermal[Kuribara12], and bending[Sekitani10] stability, as well high carrier mobility for both p-type[Kang13, Takeya07] and n-type[Sun14, Wang17] semiconductors have been recently reported. Therefore, organic electronics holds great promise for future and reliable neural interfaces.

In this introductory chapter, we are going to explore the world of organic biosensors for sensing neural activity. We will first discuss specifications and requirements that need to be considered in designing a new neural interface. Secondly, an overview on inorganic technology will be given. Then, organic neural interfaces and organic thin film transistors to sense and stimulate cells electrical activity will be reviewed. Later on, we will discuss how neural interfaces can be modelled to study and analyze how a living cell and a neural interface interact each to the other. Finally, a summary will be drawn and some future perspective will be given.

1.1. Neural Interfaces Specification and Requirements

In order to develop targeted therapy, the understanding of neurons behavior is a critical step to study neuronal and neurodegenerative diseases, such as Parkinson, Alzheimer, spinal injury, stroke, and others brain and neuronal diseases[Buzsáki12]. At this purpose, non-invasive techniques such as functional magnetic resonance imaging, positron-emission tomography, and electroencephalography allowing three-dimensional analysis have been developed[Menon97, Peyron00]. However, such techniques suffer from low spatial and temporal resolution[Fang15]. It is therefore highly important to develop technologies capable to record a large amount of data from as many neurons as possible whit both high spatial and high temporal resolutions[Alivisatos13].

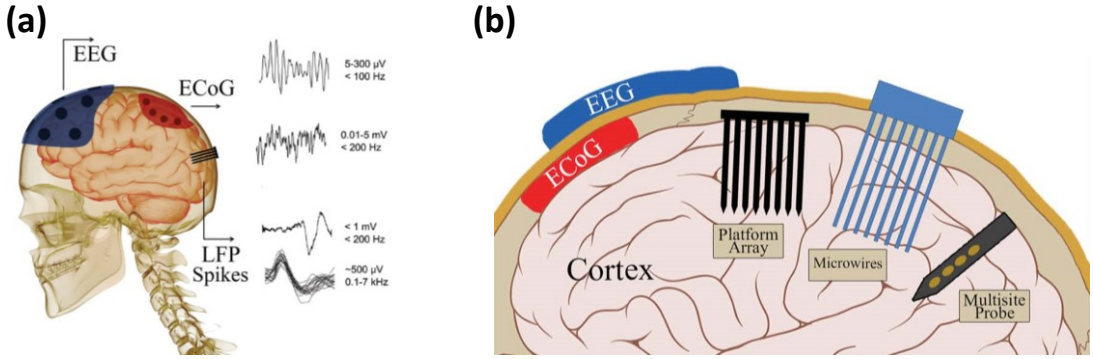

Figure 1.1. **(a)** *Schematic of neural signals (EEGs, ECoGs, LFPs, and spikes) and their properties.* **(b)** *Schematic of EEG electrode on the skull, ECoG electrode on the surface of brain, and penetrating electrodes.*
Reproduced with permission from [Fattahi14].

For brain analysis, as depicted in ***Figure 1.1***, three classes of neural interfaces and signals can be individuated[Fattahi14]: electroencephalogram (EEG) electrodes, for low frequency signals (<100Hz); electrocortiogram (ECoG) interfaces, for low frequency signals (<200Hz); and penetrating interfaces, for local field potentials (<200Hz) and action potentials (around 1kHz). Despite being non-invasive, EEG recording suffer from low spatial resolution and poor signal-to-noise ratio (SNR), hence in this review we will focused our attention to implantable neural interfaces (i.e. ECoG and penetrating electrodes).

On the one hand, penetrating electrodes allow more accurate recording with a good spatiotemporal resolution. On the other hand, ECoG interfaces are less invasive, still allowing good SNRs. Anyway, during the design and development of implantable neural interfaces (either ECoG or penetrating sensors), the following properties and requirements should be considered:

- Device sensitivity and selectivity
- Long term stability
- Surface properties
- Mechanical properties and transparency

1.1.1. Device sensitivity and selectivity

Sensitivity and selectivity are two important figures of merit to assess the quality of a biosensor. In general, the sensitivity is the capability to discriminate small differences in concentration of the test analyte, whereas the selectivity is the capability of the sensor to discriminate the analyte from interfering components[Torsi13].

For a neural interface, the analyte corresponds to the membrane potential of the cell under analysis, that can be either the intracellular potential or the extracellular potential. Hence, the device sensitivity becomes the capability to discriminate small perturbation in the membrane potentials, whereas the selectivity becomes the capability to discriminate and sense a single cell from a bunch of neurons or a neural network.

It is clear that, to achieve high SNRs, in a bio-sensing device, both selectivity and sensitivity should be maximized. However, this is not always possible and a good SNR is obtained only by a trade-off between sensitivity and selectivity[Fattahi14]. For instance, using a planar micro-electrodes array (MEA) technology, lowering the electrodes size increase the sensors selectivity, but it lowers the electrodes capacitance and consequently the sensitivity. Conversely, increasing the electrode size improves the sensitivity, but leads to a lower selectivity.

1.1.2. Long term stability

One of the most important reliability issues is the long-term stability of the neural interface[Kotov09]. As reported in ***Figure 1.2***, many different mechanisms can cause the failure of the neural implant (for a good review see [Chen17]) Indeed, such kind of sensors are required to operate in water environments with a high concentration of ions[Deslouis96, Porrazzo14]. In these conditions, electrochemical reactions could take place causing the device failure[Negi10].

Other causes of failures are due to the inflammation of the neural tissues nearby the implant typically associated to a poor biocompatibility of the implant itself[Heiduschka98, Polikov05], i.e. the living cells and/or tissues do not accept the implant. A measure of the neuron density as a function of the distance from the implant can be used to quantitative evaluate the biocompatibility of the neural interface, as well the extension of the inflammation[Edell92], and mechanisms behind the failure of the neural interface can be investigated by either electrochemical impedance spectroscopy[Williams07] or optical analysis[McLaughlin13].

It is clear that, to improve the reliability of the device, it is necessary to improve its biocompatibility. Hence, many different approaches have been proposed, including chemical and physical modification of the surface sensing area[Heiduschka98, Moxon07], scaling of the sensor size to make the implant less invasive[Szarowski03], development of more soft, flexible and conformable materials[Kim10, Rousche01], and the implementation of a rejuvenation protocol to prolong the implant life[Johnson05, Otto06].

Remarkably, implantable neural interfaces featuring sufficient long-term stability to allows *in vivo* implantation that could possibly last for years have been reported[Chestek11, Rousche01].

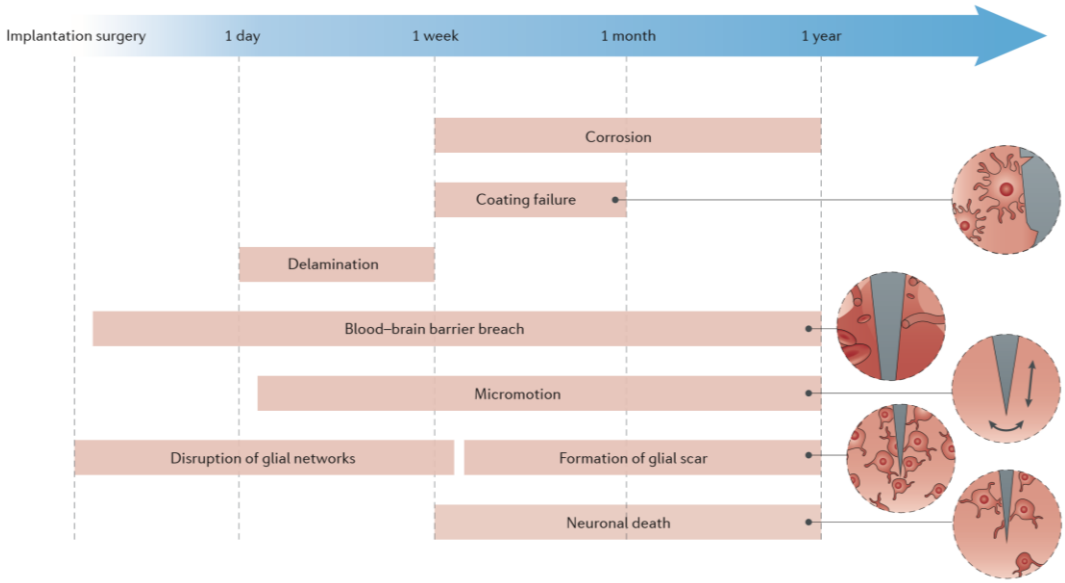

***Figure 1.2**. Failure modes of neural probes, manifested as a loss of neural recording capability, can be classified into those related to device design and those related to foreign-body response. Design failure mechanisms include mechanical failure of interconnects, degradation and cracking of the insulation, electrode corrosion and delamination of probe layers. Biological failure mechanisms include initial tissue damage during insertion; breach of the blood–brain barrier; elastic mismatch and tissue micromotion; disruption of glial networks; formation of a glial scar; and neuronal death associated with the above-mentioned factors, as well as with materials neurotoxicity and chemical mismatch. Reproduced with permission from [Chen17].*

1.1.3. Surface properties

Many materials (metals and organic compounds) have proved to be biocompatible and suitable for the realization of neural interfaces[Fattahi14, Heiduschka98]. However, the device sensitive interface, which has the role to transduce the bioelectrical signals in electrical signals (and vice versa), must be carefully designed in order to ensure good performances of the sensor as well as its long-term stability.

One important requirement in developing a good bidirectional device is the sensing surface roughness. In fact, for assure the device performance, good cells attachment onto surfaces must be guaranteed. Unlike the most of the electronic devices, a device with an optimized surface roughness does not mean it has a perfectly flat and homogenous surface. It was in fact shown that, to improve cells adhesion, a certain degree of average roughness (from ten to hundreds of nanometers, depending the material and the kind of neurons used) must be provided[Khan05, Yang04].

To further improve the interaction between cells and sensor, the chemical properties of the sensing surface play a crucial role. At this purpose, many chemical functionalizations of the surface have been proposed. In fact, to improve the cells attachment, the device sensing surface can be treated and/or coated with different approaches such as blending, physical adhesion, covalent bonding, electrostatic attachment, and electrochemical polymerization (see [Kim11] and references cited there in).

Since water is known to be highly biocompatible, the idea behind the chemical modification is to increase the surface hydrophilicity, and therefore wettability, by chemical modifications such as plasma treatment[Piskin93], coating with molecules and/or polymers[Amiji93, Arshady93, Kishida91], and cross-linking with different compounds[Guidoin89, Marois95, Marois96]. In addition, technique like self-assembled monolayer (SAM) can be used to functionalize the biosensor surface without interposing a thick layer of material, which can separate the real sensing layer from the neuron and thus affecting the device sensitivity[Widge07].

Among these techniques, the most widely used surface treatments are the functionalization with adhesion molecules like poly-D-lysine (PDL) or poly-L-lysine (PLL)[Kim11, Muzzio17], the use of protein like laminin[Kleinman85, Matsuzawa96, Offenhäusser97], and the combination of PDL (or PLL) and laminin[Joo15, Tam16, White16].

Notice that, proper surface modifications are not only important to enhance the biocompatibility of the implant and to improve cells attachment during *in vitro* experiments, but are also important to promote neurons adhesion to the implanted electrodes and sensors to help *in vivo* neurons regeneration[Cheng06, Goulart16, Suzuki99]. For instance, organosilica sol-gel coatings that promote neuronal growth against astrocytes growth, hence limiting glial scar responses, have been recently reported[Capeletti16].

Among the other requirements, we might cite the electrical properties of the interfacing devices. Indeed, the processes of stimulation and recording are characterized by movement of charge from the implant toward the cell and vice versa. However, the amount of charge during stimulation is much larger than the amount of charge during recording and, since any faradaic and corrosive processes should be avoided, the neural interface capacitance should be large enough to promote non-faradaic charge transfer only[Harnack04, Merrill05]. Hence, stimulating and sensing electrodes and sensors can feature different designs to promote stimulation rather than recording or, conversely, to enhance sensing rather than stimulation[Kotov09].

1.1.4. Mechanical properties and transparency

The mechanical properties of a neural interface are extremely important during *in vivo* application. Stiff and strong neural interfaces can provide easy and reliable implants. However, for what concerns the long-term stability and biocompatibility of the implant, soft and conformable materials are more eligible[Kotov09]. In fact, mainly due to micromotions, stiff implants are often able to operate for a limited time before the formation of cracks in the sensor substrate, delamination of the interfacial layer of the sensor[Cogan04], or formation of gaps between neurons and sensors[Twardoch94]. Moreover, micromotions between the neural tissue and the implant can cause an inflammatory response, thus leading to the device failure[Chestek11]. On the other hand, soft and flexible materials allow to fabricate conformable interfaces able to adapt to irregular surfaces[Kim10, Someya05], hence they can provide a better match between implants and neural tissues with consequent reduction of inflammations and rejections.

Finally, another important specification that might be required to a bio-sensor device is the partial or complete transparency of the device, allowing the direct monitor of the cells and tissues during the experiments. This would allow the inspection of eventual inflammations *in vivo*[Kapnisis16, Shiraishi10], or to simply follow growth and differentiation of neurons by means of confocal microscopy *in vitro*[Chen13, Suter11], as well using illumination to perform cell stimulation (both in vitro and in vivo)[Wiegert17].

1.2. Overview of inorganic devices for neural interfaces

In the 1780s, using a brass hook and a steel scalpel, Luigi Galvani found that he could stimulate the muscular activity of a dead frog. Since then, a lot of electrophysiology experiments where carried on to gain knowledge about living cells and tissues by means of electrical measurements, with particular interest in neurons (neuroscience).

Now, the state of the art technologies allows the study of the nervous system through implantable neural interfaces able to stimulation and recording of cells' electrical activity. Furthermore, neural interfaces can treat neurological conditions such as Parkinson through deep brain stimulation.

1.2.1. Micro-electrodes arrays (MEAs)

The first implantable neural interface, able to record signals from the brain, were insulated tungsten wires (with the tips exposed) developed during the fifties[Cheung07], and one of the first example of multisite recording was performed by Humphrey et al.[Humprey70] motivating the use of multi- or micro-electrode arrays (MEAs)[Hatsopoulos09].

Nowadays, thanks to its stability in water, platinum is the most common material used to make inert electrodes (i.e. only a negligible amount of platinum ions is released into aqueous solutions). In addition, also carbon and iridium are well established materials in bio-electronics[Heiduschka98]: carbon is highly stable and biocompatible; iridium is suited as stimulating electrode due to the formation of a thin and stable oxide with high charge capacitance.

The development of the silicon technology and photolithography techniques allowed to integrate a large number of electrodes in a small chip. The first silicon based MEAs, now known as Michigan array, were fabricated during the seventies[Wise70, Wise75]. State of the art Michigan MEAs allow a three-dimensional recording and consist in multiple silicon shanks, each of them hosting a number of microelectrodes with well-known spatial distribution (***Figure 1.3a***).

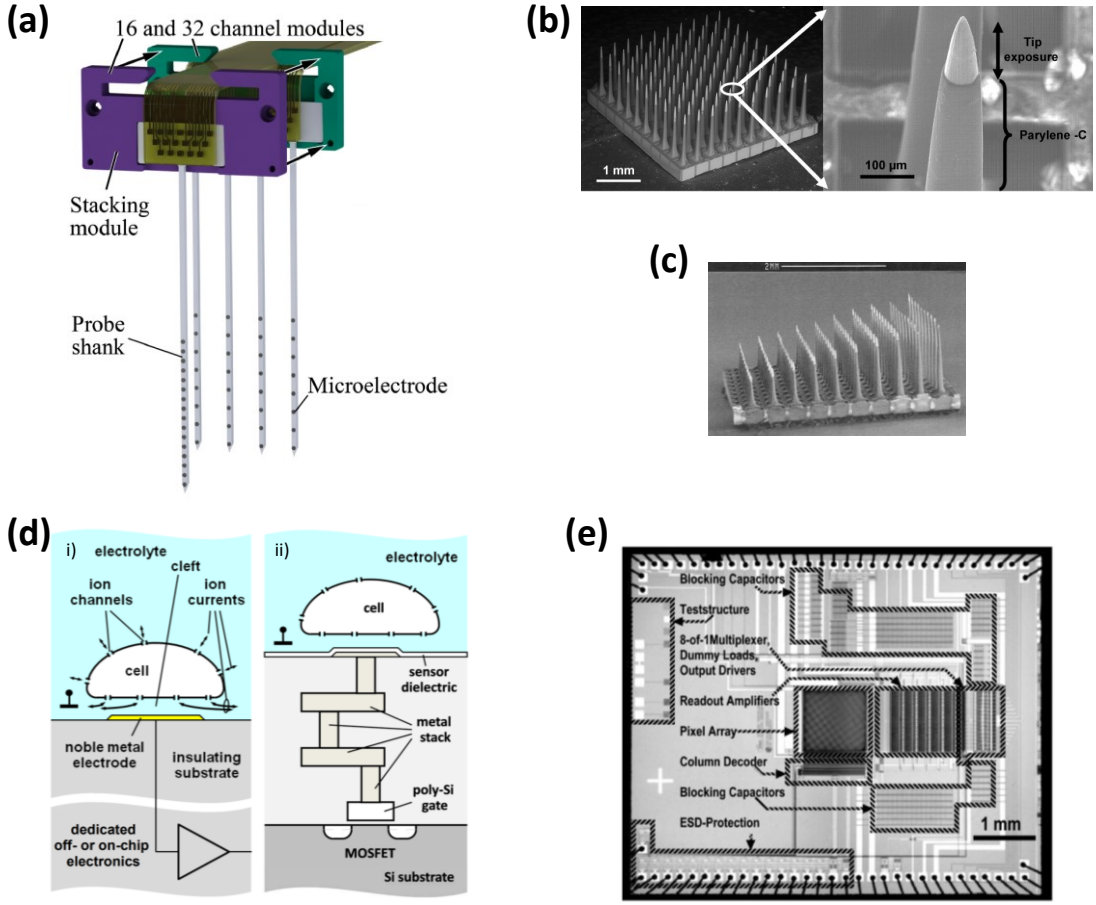

Figure 1.3. **(a)** *Schematic of two stacked Michigan array composed of a single-shank and a four-shank probe, respectively.* **(b)** *Scanning electron micrograph of a Utah electrode array and a higher magnification image of one electrode depicting tip exposure (~100 µm) which forms the active site for stimulation and/or recording of neural signals.* **(c)** *Scanning electron micrograph of a Utah array with graded variation from 0.5 to 1.5 mm in the microelectrode length.* **(d)** *Schematic cross-sections of i) a noble metal electrode interface connected to on- or off-chip readout electronics and ii) an example of dielectric interface with built-in pre-amplification CMOS transistor.* **(e)** *Microphotograph of a chip that includes the MEA sensor with pre-amplifier and other on-chip electronics.*
Reproduced with permission from: [Thewes16] for **(a)***; [Negi10] for* **(b)***; [Eversmann03] for* **(c)***; [Ballini14] for* **(d)***; [Barz17] for* **(e)**.

An alternative to Michigan electrodes are the Utah arrays (***Figure 1.3b*** and ***Figure 1.3c***). Utah arrays are typically formed by 100 sharpened needles made of silicon with the tips covered by platinum. Each needle is electrically insulated from its neighbour by a parylene coating to gain a better selectivity and, consequently, a better SNR.

Notice that, both Michigan and Utah arrays are passive electrodes. However, thanks to the CMOS fabrication processes, each electrode in the array can be realized with a built-in transistor to pre-amplify the signal, hence reducing the size of the implants. An example of integrating on chip electronic is schematically reported in ***Figure 1.3d***, whereas ***Figure 1.3e*** shows the microphotograph of an array of 128x128 electrodes with integrated on-chip electronics for pre-amplify and multiplex signals from a neural network[Barz17]. Remarkably, a highly integrated MEA with more than 26000 electrodes for *in vitro* applications was recently reported[Badi03].

Aside the most common Michigan and Utah arrays, other silicon-based, ceramic, and microwire electrodes have been proposed, and we invite the readers to refer to the following reviews: [Cheung07] and [Fattahi14].

1.2.2. Field-effect transistors-based neural interfaces

CMOS technology allows on-chip electronics for high integration of sensors and signal analysis. Moreover, to overcome the issues due to faradic processes undergoing at the electrode/solution interfaces, an insulator such as SiO2 is interpose between the pure metal and the electrolyte (***Figure 1.3d***, example *ii)*). Hence, as shown in ***Figure 1.4a***, to further improve the SNR, the MOSFET pre-amplifier can be put directly at the cell-dielectric interface without need of the metal interconnection between the transistor and dielectric interface.

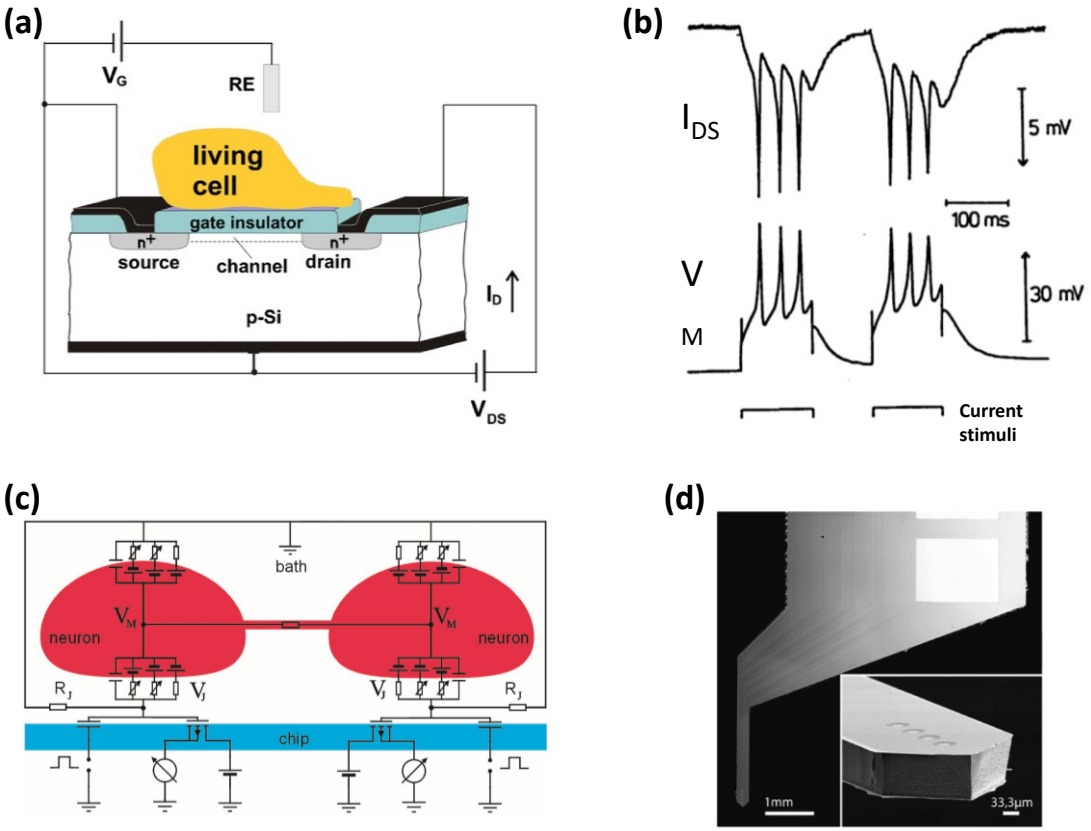

Figure 1.4. **(a)** *Schematic of an EOSFET device interfacing a living cell.* **(b)** *I_{DS} and V_M of a sequence of action potentials triggered by current pulses as marked at the bottom.* **(c)** *Schematic representation and equivalent circuit of neuron pair connected by an electrical synapse and interfaced by capacitive stimulators and field-effect transistors.* **(d)** *Electron micrograph of a transistor needle chip showing the needle with four transistors and a portion of the contact plate with one of the metalized bond pads. Reproduced with permission from: [Poghossian09] for* **(a)***; [Fromherz91] for* **(b)***; [Zeck01] for* **(c)***; [Felderer11] for* **(d)**.

This structure takes the name of EOSFET (electrolyte–oxide–semiconductor field-effect transistor) and was first studied during the seventies[Siu79]. One of the first example of interfacing a silicon EOSFET with a neuron was reported by Fromherz et al.[Fromherz91], in 1991, who showed how the transistor current (I_{DS}) could perfectly reproduce the membrane potential (V_M) measured by an implanted microelectrode (***Figure 1.4b***).

Notice that, unlike microelectrodes, EOSFETs can sense biological signals but cannot stimulate cellular activity. Thus, as schematically depicted in ***Figure 1.4c***, to perform both sensing and stimulations a microelectrode has to be placed adjacent to the transistor to stimulate the neurons. Such stimulating electrode can be easily implemented using the EOS (electrolyte–oxide–semiconductor) technology. However, insulated electrodes can provide smaller stimulating current densities as respect to iridium electrodes[Heiduschka98, Vassanelli14], hence larger electrode area and/or larger stimulation voltages are required.

Despite arrays of EOSFETs are manly used during *in vitro* experiments, silicon needles hosting four EOSFET sensors (***Figure 1.4d***) have been fabricated and successfully tested *in vivo*[Felderer11]. Moreover, an EOSFETs array composed by 16000 transistors has been succesfully tested to perform high-resolution in vivo ECoG[Vassanelli12].

1.3. Organic neural interfaces

In chapter ***1.2***, we learned that biocompatibility is the most important characteristic that a neural interface should have. However, the mechanical mismatch between the inorganic materials and the biological tissues limits the biocompatibility of the implants since, due to micromotions, the rigidity of the implanted devices might cause an inflammation of the surrounding tissues, and therefore the rejection of the implant itself[Fang15].

For this reason, soft, lightweight, and flexible organic materials able to mimic the nature of the living tissues are getting more and more interesting to develop neural interfaces for *in vivo* applications.

Given the softness of these materials, organic neural interfaces usually consist in non-penetrating implant, and are oriented towards the ECoG implants.

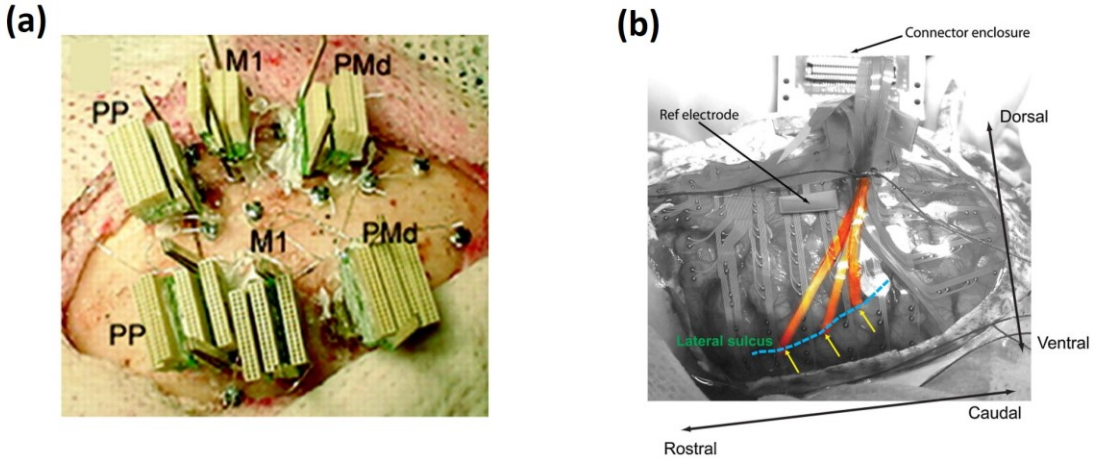

Figure 1.5. **(a)** *Multisite 672-microwire implant.* **(b)** *ECoG Electrodes on the lateral sulcus surface. Reproduced from: [Nicolelis03] for* **(a)***; [Fukushima14] for* **(b)**.

ECoG electrodes allow less invasive implants as respect to penetrating electrodes. By way of example, ***Figure 1.5a*** reports Utah arrays implanted in the brain of a monkey, whereas ***Figure 1.5b*** reports a flexible ECoG for multisite recording, showing that, unlike penetrating electrodes, ECoG stimulation and recording can be performed with minimum risk of damaging the brain tissues.

Moreover, ECoG implants, despite suffering for less selectivity as respect to penetrating electrodes, they can be used to map the brain activity and to perform activity recognitions such as the prediction of the limbs movements[Pistohl08].

We then now focus on organic technologies (electrodes and transistors) for ECoG applications.

1.3.1. Organic micro-electrodes arrays

The latest improvements in the organic bioelectronics area have proven that organic MEAs are becoming a mature technology with performance comparable, or exceeding, with the inorganic counterpart.

For instance, unlike inorganic MEAs, organic ECoG electrodes can be successfully combined with computer tomographic (CT) and magnetic resonance (MR). Indeed, Ahamdi et al. have shown that the presence of organic ECoG electrodes does not induce artefacts on CT and MR images[Ahmadi16]. Moreover, the temperature increase during MR imaging, was recorded to be 3.84°C without any electrodes, 4.05°C with organic ECoG electrodes, and 10.13°C with standard inorganic ECoG electrodes.

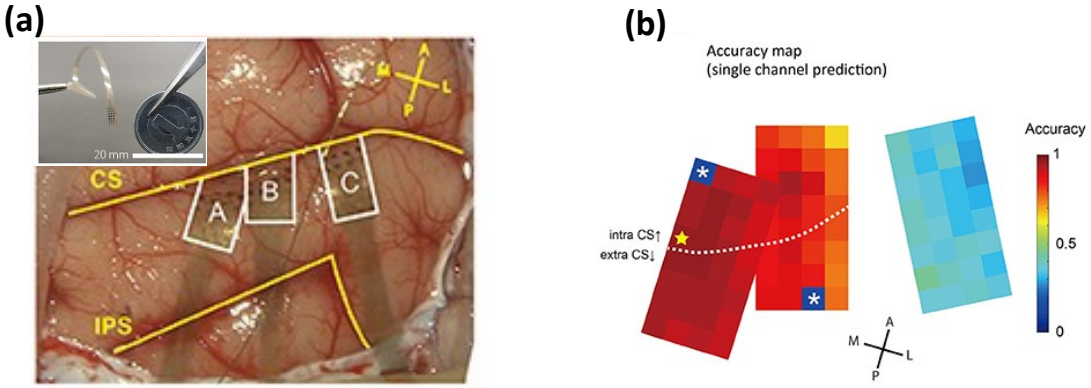

Figure 1.6. **(a)** *Operative view of electrode placement. The three areas surrounded by the white line represent each electrode patch. Patches A and B were partially overlapped. Each patch was flexible and curved along the brain surface. A section of each patch was inserted into the central sulcus. The insert shows the photograph of one MEA.* **(b)** *Accuracy obtained from single-channel predictions are showed by pseudo colors. The yellow star indicates the channel with maximum accuracy. The two asterisks indicate broken channels.*
Reproduced with permission from [Kaiju17].

Another recent example was reported by Kaiju et al. that performed somatosensory evoked potentials (SEPs) analysis on macaque monkeys[Kaiju17]. They made use of three MEAs, each counting 32 gold electrodes deposited onto a flexible parylene-C substrate, where a golden wire was used as reference electrode (***Figure 1.6a***). Stimulating the brain activity by means of a coil electrode for finger stimulation, the authors were able to predict (with maximum accuracy reached in less than 15ms) which finger was stimulated and the intensity of the stimulation (a map of the accuracy is reported in ***Figure 1.6b***). Their results are comparable to those obtained by multi-unit studies using penetrating electrodes[Nelson80, Pons87], promoting the suitability of organic ECoG electrodes in recording neural activity. Moreover, unlike penetrating electrodes, the position of organic ECoG arrays can be easily adjusted during surgery without damaging the brain tissues, thus ensuring that the organic implant perfectly adheres to the curved surface of the brain.

Another important advantage of organic ECoG electrodes is that organic implants can be easily fabricated in a lot of different forms and shapes. These are very interest and important features that allow to design electrodes optimized for the recording of specific areas. Thanks to these properties, Fukushima et al. developed an ECoG array consisting in 256 electrodes for bipolar recording at 128 sites (***Figure 1.7a***) to record neural activity simultaneously from the medial and lateral cortical surface, and from the supratemporal plane (STP) in monkeys[Fukushima14].

Figure 1.7b shows a cross section of the MEA used by Fukushima and coworkers[Fukushima14], which consist in a very thin polyimide (PI) substrate with copper electrodes that were insulated by 12µm-thick PI, except for the exposed pad that were plated in gold, hence ensuring the biocompatibility of the implant.

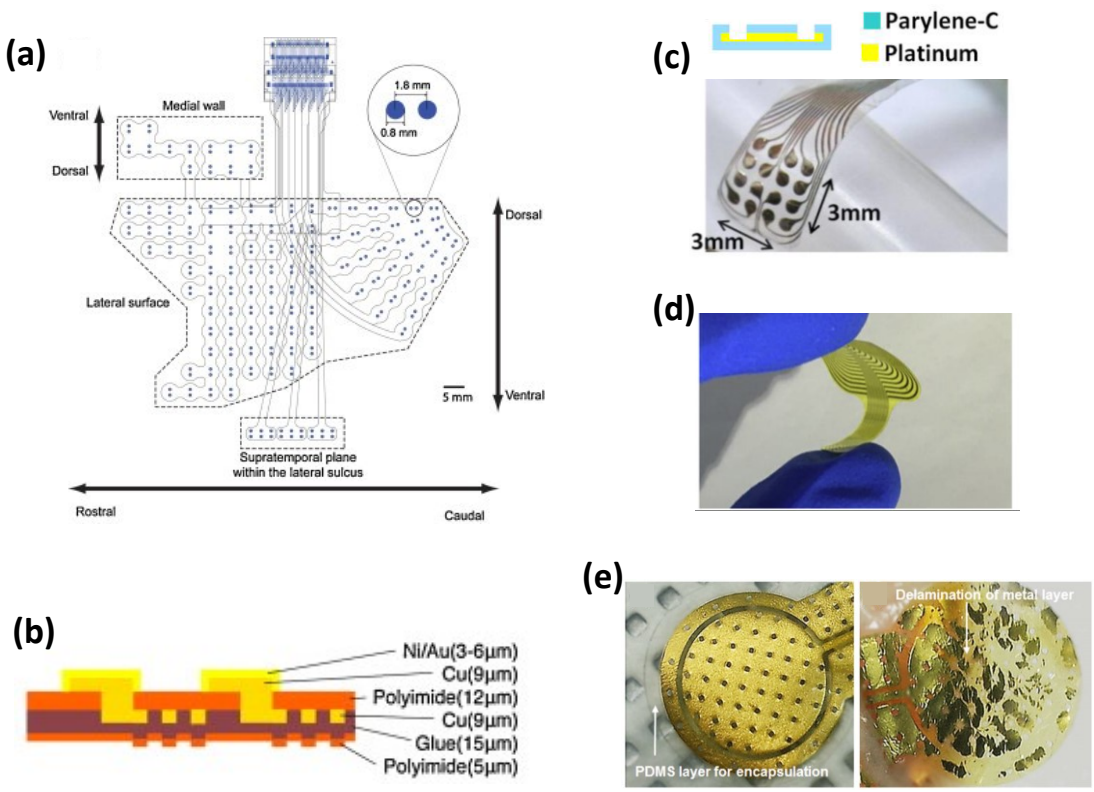

Figure 1.7. **(a)** *Spatial layout of the 256 electrodes array for multisite recording*[Fukushima14]. *The three sections outlined by the dashed lines, were designed for the medial wall (26 electrodes), the lateral surface (212 electrodes), and the supratemporal plane of the lateral sulcus (18 electrodes, STP array), respectively. A pair of electrodes designed for bipolar recording is magnified in the insert.* **(b)** *Schematic representation of a section of the array reported in* **(a)**. *The total thickness of the electrode is 53–56μm.* **(c)** *Photograph and schematic cross section of the 16 electrodes array reported in [Chang13].* **(d)** *Demonstration of the flexibility of the 32 electrodes array reported in [Dong17].* **(e)** *PDMS-encapsulated (left) and non-encapsulation (right) electrodes, retrieved 4 weeks after subcutaneous in vivo implantation.*
Reproduced with permission from: [Fukushima14] for **(a)** *and* **(b)**;
[Chang13] for **(c)**; *[Dong17] for* **(d)**; *[Lee17] for* **(e)**.

Another common organic material used to fabricate flexible substrate and biocompatible encapsulation is parylene-C[Chang07, Seymour07, Takeuchi05]. An example is reported in ***Figure 1.7c***, where a 16 platinum electrodes (one of which working as reference electrode) array was fabricated onto 12μm of flexible parylene-C substrate[Chang13].

Notice that, in order to allow minimal implantation damage and to fit the curved surface of the neuronal tissues, device thickness, flexibility and bio-compatibility are the criteria to design functional ECoG electrodes that allow *in vivo* recording during behavior. However, another important criterion is the electrochemical impedance of the implanted electrodes that should be as small as possible. For this reason, Dong et al. fabricated a 32 channel MEAs with Cr/Ag/Cr electrodes (***Figure 1.7d***) showing that the less expensive silver electrodes feature a much smaller impedance as respect to standard gold and platinum electrodes[Dong17].

Despite all the advantages with respect to the inorganic counterpart, one major failure mechanism of organic MEAs is the delamination of the metal electrodes (e.g. gold) on top of the flexible substrate. Lee et al. solved this issue by encapsulating the electrodes using polydimethylsiloxane (PDMS)[Lee17]. ***Figure 1.7e*** shows the comparison between gold electrodes with and without PDMS encapsulation. Remarkably, despite the increase of the electrode impedance, the PDMS-coated electrode is still able to correctly detect the biological signals through capacitive coupling with the living tissue while preventing the delamination of the gold electrode.

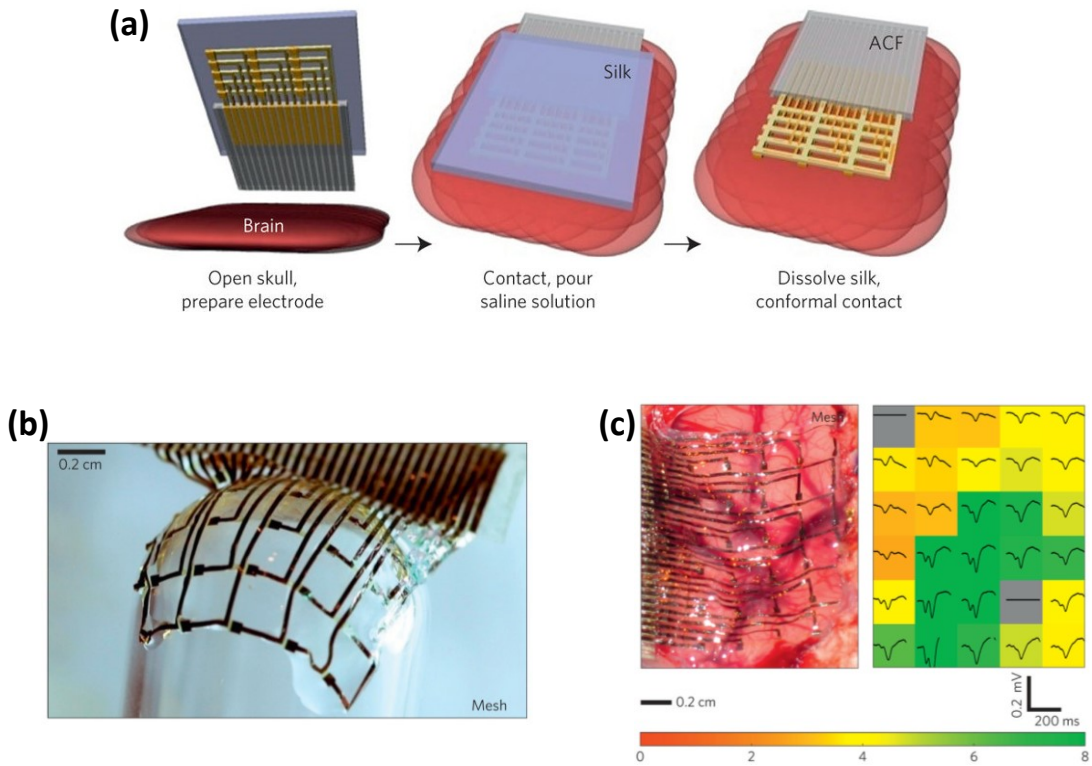

Figure 1.8. **(a)** *Schematic illustration of clinical use of a representative device in an ultrathin mesh geometry with a dissolvable silk support.* **(b)** *Image of the mesh electrodes array.* **(c)** *Image of the mesh electrode array on a feline brain (left) and the average evoked response from each electrode (right) with the color showing the ratio of the rms amplitude of each average electrode response in a 200ms window.*
Reproduced with permission from [Kim10].

Another outstanding result was achieved by Kim et al. who created a mesh of 30 gold electrodes fabricated on top of a silk bio-resorbable substrate[Kim10]. They first fabricated MEAs on top of PI substrates featuring different thicknesses (from 2.5µm up to 76µm), showing how the adhesion between the sensor and the brain surface increases reducing the thickness of the substrate. Hence, they fabricated a mesh of electrodes onto a silk support that, once applied to the wet surface of the brain, starts to dissolve, being reabsorbed by the living tissues, leaving exposed only the electrodes that get conformally wrapped to the brain surface creating a perfect adhesion (***Figure 1.8***).

At last, graphene and penetrating electrodes are worth to be mentioned.

Graphene electrodes have a slightly higher impedance and smaller charge injection capacity compared to platinum and gold electrodes. However, these metal electrodes have a low light transmission, limiting their usefulness in combining electrical recording/stimulation with optical imaging, calcium imaging or optogenetic stimulation of cells[Harris17]. Hence, to overcame this limitation, Park et al. fabricated an array of graphene-based electrodes on top of a parylene-C substrate and they performed bright-field and fluorescence images comparing the results with standard platinum electrodes (***Figure 1.9a***)[Park14].

Aside planar graphene electrodes, carbon nanofiber impregnated into conductive polyethylene[Guo17] and graphene oxide microfibers insulated with parylene-C[Apollo15] flexible and penetrating electrodes have been developed.

These flexible organic and hybrid electronics, can be introduced deep in the brain through releasable injection microneedles[Kim13], through capillary syringe needles[Liu15], stereotaxically implanted after rapid freezing in liquid nitrogen[Xie15], or by coating the electrodes with a rigid and dissolvable sucrose carrier needle (***Figure 1.9b***)[Apollo15].

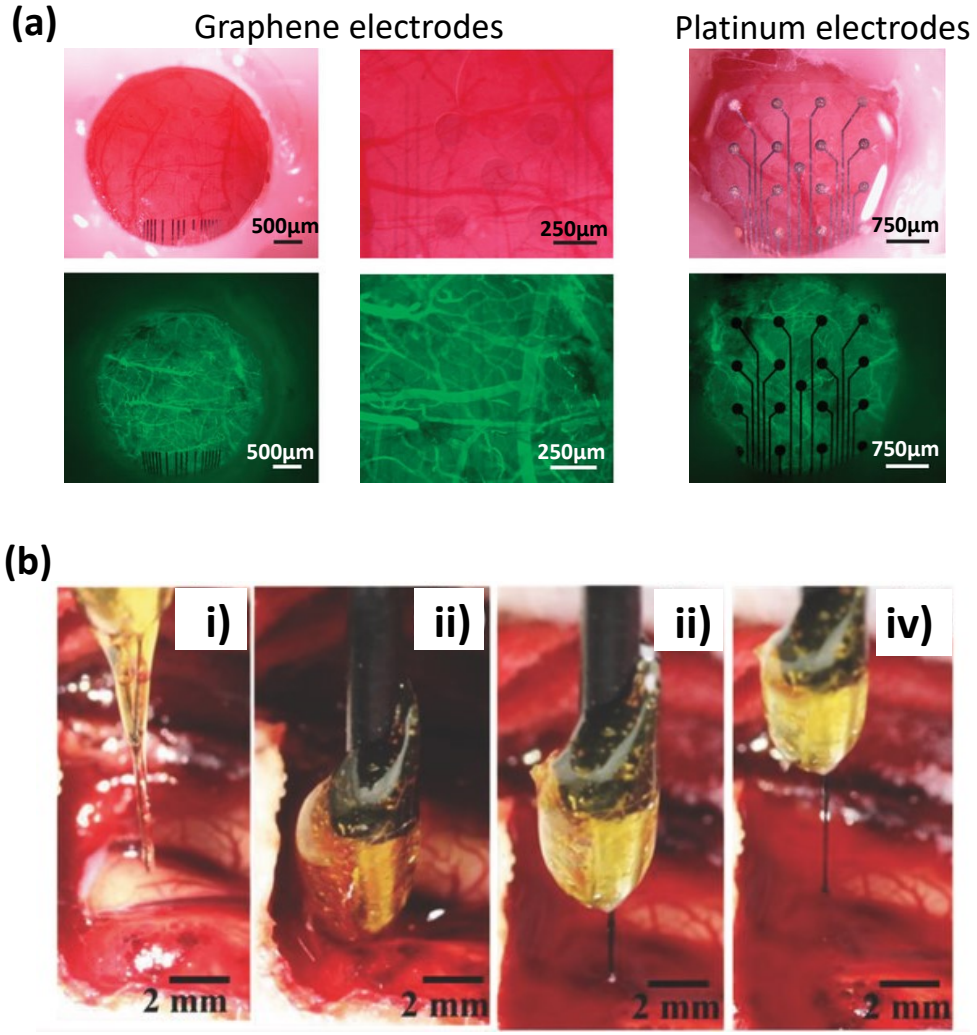

Figure 1.9. **(a)** *Bright-field (top) and fluorescence images (bottom) of semi-transparent graphene-based electrodes (left) compared to platinum electrodes (right).* **(b)** *Flexible electrode insertion into feline visual cortex. i) the electrode is coated in a rigid sucrose carrier needle and ii) implanted into the brain. iii) and iv) the electrode is removed from brain after 15 min of recording; sugar needle is completely dissolved.*
Reproduced with permission from: [Park14] for **(a)***; [Apollo15] for* **(b)**.

1.3.2. Organic field-effect transistor neural interfaces

Organic and flexible MEAs have proven to allow reliable *in vivo* recording by reducing the risk of rejection of the implant as respect to their inorganic counterpart. However, since passive electrodes can provide a limited SNR, organic transistor-based sensors able to performed in-situ amplification of the recorded signals are being investigated. Such transistors can be subdivided into two categories: organic electrochemical transistors (OECTs) and electrolyte-gated organic field-effect transistors (EGOFETs).

OECTs date back to 1984, and polypyrrole was used as conductive polymer[White84]. Now, the most commonly used material is poly(3,4-ethylenedioxythiophene) (PEDOT) that can be doped with poly(styrene sulfonate) (PSS) as well as glycosaminoglycan (GAG) to enhance its conductivity and/or its biocompatibility[Mantione16]. In a OECT, the source-to-drain current is modulated by ions penetrating the polymer hence doping/de-doping the material and consequently modulating the concentration of carriers contributing to the current[Bernards07]. Therefore, such interaction between ionic and electronic worlds promote the use of OECTs to realize flexible and biocompatible neural interfaces with high SNR.

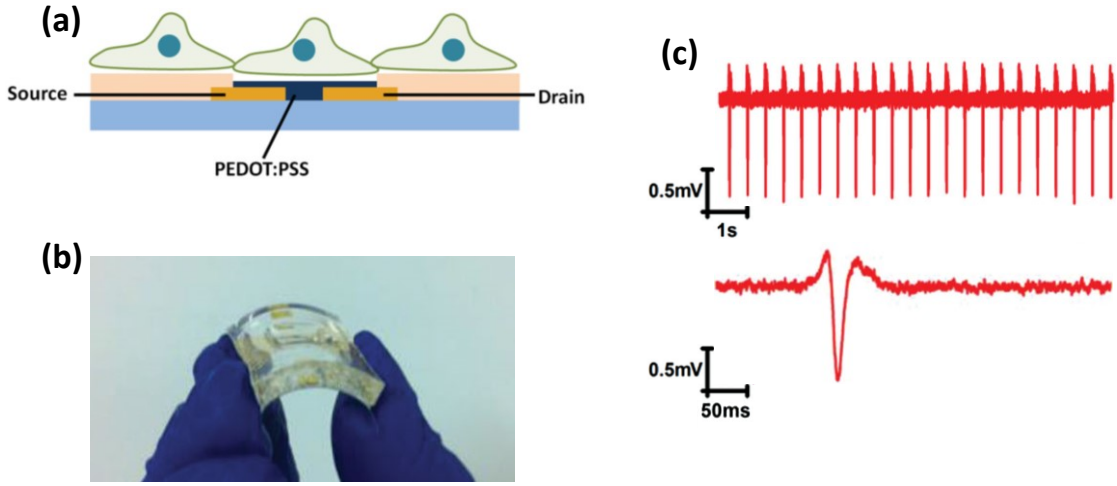

Figure 1.10. **(a)** *Schematic view of cardiomyocyte-like cells integrated with an OECT.* ***(b)*** *Photographs of a flexible OECT array device in bent condition.* ***(c)*** *Representative traces of continuous and single APs recorded by an OECTs (on rigid substrate). Current traces were converted to voltage through a 10kΩ resistor and amplified by a factor 100.*
Reproduced with permission from [Yao15].

An example was recently reported by Yao et al. whose fabricated OECTs sensors on both rigid and flexible substrates (***Figure 1.10a*** and ***Figure 1.10b***), demonstrating SNRs as high as 20dB during *in vitro* recording of spontaneously firing cardiomyocyte-like cells (***Figure 1.10b***)[Yao15].

Another example was reported by Khodagholy and coworkers who designed an ECoG probe where each OECT was juxtapose by a surface electrode, both fabricated using PEDOT:PSS as conductive polymer deposited onto a thin film of parylene (***Figure 1.11a***) [Khodagholy13a]. The authors performed *in vivo* recording experiments on a rat brain (***Figure 1.11b***), and they compare their PEDOT-based sensors with a silicon-base penetrating MEA counting 16 iridium electrodes. The OECT devices were wired in a common source configuration as shown in ***Figure 1.11b***, with the grounded screw used as the gate electrode. ***Figure 1.11c*** shows the comparison among the three different neural interfaces (OECT, organic surface electrode, and inorganic penetrating electrode) simultaneously recording from the same subject and from the same area of the rat brain. Remarkably, the two organic ECoG sensors (OECT and surface electrode) reported higher SNR as respect to the Ir-penetrating electrodes. Moreover, the OECTs devices yielded to SNRs up to 44dB, against a 24dB of the simple surface electrode, highlighting the great advantages of in-situ amplification provided by organic transistors-based neural interfaces.

The same research group realized the architecture reported in ***Figure 1.11a*** over a rigid and removable shuttle, hence fabricating a penetrating and flexible neural interface, where an OECT and an adjacent surface electrode can be inserted deep into the brain[Williamson15]. The surface electrode could be used as a local gate for each transistor, as a sink for stimulation currents, or as a simple recording or stimulation electrode. ***Figure 1.11d*** shows the penetrating probe (flexible neural interface and shuttle) as well the representation of how the probe is inserted and how the shuttle is delaminated from the parylene substrate and therefor removed from the brain.

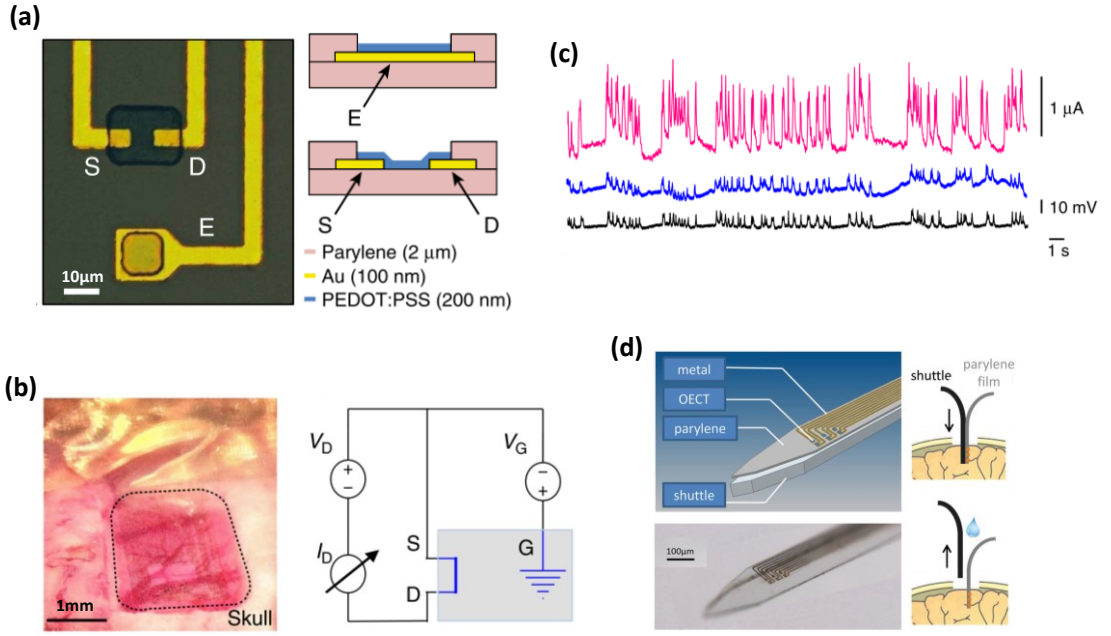

Figure 1.11. **(a)** *Optical micrograph (left) and schematic layout (right) of the channel of OECT and surface electrode (left), in which the Au films that act as source (S), drain (D) and electrode pad (E) are identified.* **(b)** *Optical micrograph of the ECoG probe placed over the somatosensory cortex (left) with the craniotomy surrounded by dashed lines; and wiring layout of the transistor (right) with the blue box indicating the brain of the animal.* **(c)** *Recordings from an OECT (pink), a PEDOT:PSS surface electrode (blue) and an Ir-penetrating electrode (black). The transistor was biased with VDS=-0.4V and VGS=-0.3V, and the scale of 10mV is for both surface and penetrating electrodes.* **(d)** *Layout of the entire probe showing the parylene and the shuttle parts (top), corresponding optical micrograph (bottom), and principle of delamination (right).*
Reproduced with permission from: [Khodagholy13a] for **(a)**, **(b)**, *and* **(c)**; *[Williamson15] for* **(d)**.

Similar to the OECTs technology, electrolyte-gated organic field-effect transistors (EGOFETs), also known as water-gated OFET, are worth to be mentioned. EGOFETs devices can operate either with pure water or saline solutions as gate medium, and they can be fabricated using many different semiconductors (both p- and n-type)[Cramer12, Kergoat10, Porrazzo14, Porrazzo17].

Such transistors are characterized by currents that are much smaller than the OECT counterpart[Khodagholy13b, Larsson11]. However, in an OECT, the on/off switch is produced by transfer of ions from the electrolyte and the semiconductor (doping/de-doping)[Kergoat12], whereas only capacitive processes occur for EGOFETs, without charge transfer[Wang16]. Consequently, EGOFETs are intrinsically faster and more stable than OECTs[Larsson11], hence they can be successfully employed as sensors for different kind of analytes (for a review see [Wang16]).

Cramer et al. deposited a thin film of pentacene, with a thickness of 9nm, to fabricate EGOFET devices to perform in vitro recording and stimulation (using the liquid gate as stimulating electrode) of neural network activity (***Figure 1.12a***)[Cramer13]. They showed that murine neural stem cells can be adhered on top of functional devices without the need for an additional layer of cell-adhesive molecules (e.g. PDL), and then differentiated into neuronal networks (***Figure 1.12b***). The EGOFET-based sensor exhibited a very good stability under standard cell culture conditions for nine days, and, after liquid-gate stimulation, it was able to successfully detect the neural network activity (***Figure 1.12c***).

The same group recently showed that EGOFETs devices with incorporated gold nanoparticles (***Figure 1.12d***) can behave both as a transistor and as a memristor[Desbief16], hence opening the door to new multifunctional bio-sensing devices.

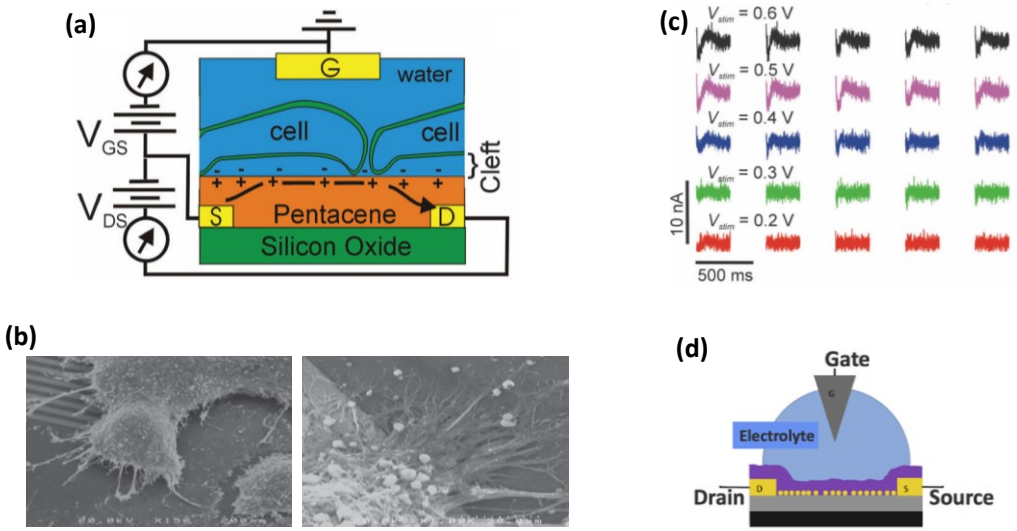

Figure 1.12. **(a)** *Schematic of the pentacene-based EGOFET interfaced with neurons.* **(b)** *SEM micrographs: details of neurons on active devices at day 9 after performing the electrical analysis.* **(c)** *Current traces measured after stimulations of varying intensity.* **(d)** *Schematic representation of the EGOFET with gold nanoparticles incorporated in the semiconductor.*
Reproduced with permission from: [Cramer13] for **(a)**, **(b)**, *and* **(c)**; *[Desbief16] for* **(d)**.

Graphene solution-gated field-effect transistors (G-SGFETs) depicted in ***Figure 1.13a***, are another alternative to stiff inorganic neural interfaces (***Figure 1.13b*** shows an array of eight G-SGFETs). Blaschke et al. demonstrated the fabrication of flexible arrays of G-SGFETs on polyimide (***Figure 1.13c***), showing that the electronic properties of their devices do not degrade during repeated bending[Blaschke16]. After cell culture, they demonstrated that it is possible to perform recording of cell action potentials from cardiomyocyte-like cells with a high SNR, as shown in ***Figure 1.13d***.

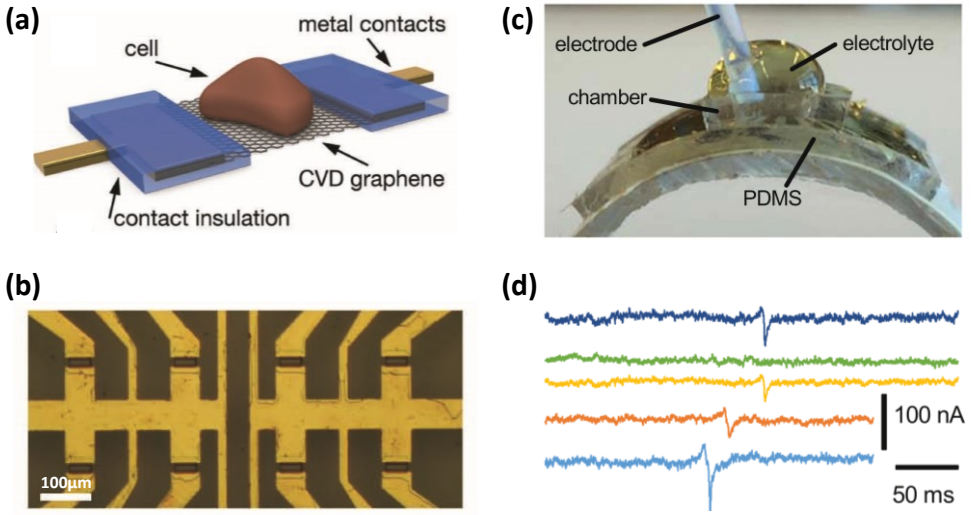

Figure 1.13. **(a)** *Schematic view of a G-SGFET with a cell on the gate area.* **(b)** *Optical microscopy image showing eight transistors in the central area of a G-SGFET array.* **(c)** *Image of a flexible G-SGFET device bent in convex shape.* **(d)** *Current of several G-SGFETs showing action potential recordings of cardiomyocyte-like cells. During cell experiments, the transistors were operated at a constant source-drain and gate voltage.*
Reproduced with permission from: [Hess11] for **(a)** *and* **(b)**; *[Blaschke16] for* **(c)** *and* **(d)**.

In another work, the same group demonstrated that G-SGFETs can record cell signals with SNRs surpassing state-of-the-art devices for bioelectronic applications[Hess11], proving that graphene-based sensors could pave the way to new high performance neural interfaces for *in vivo* recording.

Finally, it is important to notice that, each neural interface described so far require the presence of a reference electrode to set the MEA reference potential or to set the operative point of the transistor-based sensor (gate electrode). However, to maximize the suitability for *in vivo* recording and to overcame the drawback of the presence of an additional, and often invasive, electrode, it is highly desirable to avoid the presence of the reference electrode.

For this reason, Spanu et al. developed a reference-less organic transistor-based sensor called organic charge modulated field-effect transistor (OCMFET)[Spanu15]. The OCMFET device depicted in ***Figure 1.14a*** is characterized by a floating gate and a control gate. The latter set the operative point of the transistor, whereas the floating gate, i.e. the OCMFET sensing area, extends outside of the active area of the transistor. Ionic charge variations occurring in proximity of the sensing area determine a charge separation in the floating gate corresponding to a variation of the threshold voltage of the transistor, hence modulating the drain-to-source current. Since the modulation of current is induced only by the variation of ions in the proximity of the floating gate sensing area, cell activity can be successfully recorded without the need of any reference electrode put in contact with the solution (***Figure 1.14b***).

Remarkably, the OCMFET architecture allows to separate the sensing area from the transducing transistor (***Figure 1.14c***), hence the organic transistor can be design and optimized regardless its chemical stability, since it does not need to be in direct contact with any solutions and it can be opportunely encapsulated.

Notice that, the sensing area of the device can be opportunely functionalized to sense different kind of analytes. For instance, PH-sensing performed using the OCMFET architecture has been recently reported[Spanu17].

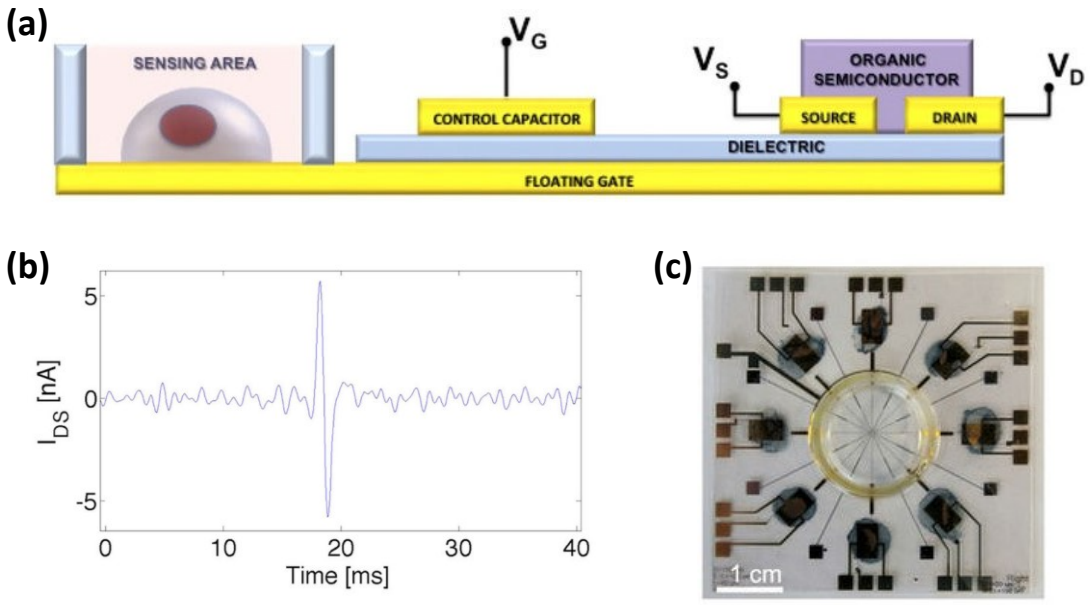

Figure 1.14. **(a)** *Cross section of an OCMFET device.* **(b)** *Single action potential measured with an OCMFET.* **(c)** *A complete device with 8 OCMFETs and 8 microelectrodes; in the center of the substrate, the sensing pads are surrounded by a glass ring that allows confining the culture medium with the cells.*
Reproduced with permission from [Spanu15].

1.4. Modeling of neural interfaces

In the previous chapters (***1.2*** and ***1.3***) we reviewed different neural interfaces, focusing our attention to the latest findings in the field of organic bio-electronics (chapter ***1.3***). It is important now to spend few words about how to model such systems, and therefore to understand how to interpret the collected data.

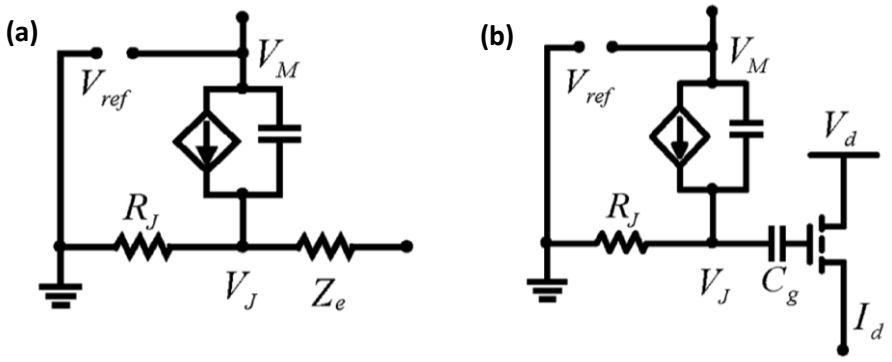

Figure 1.15. **(a)** *Simple equivalent circuit model for extracellular recording with a micro-electrode.* **(b)** *Simple equivalent circuit model for extracellular recording with a micro-electrode. Reproduced from [Fang15].*

Figure 1.15 shows the simplest equivalent circuit model that can be adapt to describe the interaction between the cell membrane and a micro-electrode (***Figure 1.15a***) as well as a generic transistor (***Figure 1.15b***). Despite their simplicity, such models are very useful to understand the general working principle of extracellular recording. Indeed, the neuronal activity is given by ionic currents flowing across the cell membrane, changing both the intracellular potential, V_M, and extracellular potential, V_J. The extracellular potential then leads to an electrochemical current at the electrode/electrolyte interface (***Figure 1.15a***) or drives the gate of the transistor-base sensor modulating its drain-to-source current (***Figure 1.15b***)[Fang15]. Although such simple models can help in the understanding of the bio-sensors working principles, they do not allow an intimate knowledge of the cell activity and how the recorded signals are affected by the interaction between neurons and sensors. This is still a subject of intense investigation that, in the last two decades, had led to a significant number of publications[Bove95, Fromherz99, Jianhui05, Joucla12, Joye09, Massobrio16, Schoen07, Thakore12, Weis97].

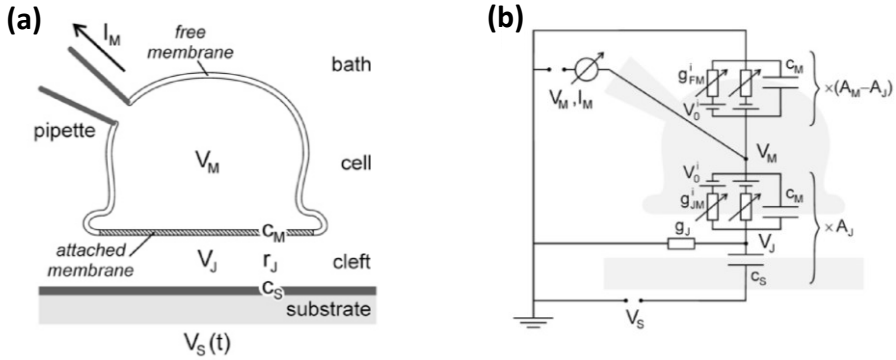

Figure 1.16. **(a)** *Schematic view of a neuron interfaced with a capacitor.* **(b)** *Equivalent circuit of the neural interface in* (a)*, where A_M is the area of the cell membrane, A_J is the area of the cell/sensor junction, and $A_M - A_J$ is the area of the free membrane. Reproduced with permission from [Schoen07].*

Figure 16 reports the equivalent circuit model for a neuron interfacing a biosensor. Even though such model dates back to the nineties[Fromherz99], it is a very powerful tool in understanding cells behavior under current and voltage stimuli as well in the interpretation of the recorded data both from micro-electrodes and transistors.

Moreover, all the different models until now proposed are derived (with suitable modifications) from the model of ***Figure 1.16b***[Jianhui05, Joucla12, Joye09, Massobrio16, Thakore12].

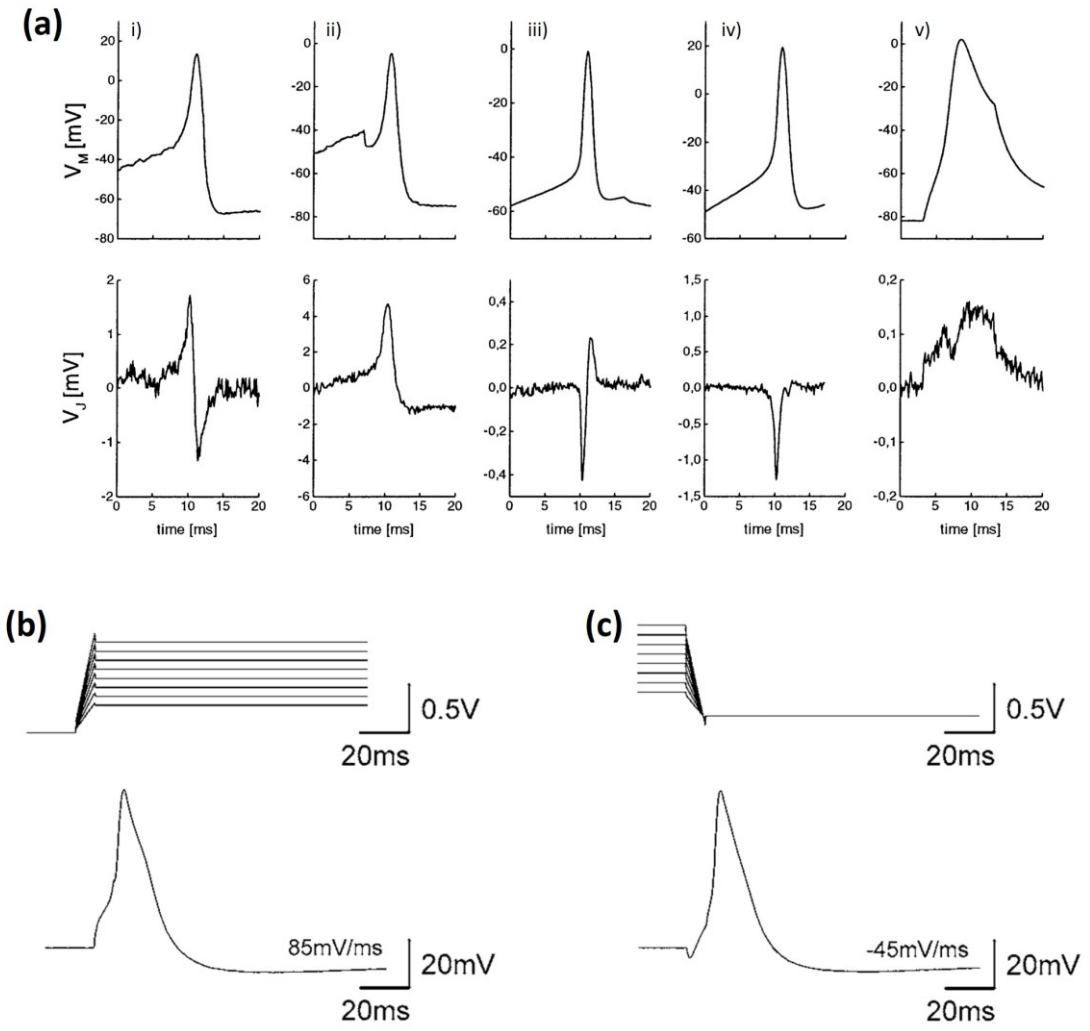

Figure 1.17. **(a)** *Intracellular voltage V_M elicited by injection of current measured with a micropipette (upper row) and extracellular voltage V_J measured with a EOSFET (lower row): i) capacitive response; ii) ohmic response; iii) anti-capacitive response; iv) Early anti-capacitive response; v) Early capacitive response with secondary positive response.* **(b)** *Capacitive stimulation under current-clamp by falling ramps.* **(c)** *Capacitive stimulation under current-clamp by rising ramps. Reproduced with permission from: [Fromherz07] for* **(a)***; [Schoen07] for* **(b)** *and* **(c)**.

Using the equivalent circuit of ***Figure 1.16b***, Fromherz proposed the approximation of a fast ($(C_M+C_S)dV_J/dt << g_JV_J$), weak ($\sum g^i_{JM} < g_J$) and small ($A_J/(A_M - A_J) << 1$) cell-silicon junction to interpret the data recorded by an EOSFET (***Figure 1.17a***)[Fromherz99].

In addition, the model in ***Figure 1.16b*** can be used to rationalize the mechanism behind the extracellular stimulations by means of a capacitive electrode[Schoen07]. Neuronal excitation is elicited under current-clamp by two mechanisms: i) falling voltage ramps and pulses depolarize the attached membrane triggering an action potential (***Figure 1.17b***); ii) rising voltage ramps and pulses, instead, depolarize the free membrane, hence an action potential is triggered (***Figure 1.17c***).

Finally, to underline the importance of equivalent circuit models, it is worth to remark that opportune models can be combined with *in vivo* electrochemical impedance spectroscopy (EIS) to monitor the state of the implant during time[Caldwell18, Hébert16, Lempka09, McConnell09, Sankar14, Venuto14, Williams07].

For instance, Williams et al. performed EIS measurements of implanted electrodes upon implants duration form 7 up to 21 days[Williams07]. ***Figure 1.18a*** reports an example of impedance variation due to an extensive histological reaction that lead to a significant increase of the measured impedance and consequently, to the implant failure.

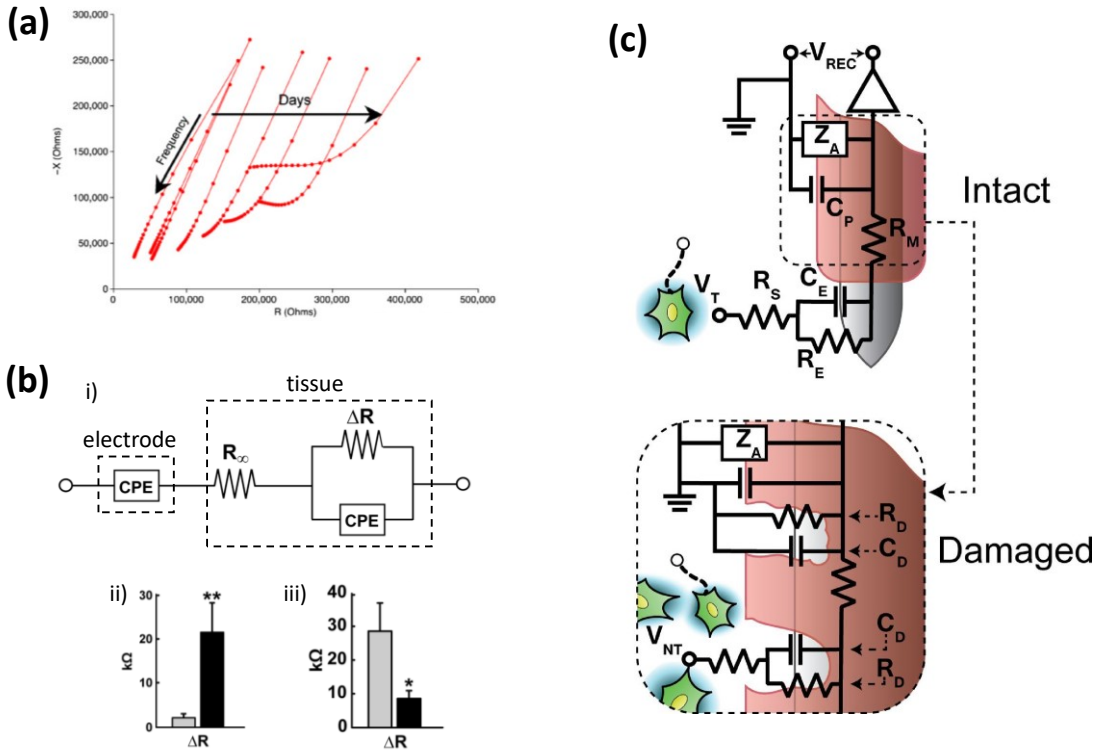

Figure 1.18. **(a)** *Nyquist plots for an electrode characterized by an extensive reaction. Data are presented immediately following implant and on each of the first 7 days post-implant.* **(b)** *i) Equivalent circuit model discriminating the electrode component and the tissue component. ii) example of resistance increase after 15 days implantation iii) example of resistance decrease after stimulation.* **(c)** *Dielectric coating on a neural electrode emphasizing how the insulation damage creates undesired current pathways.*
*Reproduced with permission from: [Williams07] for **(a)**; [Lempka09] for **(b)**; [Caldwell18] for **(c)**.*

Another example of using EIS as a tool to characterize the implant during in vivo applications was reported by Lempka et al.[Lempka09]. They characterized deep-brain stimulation electrodes using the model in ***Figure 1.18b***, where they separated the tissue components by the electrode components, and they monitor variations in the model parameters after implantations and after a neural stimulation. As previously reported by Williams et al., following the implantation, the electrode impedance increases. Remarkably, the stimulation produces a rapid decrease in electrode impedance with extensive changes in the tissue component promoting the use of voltage pulses to improve the performance of implanted electrodes[Johnson05, Otto06].

Similarly, Caldwell et al. performed EIS measurement to investigated the formation of undesired conductive paths and consequent loss of functionality in the implant[Caldwell18]. By analyzing the impedance of the implant, the authors showed that such unwanted paths are due to the damaging of the electrode insulator, as reported in the model of ***Figure 1.18c***. Hence proving how the combination of EIS measurements and proper models can pave the way to intimately understand and optimize neural interfaces for long term *in vivo* implants.

1.5. Summary and future perspectives

In this introduction, different neural interfaces have been reviewed.

We showed that state-of-the-art inorganic technologies allow both *in vivo* and *in vitro* recording of neural activity. However, the rigidity and stiffness of the inorganic materials do not fully meet the biocompatibility requirements needed to achieve long term stability and reliability *in vivo*. Hence, to promote a good interaction between living tissues and implants, reducing the risk of implant rejection and/or of inflammatory responses, opportune coatings and functionalizations with soft and biocompatible polymers are required.

For all these reasons, organic electronics (i.e. based on polymer and small molecules) appears to be a valid alternative to conventional technologies, allowing the realizations of more flexible and conformable neural interfaces that can be intrinsically biocompatible since the nature of the organic semiconductors is closer to that of the living tissues as respect with the inorganic counterpart. Moreover, organic materials can be tuned to enhance the device sensitivity to a particular analyte, and organic neural interfaces can be fabricated onto transparent substrate promoting the combination of optical and electrical analysis.

The most attractive technology is that based on organic field-effect transistors (both OECTs and EGOFETs) that allow the integration of sensing and amplification in a single device. Such neural interfaces have proven higher SNR as respect with the inorganic-based sensors, paving the way to new all-organic biosensors for *in vivo* recording of brain activity with minimum risk of tissues damaging. In addition, reference-less organic neural interfaces have been proposed.

Despite all these achievements, the comprehension of the transduction mechanism between cells and transistor-based sensors did no progressed as fast as the development of new technologies. Moreover, organic transistors and organic transistor based sensors are a relative novel technology that differs in many aspects from the standard silicon transistor. In order to master the transduction mechanism behind an organic neural interface working principle, it is therefore important the development of new tools and techniques to characterize and describe the physic of transport in organic transistors, as well to fully understand and model the interaction between ionic solution and organic semiconductor.

In addition, organic neural interfaces still suffer from a low selectivity due to a reduced integration capacity as respect with the CMOS technology. Hence, to achieve *in vivo* single-cell bidirectional communication (stimulation and sensing), new technologies and fabrication processes must be developed.

In the following chapters, with the aim of developing a reference-less organic transistor to simultaneously stimulate and record cell activity that could be suitable for the inclusion in a highly integrated array of sensors, we perform advanced characterizations of organic field-effect transistors to investigate the mechanisms of the conductive channel accumulation and depletion (chapter ***2***).

Later on, in chapter ***3***, we study the physical processes occurring at the organic semiconductor/solution interface.

Finally, in chapter ***4***, we propose the reference-less electrolyte-gated organic field-effect transistor to simultaneous stimulation and sensing of cell electrical activity without the need of any reference electrode.

References

[Ahmadi16] E. Ahmadi, H. A. Katnani, L. D. Besheli, Q. Gu, R. Atefi, M. Y. Villeneuve, E. Eskandar, M. H. Lev, A. J. Golby, R. Gupta, and G. Bonmassar, *An Electrocorticography Grid with Conductive Nanoparticles in a Polymer Thick Film on an Organic Substrate Improves CT and MR Imaging*, **Radiology**, vol. 280, issue 2, pp. 595-601, Aug. 2016.

[Akamatu52] H. Akamatu and H. Inokuchi, *Photoconductivity of Violanthrone*, **J. Chem. Phys.**, vol. 20, issue 9, pp. 1481-1483, Apr. 1952.

[Alivisatos13] A. P. Alivisatos, A. M. Andrews, E. S. Boyden, M. Chun, G. M. Church, K. Deisseroth, J. P. Donoghue, S. E. Fraser, J. L.-Schwartz, L. L. Looger, S. Masmanidis, P. L. McEuen, A. V. Nurmikko, H. Park, D. S. Peterka, C. Reid, M. L. Roukes, A. Scherer, M. Schnitzer, T. J. Sejnowski, K. L. Shepard, D. Tsao, G. Turrigiano, P. S. Weiss, C. Xu, R. Yuste, and X. Zhuang, *Nanotools for Neuroscience and Brain Activity Mapping*, **ACS Nano**, vol. 7, issue 3, pp. 1850-1866, Mar. 2013.

[Amiji93] M. Amiji and K. Park, *Surface modification of polymeric biomaterials with poly(ethylene oxide), albumin, and heparin for reduced thrombogenicity*, **J. Biomater. Sci. Polym. Ed.**, vol. 4, issue 3, pp. 217-234, 1993.

[An17] B. W. An, J. H. Shin, S.-Y. Kim, J. Kim, S. Ji, J. Park, Y. Lee, J. Jang, Y.-G. Park, E. Cho, S. Jo, and J. U. Park, *Smart Sensor Systems for Wearable Electronic Devices*, **Polymers**, vol. 9, issue 8, Jul. 2017.

[Apollo15] N. V. Apollo, M. I. Maturana, W. Tong, D. A. X. Nayagam, M. N. Shivdasani, J. Foroughi, G. G. Wallace, S. Prawer, M. R. Ibbotson, and D. J. Garrett, *Soft, Flexible Freestanding Neural Stimulation and Recording Electrodes Fabricated from Reduced Graphene Oxide*, **Adv. Funct. Mater.**, vol. 25, issue 23, pp. 3551-3559, Jun. 2015.

[Arshady93] R. Arshady, *Microspheres for biomedical applications: preparation of reactive and labelled microspheres*, **Biomaterials**, vol. 14, issue 1, pp. 5-15, 1993.

[Badi03] A. N. Badi, T. R. Kertesz, R. K. Gurgel, C. Shelton, and R. A. Normann, *Development of a Novel Eighth-Nerve Intraneural Auditory Neuroprosthesis*, **The Laryngoscope**, vol. 113, issue 5, pp. 833-842, May 2003.

[Ballini14] M. Ballini, J. Müller, P. Livi, Y. Chen, U. Frey, A. Stettler, A. Shadmani, V. Viswam, I. L. Jones, D. Jäckel, M. Radivojevic, M. K. Lewandowska, W. Gong, M. Fiscella, D. J. Bakkum, F. Heer, and A. Hierlemann, *A 1024-Channel CMOS Microelectrode Array With 26,400 Electrodes for Recording and Stimulation of Electrogenic Cells In Vitro*, **IEEE J. Solid-State Circuits**, vol. 49, issue 11, pp. 2705-2719, Nov. 2014.

[Barz17] F. Barz, A. Livi, M. Lanzilotto, M. Maranesi, L. Bonini, O. Paul, and P. Ruther *Versatile, modular 3D microelectrode arrays for neuronal ensemble recordings: from design to fabrication, assembly, and functional validation in non-human primates*, **J. Neural Eng.**, vol. 14, issue 3, p. 036010, Mar. 2017.

[Berets68] D. J. Berets and D. S. Smith, *Electrical properties of linear polyacetylene*, **Trans. Faraday Soc.**, vol. 64, pp. 823-828, 1968.

[Berggren07] M. Berggren, A. R.-Dahlfors, *Organic Bioelectronics*, ***Adv. Mater.***, vol. 19, issue 20, pp. 3201-3213, Oct. 2007.

[Bernards07] D. A. Bernards, and G. G. Malliaras, *Steady-State and Transient Behavior of Organic Electrochemical Transistors*, **Adv. Funct. Mater.**, vol. 17, issue 17, pp. 3538-3544, Nov. 2007.

[Blaschke16] B. M. Blaschke, M. Lottner, S. Drieschener, A. B. Calia, K. Stoiber, L. Rousseau, G. Lissourges, and J. A. Garrido, *Flexible graphene transistors for recording cell action potentials*, **2D Mater.**, vol. 3, issue 2, no. 025007, Apr. 2016.

[Bolto63] B. Bolto, R. McNeill, and D. Weiss, *Electronic Conduction in Polymers. III. Electronic Properties of Polypyrrole*, **Aust. J. Chem.**, vol. 16, issue 6, pp. 1090-1103, Dec. 1963.

[Bove95] M. Bove, M. Grattarola, S. Martinoia, and G. Verreschi, *Interfacing cultured neurons to planar substrate microelectrodes: characterization of the neuron-to-microelectrode junction*; **Bioelectrochem. Bioenerg.**, vol. 38, issue 2, pp. 255-265, Oct. 1995.

[Brophy61] J. J. Brophy, *Organic semiconductors*, **Phys. Today,** vol. 14, issue 8, pp. 40-41, Aug. 1961.

[Burroughes90] J. H. Burroughes, D. D. C. Bradley, A. R. Brown, R. N. Marks, K. Mackay, R. H. Friend, P. L. Burns, and A. B. Homes, *Light-emitting diodes based on conjugated polymers*, **Nature**, vol. 347, issue 6293, pp. 539-541, Oct. 1990.

[Buzsáki12] G. Buzsáki, C. A. Anastassiou, and C. Koch, *The origin of extracellular fields and currents — EEG, ECoG, LFP and spikes*, **Nat. Rev. Neurosci.**, vol. 13, issue 6, pp. 407-420, Jun. 2012.

[Caldwell18] R. Caldwell, R. Sharma, P. Takmakov, M. G. Street, F. Solzbacher, P. Tathireddy, and L. Rieth, *Neural electrode resilience against dielectric damage may be improved by use of highly doped silicon as a conductive material*, **J. Neurosci. Methods**, vol. 293, pp. 210-225, Jan. 2018.

[Capeletti16] L. B. Capeletti, M. B. Cardoso, J. H. Z. dos Santos, and W. He, *Hybrid Thin Film Organosilica Sol–Gel Coatings To Support Neuronal Growth and Limit Astrocyte Growth*, **ACS Appl. Mater. Interfaces**, vol. 8, issue 41, pp. 27553-27563, Oct. 2016.

[Chang07] T. Y. Chang, V. Yadav, S. D. Leo, A. Mohedas, B. Rajalingam, C.-L. Chen, S. Selvarasah, M. R. Dokmeci, and A. Khademhosseini, *Cell and Protein Compatibility of Parylene-C Surfaces*, **Langmuir**, vol. 23, issue 23, pp. 11718-11725, Nov. 2007.

[Chang13] C.-W. Chang and J.-C. Chiou, *A Wireless and Batteryless Microsystem with Implantable Grid Electrode/3-Dimensional Probe Array for ECoG and Extracellular Neural Recording in Rats*, **Sensors**, vol. 13, issue 4, pp. 4624-4639, Apr. 2013.

[Chen13] Z. Chen, H. Lee, S. J. Henle, T. R. Cheever, S. C. Ekker, and J. R. Henley, "*Primary Neuron Culture for Nerve Growth and Axon Guidance Studies in Zebrafish (Danio rerio)*, **PLoS ONE**, vol. 8, issue 3, no. e57539, Mar. 2013.

[Chen17] R. Chen, A. Canales, and P. Anikeeva, *Neural recording and modulation technologies*, **Nat. Rev. Mater.**, vol. 2, no. 16093, Jan. 2017.

[Cheng06] C.-Y. Cheng, C.-H. Yao, B.-S. Liu, C.-J. Liu, G.-W. Chen, and Y.-S. Chen, *The role of astragaloside in regeneration of the peripheral nerve system*, **J. Biomed. Mater. Res. A**, vol. 76A, issue 3, pp. 463-469, Mar. 2006.

[Chestek11] C. A. Chestek, V. Gilja, P. Nuyujukian, J. D. Foster, J. M. Fan, M. T. Kaufman, M. M. Churchland, Z. R.-Alvidrez, J. P. Cunningham, and S. I. Ryu, *Long-term stability of neural prosthetic control signals from silicon cortical arrays in rhesus macaque motor cortex*, **J. Neural Eng.**, vol. 8, issue 4, no. 045005, Jul. 2011.

[Cheung07] K. C. Cheung, *Implantable microscale neural interfaces*, **Biomed. Microdevices**, vol. 9, issue 6, pp. 923-938, Dec. 2007.

[Chiang77] C. K. Chiang C. R. Fincher, Y. W. Park, A. J. Heeger, H. Shirakawa, E. J. Louis, S. C. Gau, and A. G. MacDiarmid, *Electrical Conductivity in Doped Polyacetylene*, **Phys. Rev. Lett.**, vol. 39, issue 17, pp. 1098-1101, Oct. 1977.

[Cogan04] S. F. Cogan, A. A. Guzelian, W. F. Agnew, T. G. H. Yuen, and D. B. McCreery, *Over-pulsing degrades activated iridium oxide films used for intracortical neural stimulation*, **J. Neurosci. Methods**, vol. 137, issue 2, pp. 141-150, Aug. 2004.

[Cramer12] T. Cramer, A. Kyndiah, M. Murgia, F. Leonardi, S. Casalini, and F. Biscarini, *Double layer capacitance measured by organic field effect transistor operated in water*, **Appl. Phys. Lett.**, vol. 100, issue 14, pp. 143302, Apr. 2012.

[Cramer13] T. Cramer, B. Chelli, M. Murgia, M. Barbalinardo, E. Bystrenova, D. M. de Leeuw, and F. Biscarini, *Organic ultra-thin film transistors with a liquid gate for extracellular stimulation and recording of electric activity of stem cell-derived neuronal networks*, **Phys. Chem. Chem. Phys.**, vol. 15, issue 11, pp. 3897-3905, Mar. 2013.

[Desbief16] S. Desbief, M. di Lauro, S. Casalini, D. Guerin, S. Tortorella, N. Barbalinardo, A. Kyndiah, M. Murgia, T. Cramer, F. Biscarini, and D. Vuillaume, *Electrolyte-gated organic synapse transistor interfaced with neurons*, **Org. Electron.**, vol. 38, pp. 21-28, Nov. 2016.

[Deslouis96] C. Deslouis, T. E. Moustafid, M. M. Musiani, and B. Tribollet, *Mixed ionic-electronic conduction of a conducting polymer film. Ac impedance study of polypyrrole*, **Electrochim. Acta**, vol. 41, issues 7-8, pp. 1343-1349, May-Jun. 1996.

[Dong17] S. Dong, W. Chen, X. Wang, S. Zhang, K. Xu, and X. Zheng, *Flexible ECoG electrode for implantation and neural signal recording applications*, **Vacuum**, vol. 140, pp. 96-100, Jun. 2017.

[Edell92] D. J. Edell, V. V. Toi, V. M. McNeil, and L. D. Clark, *Factors influencing the biocompatibility of insertable silicon microshafts in cerebral cortex*, **IEEE Trans. Biomed. Eng.**, vol. 39, issue 6, pp. 635-643, Jun. 1992.

[Eley53] D. D. Eley, G. D. Parfitt, M. J. Perry, and D. H. Taysum, *The semiconductivity of organic substances. Part 1*, **Trans. Faraday Soc.**, vol. 49, pp. 79-86, Jan. 1953.

[Eversmann03] B. Eversmann, M. Jenkner, F. Hofmann, C. Paulus, R. Brederlow, B. Holzapfi, P. Fromherz, M. Merz, M. Brenner, M. Schreiter, R. Galb, K. Plehnert, M. Steinhauser, G. Eckstein, D. S.-Landsiedel, and R. Thewes, *A 128 x 128 CMOS biosensor array for extracellular recording of neural activity*, **IEEE J. Solid-State Circuits**, vol. 38, issue 12, pp. 2306-2317, Dec. 2003.

[Fang15] Y. Fang, X. Li, Y. Fang, *Organic bioelectronics for neural interfaces*, **J. Mater. Chem. C**, vol. 3, issue 25, pp. 6424-6430, Jun. 2015.

[Fattahi14] P. Fattahi, G. Yang, G. Kim, and M. R. Abidian, *A Review of Organic and Inorganic Biomaterials for Neural Interfaces*, **Adv. Mat.**, vol. 26, issue 12, pp. 1864-1885, March 2014.

[Felderer11] F. Felderer and P. Fromherz, *Transistor needle chip for recording in brain tissue*," **Appl. Phys. A**, vol. 104, issue 1, p. 1, May 2011.

[Fromherz91] P. Fromherz, A. Offenhausser, T. Vetter, and J. Weis, A Neuron-Silicon Junction: A Retzius Cell of the Leech on an Insulated-Gate Field-Effect Transistor. **Science**, vol. 252, issue 5010, pp. 1290-1293, May 1991.

[Fromherz99] P. Fromherz, *Extracellular recording with transistors and the distribution of ionic conductances in a cell membrane*, **Eur. Biophys. J.**, vol. 28, issue 3, pp. 254-258, Mar. 1999.

[Fukushima14] M. Fukushima, R. C. Saunders, M. Mullarkey, A. M. Doyle, M. Mishkin, and N. Fujii, *An electrocorticographic electrode array for simultaneous recording from medial, lateral, and intrasulcal surface of the cortex in macaque monkeys*, **J. Neurosci. Methods**, vol. 233, pp. 155-165, Aug. 2014.

[Garnier90] F. Garnier, G. Horowitz, X. Peng, and D. Fichou, *An all-organic 'soft' thin film transistor with very high carrier mobility*, **Adv. Mater.**, vol. 2, issue 12, pp. 592-594, Dec. 1990.

[Głowacki13] E. D. Głowacki, M. I.-Vladu, M. Kaltenbrunner, J. Gsiorowski, M. S. White, U. Monkowius, G. Romanazzi, G. P. Suranna, P. Mastrorilli, T. Sekitani, S. Bauer, T. Someya, L. Torsi, and N. S. Sariciftci, *Hydrogen-Bonded Semiconducting Pigments for Air-Stable Field-Effect Transistors*, **Adv. Mater.**, vol. 25, issue 11, pp. 1563-1569, Mar. 2013.

[Goulart16] C. O. Goulart, F. R. P. Lopes, Z. O. Monte, S. V. Dantas, A. Souto, J. T. Oliveira, F. M. Almeida, C. T.-Turo, C. C. Pereira, C. P. Borges, and A. M. B. Martinez, *Evaluation of biodegradable polymer conduits – poly(l-lactic acid) – for guiding sciatic nerve regeneration in mice*, **Methods**, vol. 99, no. Supplement C, pp. 28-36, Apr. 2016.

[Guidoin89] R. Guidoin, D. Marceau, J. Couture, T. J. Rao, Y. Merhi, P.-E. Roy, and D. D. la Faye, *Collagen coatings as biological sealants for textile arterial prostheses*, **Biomaterials**, vol. 10, issue 3, pp. 156-165, Apr. 1989.

[Guo17] Y. Guo, S. Jiang, B. J. B. Grena, I. F. Kimbrough, E. G. Thompson, Y. Fink, H. Sontheimer, T. Yoshinobu, and X. Jia, *Polymer Composite with Carbon Nanofibers Aligned during Thermal Drawing as a Microelectrode for Chronic Neural Interfaces*, **ACS Nano**, vol. 11, issue 7, pp. 6574-6585, Jun. 2017.

[Gustafsson92] G. Gustafsson, Y. Cao, G. M. Treacy, F. Klavetter, N. Colaneri, and A. J. Heeger, *Flexible light-emitting diodes made from soluble conducting polymers*, **Nature**, vol. 357, issue 6378, pp. 477-479, Jun. 1992.

[Harnack04] D. Harnack, C. Winter, W. Meissner, T. Reum, A. Kupsch, and R. Morgenstern, *The effects of electrode material, charge density and stimulation duration on the safety of high-frequency stimulation of the subthalamic nucleus in rats*, **J. Neurosci. Methods**, vol. 138, issue 1, pp. 207-216, Oct. 2004.

[Harris17] A. R. Harris and G. G. Wallace, *Organic Electrodes and Communications with Excitable Cells*, **Adv. Funct. Mater.**, Jul. 2017.

[Hatsopoulos09] N. G. Hatsopoulos and J. P. Donoghue, *The Science of Neural Interface Systems*, **Annu. Rev. Neurosci.**, vol. 32, issue 1, pp. 249-266, Apr. 2009.

[Hébert16] C. Hébert, M. Cottance, J. Degardin, E. Scorsone, L. Rousseau, G. Lissorgues, P. Bergonzo, and S. Picaud, *Monitoring the evolution of boron doped porous diamond electrode on flexible retinal implant by OCT and in vivo impedance spectroscopy*, **Mater. Sci. Eng. C**, vol. 69, pp. 77-84, Dec. 2016.

[Heiduschka98] P. Heiduschka and S. Thanos, *Implantable bioelectronic interfaces for lost nerve functions*, **Prog. Neurobiol.**, vol. 55, issue 5, pp. 433-461, Aug. 1998.

[Hepp03] A. Hepp, H. Heil, W. Weise, M. Ahles, R. Schmechel, and H. von Seggern, *Light-Emitting Field-Effect Transistor Based on a Tetracene Thin Film*, **Phys. Rev. Lett.**, vol. 91, issue 15, p. 157406, Oct. 2003.

[Hess11] L. H. Hess, M. Jansen, V. Maybeck, M. V. Hauf, M. Seifert, M. Stutzmann, I. D. Sharp, A. Offenhäusser, and J. A. Garrido, *Graphene Transistor Arrays for Recording Action Potentials from Electrogenic Cells*, **Adv. Mater.**, vol. 23, issue 43, pp. 5045-5049, Nov. 2011.

[Huang17] K.-M. Huang, H.-C. Lin, K. Kawashima, I. Osaka, H.-W. Zan, H.-F. Meng, and K. Takimiya, *2-V operated flexible vertical organic transistor with good air stability and bias stress reliability*, **Org. Electron.**, vol. 50, pp. 325-330, Nov. 2017.

[Humphrey70] D. R. Humphrey, E. M. Schmidt, and W. D. Thompson, *Predicting Measures of Motor Performance from Multiple Cortical Spike Trains*, **Science**, vol. 170, issue 3959, pp. 758-762, Dec. 1970.

[Jianhui05] L. Jianhui, W. Xiaoming, H. Pengsheng, R. Tianling, and L. Litian, *A 16-site neural recording probe array and its circuit model simulation*, **Proceedings. First International Conference on Neural Interface and Control**, pp. 68-71, 2005.

[Johnson05] M. D. Johnson, K. J. Otto, and D. R. Kipke, *Repeated voltage biasing improves unit recordings by reducing resistive tissue impedances*, **IEEE Trans. Neural Syst. Rehabil. Eng.**, vol. 13, issue 2, pp. 160-165, Jun. 2005.

[Joo15] S. Joo, J. Yeon Kim, E. Lee, N. Hong, W. Sun, and Y. Nam, *Effects of ECM protein micropatterns on the migration and differentiation of adult neural stem cells*, **Sci. Rep.**, vol. 5, p. 13043, Aug. 2015.

[Joucla12] S. Joucla and B. Yvert, *Modeling extracellular electrical neural stimulation: From basic understanding to MEA-based applications*, **J. Physiol.-Paris**, vol. 106, issues 3-4, pp. 146-158, May-Aug. 2012.

[Joye09] N. Joye, A. Schmid, and Y. Leblebici, *Electrical modeling of the cell–electrode interface for recording neural activity from high-density microelectrode arrays*, **Neurocomputing**, vol. 73, issue 1, pp. 250-259, Dec. 2009.

[Kaiju17] T. Kaiju, K. Doi, M. Yokota, K. Watanabe, M. Inoue, H. Ando, K. Takahashi, F. Yoshida, M. Hirata, and T. Suzuki, *High Spatiotemporal Resolution ECoG Recording of Somatosensory Evoked Potentials with Flexible Micro-Electrode Arrays*, **Front. Neural Circuits**, vol. 11, p. 20, Apr. 2017.

[Kang13] I. Kang, H.-J. Yun, D. S. Chung, S.-K. Kwon, and Y.-H. Kim, *Record High Hole Mobility in Polymer Semiconductors via Side-Chain Engineering*, **J. Am. Chem. Soc.**, vol. 135, issue 40, pp. 14896-14899, Sep. 2013.

[Kapnisis16] K. K. Kapnisis, C. Pitsillides, M. Prokopi, G. Lapathitis, C. Kariskos, P. C. Eleftheriou, B. C. Brott, P. G. Anderson, J. E. Lemons, and A. S. Anayiotos, *In vivo monitoring of the inflammatory response in a stented mouse aorta model*, **J. Biomed. Mater. Res. A**, vol. 104, issue 1, pp. 227-238, Jan. 2016.

[Kergoat10] L. Kergoat, L. Herlogsson, D. Braga, B. Piro, M.-C. Pham, X. Crispin, M. Berggren, and G. Horowitz, *A Water-Gate Organic Field-Effect Transistor*, **Adv. Mater.**, vol. 22, issue 23, pp. 2565-2569, Jun. 2010.

[Kergoat12] L. Kergoat, B. Piro, M. Berggren, G. Horowitz, and M.-C. Pham, *Advances in organic transistor-based biosensors: From organic electrochemical transistors to electrolyte-gated organic field-effect transistors*, **Anal. Bioanal. Chem.**, vol. 402, issue 5, pp. 1813-1826, Feb. 2012.

[Khan05] S. P. Khan, G. G. Auner, and G. M. Newaz, *Influence of nanoscale surface roughness on neural cell attachment on silicon*, **Nanomedicine Nanotechnol. Biol. Med.**, vol. 1, issue 2, pp. 125-129, Jun. 2005.

[Khodagholy13a] D. Khodagholy, T. Doublet, P. Quilichini, M. Gurfinkel, P. Leleux, A. Ghestem, E. Ismailova, T. Hervé, S. Sanaur, C. Bernard, and G. G. Malliaras, *In vivo recordings of brain activity using organic transistors*, **Nat. Commun.**, vol. 4, no. 1575, Mar. 2013.

[Khodagholy13b] D. Khodagholy, J. Rivnay, M. Sessolo, M. Gurfinkel, P. Leleux, L. H. Jimison, E. Stavrinidou, T. Herve, S. Sanaur, R. M. Owens, and G. G. Malliaras, *High transconductance organic electrochemical transistors*. **Nat. Commun.**, vol. 4, no. 2133, Jul. 2013.

[Kim10] D.-H. Kim, J. Viventi, J. J. Amsden, J. Xiao, L. Vigeland, Y.-S. Kim, J. A. Blanco, B. Panilaitis, E. S. Frechette, D. Contreras, D. L. Kaplan, F. G. Omenetto, Y. Huang, K.-C. Hwang, M. R. Zakin, B. Litt, and J. A. Rogers, *Dissolvable films of silk fibroin for ultrathin conformal bio-integrated electronics*, **Nat. Mater.**, vol. 9, issue 6, pp. 511-517, Jun. 2010.

[Kim11] Y. H. Kim, N. S. Baek, Y. H. Han, M.-A. Chung, and S.-D. Jung, *Enhancement of neuronal cell adhesion by covalent binding of poly-D-lysine*, **J. Neurosci. Methods**, vol. 202, issue 1, pp. 38-44, Oct. 2011.

[Kim13] T. Kim, J. G. McCall, Y. H. Jung, X. Huang, E. R. Siuda, Y. Li, J. Song, Y. M. Song, H. A. Pao, R.-H. Kim, C. Lu, S. D. Lee, I.-S. Song, G. Shin, R. A.-Hasani, S. Kim, M. P. Tan, Y. Huang, F. G. Omenetto, J. A. Rogers, and M. R. Bruchas, *Injectable, Cellular-Scale Optoelectronics with Applications for Wireless Optogenetics*, **Science**, vol. 340, issue 6129, pp. 211-216, Apr. 2013.

[Kishida91] A. Kishida, H. Iwata, Y. Tamada, and Y. Ikada, *Cell behaviour on polymer surfaces grafted with non-ionic and ionic monomers*, **Biomaterials**, vol. 12, issue 8, pp. 786-792, Oct. 1991.

[Kleinman85] H. K. Kleinman, F. B. Cannon, G. W. Laurie, J. R. Hassell, M. Aumailley, V. P. Terranova, G. R. Martin, and M. D.-Dalcq, *Biological activities of laminin*, **J. Cell. Biochem.**, vol. 27, issue 4, pp. 317-325, 1985.

[Kotov09] N. A. Kotov, J. O. Winter, I. P. Clements, E. Jan, B. P. Timko, S. Campidelli, S. Pathak, A. Mazzatenta, C. M. Lieber, M. Prato, R. V. Bellamkonda, G. A. Silva, N. W. S. Kam, F. Patolsky, and L. Ballerini, *Nanomaterials for Neural Interfaces*, **Adv. Mater.**, vol. 21, issue 40, pp. 3970-4004, Oct. 2009.

[Kuribara12] K. Kuribara, H. Wang, N. Uchiyama, K. Fukuda, T. Yokota, U. Zschieschang, C. Jaye, D. Fischer, H. Klauk, T. Yamamoto, K. Takimiya, M. Ikeda, H. Kuwabara, T. Sekitani, Y.-L. Loo, and T. Someya, *Organic transistors with high thermal stability for medical applications*, **Nat. Commun.**, vol. 3, issue 723, Mar. 2012.

[Larsson11] O. Larsson, A. Laiho, W. Schmickler, M. Berggren, and X. Crispin, *Controlling the Dimensionality of Charge Transport in an Organic Electrochemical Transistor by Capacitive Coupling*, **Adv. Mater.**, vol. 23, issue 41, pp. 4764-4769, Nov. 2011.

[Lee17] S. M. Lee, H. J. Byeon, B. H. Kim, J. Lee, J. Y. Jeong, J. H. Lee, J.-H. Moon, C. Park, H. Choi, S.-H. Lee, K.-H. Lee, *Flexible and implantable capacitive microelectrode for bio-potential acquisition*, **BioChip J.**, vol. 11, issue 2, pp. 153-163, Jun. 2017.

[Lempka09] S. F. Lempka, S. Miocinovic, M. D. Johnson, J. L. Vitek, and & C. C. McIntyre, *In vivo impedance spectroscopy of deep brain stimulation electrodes*. **J. Neural Eng.**, vol. 6, issue 4, no. 046001, Jun. 2009.

[Lin12] P. Lin, and F. Yan, *Organic Thin-Film Transistors for Chemical and Biological Sensing*, **Adv. Mater.**, vol. 24, issue 1, pp. 34-51, Jan. 2012.

[Liu15] J. Liu, T.-M. Fu, Z. Cheng, G. Hong, T. Zhou, L. Jin, M. Duvvuri, Z. Jiang, P. Kruskal, C. Xie, Z. Suo, Y. Fang, and C. M. Lieber, *Syringe-injectable electronics*, **Nat. Nanotech.**, vol. 10, issue 7, pp. 629-636, Jul. 2015.

[Mantione16] D. Mantione, I. del Agua, W. Schaafsma, J. D.-Garcia, B. Castro, H. Sardon, and D. Mecerreyes, *Poly(3,4-ethylenedioxythiophene):GlycosAminoGlycan Aqueous Dispersions: Toward Electrically Conductive Bioactive Materials for Neural Interfaces*, **Macromol. Biosci.**, vol. 16, issue 8, pp. 1227-1238, Aug. 2016.

[Marois95] Y. Marois, N. Chakfé, X. Deng, M. Marois, T. How, M. W. King, and R. Guidoin *Carbodiimide cross-linked gelatin: a new coating for porous polyester arterial prostheses*, **Biomaterials**, vol. 16, issue 15, pp. 1131-1139, Oct. 1995.

[Marois96] Y. Marois, N. Chakfé, R. Guodoin, R. C. Duhamel, R. Roy, M. Marois, M. W. King, and Y. Douville, *An albumin-coated polyester arterial graft: in vivo assessment of biocompatibility and healing characteristics*, **Biomaterials**, vol. 17, issue 1, pp. 3-14, Jan. 1996.

[Massobrio16] P. Massobrio, G. Massobrio, S. Martinoia, *Interfacing Cultured Neurons to Microtransducers Arrays: A Review of the Neuro-Electronic Junction Models*, **Front. Neurosci.**, vol. 10, pp. 282, Jun. 2016.

[Matsuzawa96] M. Matsuzawa, P. Liesi, and W. Knoll, *Chemically modifying glass surfaces to study substratum-guided neurite outgrowth in culture*, **J. Neurosci. Methods**, vol. 69, issue 2, pp. 189-196, Nov. 1996.

[Menon97] V. Menon, J. M. Ford, K. O. Lim, G. H. Glover, and A. Pfefferbaum, *Combined event-related fMRI and EEG evidence for temporal—parietal cortex activation during target detection*, **NeuroReport**, vol. 8, issue 14, Sep. 1997.

[Merrill05] D. R. Merrill, M. Bikson, and J. G. R. Jefferys, *Electrical stimulation of excitable tissue: design of efficacious and safe protocols*, **J. Neurosci. Methods**, vol. 141, issue 2, pp. 171-198, Feb. 2005.

[McConnell09] G. C. McConnell, R. J. Butera, and R. V. Bellamkonda, *Bioimpedance modeling to monitor astrocytic response to chronically implanted electrodes*, **J. Neural Eng.**, vol. 6, issue 5, no. 055005, Nov. 2009.

[McLaughlin13] B. L. McLaughlin, K. Kampasi, G. E. Perlin, J. LeBlanc, A. K. H. Achyuta, P. Kumar, G. Cook, G. Segura, V. Mittal, and D. Kipke, *Bi-directional Optrode for quantitative prediction of neural interface failure*, **6th International IEEE/EMBS Conference on Neural Engineering**, pp. 915-918, 2013.

[McNeill63] R. McNeill, R. Siudak, J. Wardlaw, and D. Weiss, *Electronic Conduction in Polymers. I. The Chemical Structure of Polypyrrole*, **Aust. J. Chem.**, vol. 16, issue 6, pp. 1056-1075, Dec. 1963.

[Moxon07] K. A. Moxon, S. Hallman, A. Aslani, N. M. Kalkhoran, and P. I. Lelkes, *Bioactive properties of nanostructured porous silicon for enhancing electrode to neuron interfaces*, **J. Biomater. Sci. Polym. Ed.**, vol. 18, issue 10, pp. 1263-1281, Oct. 2007.

[Muzzio17] N. E. Muzzio, M. A. Pasquale, S. E. Moya, and O. Azzaroni, *Tailored polyelectrolyte thin film multilayers to modulate cell adhesion*, **Biointerphases**, vol. 12, issue 4, no. 04E403, Aug. 2017.

[Negi10] S. Negi, R. Bhandari, L. Rieth, R. V. Wagenen, and F. Solzbacher, *Neural electrode degradation from continuous electrical stimulation: Comparison of sputtered and activated iridium oxide*, **J. Neurosci. Methods**, vol. 186, issue 1, pp. 8-17, Jan. 2010.

[Nelson80] R. J. Nelson, M. Sur, D. J. Felleman, and J. H. Kaas, *Representations of the body surface in postcentral parietal cortex of Macaca fascicularis*, **J. Comp. Neurol.**, vol. 192, issue 4, pp. 611-643, Aug. 1980.

[Nicolelis03] M. A. L. Nicolelis, D. Dimitrov, J. M. Carmena, R. Crist, G. Lehew, J. D. Kralik, and S. P. Wise, *Chronic, multisite, multielectrode recordings in macaque monkeys*, **Proc. Natl. Acad. Sci.**, vol. 100, issue 19, pp. 11041-11046, Jul. 2003.

[Offenhäusser97] A. Offenhäusser, C. Sprössler, M. Matsuzawa, and W. Knoll, *Electrophysiological development of embryonic hippocampal neurons from the rat grown on synthetic thin films*, **Neurosci. Lett.**, vol. 223, issue 1, pp. 9-12, Feb. 1997.

[Otto06] K. J. Otto, M. D. Johnson, and D. R. Kipke, *Voltage pulses change neural interface properties and improve unit recordings with chronically implanted microelectrodes*, **IEEE Trans. Biomed. Eng.**, vol. 53, issue 2, pp. 333-340, Feb. 2006.

[Park14] D.-W. Park, A. A. Schendel, T. J. Richner, J. Ness, M. R. Hayat, F. Atry, S. T. Frye, R. Pashaie, S. Thongpang, Z. Ma, and J. C. Williams, *Graphene-based carbon-layered electrode array technology for neural imaging and optogenetic applications*, **Nat. Commun.**, vol. 5, p. 5258, Oct. 2014.

[Peyron00] R. Peyron, B. Laurent, and L. García-Larrea, *Functional imaging of brain responses to pain. A review and meta-analysis (2000)*, **Neurophysiol. Clin.**, vol. 30, issue 5, pp. 263-288, May 2000.

[Piskin93] E. Piskin, *Plasma processing of biomaterials*, **J. Biomater. Sci. Polym. Ed.**, vol. 4, issue 1, pp. 45-60, Jan. 1993.

[Pistohl08] T. Pistohl, T. Ball, A. Schulze-Bonhage, A. Aertsen, and C. Mehring, *Prediction of arm movement trajectories from ECoG-recordings in humans*, **J. Neurosci. Methods**, vol. 167, issue 1, pp. 105-114, Jan. 2008.

[Poghossian09] A. Poghossian, S. Ingebrandt, A. Offenhäusser, and M. J. Schöning, *Field-effect devices for detecting cellular signals*, **Semin. Cell Dev. Biol.**, vol. 20, issue 1, pp. 41-48, Mar. 2009.

[Polikov05] V. S. Polikov, P. A. Tresco, and W. M. Reichert, *Response of brain tissue to chronically implanted neural electrodes*, **J. Neurosci. Methods**, vol. 148, issue 1, pp. 1-18, Oct. 2005.

[Pons87] T. P. Pons, J. T. Wall, P. E. Garraghty, C. G. Cusick, and J. H. Kaas, *Consistent Features of the Representation of the Hand in Area 3b of Macaque Monkeys*, **Somatosens. Res.**, vol. 4, issue 4, pp. 309-331, Feb. 1987.

[Porrazzo14] R. Porrazzo, S. Bellani, A. Luzio, E. Lanzarini, M. Caironi, and M. R. Antognazza, *Improving mobility and electrochemical stability of a water-gated polymer field-effect transistor*, **Org. Electron.**, vol. 15, issue 9, pp. 2126-2134, Sep. 2014.

[Porrazzo17] R. Porrazzo, A. Luzio, S. Bellani, G. E. onacchini, Y.-Y. Noh, Y.-H. Kim, G. Lanzani, M. R. Antognazza, and M. Caironi, *Water-Gated n-Type Organic Field-Effect Transistors for Complementary Integrated Circuits Operating in an Aqueous Environment*," **ACS Omega**, vol. 2, issue 1, pp. 1-10, Jan, 2017.

[Rousche01] P. J. Rousche, D. S. Pellinen, D. P. Pivin, J. C. Williams, R. J. Vetter, and D. R. Kipke, *Flexible polyimide-based intracortical electrode arrays with bioactive capability*, **IEEE Trans. Biomed. Eng.**, vol. 48, issue 3, pp. 361-371, Mar. 2001.

[Sankar14] V. Sankar, E. Patrick, R. Dieme, J. C. Sanchez, A. Prasad, and T. Nishida, *Electrode impedance analysis of chronic tungsten microwire neural implants: understanding abiotic vs. biotic contributions*, **Front. Neuroengineering**, vol. 7, p. 13, May 2014.

[Schoen07] J. Schoen, and P. Fromherz, *The Mechanism of Extracellular Stimulation of Nerve Cells on an Electrolyte-Oxide-Semiconductor Capacitor*, **Biophys. J.**, vol. 92, issue 3, pp. 1096-1111, Feb. 2007.

[Sekitani10] T. Sekitani, U. Zschieschang, H. Klauk, and T. Someya, *Flexible organic transistors and circuits with extreme bending stability*, **Nat. Mater.**, vol. 9, issue 12, pp. 1015-1022, Dec. 2010.

[Seymour07] J. P. Seymour and D. R. Kipke, *Neural probe design for reduced tissue encapsulation in CNS*, **Biomaterials**, vol. 28, issue 25, pp. 3594-3607, Sep. 2007.

[Shin17] S. S. Shin, E. J. Yeom, W. S. Yang, S. Hur, M. G. Kim, J. Im, J. Seo, J. H. Noh, and S. I. Seok, *Colloidally prepared La-doped BaSnO3 electrodes for efficient, photostable perovskite solar cells*, **Science**, vol. 356, issue 6334, pp. 167-171, Apr. 2017.

[Shiraishi10] A. Shiraishi, T. Uno, N. Oka, Y. Hara, M. Yamaguchi, and Y. Ohashi, *In Vivo and In Vitro Laser Confocal Microscopy to Diagnose Acanthamoeba Keratitis*, **Cornea**, vol. 29, issue 8, Aug. 2010.

[Sirringhaus00] H. Sirringhaus, T. Kawase, R. H. Friend, T. Shimoda, M. Inbasekaran, W. Wu, and E. P. Woo, *High-Resolution Inkjet Printing of All-Polymer Transistor Circuits*, **Science**, vol. 290, issue 5499, pp. 2123-2126, Dec. 2000.

[Sirringhaus09] H. Sirringhaus, *Reliability of Organic Field-Effect Transistors*, **Adv. Mater.**, vol. 21, issues 38-39, pp. 3859-3873, Oct. 2009.

[Siu79] W. M. Siu and R. S. C. Cobbold, *Basic properties of the electrolyte-SiO2-Si system: Physical and theoretical aspects*, **IEEE Trans. Electron Devices**, vol. 26, issue 11, pp. 1805-1815, Nov. 1979.

[Someya05] T. Someya, Y. Kato, T. Sekitani, S. Iba, Y. Noguchi, Y. Murase, H. Kawaguchi, and T. Sakurai, *Conformable, flexible, large-area networks of pressure and thermal sensors with organic transistor active matrixes*, **Proc. Natl. Acad. Sci. U. S. A.**, vol. 102, issue 35, pp. 12321-12325, Sep. 2005.

[Spanu15] A. Spanu, S. Lai, P. Cosseddu, M. Tedesco, S. Martinoia, and A. Bonfiglio, *An organic transistor-based system for reference-less electrophysiological monitoring of excitable cells*, **Sci. Rep.**, vol. 5, no. 8807, Mar. 2015.

[Spanu17] A. Spanu, F. Viola, S. Lai, P. Cosseddu, P. C. Ricci, and A. Bonfiglio, *A reference-less pH sensor based on an organic field effect transistor with tunable sensitivity*, **Org. Electron.**, vol. 48, pp. 188-193, Sep. 2017.

[Sun14] B. Sun, W. Hong, Z. Yan, H. Aziz, and Y. Li, *Record High Electron Mobility of 6.3 $cm^2V^{-1}s^{-1}$ Achieved for Polymer Semiconductors Using a New Building Block*, **Adv. Mater.**, vol. 26, issue 17, pp. 2636-2642, May 2014.

[Suter11] D. M. Suter, *Live cell imaging of neuronal growth cone motility and guidance in vitro*, **Methods Mol. Biol.**, vol. 769, pp. 65-86, Jan. 2011.

[Suzuki99] Y. Suzuki, M. Tanihara, K. Ohnishi, K. Suzuki, K. Endo, and Y. Nishimura, *Cat peripheral nerve regeneration across 50 mm gap repaired with a novel nerve guide composed of freeze-dried alginate gel*, **Neurosci. Lett.**, vol. 259, issue 2, pp. 75-78, Jan. 1999.

[Szarowski03] D. H. Szarowski, M. D. Andersen, S. Retterer, A. J. Spence, M. Isaacson, H. G. Craighead, J. N. Turner, and W. Shain, "Brain responses to micro-machined silicon devices," *Brain Res.*, vol. 983, issue 1, pp. 23-35, Sep. 2003.

[Takeya07] J. Takeya, M. Yamagishi, Y. Tominari, R. Hirahara, Y. Nakazawa, T. Nishikawa, T. Kawase, T. Shimoda, and S. Ogawa, *Very high-mobility organic single-crystal transistors with in-crystal conduction channels*, **Appl. Phys. Lett.**, vol. 90, issue 10, no. 102120, Mar. 2007.

[Takeuchi05] S. Takeuchi, D. Ziegler, Y. Yoshida, K. Mabuchi, and T. Suzuki, *Parylene flexible neural probes integrated with microfluidic channels*, **Lab Chip**, vol. 5, issue 5, pp. 519-523, Jun. 2005.

[Tam16] W. Y. Tam, N. P. B. Au, and C. H. E. Ma, *The association between laminin and microglial morphology in vitro*, **Sci. Rep.**, vol. 6, p. 28580, Jun. 2016.

[Tang86] C. W. Tang, *Two-layer organic photovoltaic cell*, **Appl. Phys. Lett.**, vol. 48, issue 2, pp. 183-185, Feb. 1986.

[Tang87] C. W. Tang and S. A. VanSlyke, *Organic electroluminescent diodes*, **Appl. Phys. Lett.**, vol. 51, issue 12, pp. 913–915, Jul. 1987.

[Tengvall98] P. Tengvall, I. Lundström, and B. Liedberg, *Protein adsorption studies on model organic surfaces: an ellipsometric and infrared spectroscopic approach*, **Biomaterials**, vol. 19, issues 4-5, pp. 407-422, Mar. 1998.

[Thakore12] V. Thakore, P. Molnar, and J. J. Hickman, *An Optimization-Based Study of Equivalent Circuit Models for Representing Recordings at the Neuron–Electrode Interface*, **IEEE Trans. Biomed. Eng.**, vol. 59, issue 8, pp. 2338-2347, Aug. 2012.

[Thewes16] R. Thewes, G. Bertotti, N. Dobel, S. Keil, S. Schröder, K.-H. Boven, G. Zeck, M. Mahumud, and S. Vassanelli, *Neural tissue and brain interfacing CMOS devices — An introduction to state-of-the-art, current and future challenges*, **2016 IEEE International Symposium on Circuits and Systems**, pp. 1826-1829, 2016.

[Torsi13] L. Torsi, M. Magliulo, K. Manoli, and G. Palazzo, *Organic field-effect transistor sensors: a tutorial review*, **Chem. Soc. Rev.**, vol. 42, issue 22, pp. 8612-8628, Sep. 2013.

[Twardoch94] U. M. Twardoch, *Integrity of ultramicro-stimulation electrodes determined from electrochemical measurements*, **J. Appl. Electrochem.**, vol. 24, issue 9, pp. 835-857, Sep. 1994.

[Vassanelli12] S. Vassanelli, M. Mahmud, S. Girardi, and M. Maschietto, *On the Way to Large-Scale and High-Resolution Brain-Chip Interfacing*, **Cogn. Comput.**, vol. 4, issue 1, pp. 71-81, Mar. 2012.

[Vassanelli14] S. Vassanelli, *Multielectrode and Multitransistor Arrays for In Vivo Recording*, **Nanotechnology and Neuroscience: Nano-electronic, Photonic and Mechanical Neuronal Interfacing**, pp. 239-267, 2014.

[Venuto14] D. D. Venuto, P. Ledochowitsch, M. Maharabitz, and J. Rabaey, *Impedance modeling of the intracortical microelectrode for a reliable design of a brain activity recording system*, **Fifteenth International Symposium on Quality Electronic Design**, pp. 380-385, 2014.

[Wang16] D. Wang, V. Noël, and B. Piro, *Electrolytic Gated Organic Field-Effect Transistors for Application in Biosensors–A Review*, **Electronics**, vol. 5, issue 1, no. 9, Feb. 2016.

[Wang17] L. Wang, X. Zhang, G. Dai, W. Deng, J. Jie, and X. Zhang, *High-mobility air-stable n-type field-effect transistors based on large-area solution-processed organic single-crystal arrays*, **Nano Res.**, pp. 1-10, Jul. 2017.

[Weis97] R. Weis, and P. Fromherz, *Frequency dependent signal transfer in neuron transistors*, **Phys. Rev. E**, vol. 55, issue 1, pp. 877-889, Jan. 1997.

[White16] K. M. R. White, J. A. Sabatino, M. He, N. Davis, N. Tang, and C. F. Bearer, *Toluene disruption of the functions of L1 cell adhesion molecule at concentrations associated with occupational exposures*, **Pediatr. Res.**, vol. 80, issue 1, pp. 145-150, Jul. 2016.

[White84] H. S. White, G. P. Kittlesen, and M. S. Wrighton, "*Chemical derivatization of an array of three gold microelectrodes with polypyrrole: fabrication of a molecule-based transistor*, **J. Am. Chem. Soc.**, vol. 106, issue 18, pp. 5375-5377, Sep. 1984.

[Widge07] A. S. Widge, M. Jeffries-El, X. Cui, C. F. Lagenaur, and Y. Matsuoka, *Self-assembled monolayers of polythiophene conductive polymers improve biocompatibility and electrical impedance of neural electrodes*, **Biosens. Bioelectron.**, vol. 22, issue 8, pp. 1723-1732, Apr. 2007.

[Wiegert17] J. S. Wiegert, C. E. Gee, and T. G. Oertner, *Stimulating Neurons with Heterologously Expressed Light-Gated Ion Channels*, **Cold Spring Harb. Protoc.**, vol. 2017, issue 2, pp. 85-91, Feb. 2017.

[Williams07] J. C. Williams, J. A. Hippensteel, J. Dilgen, W. Shain, and D. R. Kipke, *Complex impedance spectroscopy for monitoring tissue responses to inserted neural implants*, **J. Neural Eng.**, vol. 4, issue 4, no. 410, Nov. 2007.

[Williams70] D. F. Williams and M. Schadt, *A simple organic electroluminescent diode*, **Proc. IEEE**, vol. 58, issue 3, pp. 476-476, Mar. 1970.

[Williamson15] A. Williamson, M. Ferro, P. Leleux, E. Ismailova, A. Kaszas, T. Doublet, P. Quilichini, J. Rivnay, B. Rózsa, G. Katona, C. Bernard, and G. G. Malliaras, *Localized Neuron Stimulation with Organic Electrochemical Transistors on Delaminating Depth Probes*, **Adv. Mater.**, vol. 27, issue 30, pp. 4405-4410, Aug. 2015.

[Wise70] K. D. Wise, J. B. Angell, and A. Starr, *An Integrated-Circuit Approach to Extracellular Microelectrodes*, **IEEE Trans. Biomed. Eng.**, vol. BME-17, issue 3, pp. 238-247, Jul. 1970.

[Wise75] K. D. Wise and J. B. Angell, *A Low-Capacitance Multielectrode Probe for Use in Extracellular Neurophysiology*, **IEEE Trans. Biomed. Eng.**, vol. BME-22, issue 3, pp. 212-219, May 1975.

[Xie15] C. Xie, J. Liu, T.-M. Fu, X. Dai, W. Zhou, and C. M. Lieber, *Three-dimensional macroporous nanoelectronic networks as minimally invasive brain probes*, **Nat. Mater.**, vol. 14, issue 12, pp. 1286-1292, Dec. 2015.

[Yang04] F. Yang, C. Y. Xu, M. Kotaki, S. Wang, and S. Ramakrishna, *Characterization of neural stem cells on electrospun poly(L-lactic acid) nanofibrous scaffold*, **J. Biomater. Sci. Polym. Ed.**, vol. 15, issue 12, pp. 1483-1497, Feb. 2004.

[Yao15] C. Yao, Q. Li, J. Guo, F. Yan, and I.-M. Hsing, *Rigid and Flexible Organic Electrochemical Transistor Arrays for Monitoring Action Potentials from Electrogenic Cells*, **Adv. Healthcare Mater.**, vol. 4, issue 4, pp. 528-533, Mar. 2015.

[Zeck01] G. Zeck, and P. Fromherz, *Noninvasive neuroelectronic interfacing with synaptically connected snail neurons immobilized on a semiconductor chip*, **Proc. Nat. Acad. Sci.**, vol. 98, issue 18, pp. 10457-10462, Apr. 2001.

2. Organic Field-Effect Transistors

Organic field-effect transistors (OFETs) are getting more and more interest[Sirringhaus14, Zao13] thanks to their promising features, such as, the variety of available active materials due to the flexibility of chemical tailoring[Benincori08, Zhuang13] and the large area processing[Dimitrakopoulos02]. Moreover, OFET technology offers a very wide range of applications: from the display backplane[Mizukami15] to flexible microprocessor[Myny12]; from the light-emitting transistor[Rost04] to the chemical and/or biological sensor[Lin12].

Nowadays, OFETs performances are limited by some reliability issues related to impurities, external contaminants and charge trapping, which have been widely studied in literature (see for instance [Sirringhaus09] and [Pope99]). Many of the applications cited above require dynamic and reliable performances, and the achieving of such goals need proper investigation tools.

Besides reliability and stability, other issues related to both modeling and characterization techniques are still open, due to the many peculiarities of organic materials, which behave very differently with respect to conventional semiconductors. The presence of discrete energy levels instead of extended energy bands largely affects the static as well as the dynamic behaviors. This might strongly impact all those techniques that involve the transient response of the devices (e.g., deep level transient spectroscopy) or pulsed measurements. For instance, many research groups proposed gate voltage-pulse and voltage staircase methods to study and remove hysteresis due to charge trapping/detrapping[Manoli14, Petit08, Ucurum10]. Others groups, focused their attentions in the very short time-scale transients using the time-of-flight method, and they showed that the displacement current increases as long as injected charges move towards the drain electrode[Dost08, Dunn06, Weis09].

In the following chapters, we investigate the dynamics that rule the formation and the depletion of the electronics conducting channel in organic transistors by applying Pulsed Characterizations and Deep Level Transient Spectroscopy analysis. The firsts gave us an understanding of the physical phenomena behind the OFETs turn-on and turn-off delay times. The seconds allowed an insight view of the density of states in organic compounds and how this impact to the device performances.

2.1. Pulsed and Transient Characterizations

Besides the dynamic behavior, trapping/detrapping also affects the static characterization procedures. For this reason, the IEEE Standard for the Characterization of Organic Transistor and Materials[IEEE08] recommends a minimum dwell time of 100ms for each data point to avoid transient effects. Still, reversible transient phenomena occurring in OFETs are not wholly investigated, and, besides charge trapping, some other processes were not taken into account. In this chapter, we carried out pulse characterization techniques very similar to that already employed in inorganic devices[Bisi14, Meneghesso04, Meneghini12, Tirado07]. In those works, pulse characterizations had been done to prevent device self-heating and study phenomena such as trapping and current collapse. Here instead, we made use of Drain-Pulsed and Gate-Pulsed measurements to analyze the OFET dynamic response, with particular attention to the transition from linear to saturation regime, showing that channel formation and annihilation may affect the characterization as well as the performance of analog and digital applications.

2.1.1. Device fabrication

The OFET devices were fabricated in collaboration with the ISMN-CNR from Bologna implementing two p-type semiconductors: pentacene (P5) and dihexyl-quaterthiophene (DH4T)[Generali10]; and two n-type semiconductors: 2,2'-(2,2'-b ithiophene-5,5'-diyl)bis(5-butyl-5H-thieno[3,2-c]pyrrole-4,6-dione) (NT4N)[Melucci11] and N,N'-ditridecyl–perylene-3,4,9,10-tetracarboxylic (P13)[Koopman14]. The materials used have different HOMO and LUMO levels: respectively -4.96eV and -2.67eV for P5; -5.8eV and -2.89eV for DH4T; -6eV and -3.47eV for NT4N; -5.4eV and -3.4eV for P13. For further details about energy level distributions see the following references: [Kalb10], [Ong05], [Melucci13], and [Huang11]. We used a top-contact bottom-gate configuration, with a 150-nm ITO (indium tin oxide) layer as gate contact, grown over a glass substrate. The gate dielectric is a 450-nm poly-methyl methacrylate (PMMA) layer spin-coated over the gate that gives a gate capacitance C_i=7,08nF/cm^2. Then a 15-nm semiconductor layer was evaporated over the PMMA. Finally, 30nm (P13 and DH4T) or 70nm (P5) thick gold electrodes were deposited on top of the stack by physical vapor deposition (PVD), with a track width of 1mm. The channel length L and width W are 70µm and 15mm, respectively. To avoid parasitic effects due to charging of the region far from the source and drain electrodes[Jung07, Maddalena15, Taylor08, Ullah09], the semiconductor material is patterned as shown in ***Figure 2.1***. The devices were encapsulated with a glass capping substrate in nitrogen atmosphere to avoid degradation due to air exposure.

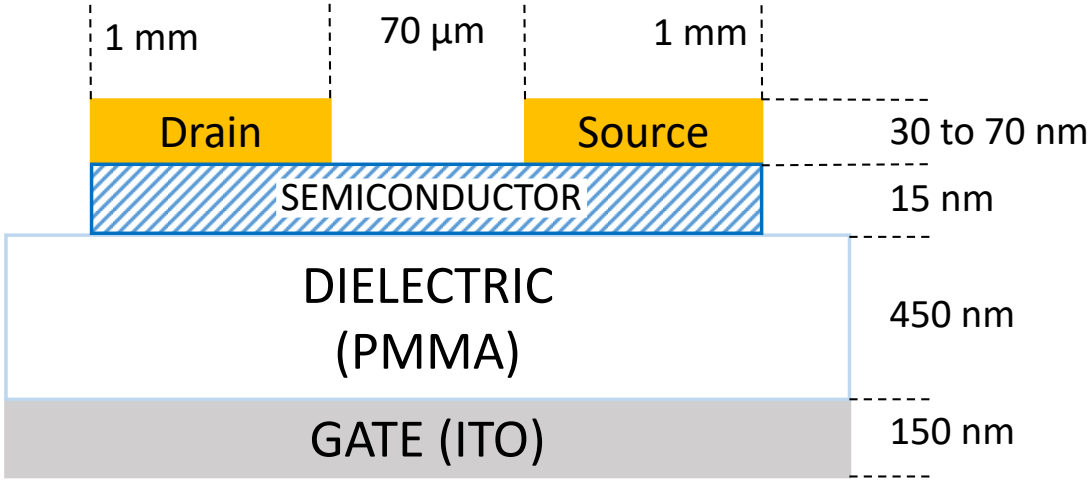

Figure 2.1 - Cross section of the OFET device. *The semiconductor is patterned to avoid parasitic effects due to charging of the region far from the Source and Drain electrodes (drawing not to scale).*

2.1.2. Results and discussions

To understand the nature of the OFET transient phenomena, we carried out DC I_{DS}-V_{DS} and pulsed I_{DS}-V_{DS} double sweep measurements on devices with different materials (P5, DH4T, NT4N and P13) and with the same structure. DC double sweep measurements are taken with 1-s dwell time. Pulsed I_{DS}-V_{DS} have been taken by applying a pulsed voltage to either gate or drain electrodes, and keeping constant the other electrodes. ***Figure 2.2a*** and ***Figure 2.2b*** shows the applied voltage waveforms during pulsed measurements: voltages are always positive for n-type FETs, and always negative for p-type FETs.

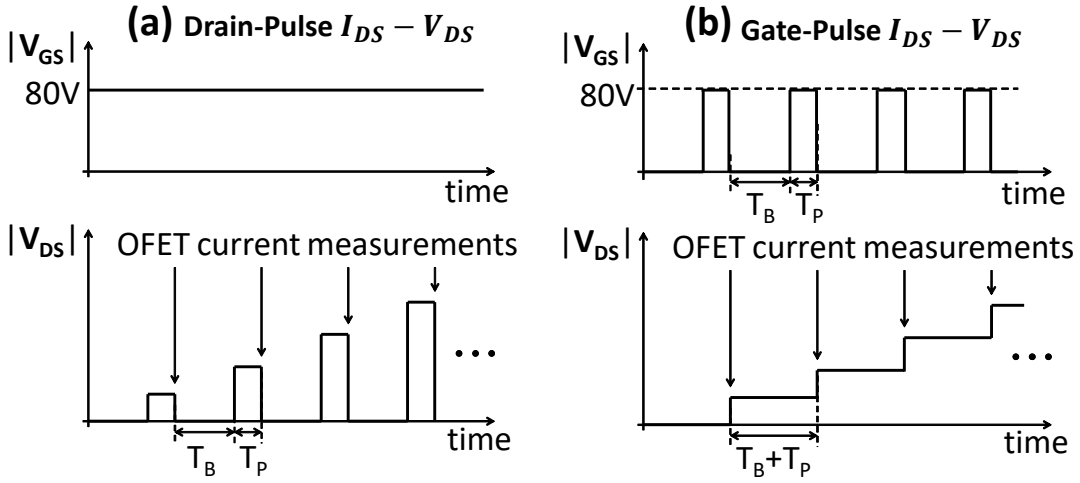

Figure 2.2. **(a)** *and* **(b)** *show the evolution of the applied voltages for Drain-Pulse I_{DS}-V_{DS} and Gate-Pulse I_{DS}-V_{DS}, respectively. Arrows mark the instants where the OFET current were acquired.*

In Drain-Pulsed I_{DS}-V_{DS} the V_{GS} is constant, while the V_{DS} is pulsed at each measurement point. In Gate-Pulsed I_{DS}-V_{DS} the V_{DS} is increased in a staircase fashion at each point, and the V_{GS} is pulsed to 80V. In both cases, the pulse base time (T_B) is 100ms, and the pulse width (T_P) ranges from 1ms to 100ms. The current is acquired at the end of each pulse (arrows in ***Figure 2.2a*** and ***Figure 2.2b***). Some representative results are shown in ***Figure 2.3*** for a P13-OFET. ***Figure 2.4*** shows the pulsed $I_{DS}V_{DS}$ for all the tested materials. All the devices behave similarly, regardless the film material. The thick-solid curve is the DC sweep. The dash curves are the three Drain-Pulse I_{DS}-V_{DS} with 1ms, 10ms and 100ms pulse width, respectively. They all lie above the DC I_{DS}-V_{DS}. Instead, the Gate-Pulse I_{DS}-V_{DS} (at 1ms, 10ms and 100ms) are below the DC curve (thin-solid lines).

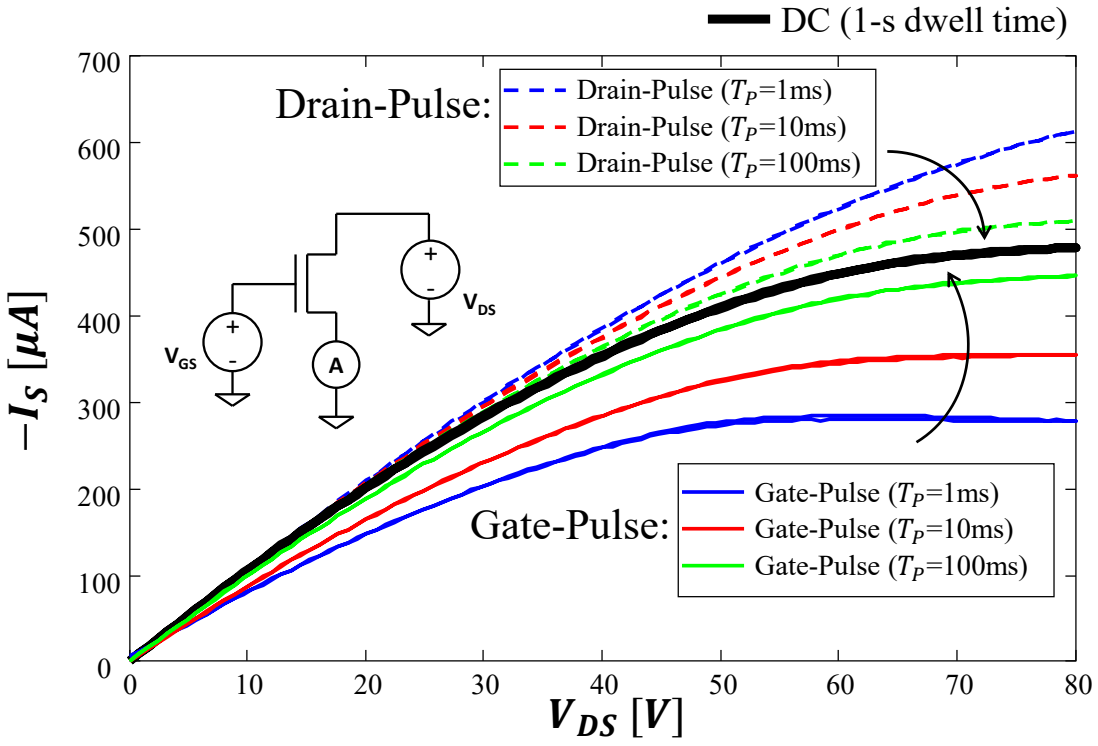

Figure 2.3 - OFET Pulsed output characterization. *DC I_{DS}-V_{DS} characterization on P13 for V_{GS}=80V performed with 1s dwell time (thick-solid line), Drain-Pulse I_{DS}-V_{DS} (dash lines), and Gate-Pulse I_{DS}-V_{DS} (thin-solid lines). The arrows indicate the increasing of T_P in Gate-Pulse and Drain-Pulse measurements. The insert shows the device connections.*

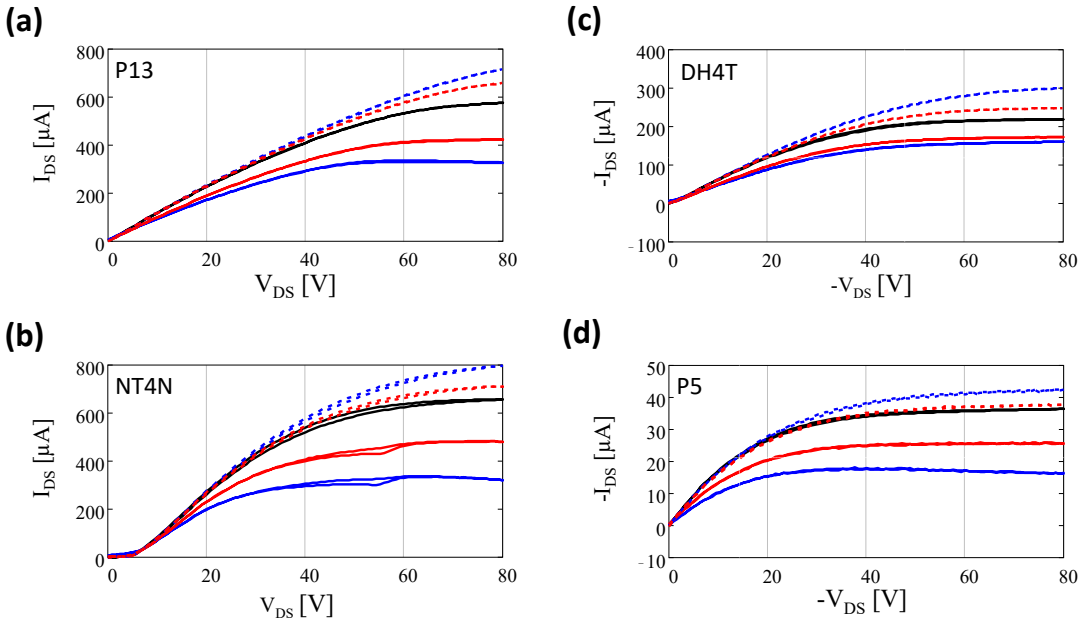

Figure 2.4 - OFETs Pulsed output characterizations for the four tested materials.
(a) *P13;* **(b)** *NT4N;* **(c)** *DH4T;* **(d)** *P5.*

To gain more insights in the OFET behavior during the pulse, we measured the current transients either by switching V_{GS} from 0V to 80V, while keeping the drain at V_{DS}=80V, or by switching V_{DS} from 0V to 80V, while keeping V_{GS}=80V. In the following, we refer to these measurements as Gate-Step and Drain-Step, respectively. Before the Gate(Drain)-Step, V_{GS} (V_{DS}) is kept at 0V for 100s, and immediately after switching, we monitored both drain (I_D) and source (I_S) currents, in order to separate the displacement currents from the channel current. These transients, plotted in ***Figure 2.5***, clearly show that, aside for a time shorter than 1ms, when capacitive couplings are still present, $I_S = -I_D$, confirming that the behaviors in ***Figure 2.3*** and ***Figure 2.4*** are not related to displacement currents. We believe that the transients are dominated by the processes of the channel formation and depletion in the long-time regime, that may take up to several seconds, in agreement with other findings achieved by Liang et al. in capacitor like structures[Liang09].

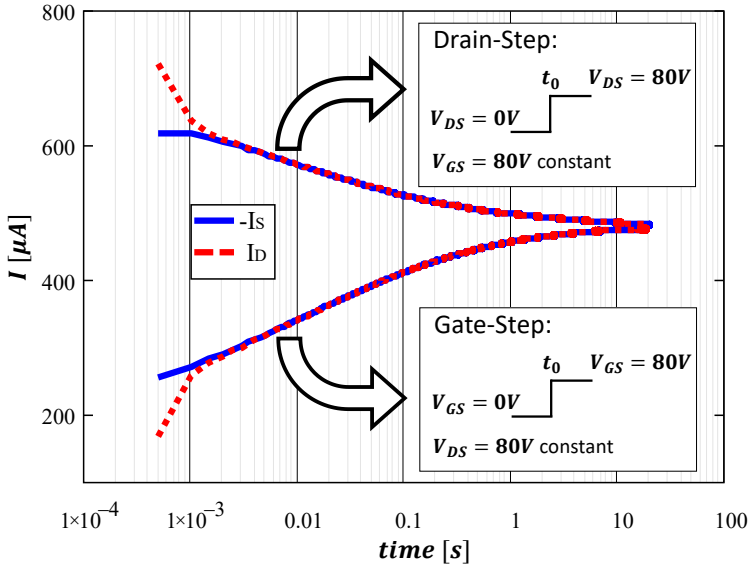

Figure 2.5*. Current transients on P13-OFET measured at both drain (solid line) and source (dash line) electrodes. Before t_0, devices were kept polarized for 100s with V_{DS}=0V and V_{GS}=80V during Drain-Step, and with V_{GS}=0V and V_{DS}=80V during Gate-Step.*

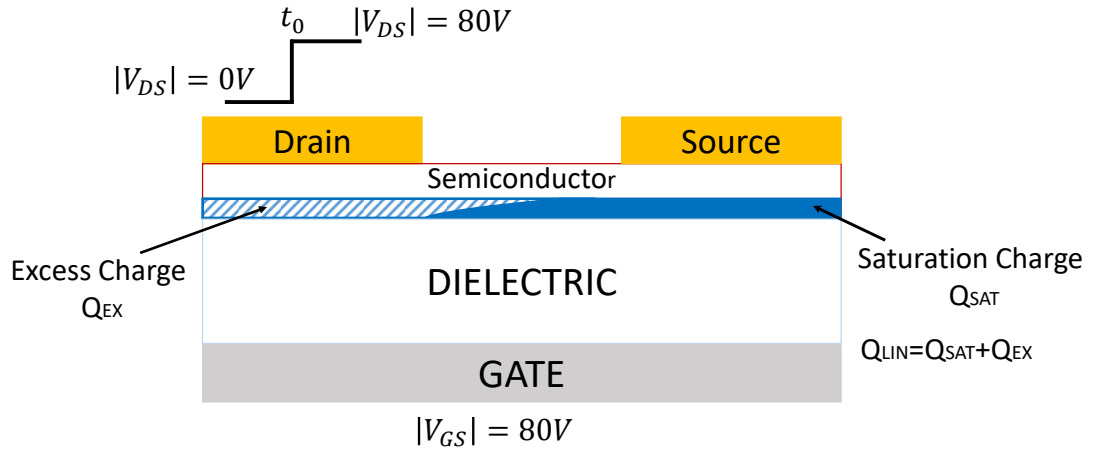

Figure 2.6 - Cross section the OTFTs. *The picture shows the saturated channel (solid area) and linear region channel (dashed area). The difference between these condition gives the excess charge* $Q_{EX}=Q_{LIN}-Q_{SAT}$.

Before the Drain-Step (V_{GS} = 80V and V_{DS} = 0V), the OFET is in linear region, thus the layer of accumulated carriers is uniformly present over the whole gate area and the channel charge is $Q_{LIN}=Q_{SAT}+Q_{EX}$ (see ***Figure 2.6***).

At the end of the transient, the OFET is in the saturation region, and the charge in the channel is only Q_{SAT}. However, this condition is not reached instantaneously after the drain voltage has been switched from 0V to 80V. To reach the steady state saturation current value, the excess charge Q_{EX} must be removed. Until the temporary excess charge Q_{EX} is not completely removed, I_{DS} is larger than expected (see Drain-Step curves in ***Figure 2.5***). To give an interpretation of this phenomenon, we can focus our attention on the density-of-states (DOS) in organic materials. In agreement with the Extended Gaussian Disorder Model[Coehoorn12], the HOMO and LUMO states show exponential tails of deep energy levels that can require a long time for carrier transport. Following this model, the average carrier energy is related to the quasi Fermi level and it is generally below the transport level. The carrier transport involves several jumps between their average energy and the transport level. The larger is the carrier concentration, the closer is the quasi Fermi level to the transport level, and the easier the jumps are.

The removal of Q_{EX} is a very slow process, because we need to depopulate also the "low mobility" states, which are the majority. Until these levels remain populated, the quasi-Fermi level is kept close to the transport band, and the carriers injected from the source move mostly in shallow levels (close to the transport band), i.e. with higher mobility.

We explain the Gate-Step in similar way, considering the time needed to populate the deep states to move the quasi-Fermi level near the transport band, and to form the channel.

To confirm this idea, we also performed the Gate Pulse and Drain-Pulsed I_{DS}-V_{GS} measurements plotted in ***Figure 2.7*** for P13.

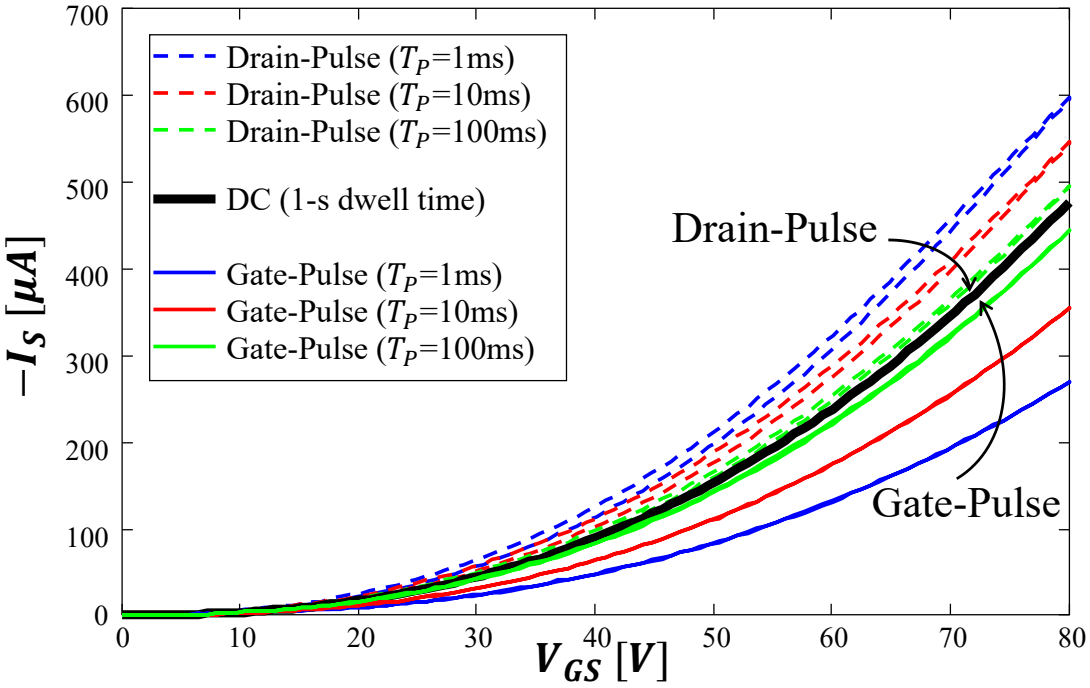

Figure 2.7 - OFET Pulsed transfer characterizations. *DC I_{DS}-V_{GS} characterization on P13 for V_{DS}=80V performed with 1s dwell time (thick-solid line), Drain-Pulse I_{DS}-V_{GS} (dash lines), and Gate-Pulse I_{DS}-V_{GS} (thin-solid lines). The arrows indicate the increasing of TP in Drain-Pulse and Gate-Pulse measurements.*

In Gate-Pulsed I_{DS}-V_{GS} the V_{DS} is constant at 80V and V_{DS} is pulsed at each measurement point as shown in ***Figure 2.8a***. In Drain-Pulsed I_{DS}-V_{GS} the V_{GS} is increased in a staircase fashion at each point, and the V_{DS} is pulsed to 80V (see ***Figure 2.8b***). T_B and T_P are the same used in I_{DS}-V_{DS} measurements.

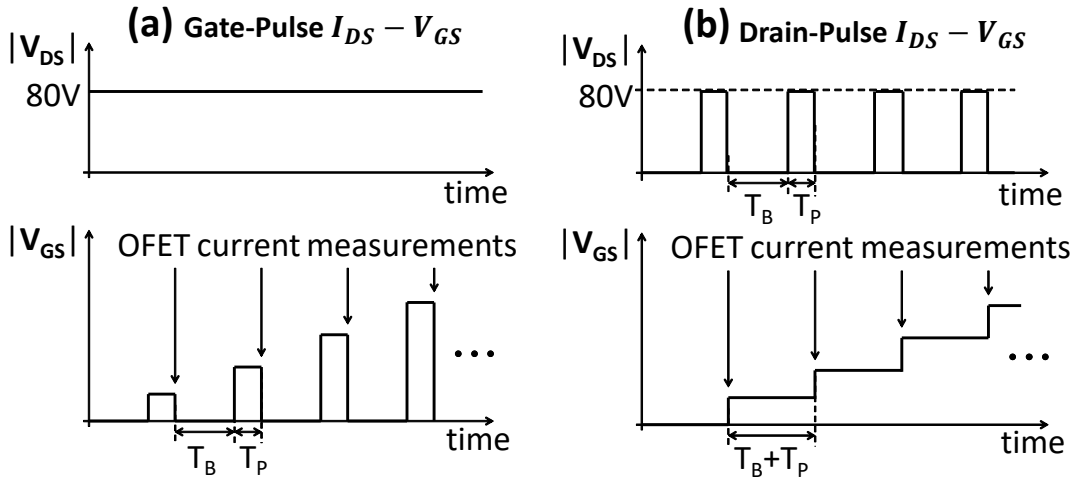

Figure 2.8. **(a)** *and* **(b)** *show the evolution of the applied voltages for Drain-Pulse and Gate-Pulse I_{DS}-V_{GS} respectively. Arrows indicate the instants where the corresponding current values were acquired.*

The mobility extracted from the Gate-Pulse I_{DS}-V_{GS} curves of ***Figure 2.7***, increases from 0.068 cm^2/Vs to 0.112 cm^2/Vs and reaches 0.12 cm^2/Vs in the DC I_{DS}-V_{GS}. In contrast, the threshold voltage is constant to 0.6V, confirming once again that charge trapping cannot explain our results. This theory is also in agreement with the time-of-flight studies, where the time-dependent relation between mobility and free carriers was analyzed[Dost08, Dunn06, Weis09].

Remarkably, this phenomenon occurs on all the tested devices independently on the material, even though with different magnitude and rates. ***Figure 2.9a*** shows the I_{DS} read at $|V_{DS}|=|V_{GS}|=80V$ during Drain-Pulsed I_{DS}-V_{DS}, as a function of the pulse width T_P, normalized to their respective DC values. In the inset of ***Figure 2.9a*** we report the decay rate for the tested materials. Noticeably, P13 is the slower material and P5 is the faster material. This may be tentatively correlated to the morphology of the material, which features smaller crystal grains in P13 rather than in P5, as shown from the two atomic force microscope (AFM) images showed in ***Figure 2.9b*** and ***Figure 2.9c*** for P5 and P13, respectively. In fact, we infer that the smaller are the crystal grains, the broader the tail state distributions are.

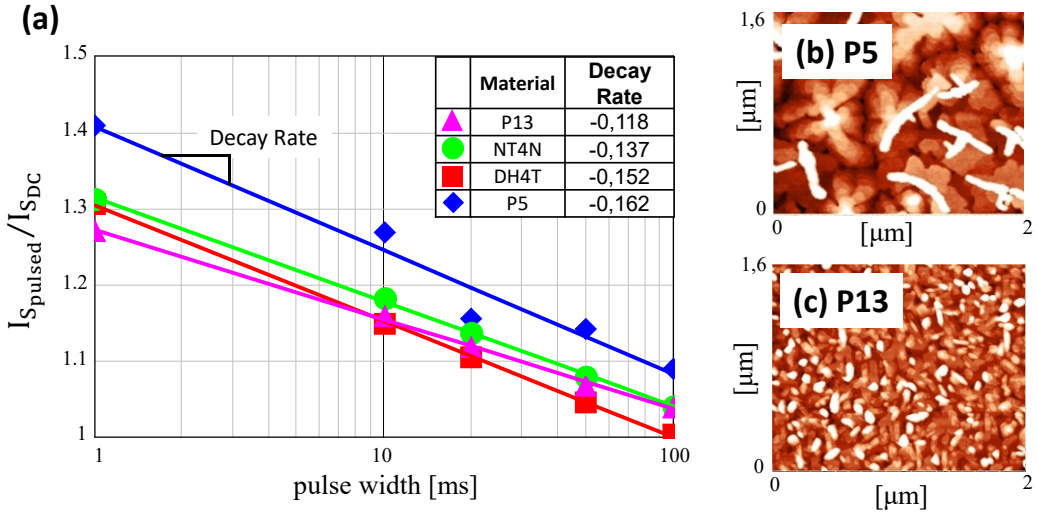

Figure 2.9. **(a)** *Drain-Pulse currents normalized as respect the DC current for $V_{DS}=V_{GS}=80V$. Symbols are the measured data, whereas the solid lines are the interpolating curves.* **(b)** *AFM images for P5.* **(c)** *AFM images for P13.*

At this point, some considerations about charge trapping are worth to be drawn. Current transients similar to our step measurements (***Figure 2.5***) were reported on HEMT devices and explained by trapping phenomena[Meneghesso04]. However, that interpretation does not apply to our devices due to the different architectures. Even though we cannot exclude the presence of charge trapping in dielectric, semiconductor, or interfaces, these phenomena cannot explain our results. In fact, during Gate-Step, switching the gate from 0V to 80V brings the OFET from cut-off to saturation. We expect that free carriers (electrons in n-type or holes in p-type FETs) are being trapped as long as the bias is applied. This should increase the threshold voltage and, in turn, reduce the channel current, i.e. the opposite to what is actually observed. Similarly, the Drain-Step would force the release of trapped carriers in the region between gate and drain leading to a partial threshold voltage decrease and, in turn, to the increase of current during time[Ucurum10].

Trapping effects during measurements are also excluded. In fact, the double sweep characterizations of ***Figure 2.3***, which last 200s, do not show hysteresis, indicating a negligible charge trapping during measurements. The same considerations hold true for charge trapping at the back interface (nitrogen/semiconductor).

2.2. Mobility Transients and DLTS measurements

In chapter ***2.1*** we demonstrated that, besides the usually considered charge trapping phenomena, more peculiar phenomena must be taken into account, such as the slow channel formation and depletion. In particular, we showed that the time requested to completely form and deplete the conductive channel can be the dominant phenomenon and it could take several seconds.

In this chapter, using the same devices fabricated in chapter ***2.1.1*** (except NT4N-base OFETs), we analysed the OFET transient response by means of the deep level transient spectroscopy (DLTS) technique[Li98, Bisi14]. To our knowledge, this technique is widely applied to inorganic devices such as HEMT and LED, and only few works have been carried out on organic devices[Stallinga00, Nguyen04], and in particular in OFET structures[Mathijssen07]. Anyway, in these works the authors focused their attention to the charge trapping phenomenon, which can last for a very long time (hundreds/thousands of seconds). In contrast other studies, using the time-of-flight method [Dunn06, Dost08, Weis09], considered very much shorter times (microseconds time-scale) in order to analyse the displacement of injected carriers that move towards the drain electrode.

In our analysis, we are now focusing on medium time-scales (around tens of seconds). We will show that, despite the transistors turn on in less than 1ms (as shown in chapter ***2.2***, ***Figure 2.5***), the drain to source current can takes several seconds to reach its steady-state value, which might be 50% larger than the current value at 1ms.

2.2.1. Experimental Procedure

The DLTS technique consists on the extrapolation of the activation energies (associated with the energetic position of gap states) by recording the transient response of a physical quantity (current, capacitance, charge, and so on) at different temperatures.

The flow chart in ***Figure 2.10a*** describes how DLTS was applied in this work. We started by taking an I_{DS}-V_{GS} curve (V_{DS}=V_{GS}) at 20°C, in order to assess the initial performance of the device (pre-characterization). Then the temperature was set at -30°C and a measurement loop was performed rising the temperature by 5°C at each step. At each step, we took the following measurements:

- *I_{DS}-V_{GS} curves.* We performed current versus voltage characterizations in order to monitor how the transistors parameters change in temperature.

- *Current transients*. These transients are collected in two phases depicted in ***Figure 2.1-b***: a filling phase, that last T_F=100s, during which the transistor is polarized in off-state with V_{DS}=0V and V_{GS}=-60V (V_{GS}=40V for p-OFETs); a sensing phase T_S, that ranges from 10s up to 50s, where the voltages are suddenly switched to V_{DS}=V_{GS}=40V (V_{DS}= V_{GS}=-60V for p-OFETs) and the I_{DS} transient is recorded by measuring the source current (we already showed in ***Figure 2.5*** that I_D=-I_S for time longer than 1ms).

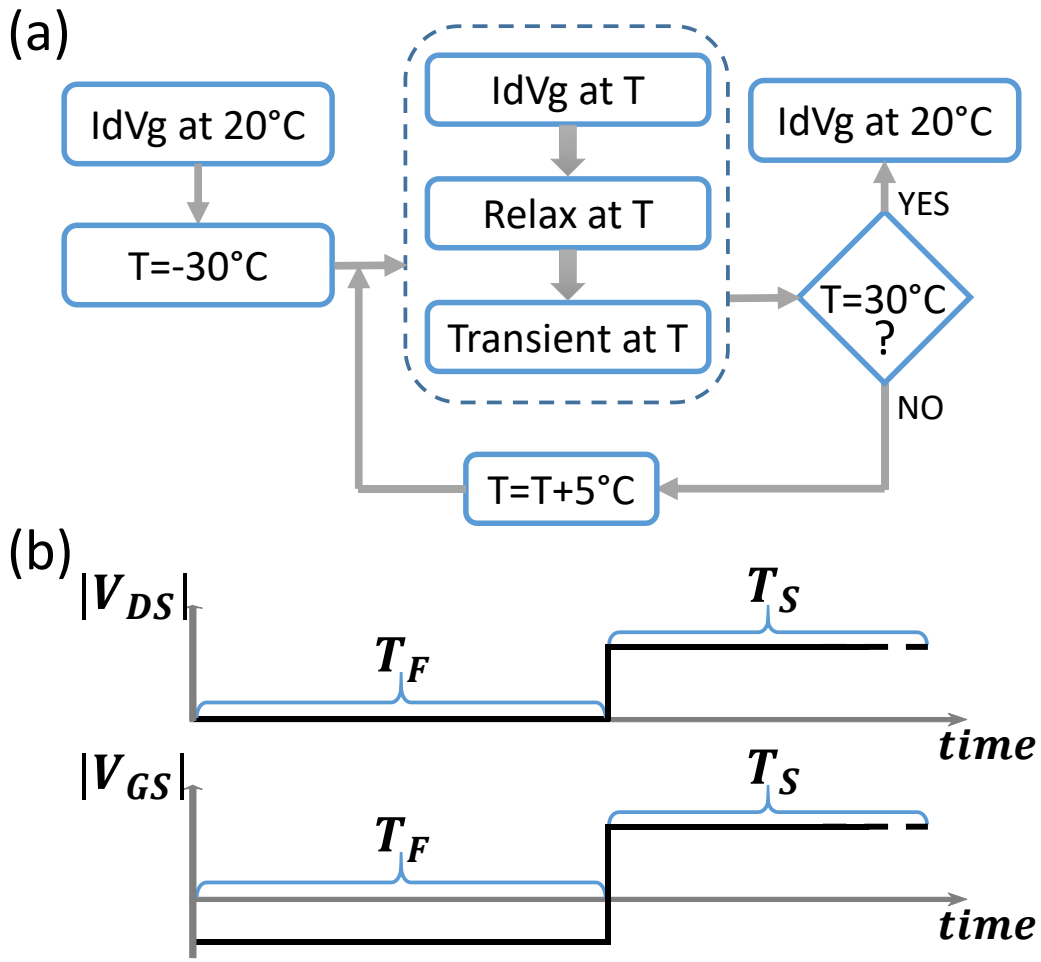

Figure 2.10. **(a)** *Flow chart describing the procedures used to collect the measurements.* **(b)** *Voltages applied in order to record the transients: T_F is the filling phase; T_S is the sensing phase.*

The measurement loop proceeds until the temperature reaches 30°C. Then, the temperature is brought back to 20°C and another I_{DS}-V_{GS} (post-characterization) is performed in order to check the performances of the device after the entire set of measurements ensuring that the device is not damaged.

To set the temperature, we used a custom heating and cooling system with two Peltier cells that bring the sample at the desire temperature through an aluminum thermal bridge. All the measurements were performed only after the device reached the imposed temperature that was measured by two thermal sensors: one embedded in the thermal bridge, the second located to the top of the device. By simulation we verify that the temperature of the organic material differs from the nominal temperature less than 1°C in the worst case (i.e., at -30°C).

2.2.2. Results and Discussion

Figure 2.10 shows the I_{DS}-V_{GS} characterizations at 20°C performed at the beginning and at the end of the whole measurement protocol. The curves show that the measurements did not significantly impact the devices performances, as there is just a small variation between pre- and post-characterizations. From ***Figure 2.11***, we extracted the field-effect mobility μ_{FET} (for V_{GS}=80V) that is reported in the inset of ***Figure 2.11***, where μ_{FET} is defined as follow[Horowitz00]:

$$\mu_{FET} = \mu_0 \left(\frac{V_{GS}-V_T}{V_0}\right)^{\alpha}, \qquad (2.1)$$

where α and V_0 are constants, and μ_0 is the low field mobility.

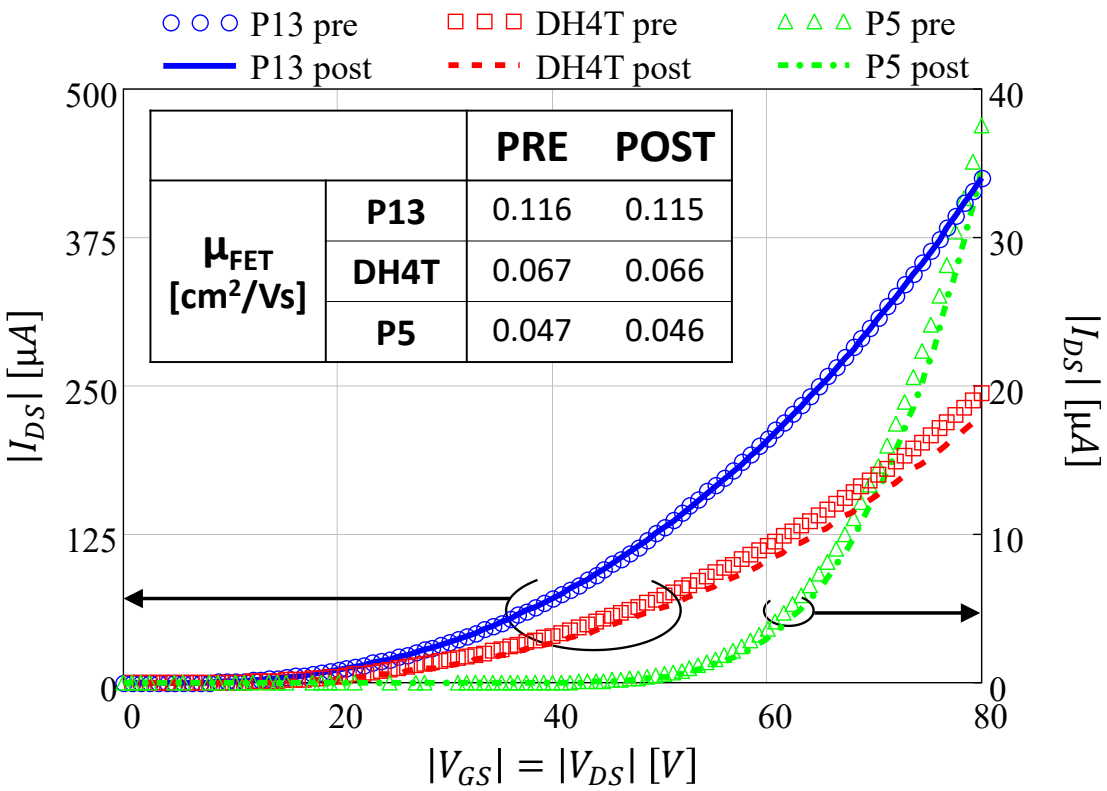

Figure 2.11 - I_{DS}-V_{GS} curves *at 20°C for P13 and DH4T devices (left axis), and for a P5 device (right axis). In the insert the relative extrapolated values of μ_{FET} at 80V are reported.*

After the entire cycle of measurements, the mobility does not change meaning that there was no degradation at all.

Since any possible degradation phenomena has a negligible impact, we focus on the measurements performed at different temperatures. In ***Figure 2.12*** we show the I_{DS} transients from -30°C up to 30°C for the three tested materials (P13, P5, and DH4T showed in ***Figure 2.12a***, ***Figure 2.12b***, and ***Figure 2.12c*** respectively), whereas in ***Figure 2.13*** we plotted the I_{DS}-V_{GS} curves, at the same temperatures, for a P13 device.

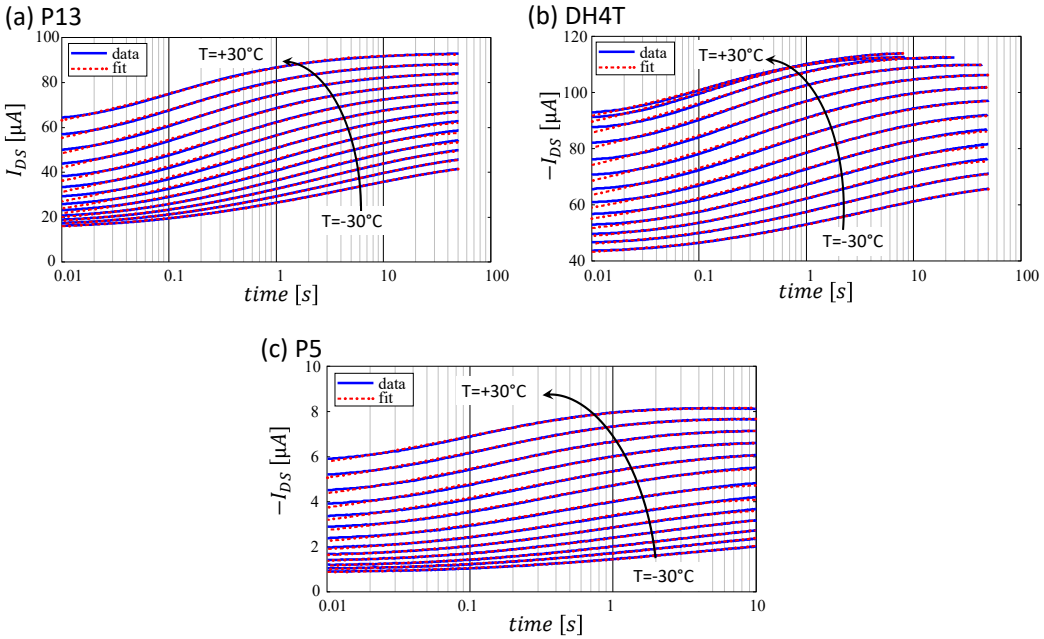

Figure 2.12 - DLTS transients *for P13* **(a)**, *DH4T* **(b)**, *and P5* **(c)** *devices. Solid lines are the measured data, whereas the dash-dotted lines are the stretched exponential fits.*

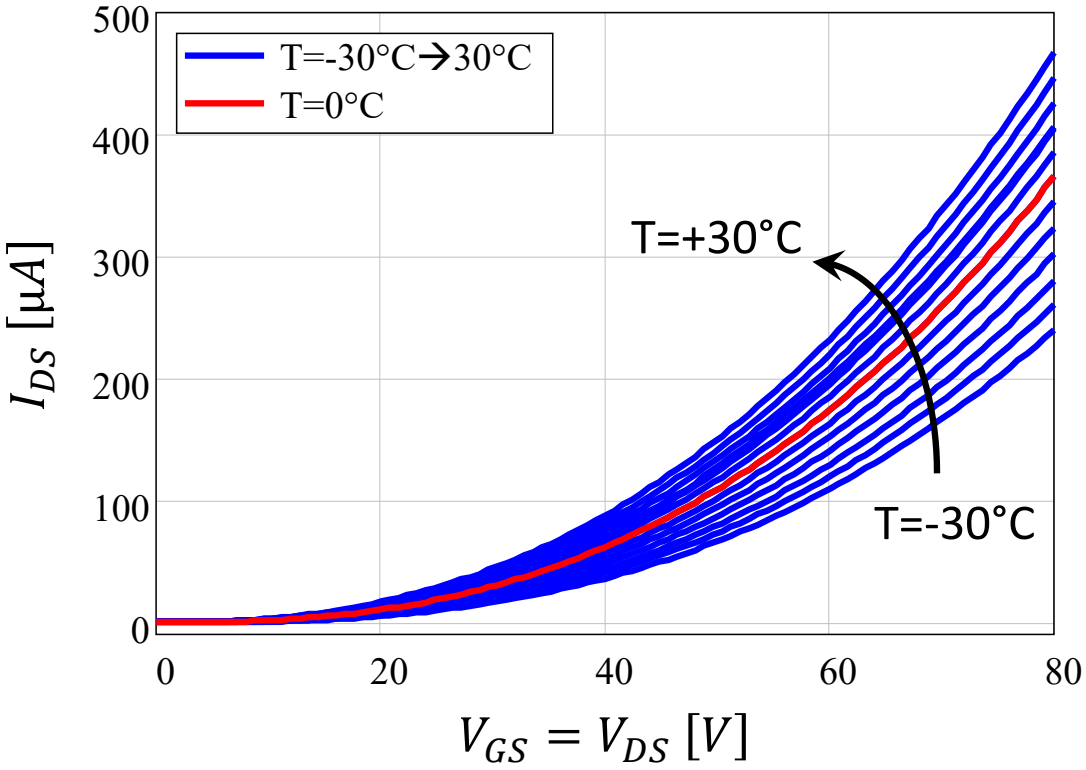

***Figure 2.13 - I_{DS}-V_{GS} curves** performed from -30°C up to 30°C for a P13 device.*

From both ***Figure 2.12*** and ***Figure 2.13*** we see that the I_{DS} current (in absolute value) increases with the increase of temperature. This behavior is directly correlated with a temperature dependent mobility. In fact, in our range of temperature, the charge transport exhibits a thermally activated behavior[Monroe85], thus the mobility can be expressed in the following form[Horowitz00]:

$$\mu_{FET} = A \cdot \exp\left(-\frac{E_\mu}{kT}\right), \qquad (\boldsymbol{2.2})$$

where T is the temperature (expressed in Kelvin degrees), k is the Boltzmann constant (in eV/K), E_μ is the activation energy defined as the difference between the transport level E_C and the Fermi level position during sensing E_{Fs} (see ***Figure 2.15***), whereas A is a mobility pre-factor that includes μ_0 and other thermal independent contributions (for further details see the following reference [Horowitz00]). The temperature dependence in equation ***2.2*** was found to occurs, not only with exponential DOS, but also in the presence of strong Gaussian disorder when there is a large charge-carrier density[Coehoorn12].

This temperature dependence of the mobility is also confirmed by the Arrhenius plots in ***Figure 2.14a*** (filled symbols) that shows the μ_{FET} values extrapolated from the I_{DS}-V_{GS} curves of ***Figure 2.13*** and plotted for the same V_{GS} bias applied during the sensing phase. From the Arrhenius plot of mobility we then estimate the activation energies E_μ for all the tested materials that are reported in ***Table 2.1*** and the results are perfectly in agreement with other results presented in literature[Chesterfield04, Mao16]. Still from the I_{DS}-V_{GS} curves of ***Figure 2.13***, we extrapolated the parameter α of equation ***2.1*** that is showed in ***Figure 2.14b*** as a function of the temperature.

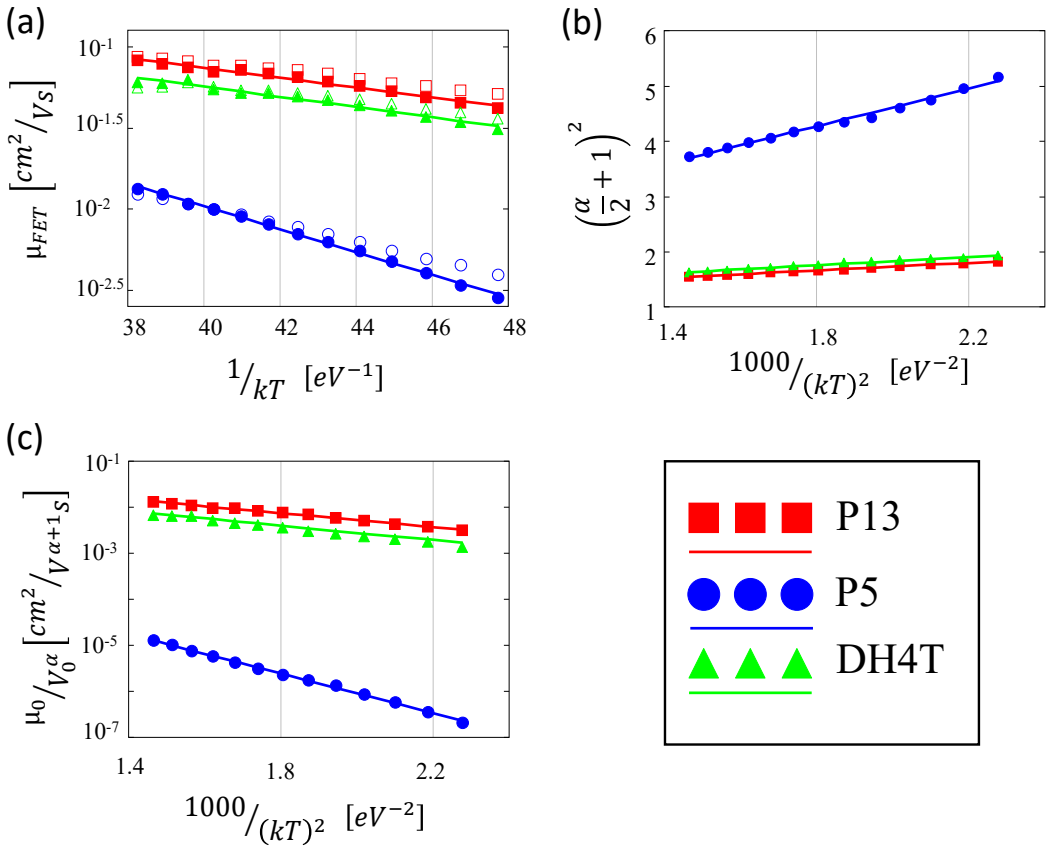

Figure 2.14. **(a)** *Arrhenius plot of the field effect mobility μ_{FET} from I_{DS}-V_{GS} curves (filled symbols) and from the transient fits (open symbols).*
(b) *α parameters as a function of temperature (symbols).* (c) *Arrhenius plot of μ_0/V_0^{α} with a $1/T^2$ dependence (symbols). The lines in the graphs are linear interpolation.*

The voltage-dependent field-effect mobility (equation ***2.1***) has derived starting from an exponential density of states[Vissenberg98]. Although, as reported by Nešpůrek[Nešpůrek72] and Steiger[Steiger02], assuming a Gaussian DOS it is possible to use the same relation by changing the meaning of the parameter α that becomes

$$\alpha = 2\left(1 + \frac{\pi\sigma^2}{8k^2T^2}\right)^{\frac{1}{2}} - 2, \qquad (2.3)$$

with σ the width of the Gaussian distribution of states. From the data of ***Figure 2.14b*** we calculated the values of σ for the tested materials and the results are reported in ***Table 2.1***. In addition, a good and widely used model that assume a Gaussian DOS is the extended Gaussian disorder model (EGDM)[Coehoorn12]. The EGDM model gives an understanding of charge transport in organic semiconductors describing the mobility as a function of temperature, carrier concentration, and electric field. Under low field and low carrier concentration conditions, the mobility shows a $1/T^2$ dependence. Thus, the parameter low field mobility μ_0 in equation (1) can be written as follows:

$$\mu_0 = B \exp\left(-c\frac{\sigma^2}{(kT)^2}\right), \qquad (2.4)$$

where *B* is a mobility pre-factor, *c* is an empirical coefficient, and σ is the width of the Gaussian distribution of states likewise in equation ***2.3***. In the literature, the coefficient *c* was found with a very broad range (from 0.35 to 0.56[Schmechel02]). In this work we refer to the work of Bässler[Bässler93] that found a value of *c*=0.44.

EXTRACTED PARAMETERS

MATERIAL	E_μ [meV]	E_τ [meV]	σ [meV] (from α)	σ [meV] (from μ_0)
P5	159±4	442±16	70±2	107±1
DH4T	68±5	404±6	32±1	66±2
P13	70±5	394±74	25±4	57±6

Table 2.1 - Parameter extracted for the different materials.

Remarkably, in our experiments, equation ***2.4*** holds true because on the one hand μ_0 is the field-effect mobility at low carrier concentration, on the other hand the estimated electric field along the channel is less than 10kV/cm thus its contribution on the mobility can be neglected. We show in ***Figure 2.14c*** an Arrhenius plot of μ_0/V_0^α as a function of $1/T^2$. From this graph the width σ can be estimated, and its value is reported in ***Table 2.1*** for the different material employed. Looking at ***Table 2.1***, we can then compare the values of σ estimated by equations ***2.3*** and equation ***2.4***. The two techniques give reasonable results within the same order of magnitude suggesting that, for all the tested material, the HOMO and LUMO DOS are well described by a Gaussian distribution. Anyway, we must remember that this assumption does not consider the presence of other states, related, for instance, to the PMMA-semiconductor interface impurities and contaminations.

Looking now at the transients shown in ***Figure 2.12***, we can see that the increase of temperature does not only induce a larger current (upwards shift), but also induces a leftward shift of the curves associated with a smaller relaxation time, suggesting that also the transient process itself is thermally activated. It is therefore important to notice that such transients do not represent the turn on of the device, indeed after looking for instance at the P13 device (***Figure 2.12a***), the current rise from 60μA (at 10ms) up to 90μA (at 50s). Yet the current features an increase of 50% respect its initial value. This is a strong limit for analog applications, such as amplifiers. Instead in digital applications, where the key parameters are the turn on and turn off times, this phenomenon translates only in a reduction of the maximum driving current at high operative frequency, and in turn a reduction of the average on-state resistance.

In chapter ***2.1*** we demonstrated that these transients are not related neither to charge trapping phenomena nor to displacement currents, but are related to the HOMO and LUMO tail-states that strongly limit the formation and the depletion of the conductive channel. Thus, the transients can be associated with a mobility variation that is limited (in time) by the HOMO and LUMO levels that has to be populated in order to move the quasi-Fermi level close enough to the respective transport level, as it is schematically depicted in ***Figure 2.15*** (referring to the LUMO levels). During the filling phase, the Fermi level position (E_{Ff}) is forced to move away from E_C and all the states between E_C and E_{Ff} are empty. During the sensing phase, the Fermi energy slowly moves from level E_{Ff} to level E_{Fs} and the time required by this process is the time needed to accumulate the charge Q_F in the low mobility states between E_{Fs} and E_{Ff}, thus inducing a mobility transient.

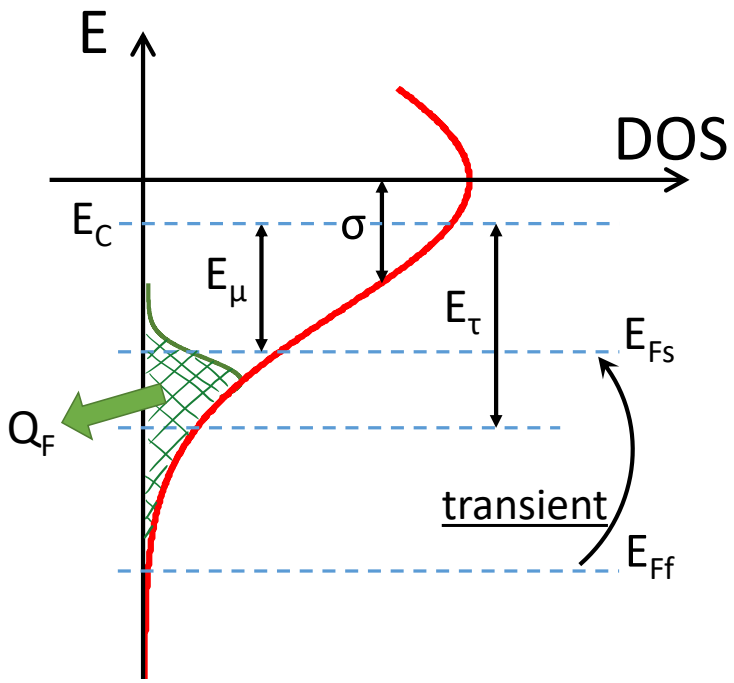

Figure 2.15 - Schematic representation of the LUMO DOS. *E_C is the conduction band, E_{Fs} is the Fermi level during the sensing phase (at stationary condition), E_{Ff} is the Fermi level during the filling phase (at stationary condition), and Q_F is the charge that need to be accumulated in the low mobility states to bring the Fermi level from E_{Ff} to E_{Fs} (drawing not to scale).*

In agreement with the work of Mathijssen et al.[Mathijssen07] we used a stretched exponential function to account for all the gap-states involved in this process, thus we fitted the transients in ***Figure 2.12*** by applying the following model:

$$I_{DS}(\mathrm{t}) = C_i \frac{\mu_{FET}(t)}{\alpha+2} \frac{W}{L} (V_{GS} - V_T)^2 \ , \qquad (2.5)$$

where C_i, W, L and V_{GS} are given; V_T and α (***Figure 2.14b***) are parameters extrapolated at each temperature from Fig. 4; and $\mu_{FET}(t)$ is a time dependent expression for the mobility:

$$\mu_{FET}(t) = \mu_\infty - \Delta_\mu \cdot \exp\left(-\left(\frac{t}{\tau}\right)^\beta\right), \qquad (2.6)$$

with β the stretching factor that indicates the spread of states[Johnston06], τ is the time constant associated with the average energy depth of the distribution, Δ_μ is a constant and μ_∞ is the field-effect mobility for t=∞ (see ***Figure 2.17a***). The good quality of the fits can be seen by the dash-dotted curves in ***Figure 2.12***.

Noticeably, the fitted values of μ_∞ (open symbols in ***Figure 2.14a***) are in perfect agreement with the values of μ_{FET} previously calculated (filled symbols in ***Figure 2.14a***), thus confirming that our model gives a good description of the observed phenomenon.

In our model, the thermal activated behavior of the transients is described by the time constant τ which has the following expression[Mathijssen07]:

$$\tau = \nu^{-1} \exp\left(\frac{E_\tau}{kT}\right), \qquad (2.7)$$

where ν is a frequency pre-factor and E_τ is the mean activation energy of the process that involve the accumulation of Q_F (see ***Figure 2.15***). In ***Figure 2.16*** we show the Arrhenius plot for the extracted values of τ from which we could estimate the activation energies E_τ that are reported in ***Table 2.1***.

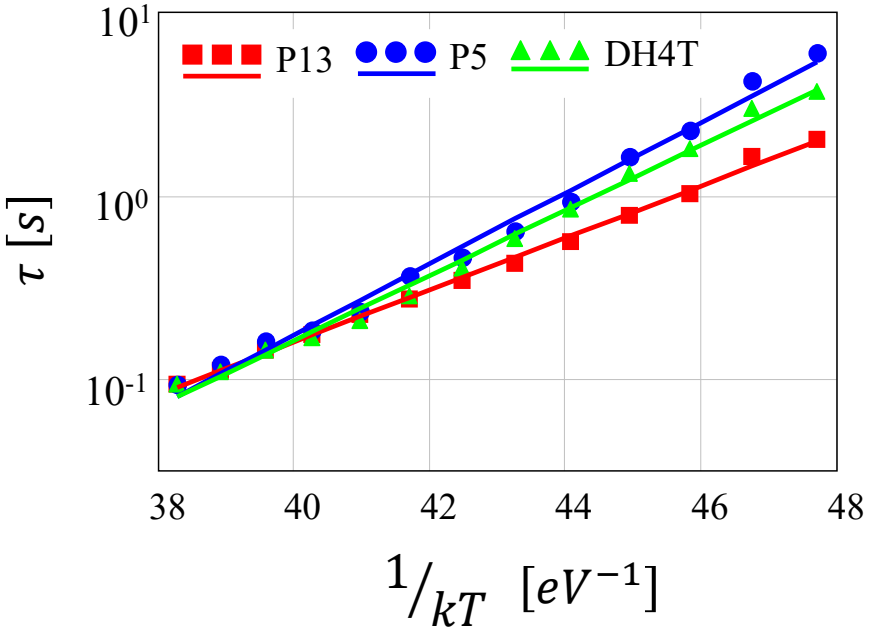

Figure 2.16 - Arrhenius plot of the relaxation time for the tested devices.

At this point, some clarifications are worth to be drawn. We defined both E_μ and E_τ as activation energies associated to a mobility related phenomenon. Incidentally, their values are different (see ***Table 2.1***) and, more important, they have different meaning and they were calculated in different conditions (E_μ from static measurements, and E_τ from transient measurements): E_μ gives a measure of the shallow levels from which carriers hop back and forth to the transport levels following the EGDM model[Coehoorn12] ($E_\mu=E_C-E_{Fs}$ showed in ***Figure 2.15***); E_τ, instead, gives an average measure of deepest sta tes included between E_{Fs} and E_{Ff} (as displayed in ***Figure 2.15***). The comparison between the values of E_μ and E_τ shows how E_μ is significantly smaller than E_τ accordingly with our reasoning.

On the one hand all the tested devices show similar values of E_τ suggesting that the transients are not only limited by the Gaussian tail-states, but also they could be limited by additional interface traps induced by the PMMA dielectric, that is the same for all the tested transistors (our OFET differ each to other only by the semiconductor material). In fact, as reported by Mathijssen et al.[Mathijssen07], the authors showed that the activation energy for the detrapping phenomenon (dual to what described by E_τ) depends mostly by the dielectric rather than the semiconductor. On the other hand, the value of E_μ seems more related to the semiconductor rather than the OFET structure. Indeed, E_μ is related to the relative position of the Fermi level E_F that depends by the charge concentration and consequently by the DOS. This reasoning also suggests that E_μ is not constant during the transient, but is expected to decrease with the increasing of the carrier concentration, i.e., with the increase of the Fermi energy level, and consequently with the increase of mobility.

To support our reasoning, we extrapolated the evolution of E_μ during the transients as a function of the normalized current variation (δ): see chapter ***2.2.3*** for details. ***Figure 2.17b*** shows that E_μ decrease with increasing δ, i.e., the current variation during each transient. In other words, ***Figure 2.17b*** shows that during each transient, as the current increases (i.e., δ increases) the value of E_μ decreases, pointing that the quasi Fermi level is slowly approaching the transport level. In addition, E_μ is always smaller than E_τ (see ***Table 2.1***) This is consistent with the fact that only the carriers at higher levels can contribute to the conduction, because they can hop to the transport level much more likely than those located at low energy.

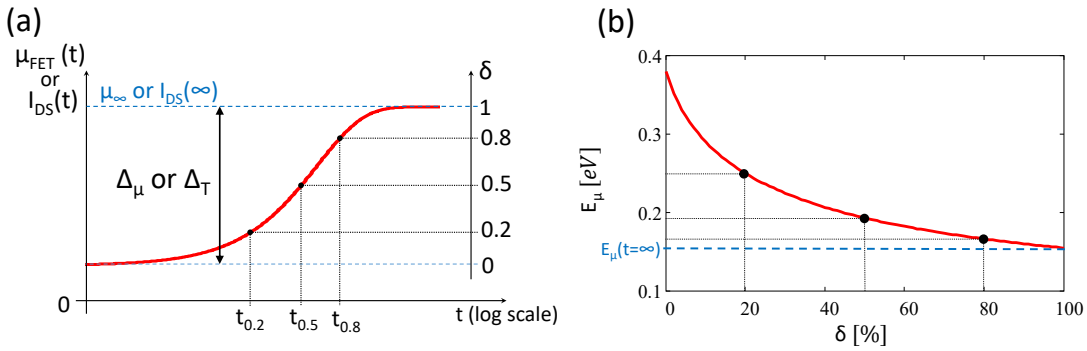

Figure 2.17. **(a)** *Qualitative behavior of μ_{FET}, as well as I_{DS}, as a function of time, as described by equation **2.6**. The relation with ΔT and δ is also reported (see chapter **2.2.3**).*
(b) *Activation Energy E_μ for a P5 device as a function of the percentage of current variation δ (see chapter **2.2.3**).*

2.2.3. Extrapolation of the mobility activation energy as a function of time and temperature

Here we report the detailed procedure used to extrapolate the data presented in ***Figure 2.17b***.

Let's start defining Δ_T as the difference between I_{DS} at the time t=∞ (i.e., the asymptotic value at the end of the transient) and I_{DS} at time t=0 (i.e., at the beginning of the transient), computed at temperature T:

$$\Delta_T = I_{DS_T}(\infty) - I_{DS_T}(0) \qquad (2.8)$$

Where the subscript T indicate that the expression has to be computed for each temperature. Notice that, despite a scale factor, Δ_T correspond to Δ_μ defined in equation ***2.6***, and represented in ***Figure 2.17a***.

We proceed defining the dimensionless parameter δ that ranges from 0 to 1 (which meaning is showed in ***Figure 2.17a***).

We then evaluate the values t_T^* (at each temperature) such as

$$I_{DS_T}(t_T^*) = I_{DS_T}(0) + \delta \cdot \Delta_T \qquad (2.9)$$

Noticeably, once δ is fixed to an arbitrary value between 0 and 1 for all temperature values, t_T^* (which is a function of the temperature T) represents the time at which the $I_{DS_T}(t)$ exhibits the same variation in percentage. Of course, t_T^* is a function of T and δ.

Knowing t_T^*, we used equation ***2.6*** to compute the values of the field effect mobilities μ_{FET} that feature the same current variation $\delta \cdot \Delta_T$ (for the same value of δ) as indicated in ***Figure 2.18a***. We then define:

$$\mu_T(\delta) = \mu_{FET_T}(t_T^*) \qquad (2.10)$$

Now, using equation ***2.10*** we can rewrite equation ***2.2*** as follows:

$$\ln\big(\mu_T(\delta)\big) = -E_\mu(\delta)\frac{1}{kT} - \ln(\mu_0') \qquad (2.11)$$

Using a linear regression (Arrhenius plot in ***Figure 2.18b***), it is easy to estimate $E_\mu(\delta)$ that is exactly what is reported in ***Figure 2.17b***.

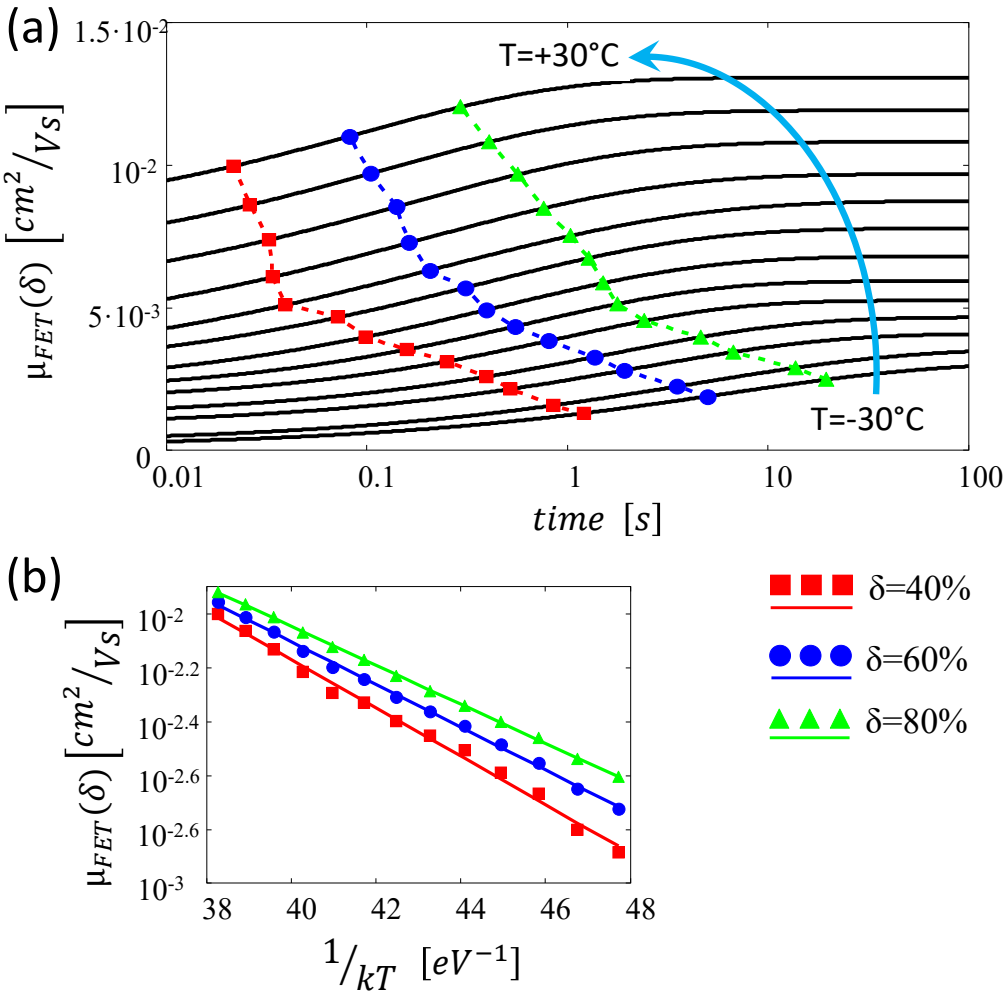

Figure 2.18. **(a)** *Field-Effect mobility μ_{FET} as a function of time at different temperature for a P5 device, the dots correspond to a given percentage variation δ.* **(b)** *Arrhenius plot for the mobilities corresponding to a given δ.*

2.3. Summary

We have shown that pulsed and transient characterizations are useful tools to analyze the dynamic channel response. The current transient duration is related to the tail-states of HOMO and LUMO that limit the speed of the channel formation and depletion, which is not only a fundamental issue for device and material characterization, but also it might severely impact some applications. In fact, characterization procedure must be carefully set up to eliminate any transient phenomena, which affect the extrapolation of mobility, trapped charge density, etc.

We also applied the DLTS technique where both p-type and n-type OFETs were analyzed and they show a similar transient behavior. We correlated the DLTS technique with electrical I_{DS}-V_{GS} characterizations and we extrapolated the activation energies Eμ and Eτ as well as the widths σ of the HOMO and LUMO distribution using the Gaussian approximation.

Our analysis clearly validates the use of pure electrical techniques to give a qualitative and quantitative description of the energy levels as well the Fermi level in polymer and molecular semiconductors. Moreover, we showed that the transient response is strongly limited by the time needed to fully populate the electronic channel. The channel formation requires to move the quasi Fermi energy close to the corresponding transport level by populating all the tale states starting from the deepest states to the shallower levels.

This phenomenon has a strong impact to the dynamic performances of the OFET devices since it can take a very long time to completely form the conductive channel and it directly impacts the mobility of the transistors. Then, even though this phenomenon moderately impacts on the digital applications, particular care must be taken in designing analog circuits.

References

[Bässler93] H. Bässler, *Charge Transport in Disordered Organic Photoconductors a Monte Carlo Simulation Study*, **Phys. Status Solidi B**, vol. 175, issue 1, pp. 15-56, Jan. 1993.

[Benincori08] T. Benincori, M. Capaccio, F. De Angelis, L. Falciola, M. Muccini, P. Mussini, A. Ponti, S. Toffanin, P. Traldi, and F. Sannicolò, *Spider-like oligothiophenes,* **Chem. Eur. J.**, vol. 14, issue 2, pp. 459-471, Jan. 2008.

[Bisi14] D. Bisi, A. Stocco, M. Meneghini, F. Rampazzo, A. Cester, G. Meneghesso, and E. Zanoni, *High-voltage double-pulsed measurement system for GaN-based power HEMTs,* **Reliability Physics Symposium: 2014 IEEE International**, Jun. 2014.

[Chesterfield04] R. J. Chesterfield, J. C. McKeen, C. R. Newman, P. C. Ewbank, D. A. da S. Filho, J.-L. Brédas, L. L. Miller, K. R. Mann, and C. D. Frisbie, *Organic Thin Film Transistors Based on N-Alkyl Perylene Diimides: Charge Transport Kinetics as a Function of Gate Voltage and Temperature*, **J. Phys. Chem. B**, vol. 108, issue 50, pp 19281-19292, Dec. 2004.

[Coehoorn12] R. Coehoorn, and P. A. Bobbert, *Effects of Gaussian disorder on charge carrier transport and recombination in organic semiconductors*, **Phys. Status Solidi A**, vol. 209, issue 12, pp. 2354-2377, Dec. 2012.

[Dimitrakopoulos02] C. D. Dimitrakopoulos, and P. R. L. Malenfant, *Organic thin film transistors for large area electronics*, **Adv. Mater.**, vol. 14, issue 2, pp. 99-117, Jan. 2002.

[Dost08] R. Dost, A. Das, and M. Grell, *Time-of-flight mobility measurements in organic filed-effect transistors*, **Appl. Phys. Lett.**, vol. 105, issue 8, pp. 084519, Oct. 2008.

[Dunn06] L. Dunn, D. Basu, L. Wang, and A. Dodabalapur, *Organic field effect transistor mobility from transient response analysis*, **Appl. Phys. Lett.**, vol. 88, issue 6, pp. 063507, Feb. 2006.

[Frisbie09] Y. Liang, C. D. Frisbie, H.-C. Chang, and P. P. Ruden, *Conducting channel formation and annihilation in organic field-effect structures*, **J. Appl. Phys.**, vol. 105, issue. 2, pp. 024514, Jan. 2009.

[Generali10] G. Generali, R. Capelli, S. Toffanin, A. Facchetti, and M. Muccini, *Ambipolar field-effect transistor based on α,ω-dihexylquaterthiophene and α,ω-diperfluoroquaterthiophene vertical heterojunction*, **Microel. Reliab.**, issue 50, no. 9-11, pp. 1861-1865, Sep.-Nov. 2010.

[Horowitz00] G. Horowitz, M. E. Hajlaoui, and R. Hajlaoui, *Temperature and gate voltage dependence of hole mobility in polycrystalline oligothiophene thin film transistors*, **J. Appl. Phys.**, vol. 87, issue 9, pp. 4456-4463, May 2000.

[Huang11] C. Huang, S. Barlow, and S. R. Marder, *Perylene-3,4,9,10-tetracarboxylic acid Diimides: Syntesis, Physical Properties, and Use in Organic Electronics*, **J. Org. Chem.**, vol. 76, no. 8, pp. 2386-2407, Mar. 2011.

[IEEE08] *IEEE Standard for Test Methods for the Characterization of Organic transistors and Materials*, **IEEE Standard 1620TM**, 2008.

[Johnston06] D. C. Johnston, *Stretched exponential relaxation arising from a continuous sum of exponential decays*, **Phys. Rev. B**, vol. 74, no. 18, pp. 184430, Nov. 2006.

[Jung07] K.-D. Jung, C.A. Lee, D.-W. Park, B.-G. Park, H. Shin, and J.D. Lee, *Admittance Measurements on OFET Channel and Its Modeling With R–C Network*, **IEEE Electron Dev. Lett.**, vol. 28, no. 3, 204-206, Mar. 2007.

[Kalb10] W. L. Kalb, S. Haas, C. Krellner, T. Mathis, and B. Batlogg, *Trap density of states in small-molecule organic semiconductors: A. quantitative comparison of thin-film transistors with single crystals*, **Phys. Rev. B**, vol. 81, issue 15, pp. 155315, Apr. 2010.

[Koopman14] W. W. A. Koopman, S. Toffanin, M. Natali, S. Troisi, R. Capelli, V. Biondo, A. Stefani, and M. Muccini, *Mapping of Charge Distribution in Organic Field-Effect Transistors by Confocal Photoluminescence Electromodulation Microscopy*, **Nano Lett.**, vol. 14, issue 4, pp. 1695-1700, Apr. 2014.

[Li98] Z. Li, *Systematic modelling and comparisons of capacitance and current- based microscopic defect analysis techniques for measurements of high-resistivity silicon detectors after irradiation*, **Nuclear Instruments and Methods in Physics Research A**, vol. 403, issue 2-3, pp. 399-416, Feb. 1998.

[Lin12] P. Lin, and F. Yan, *Organic Thin-Film Transistors for Chemical and Biological Sensing*, **Adv. Mater.**, vol. 24, issue 1, pp. 34-51, Jan. 2012.

[Maddalena15] F. Maddalena, C. de Falco, M. Caironi, and D. Natali, *Assessing the width of Gaussian density of states in organic semiconductors*, **Org. Electron.**, vol. 17, issue 2, pp. 304-318, Feb. 2015.

[Manoli14] K. Manoli, M. M. Patrikoussakis, M. Magliulo, L. M. Dumitru, M. Y. Mulla, L. Sabbatini, and L. Torsi, *Pulsed voltage driven organic field-effect transistors for high stability transient current measurements*, **Org. Electron.**, vol. 15, issue 10, pp. 2372–2380, Oct. 2014.

[Mao16] L.-F. Mao, H. Ning, C. Hu, Z. Lu, and G. Wang, *Physical Modeling of Activation Energy in Organic Semiconductor Devices based on Energy and Momentun Conservation*, **Sci. Rep.**, vol. 6, no. 24777, Apr. 2016.

[Mathijssen07] S. G. J. Mathijssen, M. Cölle, H. Gomes, E. C. P. Smits, B. de Boer, I. McCulloch, P. A. Bobbert, and D. M. de Leeuw, *Dynamics of Threshold Voltage Shifts in Organic and Amorphous Silicon Field-Effect Transistors*, **Adv. Mat.**, vol. 19, issue 19, pp. 2795-2798, Oct. 2007.

[Melucci11] M. Melucci, M. Zambianchi, L. Favaretto, M. Gazzano, A. Zanelli, M. Monari, R. Capelli, S. Troisi, S. Toffanin, and M. Muccini, *Thienopyrrolyl dione end-capped oligothiophene ambipolar semiconductors for thin film- and light emitting transistors*, **Chem. Commun.**, vol. 47, issue 43, pp. 11840–11842, Sep. 2011.

[Melucci13] M. Melucci, L. Favaretto, M. Zambianchi, M. Durso, M. Gazzano, A. Zanelli, M. Monari, M. G. Lobello, F. D. Angelis, V. Biondo, G. Generali, S. Troisi, W. Koopman, S. Toffanin, R. Capelli, M. Muccini, *Molecular Tailoring of New Thieno(bis)imide-Based Semiconductors for Single Layer Ambipolar Light Emitting Transistors*, **Chem. Mater.**, vol. 25, issue 5, pp. 668–676, Feb. 2013.

[Meneghesso04] G. Meneghesso, G. Verzellesi, R. Pierobon, F. Rampazzo, A. Chini, U. K. Mishra, C. Canali, and E. Zanoni, *Surface-related Drain Current Dispersion Effects in AlGaN-GaN HEMTs*, **IEEE Trans. Electron Devices**, vol. 51, issue 10, pp. 1554–1561, Oct. 2004.

[Meneghini12] M. Meneghini, C. De Santi, T. Ueda, T. Tanaka, D. Ueda, E. Zanoni, and G. Meneghesso, *Time- and Field-Dependent Trapping in GaN-Based Enhancement-Mode Transistors With p-Gate*, **IEEE Electron Device Lett.**, vol. 33, issue 3, pp. 375-377, Mar. 2012.

[Mizukami15] M. Mizukami, S. Oku, S.-I. Cho, M. Tatetsu, M. Abiko, M. Mamada, T. Sakanoue, Y. Suzuri, J. Kido, and S. Tokito, *A Solution-Processed Organic Thin-Film Transistor Backplane for Flexible Multiphoton Emission Organic Light-Emitting Diode Displays*, **IEEE Electron Device Lett.**, vol.36, issue 8, pp. 841-843, Aug. 2015.

[Monroe85] D. Monroe, *Hopping in Exponential Band Tails*, **Phys. Rev. Lett.**, vol. 54, issue 2, pp. 146-149, Jan. 1985.

[Myny12] K. Myny, E. van Veenendaal, G. H. Gelinck, J. Genoe, W. Dehaene, and P. Heremans, *An 8-Bit, 40-Instructions-Per-Second Organic Microprocessor on Plastic Foil*, **IEEE Journal of Solid-State Circuits**, vol. 47, issue 1, pp. 284-291, Jan. 2012.

[Nešpůrek72] S. Nešpůrek, and P. Smejtek, *Space-charge limited currents in insulators with the Gaussian distribution of traps*, **Czech. J. Phys.**, vol. 22, issue 2, pp. 160-175, Feb. 1972.

[Nguyen04] T. P. Nguyen, J. Ip, O. Gaudin, and R. B. Jackman, *Determination of localized trap parameters in organic semiconductors using charge based deep level transient spectroscopy (Q-DLTS)*, **Eur. Phys. J. Appl. Phys.**, vol. 27, issues 1-3, pp. 219-222, Jul. 2004.

[Ong05] B. S. Ong, Y. Wu, and P. Liu, *Design of high-performance regioregular polythiophenes for organic thin-film transistors*, **Proceedings of the IEEE**, vol.93, issue 8, pp.1412-1419, Aug. 2005.

[Petit08] C. Petit, D. Zander, K. Lmimouni, M. Ternisien, D. Tondelier, S. Lenfant, and D. Vuillaume, *Gate pulse electrical method to characterize hysteresis phenomena in organic field effect transistor*, **Org. Electron.**, vol. 9, issue 6, pp. 979-984, Dec. 2008.

[Pope99] M. Pope, and C. E. Swenberg, *Electronic Processes in Organic Crystals*, **Oxford University Press**, 2nd ed., 1999.

[Rost04] C. Rost, S. Karg, W. Riess, M. A. Loi, M. Murgia, and M. Muccini, *Ambipolar light-emitting organic field-effect transistor*, **Appl. Phys. Lett.**, vol. 85, issue 9, pp. 1613-1615, Aug. 2004.

[Schmechel02] R. Schmechel, *Gaussian disorder model for high carrier densities: Theoretical aspects and application to experiments*, **Phys. Rev. B**, vol. 66, issue 23, pp. 2352061-2352066, Dec. 2002.

[Sirringhaus09] H. Sirringhaus, *Reliability of Organic Field-Effect Transistors*, **Adv. Mater.**, vol. 21, issues 38-39, pp. 3859-3873, Oct. 2009.

[Sirringhaus14] H. Sirringhaus, *25th Anniversary Article: Organic Field-Effect Transistors: The Path Beyond Amorphous Silicon*, **Adv. Mater.**, vol. 26, issue 9, pp. 1319-1335, Jan. 2014.

[Stallinga00] P. Stallinga, H. L. Gomes, H. Rost, A. B. Holmes, M. G. Harrison, and R. H. Friend, "*Electronic levels in MEH-PPV*, **Synth. Met.**, vol. 111, pp. 535-537, Jun. 2000.

[Steiger02] J. Steiger, R. Schmechel, and H. von Seggern, *Energetic trap distributions in organic semiconductors*, **Synth. Met.**, vol. 129, issue 1, pp. 1-7, Jun. 2002.

[Taylor08] D. M. Taylor, and N. Alves, *Separating interface state response from parasitic effects in conductance measurements on organic metal-insulator-semiconductor capacitors*, **J. Appl. Phys.**, vol. 103, issue 5, pp. 054509, Mar. 2008.

[Tirado07] J. M. Tirado, J. L. Sanchez-Rojas, and J. I. Izpura, *Trapping effects in the transient response of AlGaN/GaN devices*, **IEEE Trans. Electron Devices**, vol. 54, issue 3, pp. 410-417, Mar. 2007.

[Ucurum10] C. Ucurum, H. Siemund, and H. Göbel, *Impact of electrical measurement parameters on the hysteresis behaviour of pentacene-based organic thin-film transistor*, **Org. Electron.**, vol. 11, issue 9, pp. 1523-1528, Sept. 2010.

[Ullah09] M. Ullah, D. M. Taylor, R. Schwödiauer, H. Sitter, S. Bauer, N. S. Sariciftci, and Th. B. Singh, *Electrical response on highly ordered organic thin film metal-insulator-semiconductor devices*, **J. Appl. Phys.**, vol. 106, issue 11, pp. 114505, Dec. 2009.

[Vissenberg98] M. C. J. M. Vissenberg, and M. Matters, *Theory of the field-effect mobility in amorphous organic transistors*, **Phys. Rev. B**, vol. 57, issue 20, pp. 1296-12967, May 1998.

[Weis09] M. Weis, J. Lin, D. Taguchi, T. Manaka, and M. Iwamoto, *Analysis of Transient Currents in Organic Field Effect Transistor: The Time-of-Flight Method*, **J. Phys. Chem. C**, vol. 113, issue 43, pp. 18459-18461, Sep. 2009.

[Zao13] Y. Zao, Y. Guo, and Y. Liu, *25th Anniversary Article: Recent Advances in n-Type and Ambipolar Organic Field-Effect Transistors*, **Adv. Mater.**, vol. 25, issue 38, pp. 5372-5391, Aug. 2013.

[Zhuang13] W. Zhuang, M. Bolognesi, M. Seri, P. Henriksson, D. Gedafaw, R. Kroon, M. Jarvid, A. Lundin, E. Wang, M. Muccini, and M. R. Andersson, *Influence of Incorporating Different Electron-Rich Thiophene-Based Units on the Photovoltaic Properties of Isoindigo-Based Conjugated Polymers: An Experimental and DFT Study*, **Macromolecules**, vol. 46, issue 21, pp. 8488-8499, Oct. 2013.

3. Organic Semiconductor – Solution Interface

The flexibility and biocompatibility of many organic semiconductors are properties that easily prompted the use of these materials for their implementation in chemical and biological sensing[Lin12]. Hence, researchers have spent many efforts in the healthcare area, working with different polymers and small molecules, where organic semiconductors (OSC) are at the interface with an ionic solution[Berggren07, Fang15].

Moreover, organic thin-film transistors (OTFTs) allow the integration of a sensor and an amplifier in a single device. In fact, it has been widely demonstrated the potentiality of these technologies in gaining better performances with respect to inorganic devices, such as silicon TFTs or micro-electrode arrays[Frega12, Khodagholy13, Mabeck06, Poghossian09]. Indeed, in the last decade, organic electrochemical transistors (OECTs) and electrolyte-gated OFETs (EGOFETs) capable to interface with neural cells directly plated on top of the organic layer were reported[Cramer13, Kodagholy13, Tarabella15, Yao15]. Nevertheless, the mechanism of transduction of ionic/electronic currents at the interface between the organic layer and the biological environment has to be fully investigated in order to master and optimize the performances of the overall device sensor.

At this purpose, we simplified the architecture of the three-electrode device in order to throughout investigate the different physical phenomena occurring in the organic transistor/cell system. We employed the electrochemical impedance spectroscopy (EIS) technique as investigating probe to extrapolate a complete model of the device. In this scenario, our results may be easily implemented without loss of generality to a plethora of other devices at the interface with the physiological/electrochemical environment such as water-gated transistors[Cramer12, Kergoat10, Kergoat11], dye sensitized solar cells (DSCs)[O'Regan91], super-capacitors[Kötz00, Simon08], light-emitting electrochemical cells (LECs)[Liu13, Tordera12], etc.

3.1. Physical-based equivalent circuit model

To the best of our knowledge, the different equivalent circuit models have been developed to study the electrodes kinetics[Barcia02, Bonora96, Franceschetti77] and to give a description of systems like water-gated transistors[Porrazzo14], dye-sensitized solar cells[Bisquert10, Halme10, Wang05], super-capacitor and fuel cells[Belhachemi00, Fouquet06, Sharma10]. However, such models do not fully describe the whole device physics. In particular, they omit the description of the diffusion layer in the electrical double layer (EDL) or they include mathematical artifices like constant phase elements (CPEs) to describe the endogenous effects of surface irregularity, roughness, porous interfaces, frequency dispersion in many processes, or other non-idealities.

Accordingly, in this chapter we are going to develop an equivalent circuit model for the metal-organic semiconductor-electrolyte stack structure in which every circuital element is correlated to a particular physical phenomenon. We kept the model as simple as possible, avoiding the use of CPEs. In fact, the introduction of more sophisticated circuital elements in the model may result in loss of physical meaning due to the increase in the number of fitting parameters. The consequent

pointless complication in the extrapolation of the parameters would make difficult the interpretation of the results, such as discerning among different phenomena.

3.1.1. Experimental procedure

To get a clearer understanding of the working principles of the organic transistor-based bio-sensor, we use a simple 2-terminal device shown in ***Figure 3.1a***. The 2-electrode device architecture is used in order to: *i)* specifically investigate the device physics at the bulk and the semiconductor electrolyte interface of the organic material *ii)* reduce parasitic couplings among the bio-sensing transistor electrodes as much as possible; and *iii)* perform measurements on devices with a larger area (roughly $2cm^2$) to increase the signal-to-noise ratio (SNR) and, consequently, the measurement accuracy. In the following, we will refer to this structure as the STACK device.

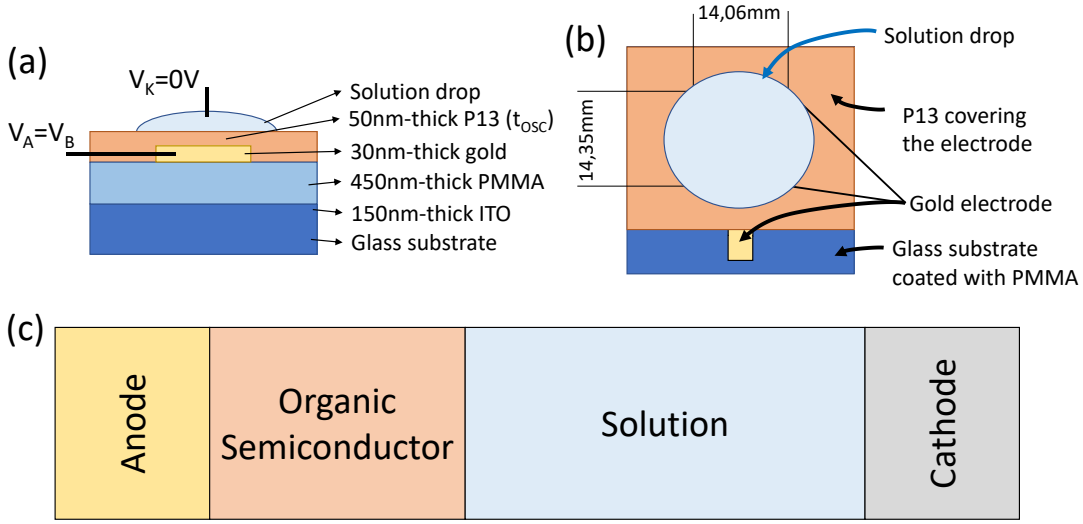

Figure 3.1. **(a)** *Stack device cross section showing the applied voltages at the anode (V_A) and cathode (V_A) electrodes.* **(b)** *Top view of the fabricated device.* **(c)** *Schematic representation of the metal/OSC/solution/metal architecture.*

Our experimental procedure is depicted in ***Figure 2a***. The procedure can be divided into eight steps, which are listed here below and described in details in the following sub-sections ***a)-e)*** of this chapter:

i) *Sample preparation*, described in section ***a)***.
ii) *Surface analysis*. We used both environmental scanning electron microscopy (ESEM) and optical profilometry (see section ***b)***).
iii) *PDL functionalization* (section ***c)***). Poly-D-lysine (PDL) is used to help cell attachment to the devices surface. We adopted the PDL treatment to keep as close as possible to the real operating condition.
iv) *NaCl flush* (section ***c)***). Because we performed EIS measurements with a NaCl solution (concentration of 0.1M), we used the same solution to clean the surface from any contaminant that might remain from the previous step.
v) *NaCl deposition* (section ***c)***). Approximately 0.1 ml of NaCl was put on top of the device for characterizations.
vi) *EIS Measurements* at different bias conditions (section ***d)***).
vii) *MilliQ wash* (section ***e)***). Immediately after the EIS measurements, devices were cleaned using an appropriate protocol using MilliQ water in order to remove NaCl residuals. After cleaning, devices were left to dry before the next step.
viii) *Surface analysis*. Same as in point *ii)* for comparing the behaviour of the device before and after measurements.

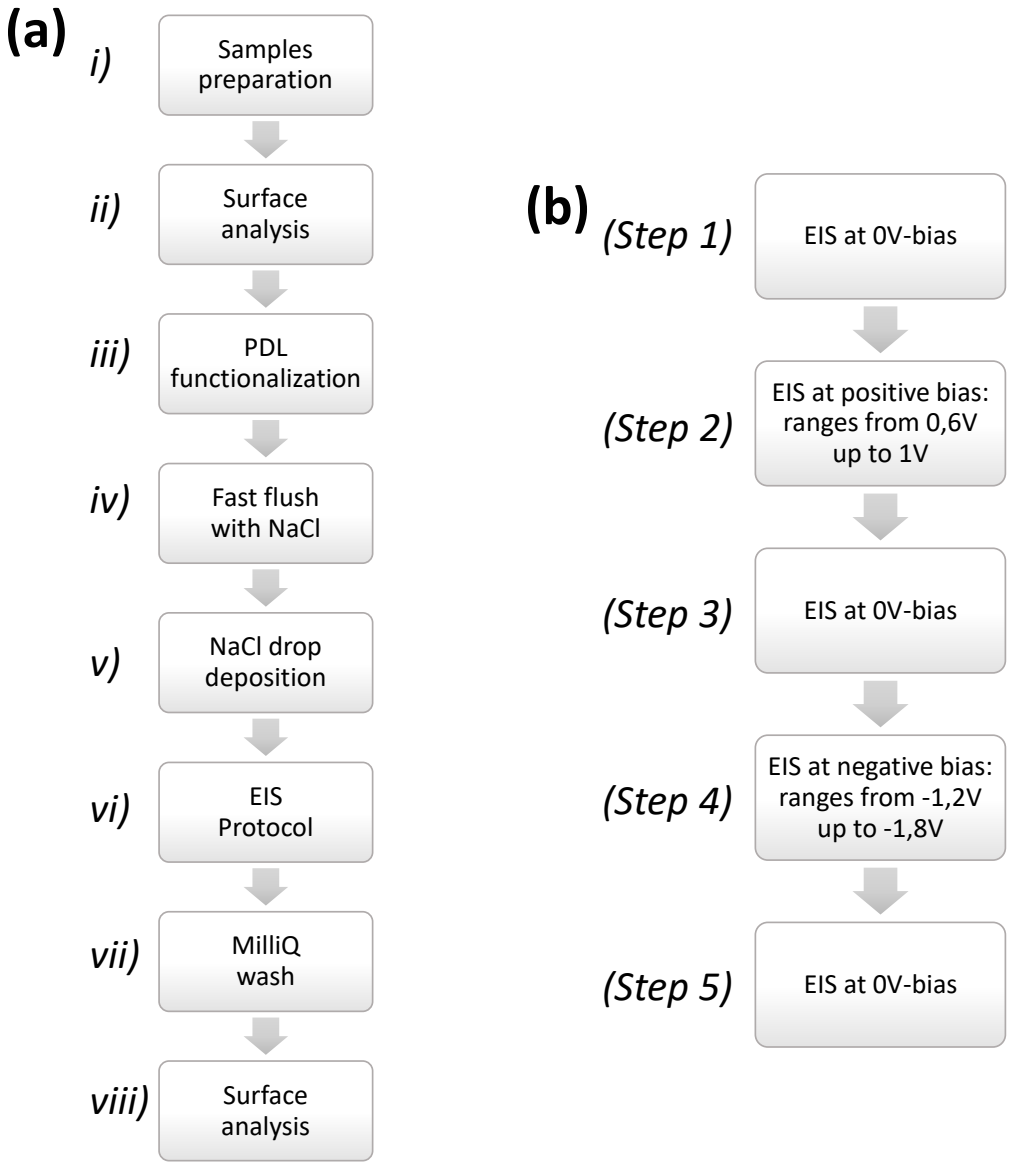

Figure 3.2. **(a)** *experimental procedure flowchart.* **(b)** *bias protocol used to perform EIS measurements.*

a) Sample Preparation

STACK devices (***Figure 3.1***) were fabricated onto a soda-lime glass substrate pre-coated with a 150nm thick indium tin oxide (ITO) layer. The substrate was cleaned by means of multiple sonications in acetone and isopropanol solutions before a 600 nm-thick PMMA film was spin-coated on it. After an overnight annealing treatment in inert atmosphere the PMMA film thickness was reduced to about 450 nm. A 30 nm-thick gold was then evaporated onto the substrate defining the active area of the device as a 14.06mm × 14.35mm rectangle (***Figure 3.1b***). Finally, a 50 nm-thick N,N'-ditridecylperylene-3,4,9,10-tetracarboxylic (P13)[Toffanin13] layer was sublimated in vacuum on top of the structure covering the entire substrate except for a single gold pad necessary to contact the electrode. The PMMA role is to ensure a good deposition of the gold electrode thus achieving a reliable fabrication process. This particular STACK device geometry allows us to deposit the electrolyte drop capable to cover the entire electrode area without short-circuiting it, and with the further advantage to well know the active area of the STACK, which is thus defined by the gold electrode itself (see ***Figure 3.1b***).

b) Surface Analysis

Surface analysis were performed on dry devices before and after EIS measurements to study the bias-induced effects in a device operating in water for a prolonged time. The pre-measure analysis (point *ii)* in ***Figure 3.2a***) was performed on fresh devices right after taking them out from their storage in nitrogen atmosphere; post-measure analysis (point *viii)* in ***Figure 3.2a***) was performed after a washing procedure with milliQ water and an overnight drying (point *vii)* in ***Figure 3.2a***; see section ***e)*** for details).

In order not to affect the physical and morphological structure of the device, two different non-invasive techniques were applied:

1. Environmental Scanning Electron Microscopy. Differently from conventional SEM (Scanning Electron microscopy), which is done in high vacuum and requires to deposit a superficial gold (or other materials) coating on top of the investigated surface, ESEM technique (environmental SEM) allows surface analysis under a controlled environmental condition and no superficial coatings are needed. Thus, this powerful tool allows to analyse a fresh device without either perturbing or damaging it. In this way, it is possible to compare the device conditions before and after EIS measurements. We used a FEI Quanta 200 ESEM, which performs both morphological and compositional spatially resolved analysis thanks to an X-ray detector. By means of morphological study, we can monitor the surface quality, whereas compositional analysis provides information about atom concentrations in percentage. We used H_2O as environment gas at the pressure of 0.53 Torr, and the electron accelerating voltage was set to 20kV.
2. Surface profile by optical profilometry. A Polytec Micro System Analyzer MSA-500 optical profilometer was employed to perform surface imaging. This system permits the non-contact and non-destructive measurements by means of a microscope scanning vibrometer. Its working principle is based on the laser interferometry using a green laser perpendicular to the surface under test. Thanks to its capability to analyze reflective surfaces, we used the optical profilometer to compare the conditions of the gold electrode, which is the most reflective part of our device.

c) PDL functionalization and NaCl drop deposition

The realization of effective bio-sensing devices for transducing cell electrophysiological signals requires a good surface cells adhesion[Widge07]. One common method to enhance cells adhesion is to use a poly-D-lysine (PDL) treatment[Kim11]. We thus perform a surface functionalization deposing a drop of PDL solution on top of our devices. The drop was left on top of the device for 20 minutes, keeping the device in a non-ventilated place to avoid a fast evaporation of the solution. During this time, PDL interact with the P13 surface. After the 20 minutes, the excess PDL solution was carefully removed leaving on top of the surface a self-assembled monolayer of PDL.

Immediately after the PDL treatment, EIS measurement protocol is performed on the devices (section ***d)***). Nevertheless, any solution process performed onto the device surface may cause contamination by solution residuals. To overcome this issue, an appropriate cleaning procedure is required. Since the next step is the deposition of NaCl solution drop, we used the same NaCl solution used for the EIS measurements to wash out the surface, thus avoiding the PDL contamination. The procedure consists in the deposition of a NaCl drop over the functionalized surface, and leaving it for 1 minute. Later on, the solution was carefully removed. Flushing was repeated three times in agreement with the biological protocols adopted by Toffanin et al.[Toffanin13].

Before performing EIS measurements, it is necessary to deposit a drop of NaCl solution on top of the STACK to realize the electrical contact. We did not use any kind of barrier to confine the solution in a particular area, to avoid any accidental damaging of the samples due to mechanical stress. For this reason, the STACK devices were properly designed and optimized by having the organic layer area much larger than the gold electrode area. Hence, the drop can cover the entire electrode area without contacting the gold pad. The P13 capping avoids short-circuits between gold electrode and solution, meaning that the NaCl drop must not extend outside the region delimited by the semiconductor, whereas it can be larger than the square electrode (see ***Figure 3.1***).

d) Electrochemical Impedance Spectroscopy

Electrochemical Impedance Spectroscopy measurements are surely a powerful tool for investigating interfaces and understanding electrochemical devices working principles.

To improve measurements repeatability and accuracy, we designed a custom sample-holder, which allows to perform stable and reproducible measurements of the devices under test while minimizing noise and other parasitic effects (such as leakage and capacitive coupling). Moreover, the platinum wire which is rigidly jointed to the sample-holder can be finely and reproducibly immersed in the solution in all the measurements in order to guarantee effective electrical contact.

We employed a Schlumberger SI 1260 impedance-gain phase analyser to perform EIS measurements in a frequency range from 50 mHz up to 500 kHz superimposing the DC polarization V_B to a small signal with an amplitude of 10 mV (20 mV peak-to-peak). The AC signal amplitude was carefully chosen to obtain the best trade-off between accuracy and linearity. In fact, even though a large AC signal reduces the low frequency noise, it is not recommended due to the risk of measuring the device in a non-linear regime[Barsoukov05]. This is one of the reasons why we employed STACK devices with such a large area.

For what concerns the choice of the DC polarization and amplitude, we defined the bias sequence described in ***Figure 3.2b***:

- *Steps 1*, *3* and *5*: measurements performed at 0 V to monitor the bias-induced degradation.
- *Step 2*: measurements performed with bias that ranges from 0.6 V up to 1 V with 0.1 V steps.
- *Step 4*: measurements performed with bias ranging from -1.2 V to -1.8 V with -0.2 V step.

All the biases are applied to the gold electrode, and they are referred to the platinum electrode (kept at 0 V). For each step, the bias is held for 5 minutes before EIS starts to avoid any transient effects.

It is worth to remark that, even though the typical operating biases are in the range of 0.4 –0.8V (in absolute value) in order to avoid water electrolysis, we decided to extend the bias range of the measurements from -1.8V to 1V. Indeed, we aim at achieving: *i)* a better understanding of the device physics; *ii)* a more comprehensive picture of all the electrochemical processes; and *iii)* the validation of the model, which must be verified in a wide range of operating conditions[Halme10]. In fact, our purpose is to analyze and describe all the mechanisms occurring in the device, which are expected to be strongly bias-depended.

Because high bias voltages could damage the device, our EIS characterization starts at 0-V bias measurement (*step 1* in ***Figure 3.2b***). After, the bias is increased up to V_B=1 V (*step 2*). This guarantees that any eventual perturbation induced by each measurement on the following one is as small as possible. Then the 0-V bias EIS measurement is performed again (*step 3*) in order to verify if the device was damaged. Subsequently, the bias is increased (in absolute value) up to -1.8V (*step 4*). Finally, the 0-V EIS is performed again (*step 5*). We chose (in absolute value) negative biases higher than positive ones because of the redox potential of the organic semiconductor. Indeed, for perylene-based semiconductors, reduction potentials higher than 0.5 V and oxidation potentials around -1.6V were reported[Lee99] (values reported vs SCE electrode).

Evidently, applying such high polarization bias to electrochemical devices could lead to electrolysis phenomena and the dissolution of the organic semiconductor and, in turn, to breakdown. However, our model will show that most of the applied voltage falls on the semiconductor layer, and just a minor voltage drop falls between the semiconductor-electrolyte interface and the platinum electrode (avoiding electrolysis).

e) MilliQ wash

Similarly to the NaCl flush described in section ***c)***, the washing procedure consists in deposing a MilliQ drop on top of the device surface and leaving it for 5 minutes. Then the MilliQ drop is removed and the flush is repeated for other four times. Cleaning is mandatory after the EIS because salt residuals are largely present on the surface which would modify the surface morphology once dried and crystallized. Thus, deionized water is employed to remove the salts residuals. After that, the surface can be safely left to dry before surface analysis (ESEM and profilometry) are repeated to monitor the bias-induced effects.

f) Compensation of the parasitic components

We performed measurements with a frequency range spanning from 50mHz up to 500kHz. At frequencies larger than hundreds of kHz, inductive behavior in the Nyquist plot can be observed. Instead of adding additional fitting parameters that take into account such parasitic, we preferred to remove the issue by correcting the measure before analyzing the data.

In the following, we describe the procedure we used to compensate our measurements where we consider the parasitic components as lumped elements because our set-up features very short cables, thus in the worst case (f=500kHz), the phase shift between the applied voltage and the measured current is negligible.

Let us define Z_{DUT} as the device impedance we want to measure, whereas we define Z_M as the impedance we actually measure with our instrumentation. Ideally $Z_M = Z_{DUT}$, but often this is not true due to the parasitic elements. Defining with Z_{Sh} all the undesired series contributions, and with Z_O all the undesired parallel contributions, we show in ***Figure 3.3*** two possible equivalent circuits that explain how these parasitic components (Z_O and Z_{Sh}) can impact the accuracy of the measures.

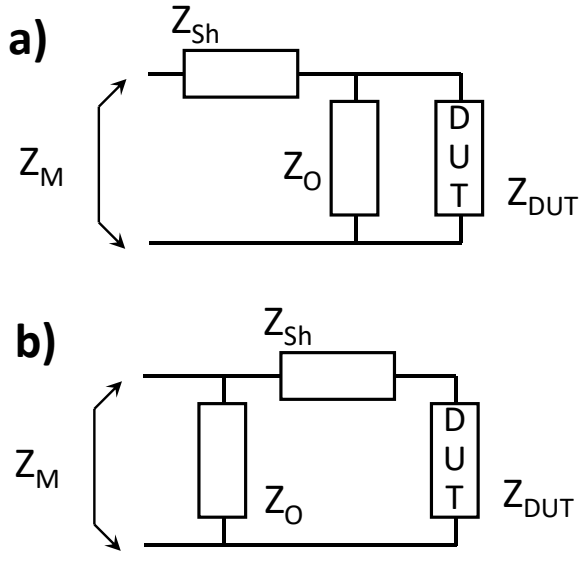

$$Z_M = Z_{Sh} + \frac{Z_{DUT} \cdot Z_O}{Z_{DUT} + Z_O} \qquad Z_{DUT} = \frac{Z_M - Z_{Sh}}{1 - \frac{Z_M}{Z_O} + \frac{Z_S h}{Z_O}}$$

$$Z_M = \frac{(Z_{DUT} + Z_{Sh}) \cdot Z_O}{Z_{DUT} + Z_O + Z_{Sh}} \qquad Z_{DUT} = \frac{Z_M - Z_{Sh} - \frac{Z_M \cdot Z_{Sh}}{Z_O}}{1 - \frac{Z_M}{Z_O}}$$

Figure 3.3. (a) *and* (b) *shows two different equivalent ciruits DUT is the device under test, whereas the concentrated parameters Z_{Sh} and Z_O are the parasitic componets due to the interconnection between sample and instrumentation.*

From the equations reported in ***Figure 3.3*** it can be noticed that, if Z_O and Z_{Sh} are known, we can correct the measured impedance Z_M, getting the correct value of Z_{DUT}. Remarkably, by simply assuming $Z_O >> Z_{Sh}$ (hypothesis that should always be verified in a good set-up), for both the example reported in ***Figure 3.3***, the expression of Z_{DUT} simplifies as follow:

$$Z_{DUT} = \frac{Z_M - Z_{Sh}}{1 - \frac{Z_M}{Z_O}} \qquad (\textbf{\textit{3.1}})$$

Thus, we measured Z_{Sh} by measuring the entire set-up by substituting the DUT with a short circuit, whereas we measured Z_O by performing the measurements by substituting the DUT with an open circuit. Then, we used equation ***3.1*** to compensate the raw data, achieving more reliable measurements and, consequently, a more precise parameters evaluation.

3.1.2. Result and Discussion

In ***Figure 3.4*** we show the real and imaginary parts of the measured impedance as a function of the frequency in Au-P13-electrolyte-Pt STACK devices. From the imaginary parts (***Figure 3.4a*** and ***Figure 3.4b***) we identify five contributions as impedance arcs that are related to five distinct phenomena. All the contributions, except the one at highest frequency, strongly depend on the applied bias. As we will discuss later, the highest-frequency contribution is associated to the platinum/electrolyte interface.

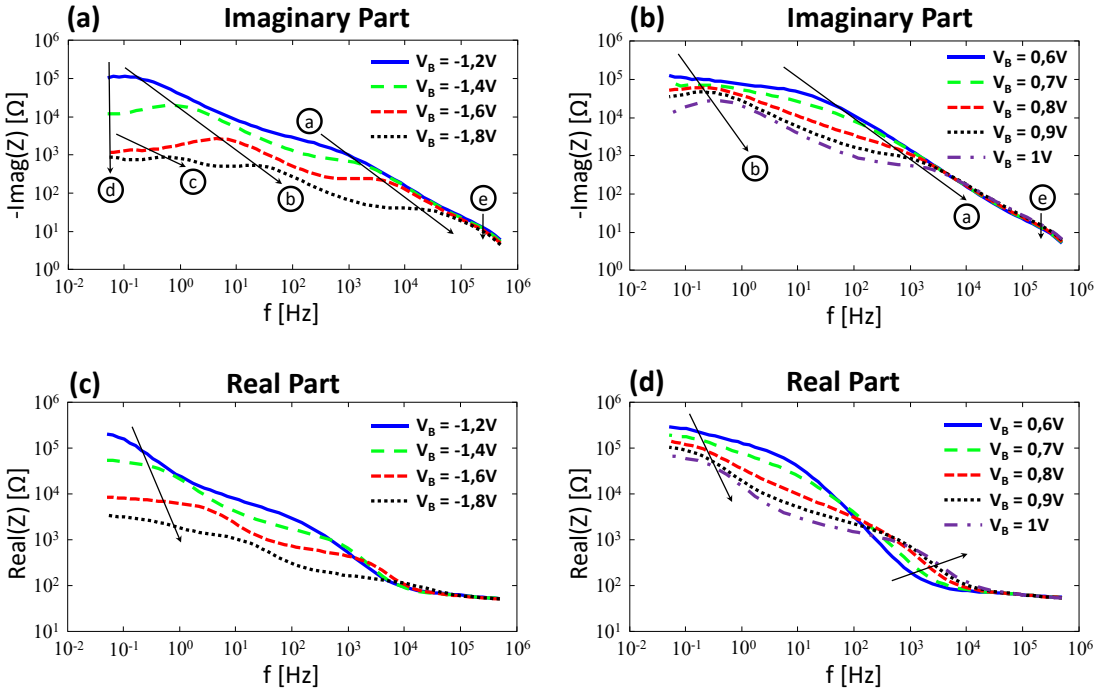

Figure 3.4. **(a)** *and* **(c)** *show the impedance behavior for negative biases.* **(b)** *and* **(d)** *show the impedance behavior for positive biases. The arrows indicate the increase of bias (in absolute value), whereas the circles in Figures* **(a)** *and* **(b)** *indicate the five different phenomena that will be described in chapter* ***3.1.2*** *section* ***a)***.

a) Impedance model description

To explain the data obtained by EIS measurements, we propose the model that is sketched in ***Figure 3.5a*** in the case of a STACK structure biased under a negative voltage. The model highlights the different processes occurring in the different STACK layers such as:

1) Adsorption of ions at the organic semiconductor interface (Helmholtz layer);
2) Accumulation of carriers and charge exchange at the semiconductor/electrolyte interface (double layer capacitance formation);
3) Percolation of the ionic species in the organic semiconductor;
4) Ion diffusion across the electrolyte;
5) Ion adsorption and charge exchange at the platinum interface.

Figure 3.5b shows the circuit model, accounting for each of the processes listed above. In other words, every circuit element can be directly related to a particular interface or layer.

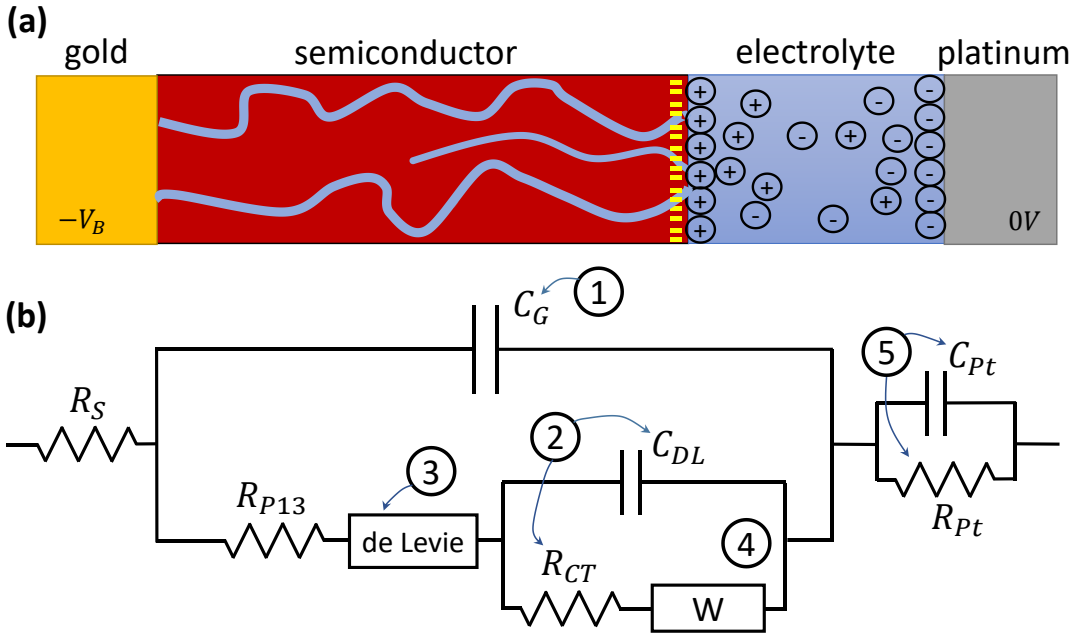

Figure 3.5. **(a)** *Schematic representation of a STACK device under a negative bias polarization.* **(b)** *Equivalent circuit model associated to the device depicted in* **(a)**. *The de Levie impedance (contribution 3) is represented in* ***Figure 3.6***.

Referring to ***Figure 3.5a***, when a negative bias is applied, anions moves away from the semiconductor interface and cations move toward the semiconductor interface, generating a compact Helmholtz layer[Bard01]. Since organic semiconductors may be considered like an insulator, the Helmholtz layer and the gold electrode form the geometrical capacitor C_G, which is modelled as a planar capacitor, having P13 as dielectric.

Ion adsorption leads to the formation of the double layer capacitor C_{DL} with an accumulation layer of electrons in the semiconductor. Given that the double layer capacitor at the organic semiconductor/electrolyte interface is largely investigated in literature[Bard01, Sharma10, Zoski07], we introduced the well-known Randles Cell model to describe the electrolyte metal and/or semiconductor interface[Randles47]. Aside from the double layer capacitor C_{DL}, the model includes the charge transfer resistance R_{CT} to describe the charge transfer reaction, and the Warburg element W (bounded diffusion[Diard12]) to take into account the diffusion process in the double layer structure, in agreement with the model proposed by Stern in 1924[Stern24].

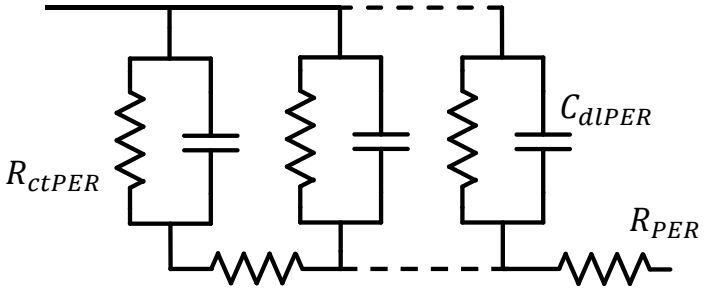

Figure 3.6 - De Levie impedance model.

When biased organic devices are exposed to ionic environment, it is plausible to suppose the presence of percolation processes by which the electrolyte can permeate the semiconductor reaching the gold electrode. In this contest, a good model to describe the ion percolation is the so-called de Levie impedance[Levie63] that is showed in ***Figure 3.6***. The de Levie circuit element is typically used in porous electrodes where the electrolyte/electrode interface is described by a transmission-line-like model[Fouquet06, Franceschetti77, Sharma10]. In this model, R_{PER} describes the solution resistance inside the pores whereas R_{ctPERr} and C_{dlPER} are related to the charge transfer and accumulation processes at the interface between organic semiconductor and percolating ionic

species. The use of the de Levie circuit element for describing the percolation phenomenon will be validated in section ***c)*** of this chapter.

The platinum-electrolyte interface was also taken into account and modelled with C_{Pt} and R_{Pt} components, which have the same nature of C_{DL} and R_{CT} respectively. Even in this case we preferred the simplest circuit scheme, rather than a more elaborated one such as the Randles Cell scheme. Moreover, we verified that the platinum/electrolyte interface gives a really fast contribution (around 10kHz to 100kHz), thus the electrolyte diffusion near the counter electrode can be neglected.

Finally, in order to take into account the series resistances between the two electrodes, we modelled the semiconductor resistance with R_{P13}, and with R_S all other series contributions. The latter parameter includes the electrolyte bulk resistance and the contacts resistance that clearly cannot be distinguished.

b) Discussion and model validation

In order to discern among the different physical processes discussed above, our approach was to extend the typical range of applied bias voltages as describe in chapter ***3.1.1*** (section ***d)***). For instance, low voltage polarization leads to mix up different arcs in the impedance plots, thus the percolation contribution is blurred by the double-layer and diffusion contributions, but it is still present. This is evident in ***Figure 3.7***, which represents the characteristic frequencies for all the phenomena as function of the applied bias: each contribution changes its characteristic frequency by changing the applied bias. Whereas the geometric capacitor and the platinum electrodes are always distinguishable, diffusion, percolation, and double layer impedances tend to overlap at lower biases, having their characteristic frequency between 0.01 and 1 Hz. Instead, all the contributions are clearly distinguishable at high negative biases, when diffusion, percolation and double layer characteristic frequencies approach 0.05 Hz, 0.8 Hz, and 30 Hz, respectively.

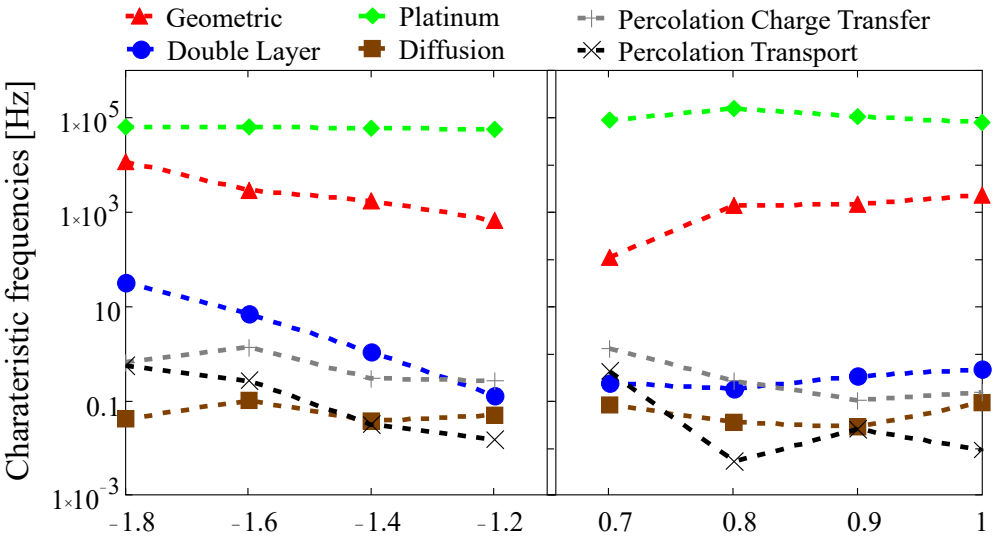

Figure 3.7 - Characteristic frequencies for all the fitted contribution.

Experimental data were fitted with the proposed model by means of a custom program developed in Matlab(R). The extrapolated parameters are reported in ***Table 3.1***. R_S, C_G, R_{Pt}, and C_{Pt} are mostly related to the geometry and structure of the device and they are almost constant (within the experimental and fitting error), as expected. C_{DL} and τ_D also show an almost constant behaviour with respect to the applied voltage in agreement with the results reported in literature[Bard01]. The other parameters instead, feature a variation much larger than 10%, which are dependent on the applied voltage V_B. R_{P13}, R_{PER}, R_{ctPER}, R_{CT}, and R_D are strongly related to the carrier concentration (electrons or holes in the semiconductor and ions in the solution). Hence, increasing the V_B (in absolute value) we increase the injection of carriers that, in turn, contribute to increase the semiconductor mobility and the charge transfer reactions at the semiconductor/electrolyte interface (decreasing the resistances). Finally, C_{dlPER} increases with increasing V_B, in absolute value, due to an enhancement in the percolation process and the consequently larger concentration of ions inside the semiconductor.

STACK fitting parameters												
V_B [V]	R_S [Ω·cm²]	R_{P13} [kΩ·cm²]	C_G [nF/cm²]	R_{PER} [kΩ·cm²]	R_{CtPER} [kΩ·cm²]	C_{dlPER} [µF/cm²]	R_{CT} [kΩ·cm²]	C_{DL} [µF/cm²]	R_D [kΩ·cm²]	τ_D [s]	R_{Pt} [Ω]	C_{Pt} [nF]
-1.8	103.0	0.14	98.5	2.84	2.44	100.2	1.38	3.68	3.72	9.6	25.3	98.7
-1.6	103.4	0.85	64.0	14.48	2.92	41.2	6.06	3.78	5.26	4.0	21.2	118.0
-1.4	105.0	1.82	50.3	158.16	16.99	31.9	39.58	3.80	37.10	11.0	19.9	105.2
-1.2	106.1	4.62	51.6	439.54	24.34	24.7	365.00	3.49	131.50	8.5	25.7	107.8
0.7	102.1	3.06	55.8	282.92	87.78	1.4	212.16	3.14	100.34	5.0	20.0	90.0
0.8	102.1	2.51	45.6	1243.78	24.64	24.9	129.31	7.10	105.12	11.4	11.5	88.0
0.9	106.1	2.24	47.6	249.78	60.84	26.1	89.18	5.34	59.06	15	17.3	88.0
1	106.1	1.53	44.4	223.62	13.56	77.6	68.60	4.64	17.00	4.6	21.4	92.8

Table 3.1 - Fitting parameters *extrapolated using the here presented model for both STACK and OCST devices. All the parameters, except for the platinum ones, are normalized as respect to the 2cm² area of the structure.*

Let us start the analysis from the series resistance. We measured the conductivity of the saline solution, which is 17 mS/cm in our samples. This value is in good agreement with the value of R_S extrapolated from the EIS measurements, indicating that R_S is dominated by the electrolyte bulk conduction, whereas the contact resistance is negligible.

Proceeding with the Randles Cell circuit, our measurements clearly show a contribution at low frequency in perfect agreement with the dynamic of the Nernst diffusion[Bonora96, Hauch01].

The electrical double layer is the key constituent element in all the different organic devices that operate in the physiological liquid conditions, which masters the transduction mechanism. The agreement between our extrapolated values of the C_{DL} capacitance and its time constant, with the values that can be found in literature[Barcia02, Kergoat11, O'Regan91] confirms the presence of a layer of adsorbed ions at the P13 surface.

Regarding the contribution of the geometric capacitor, our model partially differs from others presented in literature[Barcia02, Porrazzo14] that define the geometric capacitance as the electrolytic solution capacitance. In our model, the geometric capacitance is the capacitance of the planar capacitor comprised by the gold electrode and the Stern-Helmholtz layer that better represents a coated electrode structure[Tordera12]. The model feasibility is corroborated by the excellent agreement of the extrapolated parameters of C_G=51±6 nF/cm2 with the expected value 48 nF/cm2 calculated by assuming 50 nm as layer thickness of P13, 2cm2 as surface area, and 2.73[Nahhas12] as relative permittivity.

Even though the platinum/electrolyte interface was modelled with a very simple RC circuit, it provides an adequate fit at high frequency. This simple RC model is implemented in several works dealing with DSC devices[Bonora96, Hauch01, Wang05], where a platinum counter electrode is used to promote the electrolyte reduction[Wang05]. Our results are consistent with the nature of these reactions giving a time constant around 10µs.

Figure 3.8 shows the good matching of the EIS experimental data (blue circles) with the model (solid line), for both negative and positive biases (***Figure 3.8a*** and ***Figure 3.8b*** respectively), confirming the scientific significance of using the de Levie impedance model to account for ions percolation through the semiconductor. This percolation through the organic layer is clearly visible at relative high voltages, where the impedance imaginary part versus frequency shows four impedance arcs. However, by interpolating the EIS curves at different bias conditions, we demonstrated the presence of percolation also at low operating voltages – even though less prominent– when just three impedance arcs appear. Indeed, if we neglected the percolation by removing the de Levie impedance, the model would no longer fit correctly the experimental data, as it is clearly visible by the dashed lines in ***Figure 3.8***. This evidence confirms the hypothesis that percolation is not just the consequence of a high-bias induced damage, but it is a physical phenomenon occurring independently from the applied voltage, even though at different rate.

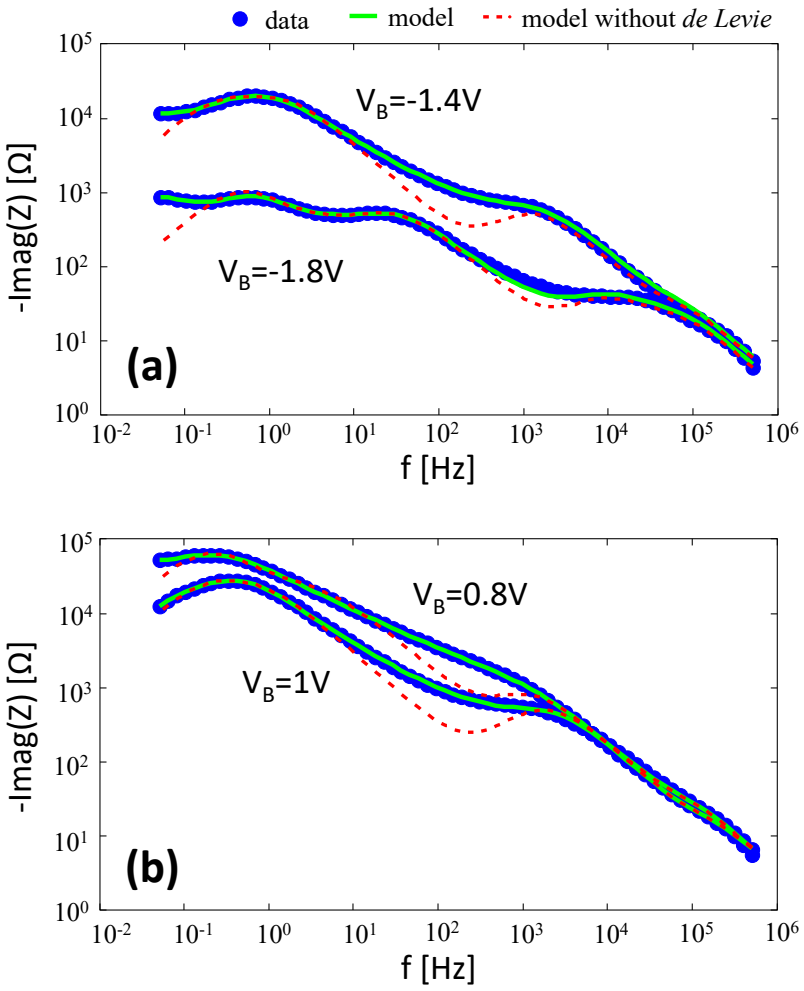

Figure 3.8 - Imaginary part of the impedance *for both negative* (a) *and positive* (b) *bias values. Symbols are experimental data, solid lines are our complet model, and dashed lines are the model without the de Levie contribution.*

We would like to underline once again that we are taking into account each phenomenon by means of either distributed or lumped parameter systems. Every regressed parameter has a precise physical meaning, given that we avoided to introduce any constant phase elements (CPEs), which are typically implemented to replace capacitors when surface irregularities, nanoporous interfaces and other non-idealities produce a broad frequency dispersion in the collected EIS measurements. In addition, some minor discrepancies between experimental data and our model could be corrected by taking into account the shape[Franceschetti77, Keiser76] and the size distribution[Song99] of the percolation paths. These improvements are not taken into account because they introduce further analytical complications, whereas we preferred focusing in the understanding of the physical mechanisms occurring at the device interfaces and at the bulk of the organic material, achieving a good trade-off between accuracy of the physical description and simplicity of the equivalent circuit. At this regard, because CPE might explain processes with wide frequency dispersion, its use would make difficult to distinguish between several processes featuring similar characteristic frequency values, as in case of diffusion and percolation. Consequently, with a CPE approach, it could be not even possible explain the data at higher voltages, such as at -1.8V.

As a final remark, the presented model could be successfully applied to analyse the behaviour of more complex devices, such as water-gated transistors, for both chemical and biological sensing. In fact, even though that many efforts have been done in order to model and characterize such devices under physiological environment conditions [Cramer12, Popescu15], a consolidated approach to study and predict the device response is still missing.

Many works presented in literature aim to describe the transduction between bio-sensing devices and living cells[Fromherz99, Schoen07, Voelker05, Weis97, Zeck01], but despite those achievements, a consolidated theory on the interaction between the organic sensing platform and neurons is still missing. At this purpose, the two-terminal circuit model fully describe the semiconductor-electrolyte interface, thus fitting the needs on describing the interaction between transistor and living cell. Indeed, we retain that each part of the transistor structure, such as source and drain electrodes (in contact with the physiological solution), can be described by our model. In particular, we believe that our model can help to understand and to master the interaction between the ionic cellular signals and the organic transistor channel. This could be combined also with other OTFT models[Horowitz04, NEcliudov00, Spijkman11, Torricelli15] to analyse and model the overall system that include the OTFT-based sensor with cells on top, as we are going to investigate in chapter ***4***.

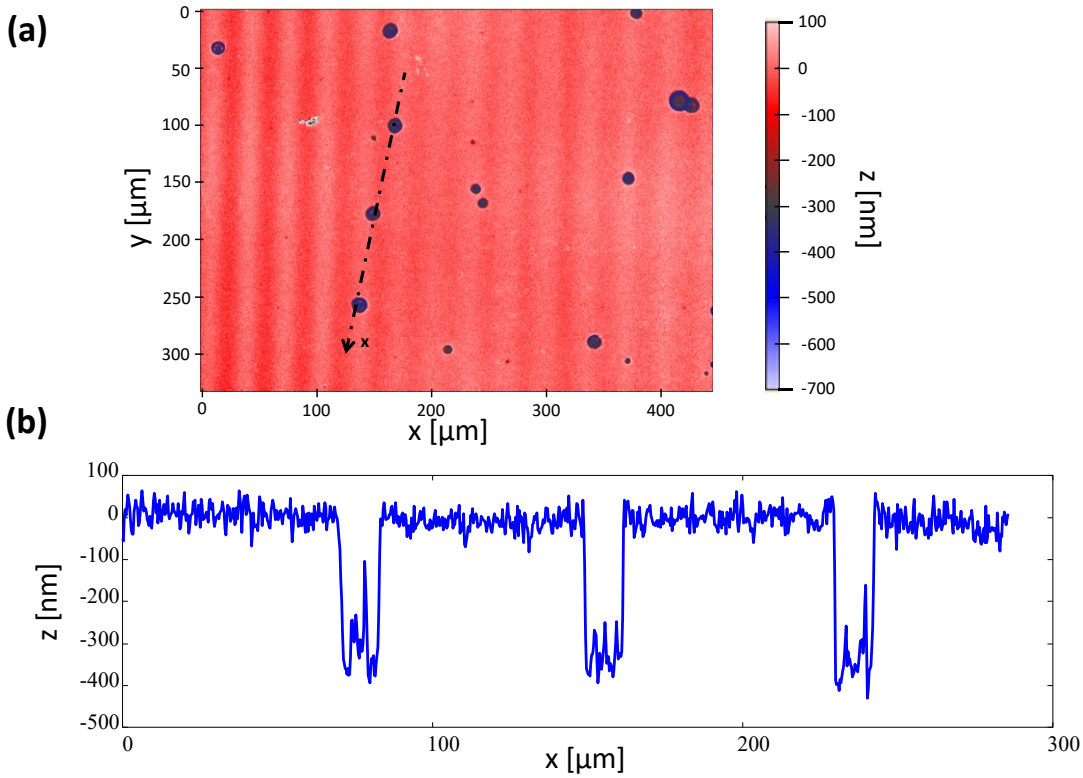

Figure 3.9. **(a)** *Two-dimensional profile picture showing the presence of different cavities.* **(b)** *A single slice taken following the arrow in* **(a)** *showing the one-dimension surface profile. Note that, since gold is the only reflecting material, the depth of the voids is bigger than the gold width. This does not implicate a PMMA degradation, but it is only a confirmation of the gold corrosion.*

c) ESEM and profilometry imaging analysis

We verified the presence of ion percolation process within the organic semiconductor layer by means of the optical profilometer and ESEM imaging reported in ***Figure 3.9*** and ***Figure 3.10*** respectively, confirming that electrolyte solution can reach the gold electrode, and react with it. The morphological analysis in ***Figure 3.9*** shows the presence of different cavities associated with the absence of gold, which is the main reflective material present in our devices, making the optical profilometer a good and reliable tool to probe the presence of percolations paths. From the ESEM analysis in ***Figure 3.10*** we gain more information about such cavities. The X-ray fluorescence analysis shows that the presence of gold (in atomic weight percentage) inside the cavity is 80% less than that present outside the cavity, demonstrating again that the electrolyte reached and corroded the gold electrode. In fact, the voids showed in ***Figure 3.9*** and ***Figure 3.10*** are likely due to water electrolysis reactions occurring at the gold electrode: electrolysis at positive biases can corrode the gold electrode, whereas at negative biases the organic layer is subjected to degradation.

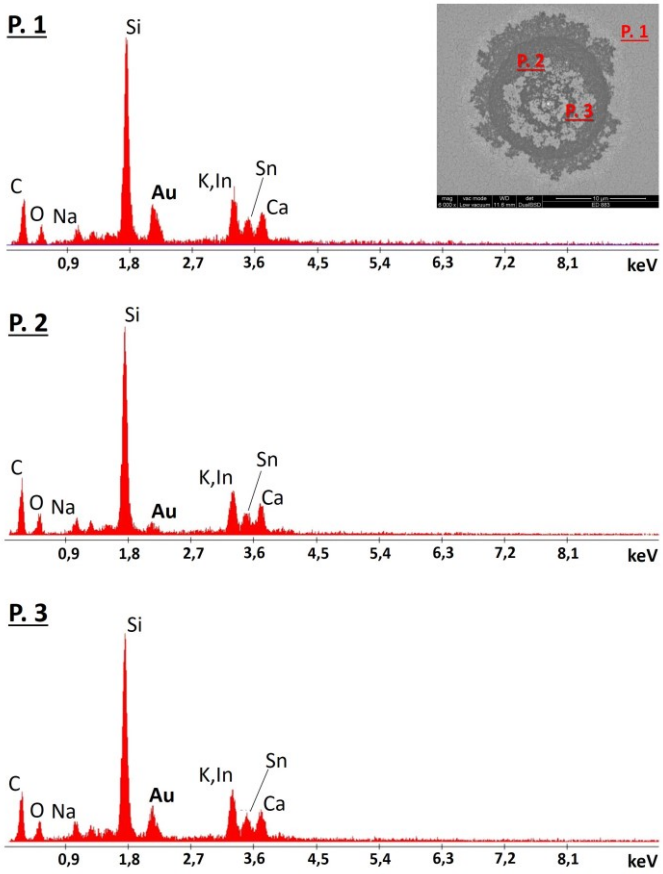

Figure 3.10 - ESEM image *which shows the cavity after the applied protocol and the X-ray fluorescence spectra taken at three different points: P.1; P.2; P.3. The X-ray analysis highlight how gold (Au) is almost missing in the cavity (P.2). Aside the peaks related due to carbon (C) and gold, that clearly are due to the PMMA-gold-P13 stack structure, many other peaks are present. These can be easily associated to the glass substrate, indeed, whereas indium (In) and tin (Sn) are due to the ITO layer, oxygen (O), sodium (Na), magnesium (Mg), aluminum (Al), silicon (Si), potassium (K), and calcium (Ca) are associated with the soda-lime glass. Of course, Mg, Al, and K, are presents in very low percentage as respect to O, Si, and Na. Nevertheless, O and Na feature small peaks because on the one hand, the X-ray detector has not a linear response at all energies. On the other hand, O and Na emission have smaller energies than the Si one, thus they have a bigger absorption.*

Therefore, our model shows that, considering the semiconductor and solution resistances, the voltage drop, in absolute value, between the semiconductor/electrolyte interface and the platinum counter electrode (i.e., the voltage difference across the solution) is less than 0.8V in the worst case (i.e., with V_B=-1.8V) whereas it is less than 200 mV in the other cases. These values of voltage are much lower than those needed for water electrolysis to take place, thus electrolysis can occur only in proximity of the gold electrode, confirming the presence of the percolation process. Incidentally, water electrolysis can be viewed as the limit case occurring when the percolation process reaches the gold interface. In such a case, the device merely becomes, at least locally, a gold-electrolyte-platinum stack. Thus, the voltage across the solution is the entire applied voltage inducing the water electrolysis reaction.

As final remark, we underline that in order to accelerate the migration processes, the devices have been deliberately kept biased with relative high voltages for several minutes (during the EIS protocol that last more than several hours). Because this is a strong stress condition, we repeated the EIS measurements at 0V bias for several times during the characterisation. Thus, we verified that devices can sustain the operative bias condition, i.e., below 0.8V or slightly higher for several days. In addition, we observed that our model is verified also when corrosion processes are taking place. Indeed, we see how the geometric capacitance C_G (usually constant) becomes larger when a high negative bias is applied, thus our model can be used to monitor device conditions during prolonged time under aqueous environments.

3.2. Equivalent circuit model generalization

In the previous chapter (***3.1***), we analyzed STACK devices featuring OSC/electrolyte (NaCl 0.1M) interfaces and we proposed a model, which fully describes all the observed phenomena. However, different devices with different materials, structures, and geometries, might show other phenomena.

In this chapter, we want to extend our model by introducing a more general one that, not only it can explain the particular case in chapter ***3.1***, but it is also adequate for a more general system. We present an equivalent circuit for the OSC/solution interface which gives a complete and comprehensive description of the most important phenomena present in a two-electrodes electrochemical system. Each circuital element is directly associated with a physical device phenomenon. This chapter will provide the reader with a tool to model a large amount of electrochemical systems, pointing out which physical phenomena can be neglected. Finally, as a case study, we analyze two architectures that differ only in the used solutions (saline solution, and deionized water) showing that the two systems are two different particular cases of the more the general model presented in this paper. Moreover, we demonstrate that this model can be successfully applied to analyze the effect of surface functionalization on the measured impedance spectra, showing that it is a powerful tool to characterize organic materials subjected to electrochemical processes at the boundaries with aqueous environments either in electronic devices or coating layers.

3.2.1. Model description

The aim of this chapter is to give a more general and theoretical description of the organic semiconductor/solution interface, nevertheless, to study such interfaces we cannot consider just one electrode but at least a two-electrode system must be considered. Moreover, a real-working device platform, such as a water-gated transistor or a dye-sensitized solar cell, has more than just one electrode.

Therefore, in the following we analyze the two-electrodes systems as depicted in ***Figure 3.1c***, where the anode is a coated electrode in contact with the electrolyte, whereas the cathode consists of an uncoated electrode immersed in the solution. The anode coating is a thin film organic semiconductor, whereas the solution can be pure water as well as an electrolyte.

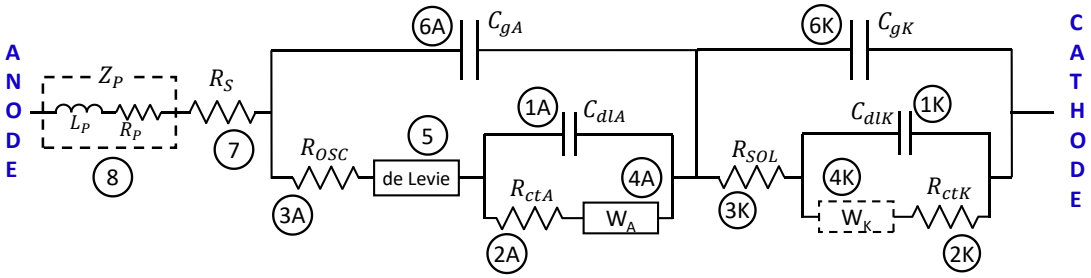

Figure 3.11 - Equivalent circuit model associated to the device depicted in Figure 3.1c.
*The parasitic component (8) and the ion diffusion at the cathode (4K) can be neglected as explained in chapter **3.2.2** (sections **a)** and **b)**, respectively).*

Figure 3.11 shows the equivalent circuit model of the device described above, where each circuital element can be directly associated with a physical observable in the device:

(1) One of the most important and discussed parameter in electrochemical devices (transistors and sensors) is the double-layer capacitance C_{dl}. The formation of a double layer capacitor occurs due to the solvent molecules and other species (ions or molecules) that are specifically adsorbed, forming the compact Helmholtz layer[Bard01]. This phenomenon leads to the formation of a charge sheet at the solution side of the interface that is compensated by the accumulation of opposite charge at the electrode (metal or semiconductor) side. Such behavior resembles the one of a capacitor, whose value is in general voltage dependent. Since this phenomenon takes place at both coated-

anode and cathode, in the general model of ***Figure 3.11*** we added two double-layer capacitances at both interfaces (C_{dlA} and C_{dlK})

(2) Unless ideal polarized electrodes are concerned (i.e. only non-faradaic processes can occur[Bard01]) charge transfer reactions (faradaic processes) at the electrode/solution interface must be taken into account. Such reactions can be quantitatively evaluated by monitoring the current flowing through the device and can be easily included in the equivalent circuit model by adding a charge transfer resistance R_{ct} in parallel with the double-layer capacitance C_{dl}. Of course, if there is a current flow, charge transfer processes are occurring at both anode and cathode, thus we included in the model R_{ctA} and R_{ctK} to describe the charge transfer phenomena at the coated-anode and cathode respectively.

(3) The faradic processes just discussed are related to current flowing between anode and cathode. Such current cannot be calculated considering only the charge transfer reaction occurring at the electrodes/solution interfaces, but it is also limited by the charge transport through the whole device that, at a fixed applied potential, limits the charge transfer process itself. Given the device structure depicted in ***Figure 3.1c***, and neglecting at first instance the contact resistances, we can divide the charge transport processes into ionic and electronic transport. The first comes from the ions flowing in the bulk of the solution due to the applied electric field. The second is the transport of electrons (or holes) that move inside the organic semiconductor. Both transport phenomena were described in the model of ***Figure 3.11*** by adding the resistances R_{SOL} and R_{OSC} to account for the ionic and electronic transport respectively. It is therefore important to notice that, the ionic transport in the bulk solution can be well approximated with a linear resistance, whereas the electronic transport has not a linear dependence with the applied voltage (see for instance the space charge limited model in organic semiconductors[Brütting01]). In fact, it is important to remark that we are presenting a small-signal model, therefore the value of each component must be calculated for each operating voltage. Thus, R_{OSC} is voltage-dependent and we can consider it as a linear resistor only in a small range centered on the operating voltage.

(4) When ions are present in solution, the double-layer structure is complicated by the presence of nonspecifically adsorbed ions that, due to thermal agitation and electrostatic forces, will interact with the charged electrodes leading to the formation of a distributed charge layer called the diffused layer (Einstein-Smoluchowski equation: $D_i = \frac{RT}{Fz_i}\mu_i$; whit D_i the diffusion coefficient, μ_i the ions mobility, and z_i the number of charges on the ionic specie i)[Bard01]. This phenomenon can be described by means of the Warburg impedance[Diard12]. Such diffusion impedance can be easily introduced at both metal/solution and OSC/solution interfaces by adding in our model the Warburg element (at both coated-anode and cathode) in series with the charge transfer resistance and in parallel with the double-layer capacitance forming the so called Randles Cell[Randles47].

(5) We demonstrated that, when organic semiconductors are exposed to aqueous environments for a prolonged time, the solution can percolate through the organic semiconductor and, as we adequately discussed in chapter ***3.1.2*** section ***c)***, this phenomenon is emphasized if bias is applied. Such percolation process can be taken into account using a distributed impedance model that is typically used to describe porous electrodes, whereas the solution/electrode interface can be successfully described by a transmission-line-like model[Sharma10]. For this reason, we include in our model the de Levie impedance[Levie63] shown in ***Figure 3.6*****,** where the R_{ctPER} and C_{dlPER} elements respectively describe the charge transfer reaction and the double-layer capacitance at the distributed interface between the porous organic semiconductor and the percolated solution, whereas the resistance R_{PER} accounts for the resistivity of the percolated solution.

(6) Since the devices under analysis is characterized by a phase separation between two different materials (organic semiconductor and solution), we must consider two geometric capacitances: C_{gA} and C_{gK}. These two constant parameters are associated to the geometry of the device and they describe the semiconductor capacitance (C_{gA}) and the solution capacitance (C_{gK}) respectively. Now, one might speculate about how C_{gA} and C_{gK} should be interconnected. Let us focus on the solution/semiconductor interface. Since this interface is thinner than 10nm[Bard01], the double-layer capacitance is typically much larger than the geometric capacitances. Thus, the time constant associated to the double layer capacitance C_{dlA} is much smaller than the time constants associated to the two geometric capacitances C_{gA} and C_{gK}.

This means that, at the characteristic frequencies of the geometric capacitances, the double layer capacitance C_{dlA} is equivalent to a short circuit. Consequently, to understand the device physics and extrapolate the model parameters, there will be a negligible difference in connecting the geometric capacitances C_{gA} and C_{gK} at the solution side of the interface rather than at the semiconductor side. In our model, we arbitrarily chose to connect both C_{gA} and C_{gK} at the solution side of the semiconductor solution interface.

(7) To complete the model, we add the series resistance R_S. This resistance takes into account the linear voltage drops associated to the device contact resistances such as the anode and cathode electrodes resistivity.

(8) At last, for the sake of generality, parasitic elements should be included in the model. Such parasitic components could have different origins depending on how the sample is connected to the instrumentation and on the cable lengths. Hence, we add in series to R_S the parasitic impedance Z_P, i.e. a distributed impedance in the most general case. Since we cannot analyze all the possible parasitic configurations, we will consider the case in which Z_P can be described by the series of the two lumped elements R_P and L_P[Petty00], which is enough in most cases. The parasitic resistance R_P takes into account all the linear voltage drops due to the interconnections between the sample under test and the instrumentations, and it must not be mistaken with the series resistance R_S that describe only the device physics. Similarly, the inductance L_P is used to described the unwanted magnetic coupling (typically at high frequencies) due to the cables and, if present, to the sample holder used to contact the device.

3.2.2. Discussion

In the previous chapter (***3.2.1***), we showed the most general model for the metal/OSC/solution/metal system.

Now, we want to discuss such model by focusing our attention in how to correctly implement it and how to do the proper simplifications depending on the case of study.

a) Parasitic components approximation

Let us start considering the parasitic components L_P and R_P. The best practice is not to model such elements, but to avoid them by using a proper set-up and performing data compensation as described in chapter ***3.1.1*** (sections ***d)*** and ***f)***, respectively). Under these assumptions, the model can be simplified removing the impedance Z_P. Notice that, without performing the impedance compensation, would not be possible to discriminate the parasitic component R_P from the series resistance R_S, with consequent loss of information on the device contact resistance.

b) Diffusion impedance simplification

Another simplification worth to be done is to implement in the model only one of the two Warburg elements. As explained in chapter ***3.2.1***, one Warburg impedance (W_A) describe the ion diffusion layer at the OSC/solution interface, and the other Warburg impedance (W_K) describe the diffusion layer at the solution/metal interface. Even though in general W_A and W_K are different due to different ions involved in the diffusion, in practice it is very hard to discern them because they feature similar time constants around 10s[Hauch01, Cester15]. Thus, it is possible to neglect W_K and leave only the terms W_A. Noticeably, the choice of which Warburg element removing is very important since it could affect the correct model parameters evaluation. One the one hand, since R_{ctK} is usually very low, the double-layer capacitance at the solution/metal interface is typically associated with a fast time constant (around 10μs[Bonora96, Hauch01, Wang05]), thus the correct evaluation of the parameters C_{dlK} and R_{ctK} are not affected by removing the impedance W_K. On the other hand, since C_{dlA} and R_{ctA} can assume very large values, the double-layer capacitance at the OSC/solution interface can have a low time constant (around 1s[Porrazzo14, Buth11]) that is closer to the diffusion impedance, thus removing the Warburg element W_A would lead to noticeable errors in the extrapolation of the parameters C_{dlA} and R_{ctA}.

c) Solution dependence

The model description in chapter ***3.2.1*** was developed regardless the materials used during the device fabrication in order to make the model as much general as possible and widely applicable to any semiconductor/solution system. However, changing the active organic semiconductor, surface functionalization, or device thickness means modifying the values of the parameters used in the model, thus emphasizing some phenomena and hiding others. It is therefore important to understand, for each case, which process is worth to be considered, hence apply the model consequently.

We will now see two examples in which we analyze the same device architecture that only differs in the used solutions: saline solution, and deionized water.

i) *Saline solution*:

For standard saline solutions, the resistivity of the solution is ρ_{SOL}=70Ω·cm[Massobrio16], whereas its relative permittivity ε_{SOL} is around 80[Nörtemann97]. Assuming that the time constant τ_{gK} associated to the solution capacitance C_{gK}, is much smaller than the time constant τ_{dlK} associated to the double-layer capacitance C_{dlK} (typically around 10µs), we can calculate the time constant $\tau_{gK} = \rho_{SOL} \cdot \varepsilon_{SOL} \cdot \varepsilon_0$ (where ε_0 is the vacuum dielectric constant).

Calculating such expression gives τ_{gK} = 0.5ns that is much smaller than τ_{dlK}, meaning that in this case it is not possible to observe the contribution of the solution capacitance from the EIS measurements.

Hence, the model reported in ***Figure 3.11*** can be simplified as shown in ***Figure 3.12***, where we remove the solution capacitance C_{gK} whereas the solution resistance R_{SOL} has been englobed into the series resistance R_S since they cannot be further discriminated. Notice that, this is exactly the same model reported in ***Figure 3.5b*** and discussed in chapter ***3.1***.

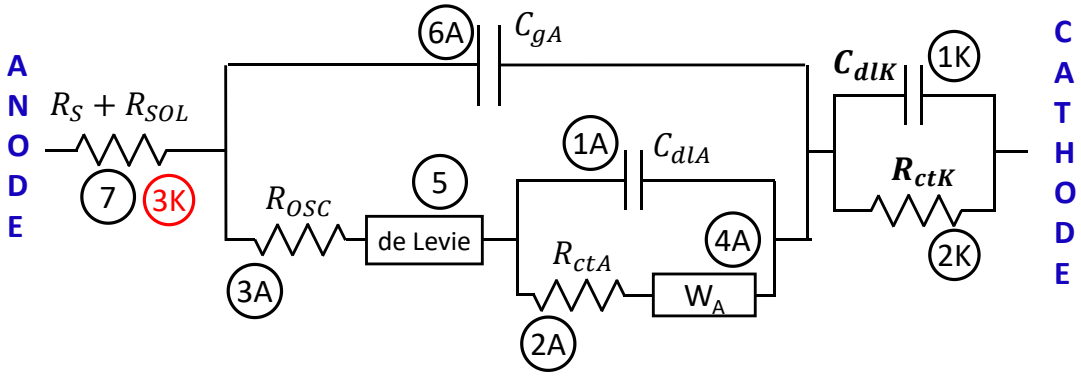

Figure 3.12 - Saline solution approximation.

In our experiments, we used NaCl (concentration of 0.1M) as saline solution whose resistivity was 60Ω·cm. ***Figure 3.13*** reports the Real and Imaginary parts as a function of frequency, performed onto a P13 coated electrode, without the PDL coating, at both positive and negative biases. As can be seen by the solid line in Fig. 6 the model reported in ***Figure 3.12*** well represents the acquired data (symbols). Moreover, the fitted parameters values reported in ***Table 3.2*** are in agreement with other results present in literature, such as the double-layer capacitance C_{dlA} that is in the range of 1÷10µF·cm^{-2} [Porrazzo14, Cramer12], or the geometrical capacitance that is close to the expected value of C_{gA} = 48nF·cm^{-2} calculated using $C_{gA} = \frac{\varepsilon_r \cdot \varepsilon_0}{t_{osc}}$, where ε_r = 2.7[Nahhas12].

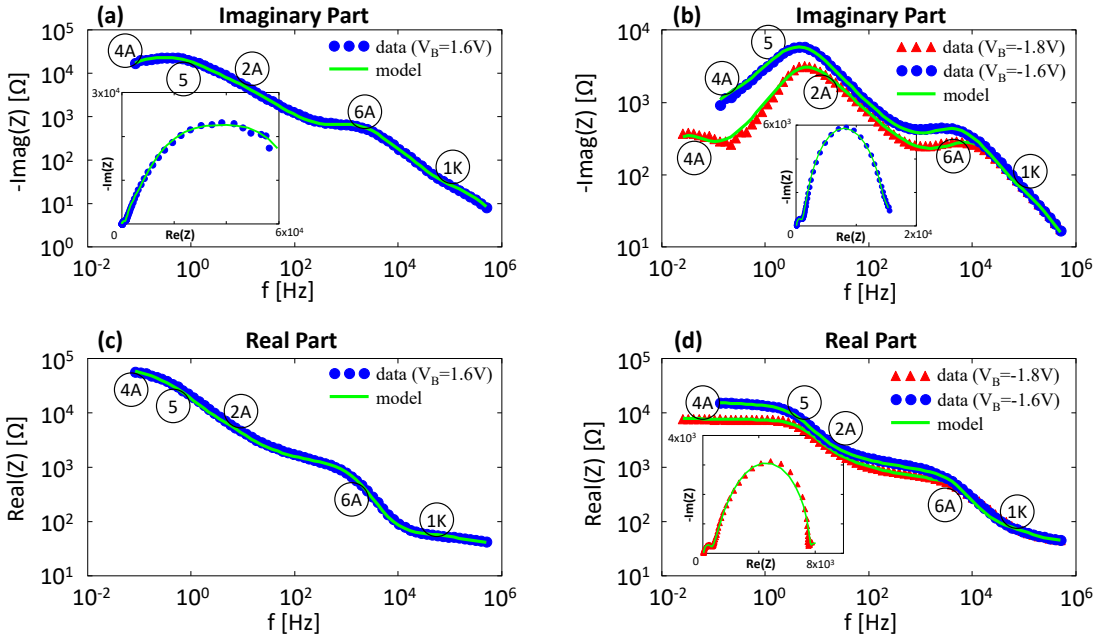

***Figure 3.13**. Impedance plots for a P13 coated electrode (without PDL) with NaCl 0.1M as solution.* **(a)** *and* **(c)** *show the impedance behavior for negative biases.* **(b)** *and* **(d)** *show the impedance behavior for positive biases. The filled symbols are the measured data, whereas the solid lines are the model of* ***Figure 3.12**. Insert in the figures are the corresponding Nyquist plot.*

Noticeably, to correctly discern the different contribution discussed in chapter ***3.2.1***, the measured devices have to be polarized at biases exceeding the normal operative voltages, thus emphasizing some phenomena such as the ionic diffusion and the solution percolation, and consequently, allowing the complete parameters evaluation. The choice of the DC polarization has to be investigated for each different kind of device, because different organic materials or surface morphologies can show different characteristics that emphasize one phenomenon with respect to the others.

Indeed, in chapter 3.1 we performed EIS measurement onto P13 STACK devices functionalized by a PDL coating and, as reported in ***Figure 3.4***, the model of ***Figure 3.12*** perfectly describe all the five different impedance contributions that are clearly observable in the imaginary part plot. Remarkably, after the PDL treatment, possibly due to the increased surface wettability[Toffanin13] that could reduce the overall electrode impedance, lower DC biases are required to fully characterize the devices.

NaCl fitting parameters

	Bias	Series Resist.	OSC contribution		Percolation (de Levie)			Double Layer		Diffusion (W_A)		Cathode electrode	
	V_B [V]	R_S+R_{SOL} [Ω·cm²]	R_{P13} [kΩ·cm²]	C_G [nF/cm²]	R_{PER} [kΩ·cm²]	R_{CtPER} [kΩ·cm²]	C_{dlPER} [μF/cm²]	R_{CT} [kΩ·cm²]	C_{DL} [μF/cm²]	R_D [kΩ·cm²]	τ_D [s]	R_{etK} [Ω]	C_{dlK} [nF]
Without PDL	-1.8	64.5	0.8	21.7	6.2	2.5	10.5	6.2	4.1	1.1	13.5	30.0	40.8
	-1.6	66.0	1.2	25.0	21.6	3.5	25.1	11.3	2.7	2.3	2.1	35.0	41.3
	1.6	60.0	1.7	57.3	4.8	37.9	0.7	8.2	1.9	23.3	2.7	18.0	58.9
With PDL	-1.8	103.0	0.1	98.5	2.8	2.4	100.2	1.4	3.7	3.7	9.6	25.3	98.7
	-1.4	105.0	1.8	50.3	158.2	17.0	31.9	39.6	3.8	37.1	11.0	19.9	105.2
	0.8	102.1	2.5	45.6	1243.8	24.6	24.9	129.3	7.1	105.1	11.4	11.5	88.0
	1	106.1	1.5	44.4	223.6	13.6	77.6	68.6	4.6	17.0	4.6	21.4	92.8

***Table 3.2**. Parameters values from the data of **Figure 3.4** and **Figure 3.13** using the model of **Figure 3.12** for NaCl solution. All the parameters are normalized as respect to the device area except for the cathode electrode (platinum wire).*

ii) *Deionized Water*:

Deionized water is characterized by resistivity ρ_{SOL} larger than 10MΩ·cm[Kergoat10], which value may decrease to hundreds of kΩ·cm after handling[Porrazzo14]. In such cases, keeping $\varepsilon_{SOL} = 80$, the τ_{gK} calculated with the approximated formula discussed above ranges from 1µs up to 100µs. We notice that the calculated value of τ_{gK} (associated to the solution capacitance C_{gK}) is closer to the typical value of τ_{dlK} (associated to the double-layer capacitance C_{dlK}). Despite that, the approximation $\tau_{gK} = \rho_{SOL} \cdot \varepsilon_{SOL} \cdot \varepsilon_0$ still holds true because in this case $R_{SOL} >> R_{ctK}$. Consequently, the contribution of the double-layer capacitance C_{dlK} is completely hidden by the solution capacitance C_{gK} in parallel with the solution resistance R_{SOL}. Hence, the general model in ***Figure 3.11*** can be simplified by removing the parameters C_{dlK} and R_{ctK}. Furthermore, in presence of deionized water, the model further simplifies by removing the contribution of the Warburg impedance. Indeed, the only ions present in the solution are due to impurities or dissociated water species (H_3O^+ and OH^-) that are very low in concentration[Kergoat10], thus the ion diffusion can be neglected.

In summary, considering these two simplifications, the model in presence of deionized water becomes as reported in ***Figure 3.14***.

We performed our experiments using Milli-Q water and the results are reported in ***Figure 3.15***, whereas the model parameters are collected in ***Table 3.3***. The model excellently fits the data, and each contribution can be discriminated as indicated by the labels in the figures.

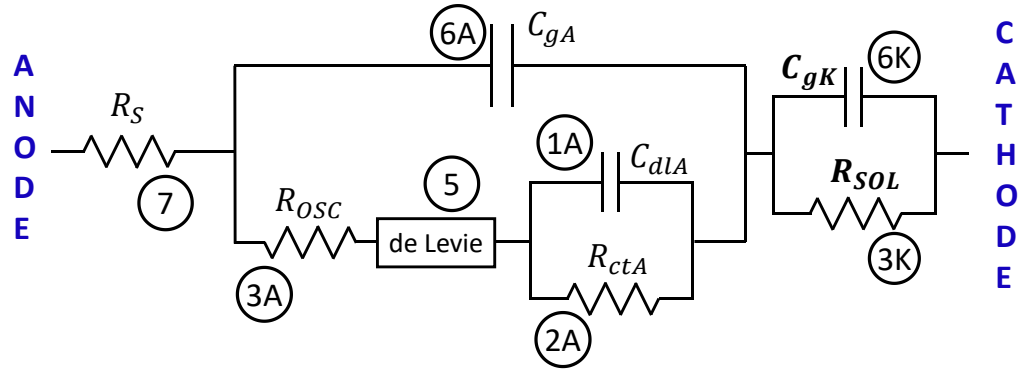

Figure 3.14 - Deionized water approximation.

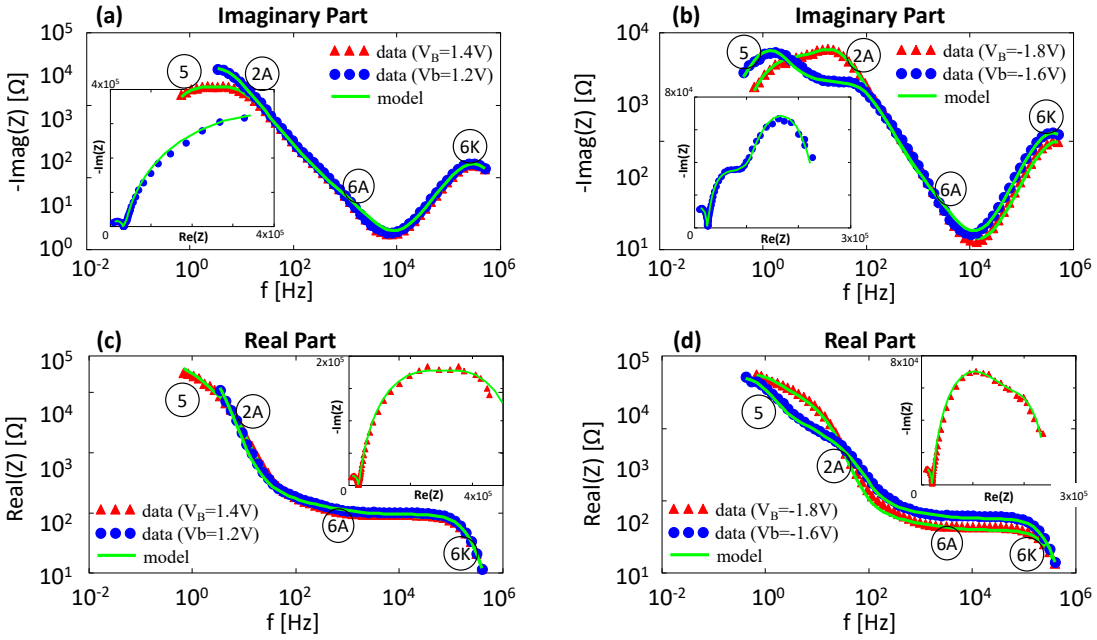

Figure 3.15*. Impedance plots for a P13 coated electrode (without PDL) using MilliQ water as solution.* **(a)** *and* **(c)** *show the impedance behavior for negative biases.* **(b)** *and* **(d)** *show the impedance behavior for positive biases. The filled symbols are the measured data, whereas the solid lines are the model of* ***Figure 3.14****. Insert in the figures are the corresponding Nyquist plot.*

In particular, the contribution of the MilliQ water is clearly visible in the Nyquist plot where the estimated value of R_{SOL} is around 30÷50kΩ·cm^2. Moreover, the presence of the diffusion impedance is not appreciable, confirming the model simplification discussed above. It is worth to remark that, the double-layer capacitance C_{dlA} is much lower using MilliQ water instead of NaCl solution. This can be ascribed to the lower ionic strength[Melzer14], combined with the high hydrophobicity of the organic layer[Toffanin13].

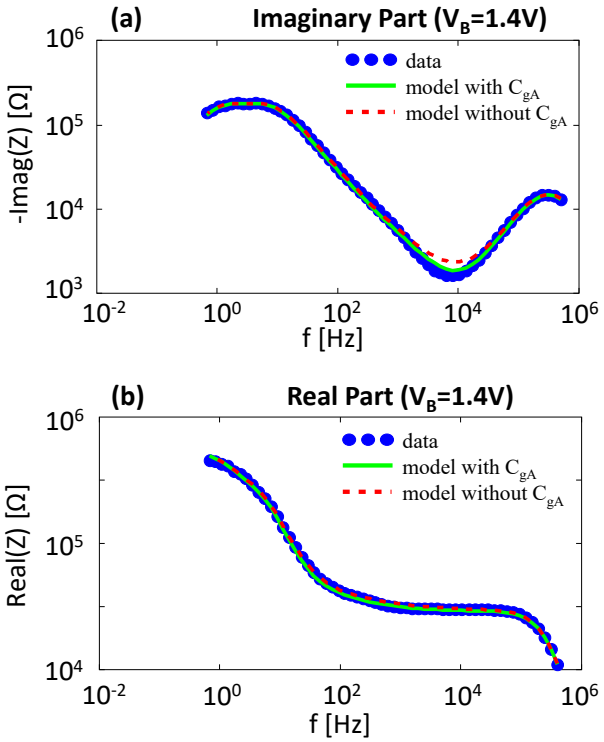

***Figure 3.16**. Imaginary* **(a)** *and real* **(b)** *impedance plots for a P13 device with MilliQ as solution for V_B=1.4V. Symbols are the measured data, the solid line is the model of* **Figure 3.14**, *whereas the dashed line is the same model without the OSC capacitance C_{gA}.*

In addition, as can be seen from ***Table 3.3***, the value of geometric capacitance C_{gA} is underestimated since its contribution is partially hidden by the contributions of the solution capacitance C_{gK} and the double layer capacitance C_{dlA}. Moreover, despite its presence is needed to fully described the impedance spectra, neglecting C_{gA} in the model (dashed lines in ***Figure 3.16***) has not a strong impact in the extrapolation of the others parameters that slightly vary as reported in ***Table 3.3***.

MilliQ fitting parameters

	Bias	Series Resist.	OSC contribution		Percolation (de Levie)			Double Layer		MilliQ Contribution	
	V_B [V]	R_S^* [Ω·cm^2]	R_{P13} [kΩ·cm^2]	C_G [nF/cm^2]	R_{PER} [kΩ·cm^2]	R_{CtPER} [kΩ·cm^2]	C_{dlPER} [µF/cm^2]	R_{CT} [kΩ·cm^2]	C_{DL} [µF/cm^2]	R_{ctK} [Ω]	C_{dlK} [nF]
Without OSC Contribution	-1.8	/	-	-	326.5	110.4	775.0	134.6	49.6	29.7	11.4
	-1.6	/	-	-	834.8	92.1	2247.7	55.7	47.0	35.8	11.3
	1.2	/	-	-	219.2	349.6	455.1	751.2	58.5	46.0	11.8
	1.4	/	-	-	144.4	383.7	352.3	380.5	57.9	43.9	11.8
With OSC Contribution	-1.8	/	5.1	10.4	314.4	101.4	843.8	138.0	32.2	29.7	11.4
	-1.6	/	7.2	11.1	204.3	189.4	649.2	56.0	28.4	35.8	11.3
	1.2	/	10.5	12.7	281.3	377.9	421.2	746.7	45.7	46.0	11.8
	1.4	/	2.3	9.4	260.2	353.6	352.5	350.5	53.3	43.9	11.8

** The R_S values were not calculated because it is much smaller than the R_{SOL} values that are dominant at high frequencies. Assume to zero.*

***Table 3.3 - Parameters values** from the data of **Figure 3.15** using the model of **Figure 3.14** for MilliQ water. All the parameters are normalized as respect to the device area.*

To confirm that our model (***Figure 3.11***) can be widely applied independently of the employed material, we fabricated STACK devices using a different organic semiconductor (MX: the name of the molecule is not reported for publication reasons). We performed measurements with both NaCl (***Figure 3.17a***) and MilliQ water (***Figure 3.17b***) proving that, using the simplification reported in ***Figure 3.12*** and ***Figure 3.14***, respectively, our model can give a general description of different devices and materials.

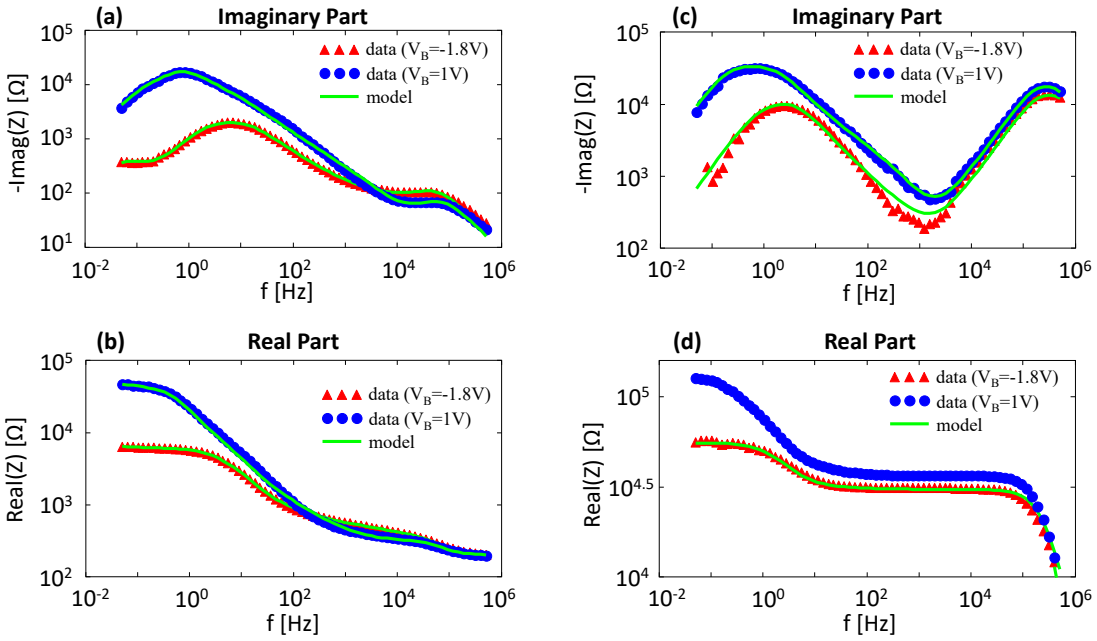

Figure 3.17. **(a)** *and* **(b)** *Imaginary and real impedance plots for a MX device with NaCl (data are fitted with the model of* **Figure 3.12***).* **(c)** *and* **(d)** *Imaginary and real impedance plots for a MX device with MilliQ (data are fitted with the model of* **Figure 3.14***).*

At this point, another consideration is worth to be drawn. We proposed a model that explains various phenomena which might be related either to electrical properties, chemical reactions, and possibly unwanted effects, such as solution or ion percolations. Using this model, one could assess in which extent those phenomena occur, by performing a simple electrical measurement, instead of a more complex microscopy and chemical analysis.

Not only this is useful for the characterization and failure analysis of electronic devices, such as water-gated transistors, electrophysiological interfaces, fuel cells, and many others electrochemical systems, but also this model might be used in other applications, in which a solution is in intimate contact with another material (metals, painting, coating, etc.[Bonora96]), to determine and quantify, if percolation and/or redox corrosive processes occur.

3.3. Summary

We presented and validated a comprehensive model that considers and rationalizes all the processes taking place at the interface or in the bulk of the different layers comprising a metal-organic-electrolyte stack. In particular, the model takes into account the following processes: adsorption of ions in the semiconductor (Helmholtz layer); accumulation of carriers and charge transfer at the semiconductor/electrolyte interface (double layer capacitance); percolation of the ionic species through the organic semiconductor; ion diffusion across the electrolyte; ion absorption and charge transfer at the platinum interface.

In order to identify all the possible mechanisms, we performed EIS measurements both at low and at high operating bias voltages applied between the gold layer and the platinum electrode, thus avoiding the use of any constant phase element in the equivalent circuit. This measurement protocol allowed us to separate in the frequency domain the different contributions and, in particular, to demonstrate the occurrence of ion percolation through the organic layer by using a de Levie circuital element. The presence of percolation is demonstrated by ESEM analysis and optical profilometry. Although percolation is much faster and more intense at high negative bias, it is still present at low bias conditions (close to the real operating conditions), even if with different rate.

We further extended our findings presenting a more general model for the metal/organic semiconductor/solution/metal structure, where the solution can be an electrolyte as well as poor water. A detailed description of the most important physical phenomena and processes that are involved in the device operations is reported, thus explaining the presence of each circuital element and, consequently, motivating the model complexity.

We considered also two case studies, by introducing some simplifications, which are often meaningful in many device architectures. In particular, we studied the use of two different solutions (NaCl 0.1M, and MilliQ water) and we showed that they can be described using two different models. On the one hand, the devices featuring deionized water are characterized by the absence of the diffusion impedance, and by an impedance lobe, associated to the solution capacitance C_{gK}, which hides, at least partially, the contribution of the counter electrode and the organic semiconductor capacitance C_{gA}. On the other hand, the devices measured with saline solutions are characterized by the absence of the solution capacitance C_{gK}, whereas the organic semiconductor geometry capacitance is perfectly observable, especially at high biases, and it can be easily estimated using our model. Noticeably, it can be easily shown that both models are a particular case of the general equivalent circuit model presented in this work, that can be successfully applied to a plethora of other architectures characterized by different electrical and chemical properties. In particular, we showed that, changing the nature of the OSC or of the OSC/solution interface, our model, with the proper parameters sets, is able to correctly describe the whole impedance spectra.

We demonstrated a very good accordance between model and the experimental data, proving that, as will be shown in the following chapter (***4***), this model is a valid tool for studying the interaction between bio-sensing devices and physiological environment, such as OECTs, EGOFET, and many other electrochemical systems, where electrodes are coated with organics or porous material, with particular emphasis to organic neural interfaces.

Lastly, we believe that, not only this model can be used to study and characterized electronics and electrochemical devices, but it might be a useful tool in a wide range of other applications in which it is important to verify the quality of coatings and surfaces, or to detect the presence of unwanted phenomena such as solution percolation or corrosive currents.

References

[Barcia02] O. E. Barcia, E. D'Elia, I. Frateur, O. R. Mattos, N. Pébère, and B. Tribollet, *Application of the impedance model of de Levie for the characterization of porous electrodes*, **Electrochim. Acta**, vol. 47, issues 13-14, pp. 2109-2116, May 2002.

[Bard01] A. J. Bard, and L. R. Faulkner, *Electrochemical Methods, Fundamentals and Application*, **Wiley J. and Sons**, 2nd ed., 2001.

[Barsoukov05] E. Barsoukov, and J. R. Macdonald, *Impedance Spectroscopy Theroy, Experiment, and Applications*, **Wiley J. and Sons**, 2nd ed., 2005.

[Belhachemi00] F. Belhachemi, S. Raël, and B. Davat, *A physical based model of power electric double-layer supercapacitors*, **IEEE Industry Applications Society Annual Meeting**, vol. 5, pp. 3069-3076, Oct. 2000.

[Berggren07] M. Berggren, A. R.-Dahlfors, *Organic Bioelectronics*, ***Adv. Mater.***, vol. 19, issue 20, pp. 3201-3213, Oct. 2007.

[Bisquert10] J. Bisquert, and F. F.-Santiago, *Impedance spectroscopy: A general Introduction and application to dye-sensitized solar cells*, in *Dye-sensitized Solar Cells,* **CRC Press**, 1st ed., 2010.

[Bonora96] P. L. Bonora, F. Deflorian, and L. Fedrizzi, *Electrochemical impedance spectroscopy as a tool for investigating underpaint corrosion*, **Electrochim. Acta**, vol. 41, issues 7-8, pp. 1073-1082, May-Jun. 1996.

[Brütting01] W. Brütting, S. Berleb, A. G. Mückl, *Device physics of organic light-emitting diodes based on molecular materials*, **Org. Electron.**, vol. 2, issue 1, pp. 1-36, Mar. 2001.

[Buth11] F. Buth, D. Kumar, M. Stutzmann, J. A. Garrido, *Electrolyte-gated organic field-effect transistors for sensing applications*, **Appl. Phys. Lett.**, vol. 98, issue 15, pp. 153302, Mar. 2011.

[Cester15] A. Cester, N. Wrachien, M. Bon, G. Meneghesso, R. Bertani, R. Tagliaferro, S. Casolucci, T. M. Brown, A. Reale, A. D. Carlo, *Degradation mechanisms of dye-sensitized solar cells: Light, bias and temperature effects*, **IEEE International Reliability Physics Symposium,** pp. 3E.2.1-3E.2.8, Apr. 2015.

[Cramer12] T. Cramer, A. Kyndiah, M. Murgia, F. Leonardi, S. Casalini, and F. Biscarini, *Double layer capacitance measured by organic field effect transistor operated in water*, **Appl. Phys. Lett.**, vol. 100, issue 14, pp. 143302, Apr. 2012.

[Cramer13] T. Cramer, B. Chelli, M. Murgia, M. Barbalinardo, E. Bystrenova, D. M. de Leeuw, and F. Biscarini, *Organic ultra-thin film transistors with a liquid gate for extracellular stimulation and recording of electric activity of stem cell-derived neuronal networks*, **Phys. Chem. Chem. Phys.**, vol. 15, issue 11, pp. 3897-3905, Mar. 2013.

[Diard12] J.-P. Diard, B. Le Gorrec, and C. Montella, *Diffusion Impedance, Handbook of Electrochemical Impedance Spectroscopy*, **BioLogic Science Instrumentation**, 2012.

[Fang15] Y. Fang, X. Li, Y. Fang, *Organic bioelectronics for neural interfaces*, **J. Mater. Chem. C**, vol. 3, issue 25, pp. 6424-6430, Jun. 2015.

[Fouquet06] N. Fouquet, C. Doulet, C. Nouillant, G. D.-Tanguy, and B. O.-Bouamama, *Model based PEM fuel cell state-of-health monitoring via ac impedance measurements*, **J. Power Sources**, vol. 159, issue 2, pp. 905-913, Sep. 2006.

[Franceschetti77] D. R. Franceschetti, and J. R. Macdonald, *Electrode kinetics, equivalent circuits, and system characterization: Small-signal conditions*, **J. Electroanal. Chem.**, vol. 82, issues 1-2, pp. 271-301, Sep. 1977.

[Frega12] M. Frega, V. Pasquale, M. Tedesco, M. Marcoli, A. Contestabile, M. Nanni, L. Bonzano, G. Maura, and M. Chiappalone, *Cortical cultures coupled to Micro-*

Electrode Arrays: A novel approach to perform in vitro exitotoxicity testing, **Neurotoxicol. Teratol.**, vol. 34, issue 1, pp. 116-127, Jan. 2012.

[Fromherz99] P. Fromherz, *Extracellular recording with transistors and the distribution of ionic conductances in a cell membrane*, **Eur. Biophys. J.**, vol. 28, issue 3, pp. 254-258, Mar. 1999.

[Halme10] J. Halme, P. Vahermaa, K. Miettunen, and P. Lund, *Device Physics of Dye Solar Cells*, **Adv. Mat.**, vol. 22, issue 35, pp. E201-E234, Sep. 2010.

[Hauch01] A. Hauch, and A. Georg, *Diffusion in the electrolyte and charge-transfer reaction at platinum electrode in dye-sensitized solar cells*, **Electrochim. Acta**, vol. 46, issue 22, pp. 3457-3466, Aug. 2001.

[Horowitz04] G. Horowitz, P. Lang, M. Mottaghi, and H. Aubin, *Extracting Parameters from the Current-Voltage Characteristics of Organic Field-Effect Transistors*, **Adv. Funct. Mater.**, vol. 14, issue 11, pp. 1069-1074, Nov. 2004.

[Keiser76] H. Keiser, K. D. Beccu, and M. A. Gutjahr, *Estimation of the Pore Structure of Porous electrodes by Impedance Measurements*, **Electrochim. Acta**, vol. 21, issue 8, pp. 539-543, Aug. 1976.

[Kergoat10] L. Kergoat, L. Herlogsson, D. Braga, B. Piro, M.-C. Pham, X. Crispin, M. Berggren, and G. Horowitz, *A Water-Gate Organic Field-Effect Transistor*, **Adv. Mater.**, vol. 22, issue 23, pp. 2565-2569, Jun. 2010.

[Kergoat11] L. Kergoat, N. Battaglini, L. Miozzo, B. Piro, M.-C. Pham, A. Yassar, and G. Horowitz, *Use of poly(3-hexylthiophene)poly(methyl methacrylate) (P3HT:PMMA) blends to improve the performance of water-gated organic field-effect transistors*, **Org. Electron.**, vol. 12, issue 7, pp. 1253-1257, Jul. 2011.

[Khodagholy13] D. Khodagholy, T. Doublet, P. Quilichini, M. Gurfinkel, P. Leleux, A. Ghestem, E. Ismailova, T. Hervé, S. Sanaur, C. Bernard, and G. G. Malliaras, *In vivo recordings of brain activity using organic transistors*, **Nat. Commun.**, vol. 4, no. 1575, Mar. 2013.

[Kim11] Y. H. Kim, N. S. Baek, Y. H. Han, M.-A. Chung, and S.-D. Jung, *Enhancement of neuronal cell adhesion by covalent binding of poly-D-lysine*, **J. Neurosci. Methods**, vol. 202, issue 1, pp. 38-44, Oct. 2011.

[Kötz00] R. Kötz, and M. Carlen, *Principles and applications of electrochemical capacitors*, **Electrochim. Acta**, vol. 45, issues 15-16, pp. 2483-2498, May 2000.

[Lee99] S. K. Lee, Y. Zu, A. Herrmann, Y. Geerts, K. Mllen, and A. J. Bard, *Electrochemistry, spectroscopy and Electrogenerated Chemiluminescence of Perylene, Terrylene, and Qaterrylene Diimides in Aprotic Solution*, **J. Am. Chem. Soc.**, vol. 121, issue 14, pp. 3513-3520, Mar. 1999.

[Levie63] R. de Levie, *On porous electrodes in electrolyte solutions*, **Electrochim. Acta**, vol. 8, issue 10, pp. 751-780, Oct. 1963.

[Lin12] P. Lin, and F. Yan, *Organic Thin-Film Transistors for Chemical and Biological Sensing*, **Adv. Mater.**, vol. 24, issue 1, pp. 34-51, Jan. 2012.

[Liu13] J. Liu, I. Engquist, and M. Berggren, *Double-Gate Light-Emitting Electrochemical Transistor: Confining the Organic p-n Junction*, **J. Am. Chem. Soc.**, vol. 135, issue 33, pp. 12224-12227, Aug. 2013.

[Mabeck06] J. T. Mabeck, and G. G. Malliaras, *Chemical and biological sensors based on organic thin-film transistors*, **Anal. Bioanal. Chem.**, vol. 384, issue 2, pp. 343-353, Jan. 2006.

[Massobrio16] P. Massobrio, G. Massobrio, S. Martinoia, *Interfacing Cultured Neurons to Microtransducers Arrays: A Review of the Neuro-Electronic Junction Models*, **Front. Neurosci.**, vol. 10, pp. 282, Jun. 2016.

[Melzer14] K. Melzer, M. Brändlein, B. Popescu, D. Popescu, P. Lugli, G. Scarpa, *Characterization and simulation of electrolyte-gated organic field-effect transistors*, **Faraday Discuss.**, vol. 174, pp. 399-411, Jun. 2014.

[Nahhas12] M. M. E.-Nahhas, H. A.-Khalek, and E. Salem, *Structural and Optical Properties of Nanocrystalline 3,4,9,10-Perylene-Tetracarboxylic-Diimide Thin Film*, **Adv. Cond. Matter. Phys.**, vol. 2012, no. 698934, Apr. 2012.

[Necliudov00] P.V. Necliudov, M. S. Shur, D. J. Gundlach, and T. N. Jackson, *Modeling of organic thin film transistors of different designs*, **J. Appl. Phys. Lett.**, vol. 88, issue 11, pp. 6594-6597, Dec. 2000.

[Nörtemann97] K. Nörtemann, J. Hilland, U. Kaatze, *Dielectric Properties of Aqueous NaCl Solutions at Microwave Frequencies*, **J. Phys. Chem. A**, vol. 101, issue 37, pp. 6864-6869, Sep. 1997.

[O'Regan91] B. O'Regan, M. Grätzel, *A low-cost, high-efficiency solar cell based on dye-sensitized colloidal TiO_2 films*, **Nature**, vol. 353, issue 6346, pp. 737-740, Oct. 1991.

[Petty00] M. C. Petty, C. Pearson, A. P. Monkman, R. Casalini, S. Capaccioli, J. Nagel, *Application of impedance spectroscopy to the study of organic multilayer devices*, **Colloids Surf. A**, vol. 171, issues 1-3, pp. 159-166, Oct. 2000.

[Popescu15] D. Popescu, B. Popescu, M. Brändlein, K. Melzer, and P. Lugli, *Modeling of Electrolyte-Gated Organic Thin-Film Transistors for Sensing Applications*, **IEEE Trans. Electr. Dev.**, vol. 62, issue 12, pp. 4206-4212, Dec. 2015.

[Poghossian09] A. Poghossian, S. Ingebrandt, A. Offenhäusser, and M. J. Schöning, *Field-effect devices for detecting cellular signals*, **Semin. Cell Dev. Biol.**, vol. 20, issue 1, pp. 41-48, Feb. 2009.

[Porrazzo14] R. Porrazzo, S. Bellani, A. Luzio, E. Lanzarini, M. Caironi, and M. R. Antognazza, *Improving mobility and electrochemical stability of a water-gated polymer field-effect transistor*, **Org. Electron.**, vol. 15, issue 9, pp. 2126-2134, Sep. 2014.

[Randles47] E. B. Randles, *Kinetics of Rapid Electrode Reactions*, **Disc. Faraday Soc.**, vol. 1, pp. 11-19, Mar. 1947.

[Schoen07] J. Schoen, and P. Fromherz, *The Mechanism of Extracellular Stimulation of Nerve Cells on an Electrolyte-Oxide-Semiconductor Capacitor*, **Biophys. J.**, vol. 92, issue 3, pp. 1096-1111, Feb. 2007.

[Sharma10] P. Sharma, and T. S. Bhatti, *A review on electrochemical double-layer capacitors*, **Energy Convers. Manage.**, vol. 51, issue 12, pp. 2901-2912, Dec. 2010.

[Simon08] P. Simon, and Y. Gogotsi, *Materials for electrochemical capacitors*, **Nat. Mat.**, vol. 7, issue 11, pp, 845-854, Nov. 2008.

[Song99] H.-K. Song, Y.-H. Jung, K.-H. Lee, and L. H. Dao, *Electrochemical impedance spectroscopy of porous electrodes: the effect of pore size distribution*, **Electrochim. Acta**, vol. 44, issue 20, pp. 3513-3519, Jun. 1999.

[Spijkman11] M.-J. Spijkman, K. Myny, E. C. P. Smits, P. Heremans, P. W. M. Blom, and D. M. de Leeuw, *Dual-Gate Thin-Film Transistors, Integrated Circuits and Sensor*, **Adv. Mater.**, vol. 23, issue 29, pp. 3231-3242, Aug. 2011.

[Stern24] O. Stern, *Zur Theorie der Elektrolytischen Doppelschicht*, **Z. Elektochem.**, vol. 30, issues 21-22, pp. 508-516, Nov. 1924.

[Tarabella15] G. Tarabella, P. D'Angelo, A. Cifarelli, A. Dimonte, A. Romeo, T. Berzina, V. Erokhin, and S. Iannotta, *A hybrid living/organic electrochemical transistor based on the Physarum polycephalum cell endowed with both sensing and memristive properties*, **Chem. Sci.**, vol. 6, issue 5, pp. 2859-2868, Feb. 15.

[Toffanin13] S. Toffanin, V. Benfenati, A. Pistone, S. Bonetti, W. Koopman, T. Posati, A. Sagnella, M. Natali, R. Zamboni, G. Ruani, and M. Muccini, *N-type perylene-*

based organic semiconductors for functional neural interfacing, **J.Mater.Chem.B**, vol. 1, issue 31, pp. 3850-3859, Jun. 2013.

[Tordera12] D. Tordera, S. Meier, M. Lenes, R. D. Costa, E. Ortí, W. Sarfert, and H. J. Bolink, *Simple, Fast, Bright, and Stable Light Sources*, **Adv. Mat.**, vol. 24, issue 7, pp. 897-900, Feb. 2012.

[Torricelli15] F. Torricelli, M. Ghittorelli, M. Rapisarda, A. Valletta, L. Mariucci, S. Jacob, R. Coppard, E. Cantatore, Z. M. K.-Vajna, and L. Colalongo, *Unified drain-current model of complementary p- and n-type OTFTs*, **Org. Electron.**, vol. 22, pp. 5-11, Jul. 2015.

[Voelker05] M. Voelker, and P. Fromherz, *Signal Transmission from individual Mammalian Nerve Cell to Field-Effect Transistor*, **Small**, vol. 1, issue 2, pp. 206-210, Feb. 2005.

[Wang05] Q. Wang, J.-E. Moser, and M. Grätzel, *Electrochemical Impedance Spectroscopic Analysis of Dye-Sensitized Solar Cells*, **J. Phys. Chem. B**, vol. 109, issue 31, pp. 14945-14953, Jul. 2005.

[Weis97] R. Weis, and P. Fromherz, *Frequency dependent signal transfer in neuron transistors*, **Phys. Rev. E**, vol. 55, issue 1, pp. 877-889, Jan. 1997.

[Widge07] A. S. Widge, M. J.-El, X. Cui, C.F. Lagenaur, and Y. Matsuoka, *Self-assembled monolayers of polythiophene conductive polymers improve biocompatibility and electrical impedance of neural electrodes*, **Biosens. Bioelectron.**, vol. 22, issue 8, pp. 1723-1732, Mar. 2007.

Yao15] C. Yao, Q. Li, J. Guo, F. Yan, and I.-M. Hsing, *Rigid and Flexible Organic Electrochemical Transistor Arrays for Monitoring Action Potentials from Electrogenic Cells*, **Adv. Healthcare Mater.**, vol. 4, issue 4, pp. 528-533, Mar. 2015.

[Zeck01] G. Zeck, and P. Fromherz, *Noninvasive neuroelectronic interfacing with synaptically connected snail neurons immobilized on a semiconductor chip*, **Proc. Nat. Acad. Sci.**, vol. 98, issue 18, pp. 10457-10462, Apr. 2001.

[Zoski07] C. G. Zoski, *Handbook of Electrochemistry*, **Elsevier**, 1st ed., 2007.

4. Reference-Less Electrolyte-Gated OFET-based neural interfaces

The understanding of neuronal behaviors is an important step to study neuronal and neurodegenerative diseases, which requires the development of new tools and technologies to create functional neural interfaces that allow both stimulation and recording of cellular electrical activity. For this purpose, several technologies have been developed and improved in the last years[Fattahi14]. These achievements span from inorganic field effect devices[Duan12, Karni09, Patolsky06, Poghossian09, Timko10] and microelectrode arrays[Frega12, Maccione13], to organic microelectrodes[Kim10] and organic field-effect transistor (OFET) based sensors[Cramer13, Khodagholy13a]. In parallel with these technological improvements, several theoretical works have been presented, including mathematical analysis of the neural interfaces[Bove95, Fromherz99, Schoen07], impedance spectroscopy performed on living cells[Lempka09, Weis96], and modelling of electrolyte-gate organic transistors (EGOFETs)[Podescu15].

Among these technologies, those based on organic electronics feature advantages with respect to their inorganic counterparts[Fang15]. Indeed, organic electronics is becoming increasingly attractive for neuronal applications, thanks to its promising properties such as low-cost materials and fabrication processes, eco- and bio-compatibility, transparency, and large-area production.

EGOFETs, also known as water-gated OFETs, have been widely investigated in recent years[Cramer12, Kergoat10, Kergoat11, Porrazzo14]. Their working principle is similar to the classic OFET, differing only in the gate contact, which is obtained by means of an ionic solution or electrolyte (or deionized water[Kergoat10]). This allows for devices that work at very low voltages, thanks to the formation of a double-layer capacitance C_{dl} at the electrolyte/semiconductor interface that features thickness of few nanometers[Sharma10].

Aside from EGOFETs, organic electrochemical transistors (OECTs) are worth to be mentioned. Such transistors are characterized by currents that are much larger than the EGOFET counterpart[Larsson11, Khodagholy13b]. However, in an OECT, the on/off switch is produced by transfer of ions from the electrolyte and the semiconductor (doping/de-doping)[Kergoat12], whereas only capacitive processes occur for EGOFETs, without charge transfer[Wang16]. Consequently, EGOFETs are intrinsically faster and more stable than OECTs[Larsson11].

4.1. Reference-Less EGOFET neural interface working principle and modelling

To make the device less invasive, maximizing its suitability for *in vivo* applications, and overcoming one of the major drawbacks of standard technologies[Spanu15], it is desirable to avoid the reference electrode (i.e. the electrode directly in contact with the solution). The organic charge-modulated field-effect transistor (OCMFET) was recently reported as a tool to sense extracellular cells' potentials[Spanu15]. However, the OCMFET structure does not allow simultaneous sensing and simulation of the same cell. Moreover, the device sensing area is far from the transducing transistor, thus reducing the signal-to-noise ratio.

More recently, a reference-less semiconductor ion sensor (RELESIS) was reported[Zeng17], however the authors used an additional insulated electrode to determine the RELESIS working region.

Despite the experimental efforts described above, to our knowledge, a comprehensive model that describes the whole bidirectional interaction between the neural cell and an organic field-effect device is still missing. Indeed, the models present in literature consider only a single microelectrode (for a comprehensive review see [Massobrio16]). Moreover, a model describing the working principle of a reference-less device has not been presented yet.

In this chapter, we aim to provide an equivalent circuit model of an EGOFET interacting with a cell to investigate the feasibility of simultaneous stimulation and sensing without the need of a reference electrode. Proof-of-principle experiments confirm the practicability of the device, predicted from the model. Our model can be successfully used both as an aid in understanding experimental data, and to guide the design of new stimulation and sensing platforms.

4.1.1. Reference-Less EGOFET working principle

In our analysis, we consider EGOFETs (with and without the reference electrode), which Back-Gate (BG) is capacitively coupled with the semiconductor by an insulator. On top of the platform we include the presence of a neuron that is directly coupled with the sensing area of the device. The device structure is depicted in ***Figure 4.1***, and the reader may notice that there is no reference (gate) electrode in contact with the physiological solution to set the DC working point of the electrolyte-gated device. In chapters ***4.3.3*** and ***4.4*** we will show that such a device is able to sense cellular signals without any reference electrode, because the EGOFET can set its DC working point by a "self-polarization" through the source and drain electrodes that polarize the solution. Since the drain-to-source current (I_{DS}) is a function of the extracellular potential V_{out}, any variation of the extracellular voltage ΔV_{out} induces a variation of the transistor current ΔI_{DS}, therefore the device works as a sensor.

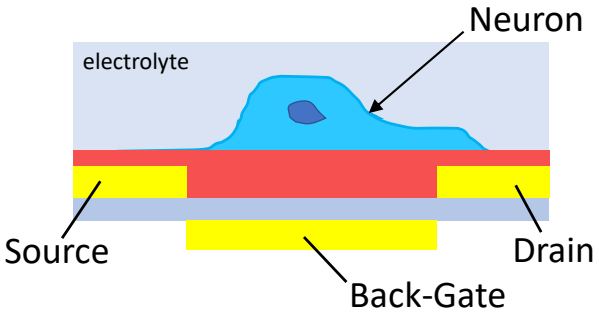

Figure 4.1 - Schematic representation of the RL-EGOFET`. *The cell is placed on top of the organic semiconducting layer, where there is no reference electrode (reference-less). The Back-Gate electrode works as stimulating electrode, whereas the I_{DS} current is directly modulated by the cell potential.*

Cell stimulation can be achieved by applying a pulse to the BG electrode, thus varying the extracellular potential, inducing a small perturbation (around 10mV) at the EGOFET/cell interface sufficient to stimulate action potentials (Aps). One may speculate that such a pulse may lead to undesired variation of the threshold voltage V_T, and consequently an undesired variation of the output current I_{DS}. To evaluate the effective impact of the back-gate stimulation on the threshold voltage variation, we can use the following equation that relates the threshold voltage V_T with the Back-Gate voltage V_{BG}[Colinge04]:

$$V_T = V_{T0} - \frac{C_{BG}}{C_{dl}} V_{BG} \qquad (4.1)$$

Usually, the double layer capacitance C_{dl} is much larger than the BG capacitance C_{BG}, thus only small variations of V_T (and consequently in I_{DS}) are induced.

Experimental evidences of self-polarization and Back-Gate cell stimulation are reported in chapter ***4.4***.

4.1.2. Modelling of (RL-) EGOFET neural interfaces

To show the potentialities of the reference-less EGOFET (RL-EGOFET) technology in sensing membrane potentials and stimulating neuronal action potentials by means of a Back-Gate electrode, we developed and simulated the model presented in ***Figure 4.2***.

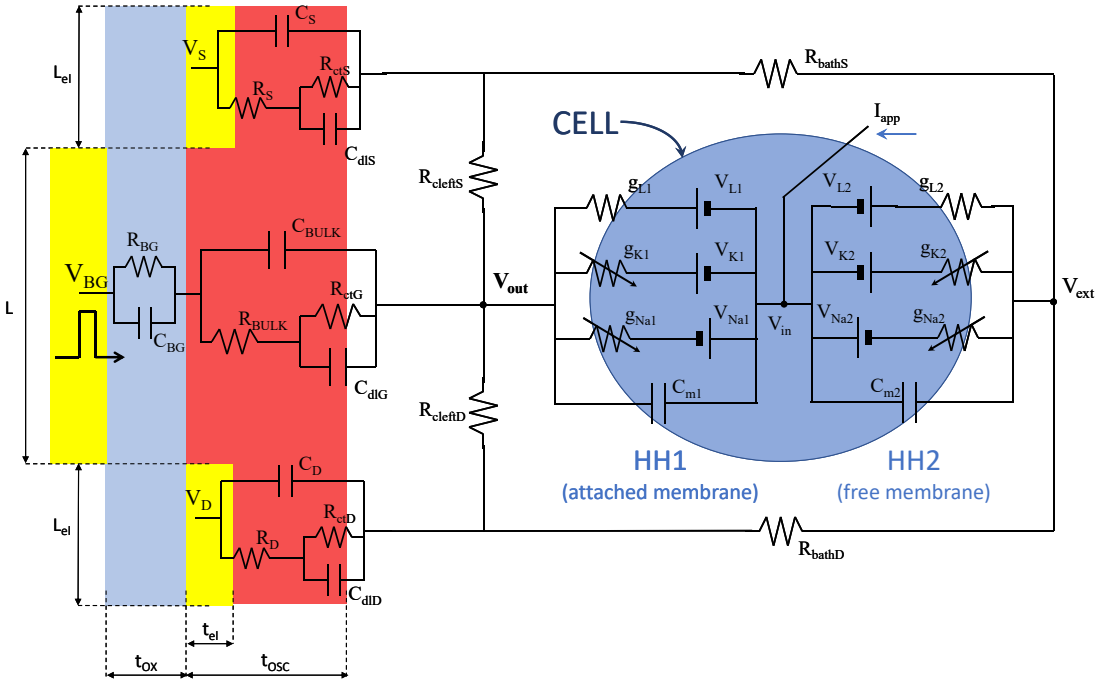

Figure 4.2 - Equivalent circuit model for the RL-EGOFET interfacing a neuron. *Two Hodgkin-Huxley models describe the cell membrane interfacing with the transistor (attached membrane described by HH1) and the cell membrane interfacing with the external bath solution (free membrane described by HH2). The $R_{cleft(S,D)}$ and $R_{bath(S,D)}$ resistances describe the conductive paths through the electrolyte.*

The neuron was modelled using two Hodgkin-Huxley (HH) models[Hodgkin52]: the first HH (HH_1) takes into account the cell membrane that is directly coupled with the stimulating and sensing area of the transistor (attached membrane); the second HH (HH_2), instead, allows an overall description of the membrane that does not directly interact with the device (free membrane).

Since the physiological solution will cover the entire EGOFET, we cannot neglect the "secondary" interaction between the cell and the source and drain electrodes. To model such secondary interaction, we add the cleft resistances (R_{cleftS} and R_{cleftD}) and the bath resistances (R_{bathS} and R_{bathD}). On the one hand, these elements describe the undesired conductive paths between source and drain. On the other hand, they describe the coupling between the sensing device and the cell (R_{cleftS} and R_{cleftD}). Furthermore, they permit the DC polarization of the electrolyte-gated device (V_{out}) through the polarization of the bulk solution V_{ext} (R_{bathS} and R_{bathD}). In fact, at equilibrium, $V_{out}=V_{ext}$, thus motivating our choice of not using a reference electrode.

The interaction between the physiological environment and the organic semiconductor was described using a simplification of the equivalent circuit model reported in ***Figure 3.5b***. In particular, such simplified model is depicted in ***Figure 4.3*** where the reader may notice that we neglected the percolation and diffusion impedances, because these processes have characteristics frequencies under 100mHz in normal operating conditions, which is a value much smaller than the action potential signal frequency that typically ranges from 1Hz to 1kHz[Fall02]. The model reported in ***Figure 4.3*** is then applied to both source and drain electrodes, and to the device sensing area (***Figure 4.2***).

To complete our model, we add an R-C (R_{BG} and C_{BG}) circuit at the BG electrode in order to take into account the insulator. Notice that, R_{BG} should be infinite in an ideal insulator. However, a finite resistance arises due to the insulator quality that leads to a non-zero conductibility.

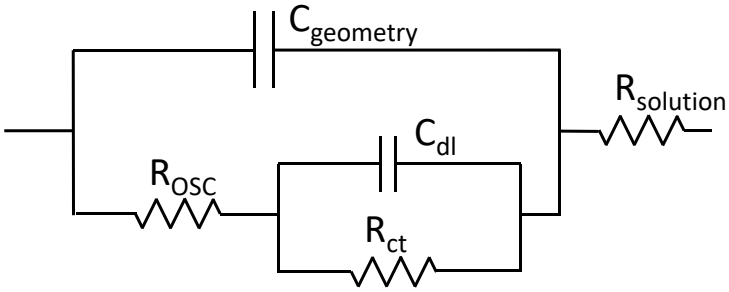

Figure 4.3 - Equivalent circuit model *describing the interaction between solution and the EGOFET electrodes.*

In addition, to keep the model as general as possible, we can run the simulation either with a self-polarized extracellular voltage V_{ext}, thus emulating a reference-less structure, or by forcing an arbitrary voltage V_{ext}, to emulate the presence of a reference electrode, thus simulating typical *in vitro* experiments.

In our simulations, we arbitrarily considered an EGOFET with pentacene as organic semiconductor, and silicon-dioxide as back-gate dielectric material. Unless otherwise specified in the text, ***Table 4.1*** reports the model parameters used in the simulation, where the data are calculated accordingly to the typical scenario found in the literature.

The device source and drain current (I_{DS}) is modulated by the potential at the semiconductor/solution interface (i.e., V_{out} in ***Figure 4.2***) as reported by the following equation[Marinov09]:

$$I_{DS} = \frac{C_{dl}W}{L}\mu_{FET}V_{SS}^{\alpha+2}\frac{\left\{\ln\left[1+\exp\left(\frac{V_{out}-V_T-V_S}{V_{SS}}\right)\right]\right\}^{\alpha+2}-\left\{\ln\left[1+\exp\left(\frac{V_{out}-V_T-V_S}{V_{SS}}\right)\right]\right\}^{\alpha+2}}{\alpha+2} \qquad (4.2)$$

where, V_S and V_D are the Source and Drain potentials, μ_{FET} is the field-effect mobility, V_T is the threshold voltage, V_{SS} is a voltage parameter related to the steepness of the subthreshold characteristics, and $\alpha \geq 0$ is the mobility enhancement factor.

In our simulations, unless otherwise specified, to describe a general OFET with fairly good performance, we use V_S=0V, V_D=-0.2V, V_T=0V, V_{SS}=0.1V, μ_{FET}=0.1cm^{2}V^{-1}s^{-1}, and α=0.

Symbol	Description	Equation	Value
q	Elementary charge		$1.6 \cdot 10^{-14}$ C
ε_0	Vacuum permittivity		$8.854 \cdot 10^{-14}$ F·cm^{-1}
$\varepsilon_{r_{ox}}$	Relative permittivity of the Back-Gate dielectric (silicon dioxide)		3.9
$\varepsilon_{r_{osc}}$	Relative permittivity of the organic semiconductor (pentacene [30])		4
ρ_{OX}	Back-Gate oxide resistivity. (silicon dioxide)		10^{17} Ω·cm
p_0	Hole carrier density in the organic semiconductor[Lucas12]		$2.2 \cdot 10^{14}$ cm^{-3}
μ_t	Organic semiconductor transversal mobility[Lucas12]		$1.7 \cdot 10^{-5}$ cm^2·V^{-1}·s^{-1}
σ_{sol}	Saline solution conductivity[Massobrio16]		$14 \cdot 10^{-3}$ S·cm^{-1}
$R_{cleft(S,D)}$	Cleft resistance at the Source and Drain electrodes[1]		$50 \cdot 10^9$ Ω
W	Width of the organic transistor		$20 \cdot 10^{-4}$ cm
L	Channel length of the organic transistor		$20 \cdot 10^{-4}$ cm
L_{el}	Length of the source and drain electrodes[2]		$20 \cdot 10^{-4}$ cm
t_{OX}	Back-Gate oxide thickness		$200 \cdot 10^{-7}$ cm
t_{OSC}	Organic semiconductor thickness		$150 \cdot 10^{-7}$ cm
t_{el}	Source and Drain electrodes thickness		$100 \cdot 10^{-7}$ cm
t_{cell}	Cell thickness		$20 \cdot 10^{-4}$ cm
A_{el}	Source and Drain electrodes area	$A_{el} = W \cdot L_{el}$	$4 \cdot 10^{-6}$ cm^2
$A_{ch} = A_{m1}$	Electronic channel area, corresponding to the area of the cell membrane interfacing with the EGOFET sensing area[3]	$A_{ch} = A_{m1} = W \cdot L$	$4 \cdot 10^{-6}$ cm^2
A_{m2}	Area of the cell membrane that does not interface with the EGOFET sensing area[3]	$A_{m2} = W \cdot L + 2t_{cell}(W + L)$	$20 \cdot 10^{-6}$ cm^2
$C_{m(1,2)}$	Cell membrane capacitance[5] [Keener09]		10^{-6} F·cm^{-2}
$g_{K(1,2)}$	Potassium channel conductivity[5] [Keener09]		$36 \cdot 10^{-3}$ S·cm^{-2}
$g_{Na(1,2)}$	Sodium channel conductivity[5] [Keener09]		$120 \cdot 10^{-3}$ S·cm^{-2}
$g_{L(1,2)}$	Leakage channel conductivity[5] [Keener09]		$0.3 \cdot 10^{-3}$ S·cm^{-2}
$V_{K(1,2)}$	Potassium channel potential [Keener09]		$77 \cdot 10^{-3}$ V
$V_{Na(1,2)}$	Sodium channel potential [Keener09]		$50 \cdot 10^{-3}$ V
$V_{L(1,2)}$	Leakage channel potential [Keener09]		$54.4 \cdot 10^{-3}$ V
$C_{dl(G,S,D)}$	Double-layer capacitance at the semiconductor/solution interface[6,7] [Franks05]		$10.8 \cdot 10^{-6}$ F·cm^{-2}
$R_{ct(G,S,D)}$	Charge transfer resistance at the semiconductor/solution interface[6] [Franks05]		$1.24 \cdot 10^6$ Ω·cm^2
$R_{bath(S,D)}$	Bath resistances interfacing the cell with the Source and Drain electrodes	$R_{bath(S,D)} = \frac{t_{cell}}{\sigma_{sol} A_{el}}$	$35.7 \cdot 10^3$ Ω
R_{BG}	Back-Gate dielectric resistance	$R_{BG} = \rho_{OX} \frac{t_{OX}}{A_{ch}}$	$5 \cdot 10^{17}$ Ω
C_{BG}	Back-Gate dielectric capacitance	$C_{BG} = \varepsilon_{r_{OX}} \varepsilon_0 \frac{A_{ch}}{t_{OX}}$	$6.9 \cdot 10^{-14}$ F
R_{BULK}	Transversal transport resistance of the organic semiconductor in the channel region[8]	$R_{BULK} = \frac{t_{OSC}}{q p_0 \mu_t A_{ch}}$	$6.3 \cdot 10^9$ Ω
C_{BULK}	Capacitance of the organic semiconductor in the channel region	$C_{BULK} = \varepsilon_{r_{OSC}} \varepsilon_0 \frac{A_{ch}}{t_{OSC}}$	$7.1 \cdot 10^{-14}$ F
$R_{S,D}$	Transversal transport resistance of the organic semiconductor in the Source and Drain region	$R_{S,D} = \frac{t_{OSC} - t_{el}}{q p_0 \mu_t A_{el}}$	$2.1 \cdot 10^9$ Ω
$C_{S,D}$	Organic semiconductor capacitance at the source and drain electrodes	$C_{S,D} = \varepsilon_{r_{OSC}} \varepsilon_0 \frac{A_{el}}{t_{OSC} - t_{el}}$	$2.1 \cdot 10^{-13}$ F

*[1] The reported value is in the same order of magnitude of what found in [Fromherz91] where an R_{cleft} larger than 10GΩ is needed to explain the reported data. As explained in the chapter **4.2.1**, we found that 50GΩ better fits the data reported in **Figure 4.4**.*
[2] For simplicity we assume a symmetrical system, thus the Source and Drain electrodes have the same geometry.
[3] For simplicity we assume that the channel area A_{ch} its equal to the cell area.
[4] For simplicity we schematically represent the cell geometry as a parallelepiped of height t_{cell}.
[5] We reported the values per unit area. To calculate the parameters used in the simulation, the values must be multiplied for the corresponding membrane area (A_{m1} or A_{m2})
[6] The reported value refers to an electrode coated by poly-L-lysine as reported in [Franks05]. The values are reported per unit area. Hence, the values must be multiply (or divided) for A_{ch} to calculate C_{dlG} and R_{ctG}, and for A_{el} to calculate $C_{dl(S,D)}$ and $R_{ct(S,D)}$.
[7] The reported value as been calculated from the data reported in [Franks05] by using the equation reported in [Porrazzo14].
[8] The value has been calculated in ohmic regime due to the low operative voltages[Lucas12].

***Table 4.1 - Parameters** used to simulate the model of **Figure 4.2**.*

4.2. Model Validation

Before analyzing the sensing and stimulation properties of the EGOFET device without the reference electrode, we validate our model using two sets of experimental data found in the literature. These two examples were chosen for the high quality of the reported data, and for the simplicity in extrapolating the data from the published figures. In both cases the transistors were polarized by means of a reference electrode immersed in the solution (fixed V_{ext}).

Where not explicitly specified, all the model parameters are reported in ***Table 4.1***.

4.2.1. Sensing the neural activity from Retzius cells in vitro with a p-type silicon FET

Fromherz at al.[Fromherz91] were the first ones who demonstrated that it is possible to record neuronal activity from cells attached on top of a field-effect device. They made use of Retzius cells from leeches, characterized by action potentials with an amplitude between 30 mV and 50 mV.

Their sensing device was a p-type insulated-gate FET, fabricated using planar technology starting from a n-doped silicon substrate. Including the channel region, the FET device was completely insulated by 20-nm thick SiO_2 that has the double function of acting as gate dielectric and preventing any faradic process.

The device width and length were W = 30 μm and L = 6 μm, respectively, whereas the source and drain lengths were L_{el} = 8 μm for both electrodes.

Although our model aims to describe organic devices with structure quite different from the inorganic transistor used by Fromherz, we can still apply our model to this category of devices, by introducing suitable modifications, such as substituting the double layer capacitance with the SiO_2 insulator and removing the back-gate dielectric.

Stimulating cellular activity by current injection, Fromherz et al. showed that their transistor works as a sensor by comparing the signals collected by the FET device with the signal recorded by an implanted microelectrode (V_{in}) measured with respect to a grounded reference electrode (V_{ext}=0V). In addition, the authors found that a cleft resistance larger than 10 GΩ was needed to explain their data. With our model, we found that the best fits are achieved with $R_{cleft(S,D)}$ = 50 GΩ. Such high resistance is in agreement with the reduction of the electrolyte conductivity when the thickness of solution path (cleft between cell and transistor) reduces below hundreds of nanometres[Stein04].

Figure 4.4 shows the comparison between the data reported by Fromherz et al. and our simulation where a 25-pA current pulse (I_{app}) is used to stimulate the neuron response (dotted lines).

From ***Figure 4.4***, it is clear that our model reproduces both the membrane voltage V_m and the transistor I_{DS} current, confirming that this model can successfully describe the interaction between transistor and living cell.

To run the simulations reported in ***Figure 4.4***, we set C_{dl}=0.17 μF·cm^{-2} and R_{ct}=2·10^{11} Ω·cm^2 to describe the 20-nm thick dielectric. For the sake of simplicity, we write C_{dl} and R_{ct} instead of C_{SiO2} and R_{SiO2} to keep the notation of ***Figure 4.2***.

Using a semiconductor thickness of 100 μm, and a resistivity of 4 Ω·cm, we calculate R_{BULK} = 222 kΩ and C_{BULK} = 1.9·10^{-17} F. The back-gate electrode (bulk electrode) parameters were set to C_{BG}=0F and R_{BG}=1GΩ (the bulk electrode is a rectifying contact with the semiconductor). Since the neuron was characterized by a diameter of 60 μm, meaning that the cell covers the entire device, we set $R_{bath(S,D)} = R_{cleft(S,D)}$. To complete the device parameters definition, we set V_T = -0.1 V, t_{cell} = 40 μm, and μ_{FET} = 20 cm^2·V^{-1}·s^{-1}, in agreement with the data presented in [Fromherz91].

In agreement with the protocol adopted by the autors, the simulation was carried out by setting $V_{BG} = V_S$ = 2.7V, V_D = 0.7V, and V_{ext} = 0V

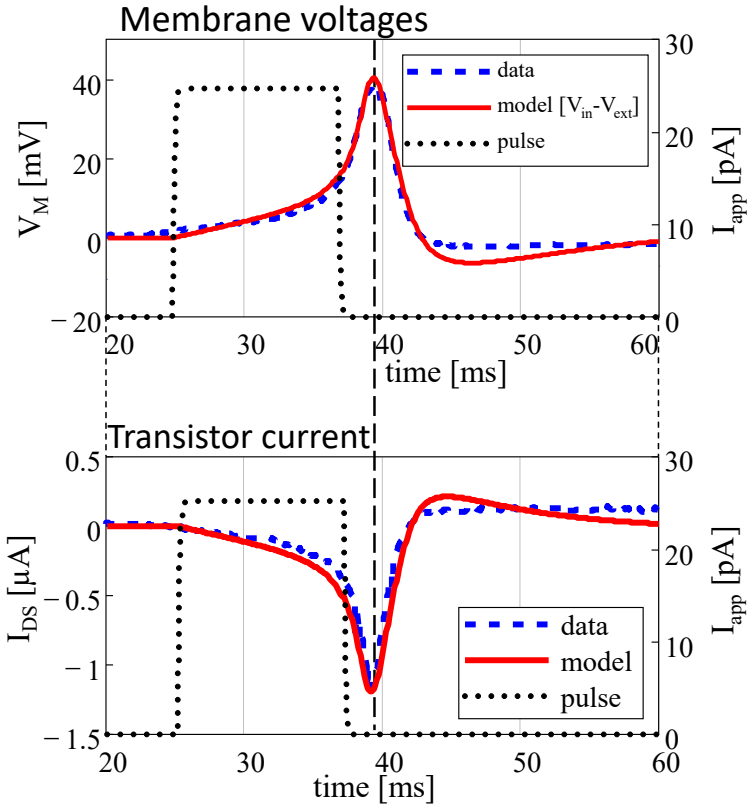

Figure 4.4 - Comparison between the data from [Fromherz91] and the simulation *showing the membrane voltage ($V_M = V_{in} - V_{ext}$) and the transistor I_{DS} current.*

To better represent the smaller amplitude shape of the AP, we slightly modified the original Hodgkin-Huxley (HH) model by reducing the membrane channels conductivities ($g_{L(1,2)}$ = 0.1 mS/cm^2; $g_{K(1,2)}$ = 2 mS/cm^2; $g_{Na(1,2)}$ = 15 mS/cm^2) and by increasing the rate constants α and β for both HH1 and HH2 by a factor 1.3.

4.2.2. Recording action potentials from spontaneously firing cardiomyocyte HL-1 cells by means of organic electrochemical transistors

A very recent achievement in organic bio-sensing was reported by Yao et al. [Yao15]. Their sensing device was an array of p-type organic electrochemical transistors (OECTs) using PEDOT:PSS as active material that covers the entire structure. On top of the array they grew a network of cardiomyocytes exhibiting spontaneous activity.

A single transistor was characterized by W = 30 µm and L = 6 µm, whereas the source and drain contact lengths were L_{el}= 17 µm (active area of 40x30 µm^2). The electrodes and semiconductor thicknesses were t_{el} = 110 nm and t_{OSC} = 210nm, respectively. The device structure adopted by Yao et al. is very similar to the layout considered in this manuscript, except for the absence of a back-gate electrode. Thus, in our simulation we take this difference into account by assuming a zero C_{BG}, an infinite R_{BG}, and V_{BG} = 0V.

To set the operating point of the transistors in the array, the authors made use of a reference electrode immersed in the solution at a potential V_{ext}=-0.2V, whereas the source and drain voltages was V_S = 0V and V_D = -0.4V, respectively.

To simulate the I_{DS} current we set V_T = 0.2V, and μ_{FET} = 40 cm^{2}V^{-1}s^{-1}. Notice that, since OECTs and EGOFETs have different working principles, equation ***4.2*** does not fully reflect the OECT physics[Bernards07]. Thus, we use a large value of μ_{FET} to compensate such difference and to keep the model as general as possible.

Figure 4.5a and ***Figure 4.5b*** show two different simulations that represent the data measured by Yao et al.[Yao15]. In ***Figure 4.5a*** we simulated an AP stimulation by a large negative current, whereas in ***Figure 4.5b*** we simulate a short and small current pulse to induce a weak stimulation unable to generate APs. Both simulations differ from the real data by the absence of one of the two overshoots in the cellular signal. Such difference is likely due to the fact that the HH model cannot fully describe spontaneous firing cells, and to better match the duration of the action potentials, we reduce the rate constants α and β for both HH1 and HH2 by a factor 0.2 (***Figure 4.5a***) and 0.12 (***Figure 4.5b***). However, the examples reported in ***Figure 4.4*** and ***Figure 4.5*** show that our model can describe different device architectures and different cellular signals.

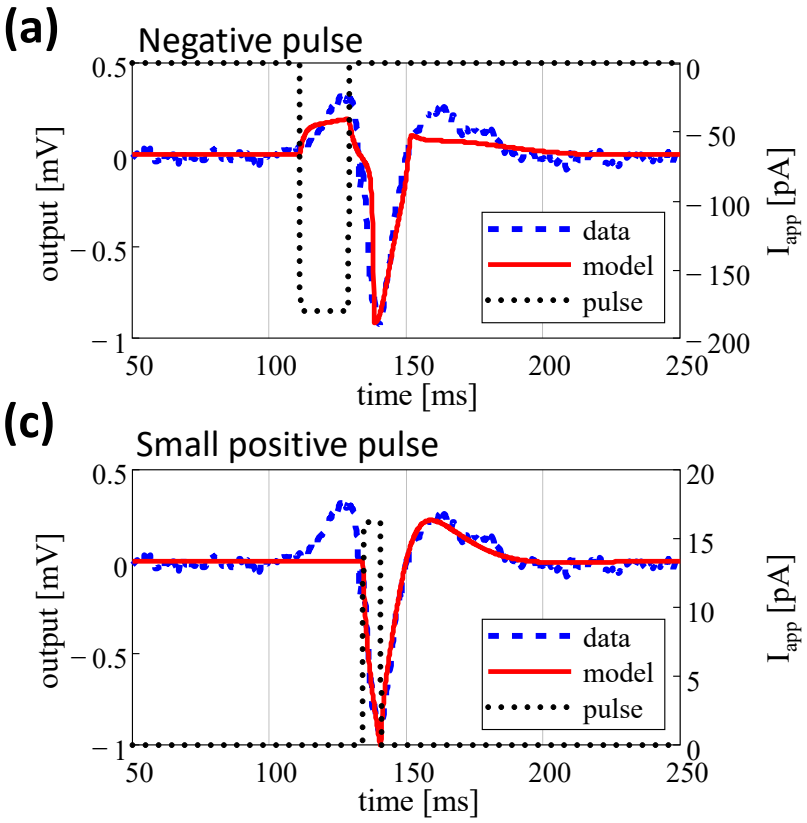

Figure 4.5 - Comparison between data from [Yao15] and simulation.
The output voltage is the I_{DS} current measured by a 10 kΩ resistor and further amplified by a factor 100. **(a)** *AP stimulation by a large negative pulse with $R_{cleft(S,D)}$ = 100 GΩ (the simulated curved is divided by a factor 50).* **(b)** *Shows the stimulation by a small positive pulse without AP generation.*

4.3. Simulation Analysis

In the previous chapter (***4.2***), we validated our model by adapting it to two sets of experimental data found in the literature, recordings of neural activity with a p-type silicon FET[Fromherz91] and AP firing in cardiomyocyte HL-1 cells by organic electrochemical transistors (OECTs)[Yao15].

In this chapter, we study our model by varying some of its main parameters to assess their impact on the device stimulation and sensing properties and to see how the RL-EGOFET might be designed and optimized. We first define a *basic case study* (chapter ***4.3.1***), and then analyse different scenarios, in which we vary one of the model parameters and compare the results with the basic case study (chapter ***4.3.2***). Then, we simulate the result of removing the reference electrode, thus leaving the bulk of the solution floating, i.e. its polarization V_{ext} will be determined by the source and drain potentials (chapter ***4.3.3***).

4.3.1. Basic case study

As a case study, we want to simulate a hypothetical device, which parameters are defined in ***Table 4.1***. For the moment, we assume the presence of a reference electrode (V_{ext}=0V).

We analyse the model by simulating the cell stimulation either by current injection into the cell (current stimulation) or by a voltage pulse applied at the Back-Gate electrode of the EGOFET device (voltage stimulation). We check the effect of the stimulations by simultaneously looking at the membrane voltages and at the I_{DS} current of the EGOFET. Noticeably, the free membrane voltage V_{in}–V_{ext} corresponds to the potential difference that can be measured during patch-clamp experiments.

Figure 4.6a reports the membrane voltage variation due to the current stimulation, and the corresponding I_{DS} current that senses the cell potential V_{out}. On the one hand, the injection of current induces an increase of the V_{in} potential with consequent depolarization of the free membrane that leads to the generation of an AP. On the other hand, due to the high coupling and tight sealing between the cell and the sensing device, the attached membrane is not charged by the injected current I_{app} (no membrane depolarization and no AP) and the trend of V_{out} follows that of the internal potential V_{in}.

Noticeably, an increase of the V_{out} potential corresponds to a decrease of the I_{DS} current, because we are considering a p-type transistor. In addition, the reported source (I_S) and drain (I_D) currents are the transistor currents I_{DS} plus the leakage current between the source and drain electrodes and the saline solution, which is clearly negligible in this case.

Similarly to ***Figure 4.6a***, ***Figure 4.6b*** reports the curves obtained by a simulated voltage stimulation showing that the applied voltage at the Back-Gate electrode can successfully trigger the AP generation, thanks to the capacitive coupling between EGOFET and cell.

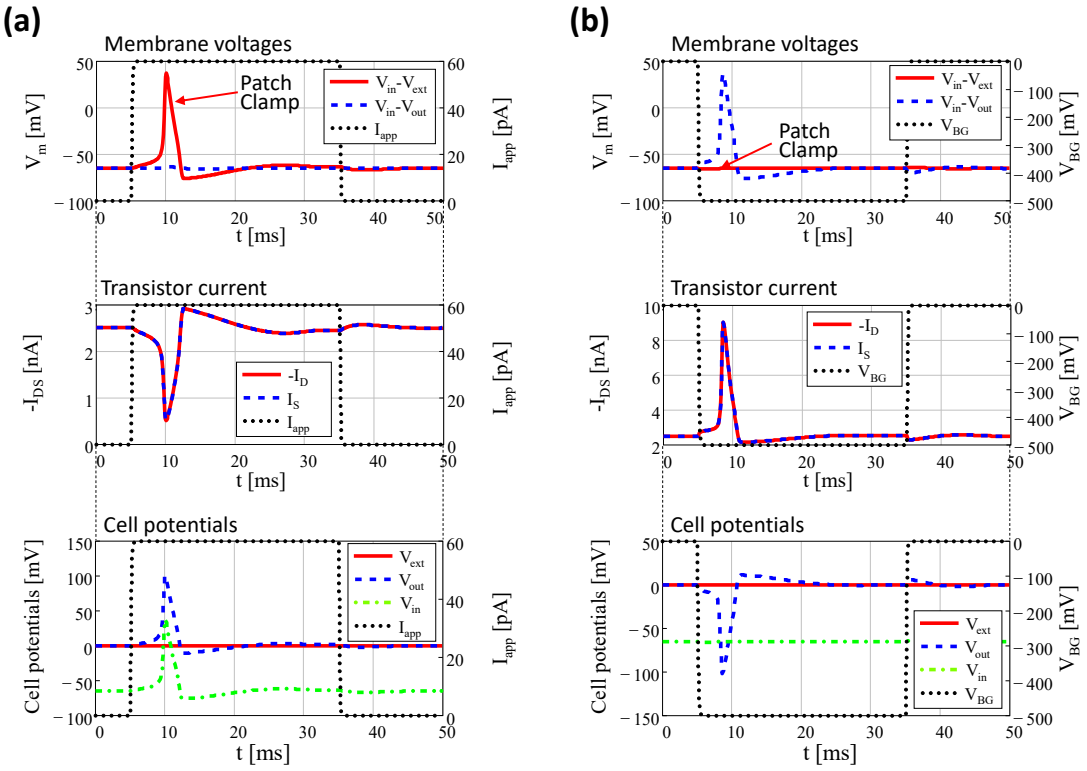

Figure 4.6 - Simulation analysis of the basic case study (with reference electrode). *Simulated membrane voltages (V_{in}-V_{out}, and V_{in}-V_{ext}) and corresponding EGOFET I_{DS} current in response to a current* **(a)** *and a voltage* **(b)** *stimulation (dotted line). The free membrane voltage V_{in}-V_{ext} (solid line) emulate the patch-clamp measurement. The simulations were carried out by forcing the external solution potential V_{ext} = 0V to mimic the presence of a reference electrode. The transistor current is calculated using V_{out} as gate input. The three cell potentials (V_{in}, V_{out}, and V_{ext}) are referred to the EGOFET source potential (V_S = 0V).*

Comparing ***Figure 4.6a*** and ***Figure 4.6b***, two important opposite behaviours can be seen: *i)* the V_{out} potential decreases towards negative voltages inducing an increase of the I_{DS} current; *ii)* the voltage pulse stimulates the AP generation at the attached membrane whereas there is no AP at the free membrane.

While the current stimulation acts by increasing the internal potential V_{in}, the negative voltage pulse (hundreds of mV), induces a sudden decrease of V_{out} (few mV), causing the depolarization of the attached membrane, and consequently the generation of an AP. Since V_{ext} is fixed (V_{ext}=0V constant) and the external membrane capacitance C_{m2} is much larger than the equivalent capacitance in the path between V_{in} and V_{BG}, the back-gate voltage pulse induces only a marginal variation of the inner potential V_{in} and, consequently, the free membrane does not respond with an AP. Thus, only V_{out} can contribute to the generated AP giving rise to the negative peak in the cell potential V_{out} (***Figure 4.6b***).

This reasoning suggests that, even though during a patch-clamp experiment no membrane voltage variation (V_{in}-V_{ext} in ***Figure 4.6b***) would be recorded, the cell could be generating APs at the interface with the transistor (V_{in}-V_{out} in ***Figure 4.6b***). In contrast to patch-clamp, such variation in the cell potentials can be successfully detected by the EGOFET, suggesting the development of fully transparent devices to monitor cell activity at the membrane facing the sensor by combined live cell imaging and electrical sensing.

In addition, it is interesting to notice that, at the falling edge of the voltage pulse, we are depolarizing the attached membrane, while hyperpolarizing the free membrane (vice versa at the pulse rising edge), thus to stimulate the AP at the external membrane, a larger voltage pulse is needed as shown in ***Figure 4.7a***.

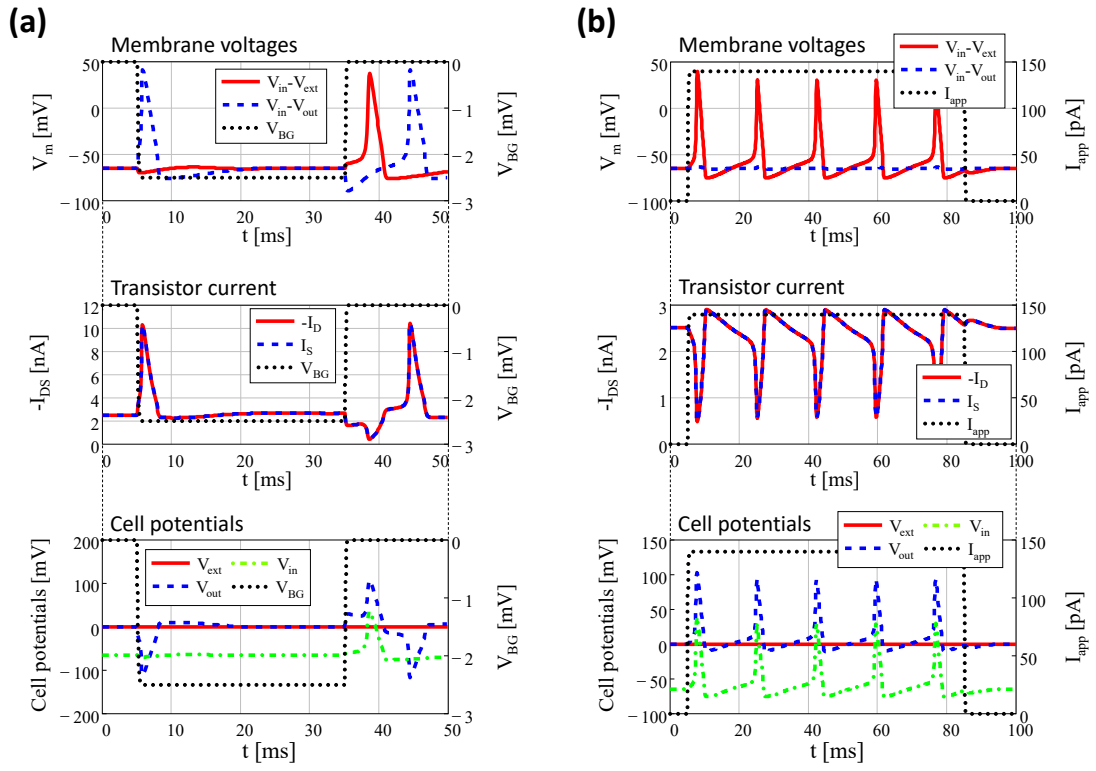

Figure 4.7 - Analysis of the basic case study by large voltage and large current stimulations.
(a) *Membrane voltages (V_{in}-V_{out}, and V_{in}-V_{ext}), EGOFET I_{DS} current, and cell potentials (V_{in}, V_{out}, and V_{ext}) behaviours due to a -2.5V Back-Gate voltage stimulation.*
(b) *Membrane voltages (V_{in}-V_{out}, and V_{in}-V_{ext}), EGOFET I_{DS} current, and cell potentials (V_{in}, V_{out}, and V_{ext}) behaviours due to a 140pA current stimulation.*

The rising edge of the voltage pulse induces the depolarization of the free membrane, but, since the coupling between V_{BG} and V_{out} is higher than the coupling between V_{BG} and V_{in}, it also induces a large hyperpolarization of the attached membrane with consequent AP generation. Once again, we remark that we are considering a p-type EGOFET, hence the I_{DS} current well represents the negative peaks of V_{out} (APs of the attached membrane) but tends to hide the positive peaks (APs of the free membrane) as shown by the transistor current I_{DS} in ***Figure 4.7a***.

In ***Figure 4.7b*** we show the current stimulations due to a large injected current I_{app}. Such high current induces a continuous depolarization of the external membrane, with consequent continuous firing.

4.3.2. Parameter analysis (with reference electrode)

One of the most discussed parameters in neural interfaces is the cleft resistance R_{cleft}[Braun98, Braun 04, Massobrio16], because it is directly ascribable to the quality of the sensor/cell interface: the larger R_{cleft}, the tighter the coupling between sensor and cell. On the other hand, when the value of R_{cleft} is decreased, the output voltage V_{out} sensed by the transistor during current stimulation assumes the shape of the first derivative of the signal V_{in}[Fromherz99], as reported in ***Figure 4.8a*** for R_{cleft} = 5 GΩ, whereas no appreciable differences can be seen during voltage stimulation (***Figure 4.8b***).

Notice that, the first derivative shape in ***Figure 4.8a*** appears because the injected current not only stimulates the AP at the free membrane, but also generates a delayed AP at the attached membrane.

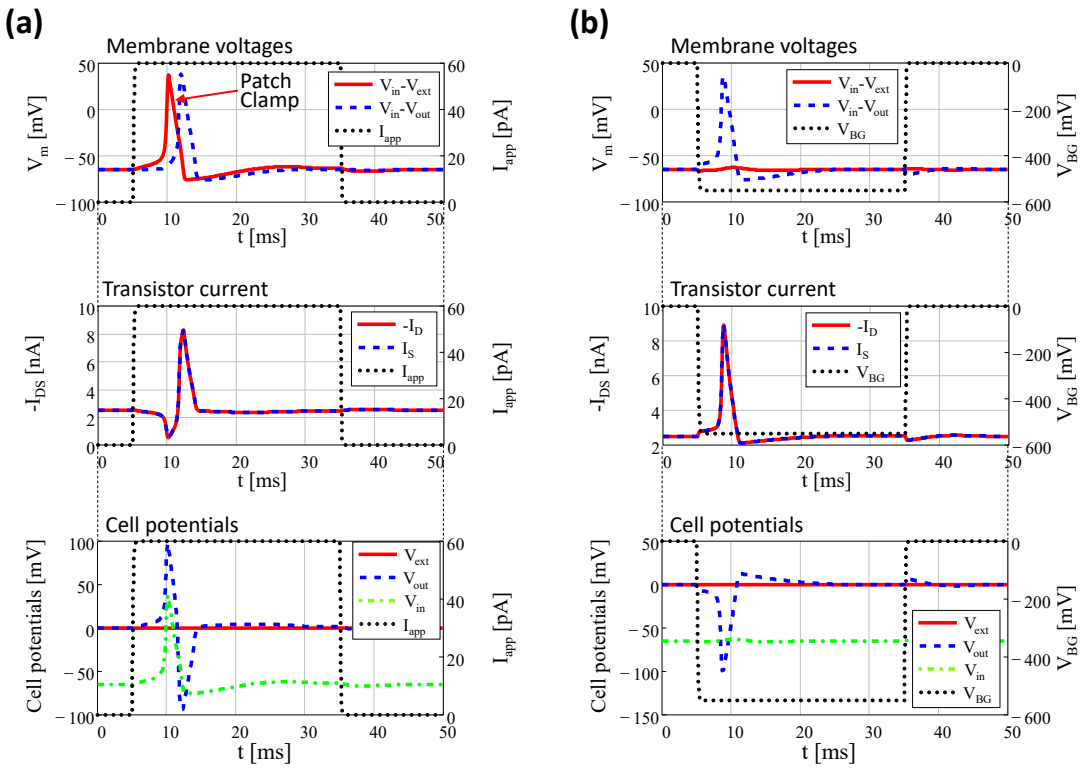

Figure 4.8 - Impact of the cleft resistance on the EGOFET properties (R_{cleft}=5GΩ).
Membrane voltages (V_{in}-V_{out}, and V_{in}-V_{ext}), EGOFET I_{DS} current, and cell potentials (V_{in}, V_{out}, and V_{ext}) behaviours due to: **(a)** *60pA current stimulation;* **(b)** *-550mV Back-Gate voltage stimulation.*

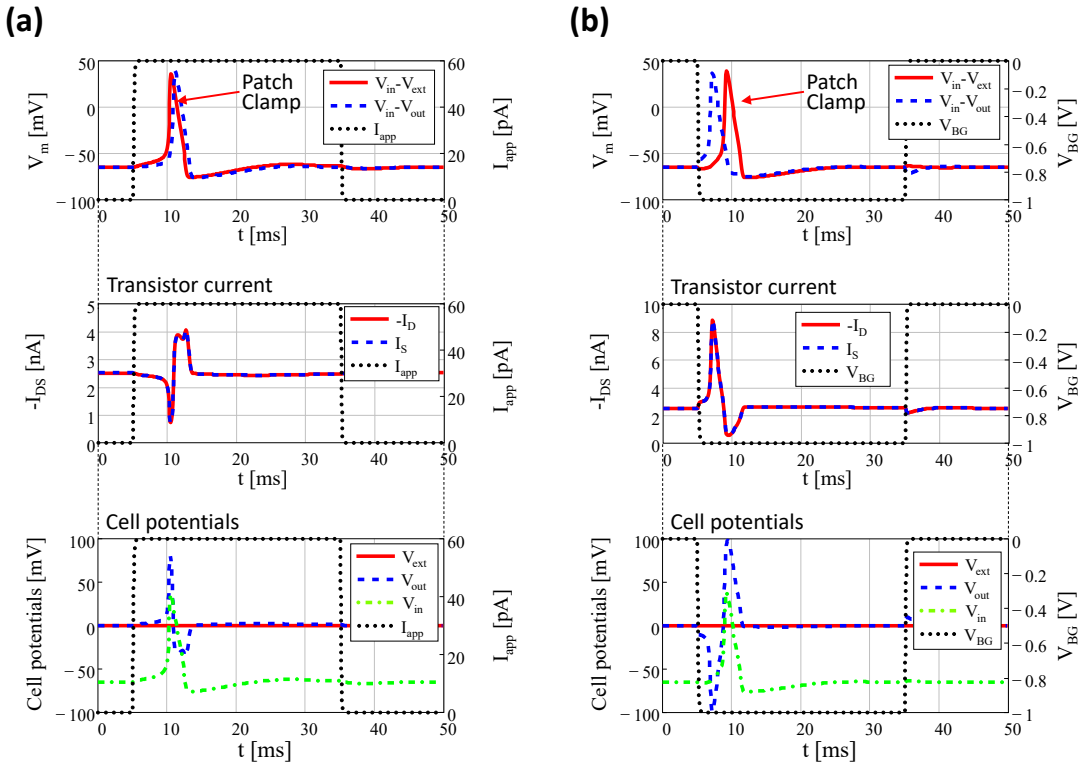

Figure 4.9 - Impact of the cleft resistance on the EGOFET properties (R_{cleft}=1GΩ).
Membrane voltages (V_{in}-V_{out}, and V_{in}-V_{ext}), EGOFET I_{DS} current, and cell potentials (V_{in}, V_{out}, and V_{ext}) behaviours due to: **(a)** *60pA current stimulation;* **(b)** *-1V Back-Gate voltage stimulation.*

Further decreasing R_{cleft} reduces the delay between the APs of the two membranes during current stimulation, inducing a further distortion of the output signal V_{out} as shown in ***Figure 4.9a*** for R_{cleft} = 1 GΩ. In addition, such a low resistance negatively affects also the back-gate voltage stimulation. Hence, larger voltages are needed to stimulate APs that, like during current stimulation, are generated at both the attached and the free membranes, leading to the first derivative shape of V_{out} as reported in ***Figure 4.9b***.

Let us now consider the interface between the organic semiconductor and the bath saline solution (R_{ct} and C_{dl}). Since R_{ctG} is much smaller than the dielectric resistance R_{BG}, changing its value in the simulations does not affect the sensing and stimulation properties of the device, and the simulation results are quite similar to what observed in ***Figure 4.6a*** and ***Figure 4.6b***.

Instead, if the C_{dl} value is lower than 100nF/cm^2 (or in general much smaller than the cell membrane capacitance), the voltage drop across the double layer capacitance is no longer negligible and, consequently, higher back-gate voltage pulses are required to effectively stimulate the cell (***Figure 4.10a***).

In addition, a lower C_{dl} means a lower I_{DS} current (equation ***4.2***). Hence, reducing the double-layer capacitance impacts the sensing properties of the EGOFET device, and increases the effect of the leakage current onto the I_{DS} output as reported in ***Figure 4.10b***.

Moreover, from ***Figure 4.10a***, we see that the I_{DS} current reflects the shape of the back-gate voltage pulse. In fact, from equation ***4.1*** we calculate that, during the pulse, the EGOFET threshold voltage becomes V_T=1.3V, due to the lower C_{dl}. Hence the transistor is always in ON state, making the AP less observable.

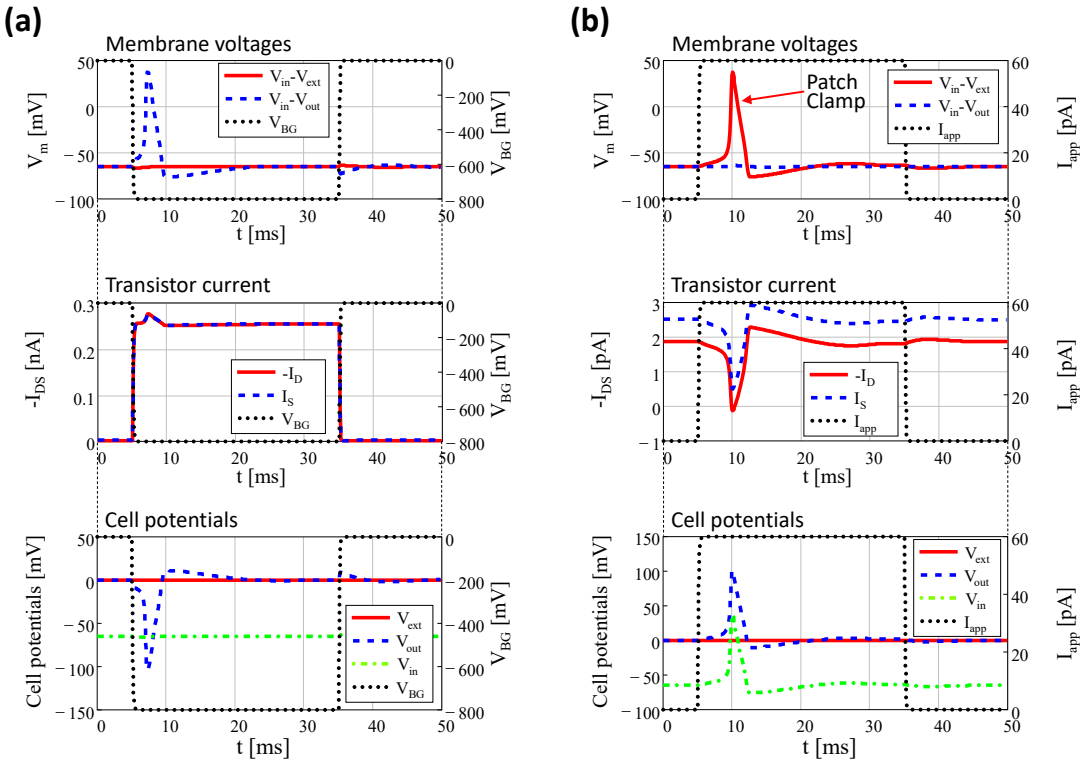

Figure 4.10 - Impact of the double-layer capacitance on the EGOFET properties (C_{dl}=10nF).
Membrane voltages (V_{in}-V_{out}, and V_{in}-V_{ext}), EGOFET I_{DS} current, and cell potentials (V_{in}, V_{out}, and V_{ext}) behaviours due to: **(a)** *-800mV Back-Gate voltage stimulation;* **(b)** *60pA current stimulation.*

Let us consider now the effect of the insulator thickness t_{OX}. Since C_{BG} is the smaller capacitance in the path between the back-gate electrode and the cell, its value manly affects the voltage stimulation. Indeed, if the dielectric thickness is reduced, i.e. the C_{BG} capacitance is increased, the amplitude of the voltage pulse reduces (***Figure 4.11a***). The opposite happens if t_{OX} is made larger, i.e. a smaller C_{BG} and consequently a larger V_{BG} is needed (***Figure 4.11b***).

Similar considerations apply also for the semiconductor thickness t_{OSC}, even though its effects are less evident than t_{OX}: a larger t_{OSC} means a weaker coupling between back-gate and cell, that means a larger back-gate pulse amplitude is needed to stimulate the cell.

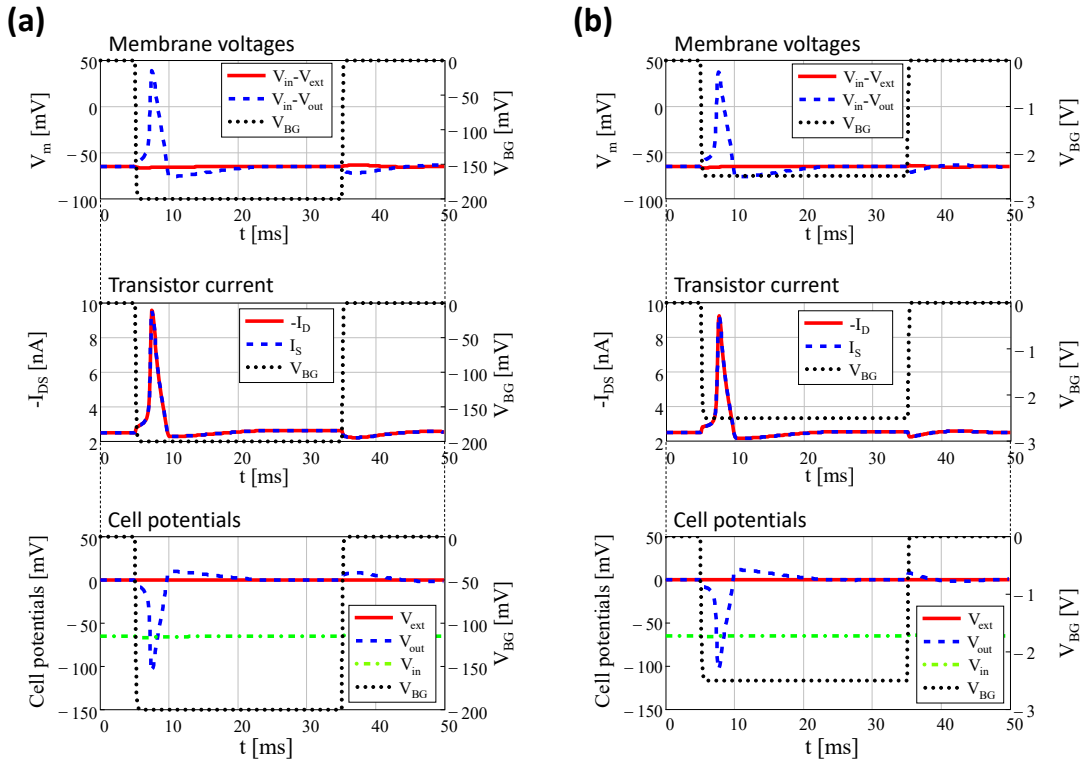

Figure 4.11 - Impact of the insulator thickness t_{OX} on the EGOFET properties.
Simulation of Back-Gate voltage stimulation for t_{OX} = 20nm **(a)** *and for t_{OX} = 1μm* **(b)**. *Notice that, increasing the back-gate dielectric thickness, larger voltages are needed to stimulate an AP due to the reduction of the back-gate capacitance C_{BG}. All the figures report the behaviour of the membrane voltages (V_{in}-V_{out}, and V_{in}-V_{ext}), the EGOFET I_{DS} current, and the cell potentials (V_{in}, V_{out}, and V_{ext}).*

4.3.3. Model with no reference electrode

We analyse now the model by removing the reference electrode (RL-EGOFET). Since we removed the reference electrode, we use the source electrode as reference potential (V_S=0V). Hence, using the electric circuit in ***Figure 4.2*** and considering a large back-gate resistance, the DC external potential can be calculated as $V_{ext} = \frac{V_D - V_S}{2} = \frac{V_D}{2}$. Notice that this result derives from the fact that we are considering a symmetrical system. Generally, V_{ext} would be between the source and drain potentials (see chapter ***4.4.1c***). Remarkably, at equilibrium V_{out}=V_{ext}, thus the RL-EGOFET device can be turn on and off without the need of any reference electrode. We define this phenomenon *self-polarization*.

Figure 4.12a shows that the RL-EGOFET can stimulate (by back-gate voltage stimulation) and sense (by reading of the I_{DS} current) AP of a cell directly plated on top of the device sensing area. We notice that, unlike what we saw by externally forcing V_{ext}=0V (***Figure 4.6b***), the back-gate pulse does not directly induce the depolarization of the In/Out membrane but, since the external bath potential is not fixed, it induces an abrupt decrease of the cell potentials (V_{out}, V_{in}, V_{ext}). The variation in the cell potentials is due to capacitive coupling, thus all three cell potentials feature the same variation, giving the unwanted I_{DS} spike in correspondence to the back-gate pulse (the same happens at the end of the voltage pulse).

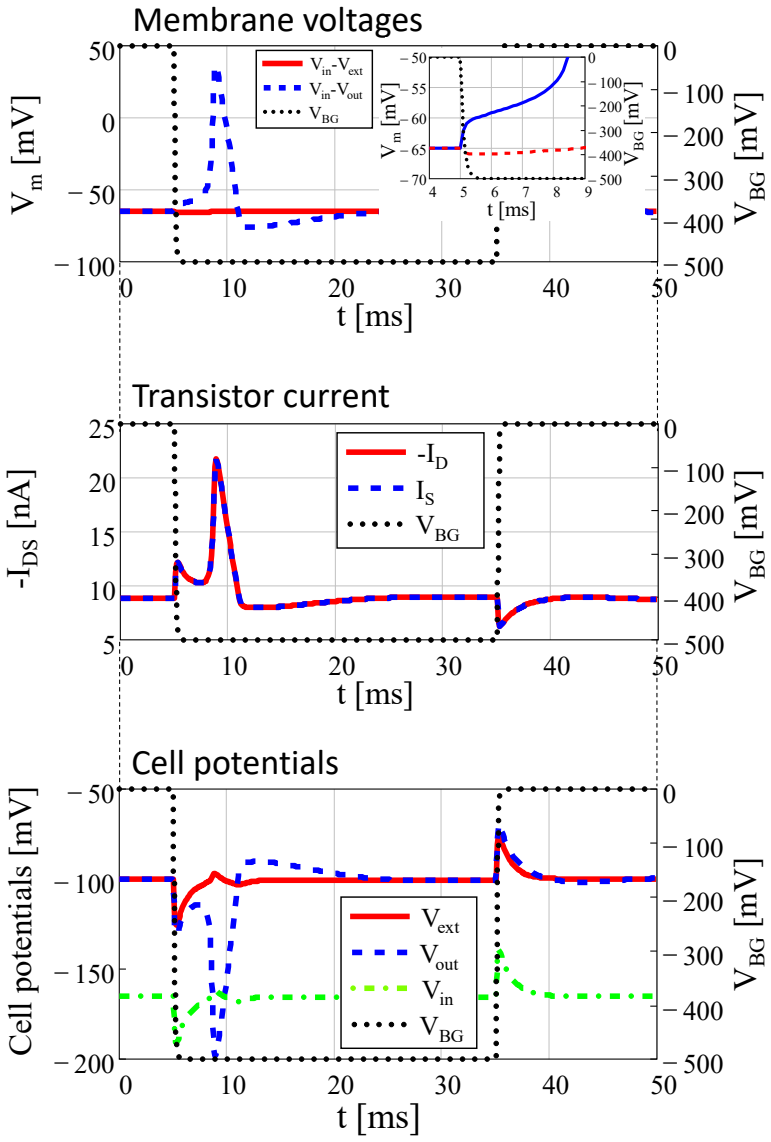

Figure 4.12 - Simultaneous stimulation and recording simulations by a RL-EGOFET. *Simulated membrane voltages (V_{in}-V_{out}, and V_{in}-V_{ext}) and corresponding RL-EGOFET I_{DS} current in response to a -500mV Back-Gate voltage stimulation. The transistor current is calculated using V_{out} as gate input. The three cell potentials (V_{in}, V_{out}, and V_{ext}) are referred to the RL-EGOFET source potential (V_S = 0V). Notice that without the reference electrode V_{ext} is no longer constant and responds to the applied stimulation. The free membrane voltage V_{in}-V_{ext} (solid line) emulates a non-standard patch-clamp measurement, where the reference voltage is taken at the source electrode rather than at the reference electrode (that has been removed).*

After this spike, the cell potentials start increasing exponentially to reach its equilibrium value. However, V_{in} increases faster than V_{out}, thus slowly depolarizing the In/Out membrane (inset in ***Figure 4.12a***), with consequent delayed AP generation.

One way to reduce the delay between the generated AP and the applied stimulus (***Figure 4.12a***) is to increase the amplitude of the back-gate pulse (***Figure 4.13a***). However, increasing the voltage pulse also increases the appearance of unwanted spikes that could be misinterpreted as action potentials as reported in ***Figure 4.13b***.

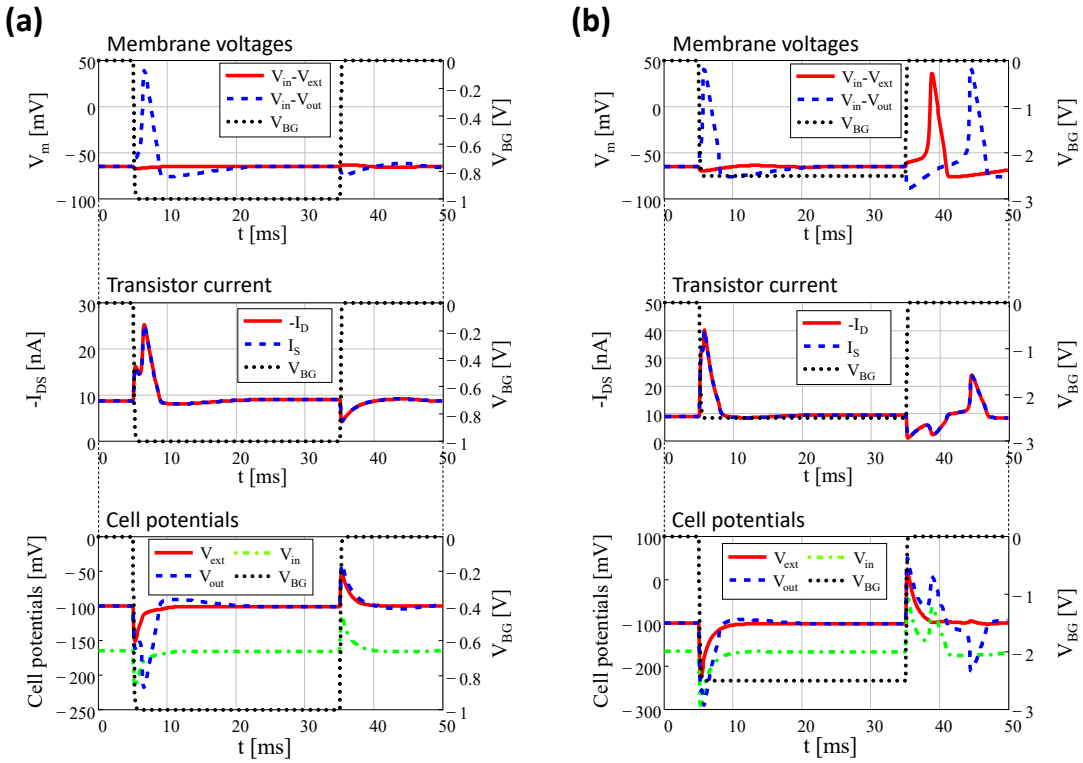

Figure 4.13 - Analysis of the RL-EGOFET by large voltage stimulations.
Membrane voltages (V_{in}-V_{out}, and V_{in}-V_{ext}), RL-EGOFET I_{DS} current, and cell potentials (V_{in}, V_{out}, and V_{ext}) behaviours due to: **(a)** *-1V Back-Gate voltage stimulation;* **(b)** *-2.5V Back-Gate voltage stimulation.*

Even though the aim of an RL-EGOFET is the in-vivo application for extracellular recording avoiding any implanted electrodes, patch clamp experiments without the gate-reference electrode may be possible, by using the source electrode as reference potential for the patch-clamp set-up and stimulating the cells by current injection, also *in vivo*[Petersen17]. Optogenetics, where light-sensitive ion channels in neurons are controlled by direct illumination is another means to provide current stimulation *in vivo*[Wiegert17]. In these configurations, current stimulations would be possible as shown by the simulations reported in ***Figure 4.14a*** showing that the current pulse actually stimulates membrane APs.

However, three important differences, with respect to the base example, are visible:

- During the injection of current I_{app}, the cell potentials increase due to charging of the device capacitances. On the one hand, the injected current induces an exponential charging of the source and drain capacitances $C_{S,D}$ that is limited by the source/drain resistance $R_{S,D}$ ($\Delta V_m \sim R_{S,D} I_{app} \cdot \left[1 - \exp\left(-\frac{\Delta t}{R_{S,D} C_{S,D}}\right)\right]$). On the other hand, the I_{app} current also charges the double-layer capacitances $C_{dl(S,D)}$ but, due to the large value of the $R_{ct(G,S,D)}$ resistances, the cell potentials variation is no longer exponential but it features a linear increase ($\Delta V_m \sim \frac{I_{app}}{C_{dl}} \cdot \Delta t$; ***Figure 4.14b***).
- At the end of the current pulse, we can see the discharge of the source and drain capacitances, however the double-layer capacitances do not discharge, because of the large charge-transfer resistances R_{ct}, explaining the voltage differences between the cell potentials before and after the applied pulse.
- Lastly, since we are considering a p-type RL-EGOFET, the increase of the cell potentials, and especially of V_{out}, tends to turn off the sensing transistor. This is clearly visible when a long current pulse is applied to generate continuous APs, hence only the first generated APs are detectable (***Figure 4.14b***).

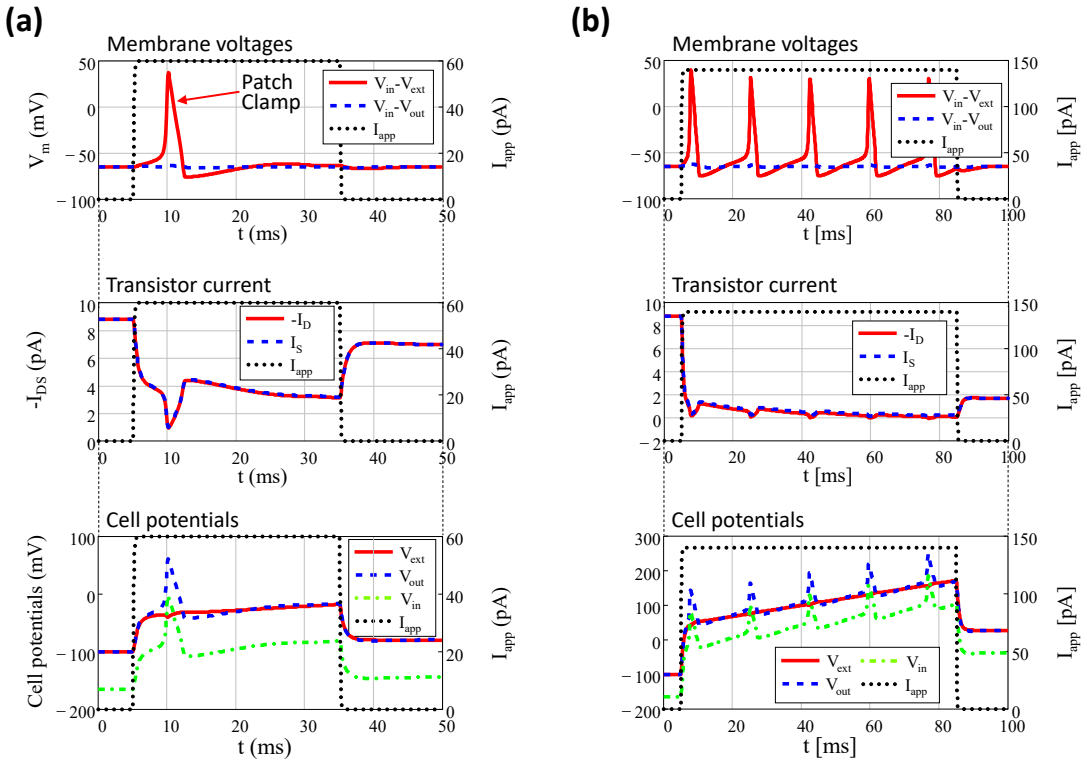

Figure 4.14 - Analysis of the RL-EGOFET by current stimulations.
Membrane voltages (V_{in}-V_{out}, and V_{in}-V_{ext}), RL-EGOFET I_{DS} current, and cell potentials (V_{in}, V_{out}, and V_{ext}) behaviours due to a 60pA current stimulation lasting 30ms **(a)** *and 80ms* **(b)**.

Remarkably, reducing the R_{ct} and $R_{S,D}$ resistances means faster transients and smaller amplitude that could avoid the transistor turn-off but, in turn, could lead to excessive current leakage between the solution and the source and drain electrodes. On the other hand, larger resistances translate into larger and slower variations in the cell potentials. If very large values are involved, the cell potentials will feature a linear behaviour. Similarly, lowering the double-layer capacitance C_{dl} and/or the source/drain capacitance $C_{S,D}$ implies a faster increase of the cell potentials, with consequently faster transistor turn-off. On the other hand, larger capacitances induce slower potential variations.

This reasoning holds true also for the Back-Gate voltage stimulation, which is the more interesting application for an RL-EGOFET. Moreover, the sensor without the reference electrode is more sensitive to the parameter variation than the device with the reference electrode, and an example is the double-layer capacitance C_{dl}. We have seen that lowering its value (***Figure 4.10***) induces a lower I_{DS} current, the constant on-state of the EGOFET during the voltage pulse, and the need of higher voltages to effectively stimulate the cell. In addition to all these phenomena, reducing the double-layer capacitance strongly affects the time constant (associated to the geometrical capacitance $C_{Geometry}$) of the equivalent circuit in ***Figure 4.3***, used to describe the source and drain electrodes. Counterintuitively, the reduction of C_{dl} below a certain value could lead to unexpected results. In fact, when C_{dl} is large enough, R_{ct} can be neglected during the pulse, hence the time constant of the circuit in ***Figure 4.3*** is approximately $C_{Geometry} \cdot R_{OSC}$. Conversely, a very small C_{dl} value leads to a time constant that is approximately $C_{Geometry} \cdot (R_{OSC}+R_{ct})$, which can be much larger than the previous case. Such a large time constant will impact the transient of the membrane potentials in response of the voltage pulse: the decrease of the back-gate voltage induces an abrupt decrease of the membrane potentials as already shown in ***Figure 4.12***. However, due to the low time constant, during the pulse the membrane potentials feature a very low increase, resembling a constant behaviour (***Figure 4.15a***) further hiding the AP in the I_{DS} current. Actually, the membrane potentials are not constant, but they feature a very slow exponential decay, as can be seen in ***Figure 4.15b***, where we perform the same simulations but with a larger pulse width.

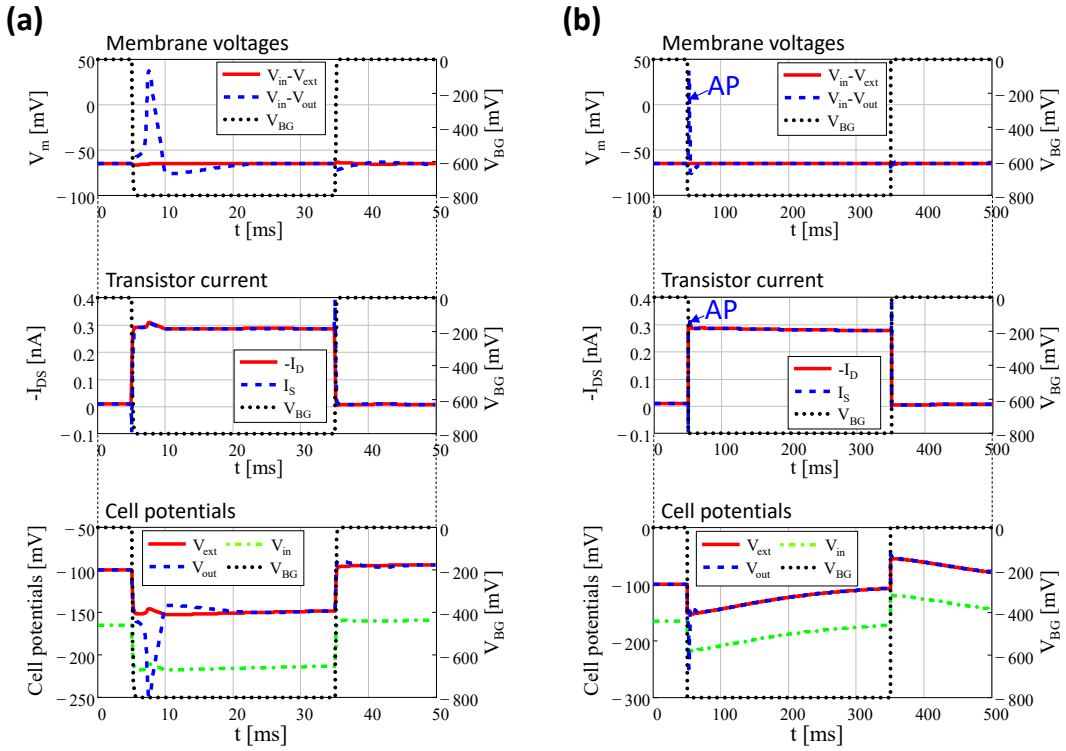

Figure 4.15 - Impact of the double-layer capacitance on the RL-EGOFET properties (C_{dl}=10nF). *Membrane voltages (V_{in}-V_{out}, and V_{in}-V_{ext}), RL-EGOFET I_{DS} current, and cell potentials (V_{in}, V_{out}, and V_{ext}) behaviours due to a -800mV Back-Gate voltage stimulation lasting 30ms* **(a)** *and 300ms* **(b)**.

Thus, an ideal RL-EGOFET should be characterized by very large capacitance (both $C_{S,D}$ and C_{dl}) and large R_{ct} resistances. In contrast, the $R_{S,D}$ resistances should be as small as possible. One way to achieve these specifications is by reducing the thickness of the organic layer t_{OSC}, which does not impact the capability to stimulate the cell AP by back-gate voltage stimulation. Moreover, changing the semiconductor thickness means changing the difference between the semiconductor and the electrode thicknesses ($t_{OSC} - t_{el}$). In fact, lowering both t_{OSC} and t_{el}, keeping $t_{OSC} - t_{el}$ constant, does not induce any relevant changes in the simulations (***Figure 4.16a***). However, if we reduce only t_{OSC}, keeping t_{el} constant, the coupling between the source and drain electrodes and the water solution becomes stronger, hence reducing the undesired spikes due to the voltage stimulation (***Figure 4.16c***) and the decrease of the cell potentials during current stimulation (***Figure 4.16d***), making the performance of the RL-EGOFET close to the device with the presence of the reference electrode. In turn, increasing the difference between $t_{OSC} - t_{el}$ makes the coupling with the solution weaker with consequent larger undesired spikes (***Figure 4.16b***). These last observations point out the importance of an opportune design of the source and drain electrodes in order to reach the best trade-off between high carrier injection and stable self-polarization.

In addition, since the working principle of the RL-EGOFET is based on the self-polarization of the solution, it is important not only to choose the semiconductor and electrodes thicknesses, but also to consider the source and drain electrode areas. We analyse the variation of the electrode areas by varying the length of the electrodes L_{el}. Smaller source and drain electrodes are desirable to reduce parasitic couplings and leakage, and to enhance the sensor integration and selectivity. However, the smaller area reduces the bath resistances and in turn the self-polarization become weaker. Even though this phenomenon does not affect the capability of stimulating cell APs, it results in undesired spikes (voltage stimulation in ***Figure 4.17a***) or excessive increase of the cell potentials (current stimulation in ***Figure 4.17b***) that hide the real AP in the transistor current. In turn, even though larger electrodes lead to larger leakage, the larger area also induces a stronger self-polarization of the bath potential V_{ext}. Consequently, due to the very low variation of V_{ext} during the voltage pulse, the device stimulating and sensing properties become closer to those reported in ***Figure 4.6*** as shown in ***Figure 4.17c*** and ***Figure 4.17d***, strengthening once again the possibility of realizing bidirectional neural interfaces that do not need any reference electrode.

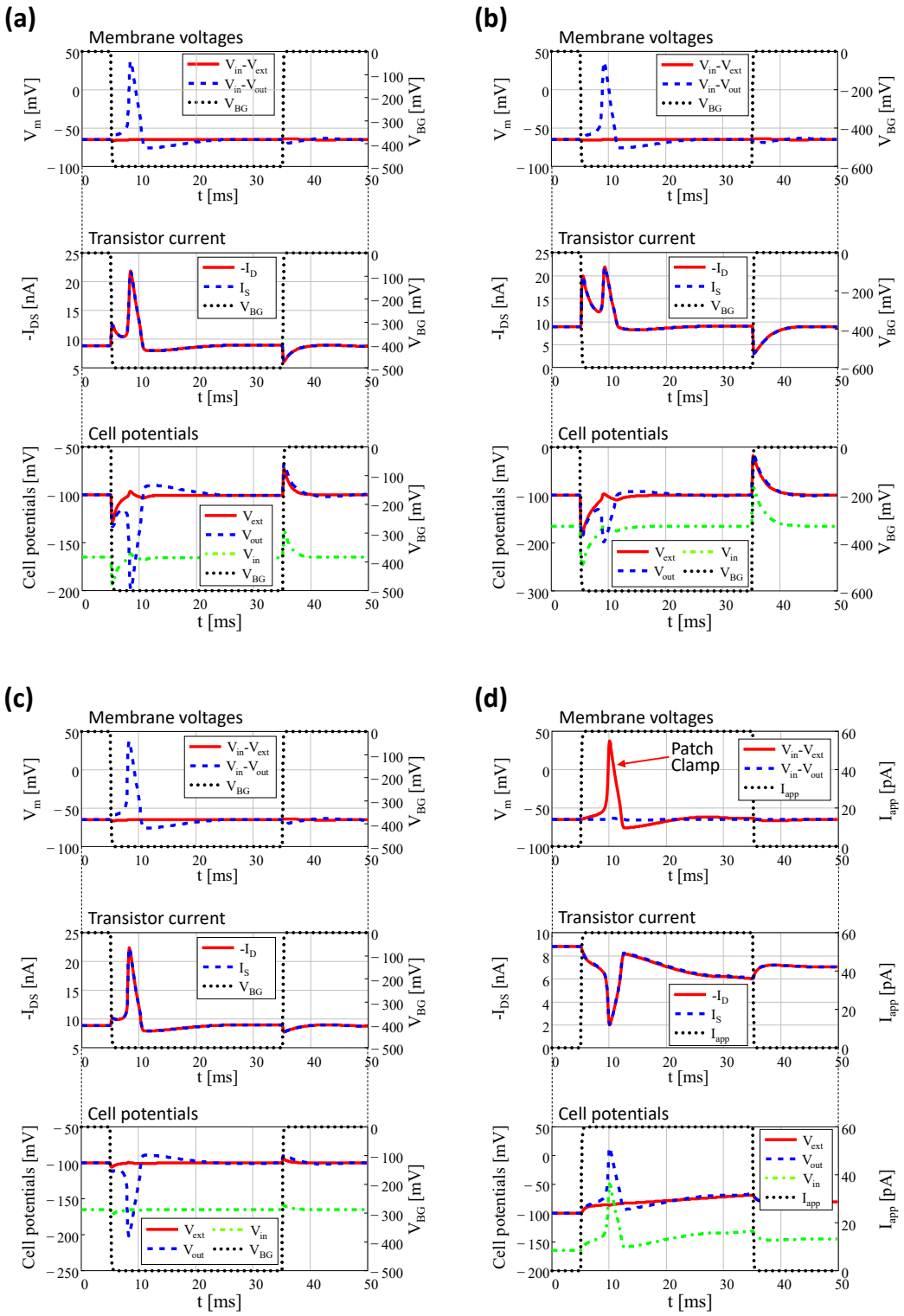

Figure 4.16 - Impacts of the semiconductor thickness t_{OSC} on the RL-EGOFET properties.
RL-EGOFET simulation by -500mV Back-Gate voltage stimulation for **(a)** t_{OSC} *= 110nm and* t_{el} *= 60nm* ***(t_{OSC}-t_{el} =50 nm)****, and for* **(b)** t_{OSC} *= 300nm and* t_{el} *= 100nm* ***(t_{OSC}-t_{el} =200 nm)****.*
Simulated membrane voltages (V_{in}-V_{out}, and V_{in}-V_{ext}) and corresponding I_{DS} current in response to a voltage **(c)** *and a current* **(d)** *stimulation (dotted line) for an RL-EGOFET with* t_{el} *= 100nm and* t_{OSC} *= 110nm* ***(t_{OSC}-t_{el} =10 nm)****.*
All the figure reports the behaviour of the membrane voltages (V_{in}-V_{out}, and V_{in}-V_{ext}), the RL-EGOFET I_{DS} current, and the cell potentials (V_{in}, V_{out}, and V_{ext}).The transistor current is calculated using V_{out} as gate input. The three cell potentials (V_{in}, V_{out}, and V_{ext}) are referred to the RL-EGOFET source potential (V_S = 0V).
Notice that decreasing the difference $t_{OSC} - t_{el}$ makes the performance of the RL-EGOFET close to the scenario in the presence of a reference electrode, reported in ***Figure 4.6***

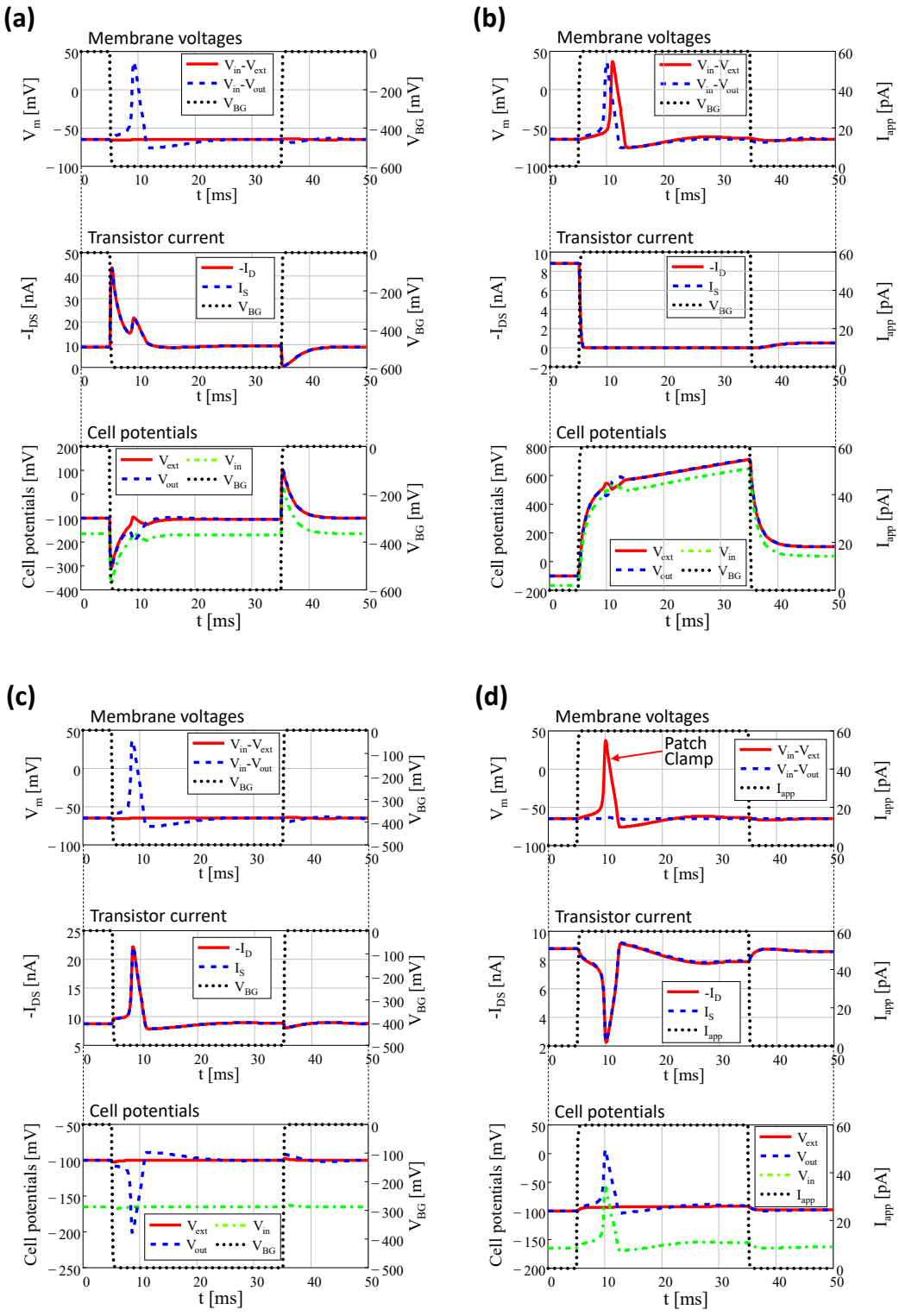

Figure 4.17 - Impacts of the electrodes length L_{el} on the RL-EGOFET properties.
(a) *RL-EGOFET -500mV Back-Gate voltage stimulation, and* **(b)** *60pA current stimulation, simulated for* ***L_{el} = 2µm***.
(c) *RL-EGOFET -500mV Back-Gate voltage stimulation, and* **(d)** *60pA current stimulation, simulated for* ***L_{el} = 200µm***.
All the figures report the behaviour of the membrane voltages (V_{in}-V_{out}, and V_{in}-V_{ext}), the RL-EGOFET I_{DS} current, and the cell potentials (V_{in}, V_{out}, and V_{ext}).

4.4. Proof-of-Concept Experiments

To prove that self-polarization and Back-Gate voltage stimulation are feasible, we fabricated and characterize both EGOFETs and RL-EGOFETs devices (chapter ***4.4.1***). Then, we further motivate the use of a RL-EGOFET by emulating the presence of a cell on top of the device (chapter ***4.4.2***).

4.4.1. (RL-) EGOFETs Fabrication and Characterization

a) Devices fabrication

(RL-) EGOFETs devices were fabricated starting from an n-type silicon wafers with a resistivity of 0.01-0.03 Ω·cm. The Back-Gate insulator was a thermally grown silicon oxide with a thickness of 200nm. Interdigitated source and drain gold electrodes with a thickness of 100-150nm were obtained by photolithography above a chrome adhesion layer of 3-5nm, defining the transistor channel width W=11.2mm and length L=20µm. The electrodes track width was Lel=20µm. TIPS-pentacene (Ossila) p-type semiconductor was drop casted in air at room temperature (22°C with less than 30% of humidity) from a 0.5% solution (in weight) using toluene (Sigma Aldrich) as organic solvent.

b) EGOFETs characterization

EGOFETs were characterized using MilliQ water. A platinum wire immersed in the solution was used as gate contact. Standard characterizations were performed using an Agilent B1500A parameter analyser equipped with two high-resolution source-measurement-units (HR-SMUs) and two high-power source-measurement-units (HP-SMUs). Transfer $I_{DS}V_{GS}$ curves (***Figure 4.18a***) and output $I_{DS}V_{DS}$ curves (***Figure 4.18b***) were obtained by double sweeping the V_{GS} or the V_{DS} voltage, respectively, by setting 1s hold time and 100ms delay time. Each sweep counts 101 measurement points.

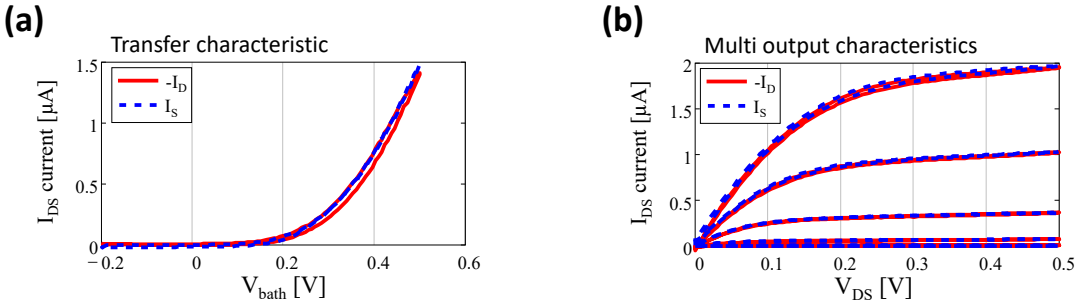

Figure 4.18 – EGOFET characterization.
(a) *EGOFET transfer $I_{DS}V_{GS}$ curve with V_{DS} = -0.2V and V_{BG} = 0V.* **(b)** *EGOFET ouput $I_{DS}V_{DS}$ curves for V_{BG} ranging from 0 V up to -0.5V (V_{BG} = 0V).*

c) RL-EGOFETs characterization

RL-EGOFETs were characterized using MilliQ water. A platinum wire immersed in the solution was used to sense the water potential V_{bath} as respect to the source potential (V_S=0V), by setting the B1500a HR-SMU in constant current mode and forcing a current of 0A. The solution potential V_{bath} was measured during a V_{DS} sweep (***Figure 4.19a***), and during a V_{BG} pulsed sweep (***Figure 4.19b*** and ***Figure 4.19c***) where a sequence of increasing pulses with a period of 100ms were applied at the Back-Gate electrode. In ***Figure 4.19d***, instead, V_{bath} was measured during time, while a -1V Back-Gate voltage step was applied after 90ms from the beginning of the sampling.

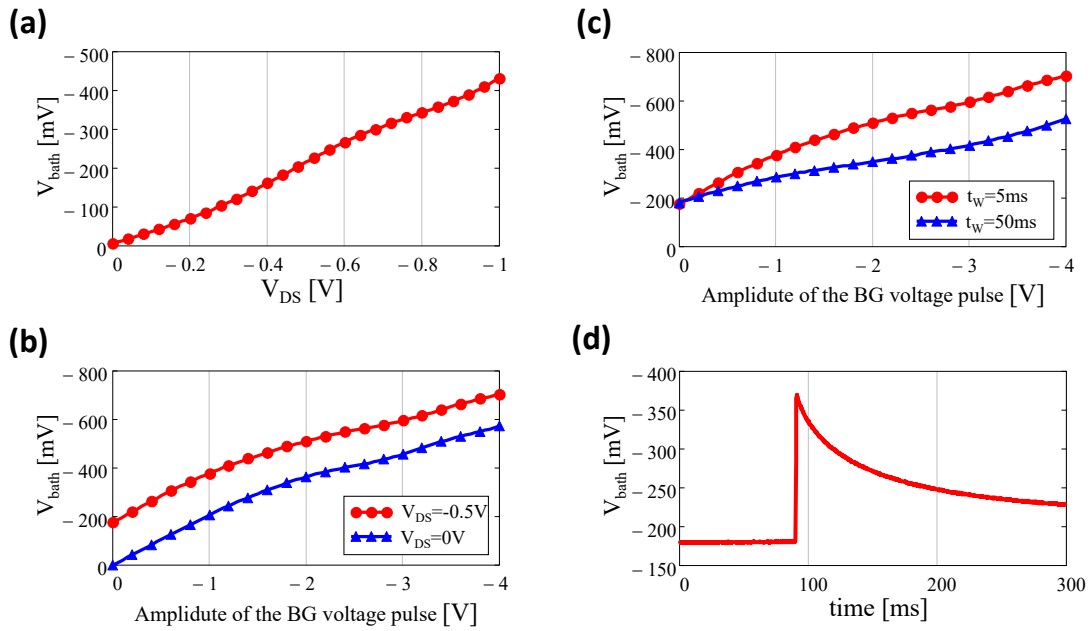

Figure 4.19 – RL-EGOFET characterization.

(a) *Solution potential V_{bath} of an RL-EGOFET as a function of the drain-to-source voltage V_{DS}, showing that an EGOFET can be self-polarized without the need of a reference electrode (RL-EGOFET).* **(b)** *Solution potential as a function of the amplitude of a 50ms Back-Gate voltage pulse, showing that the Back-Gate voltage pulse can stimulate a cell on top of an RL-EGOFET device by perturbating the DC solution potential (the larger the pulse, the larger the stimulus).* **(c)** *RL-EGOFET solution potential as a function of the amplitude of a 5ms (solid line) and 50 ms (dashed line) Back-Gate voltage pulse (V_{DS} = -0.5V).* **(d)** *RL-EGOFET solution potentials consequenly to a Back-Gate voltage pulse with an amplitude of -1V (V_{DS} = -0.5V).*

Notice that, if the cell is removed, $V_{out}=V_{ext}$ is always true. To avoid any missinterpratation, we define V_{bath} as the solution potential.

From ***Figure 4.19a*** we see that the drain-to-source voltage V_{DS} can actually polarize the solution of the RL-EGOFET (i.e., self-polarization): the larger the V_{DS}, the larger the self-polarized V_{bath} (water-gate), hence the larger the I_{DS}. Moreover, ***Figure 4.19b*** and ***Figure 4.19c*** demonstrate that a Back-Gate voltage pulse can successfully induce a variation in the solution potential that is proportional to the amplitude of the stimulation, therefore, a cell can be stimulated. In addition, from ***Figure 4.19c*** we see that the amplitude of the measured V_{bath} (measured at the end of the applied Back-Gate pulse) depends on the duration of the pulse. Indeed, in agreement with what discussed in chapter ***4.4.3***, ***Figure 4.19d*** shows how the Back-Gate voltage stimulation actually induces an abrupt increase of the solution potential V_{bath} which, after the pulse, features an exponential decay reaching its steady-state potential.

4.4.2. Emulation of cell stimulation and sensing with an RL-EGOFET-based neural interface

A custom instrument was used to emulate cells' APs in response to a BG stimulus. We applied the RL-EGOFET DC polarization (V_S=0V, V_D=-0.2V, and V_{BG}=0V), and we monitored the solution potential V_{bath} by means of a platinum wire immersed in the solution and connected to a high-impedance voltage probe. A Back-Gate voltage pulse with an amplitude of -500mV was then applied, inducing the variation of V_{bath}. When ΔV_{bath} exceeded -10mV, an emulated AP is generated directly in the solution by means of the same platinum wire used during the sensing. In correspondence of the AP, the RL-EGOFET I_{DS} is recorded as reported in ***Figure 4.20***. The emulated AP was reproduced using the Hodgkin-Huxley model.

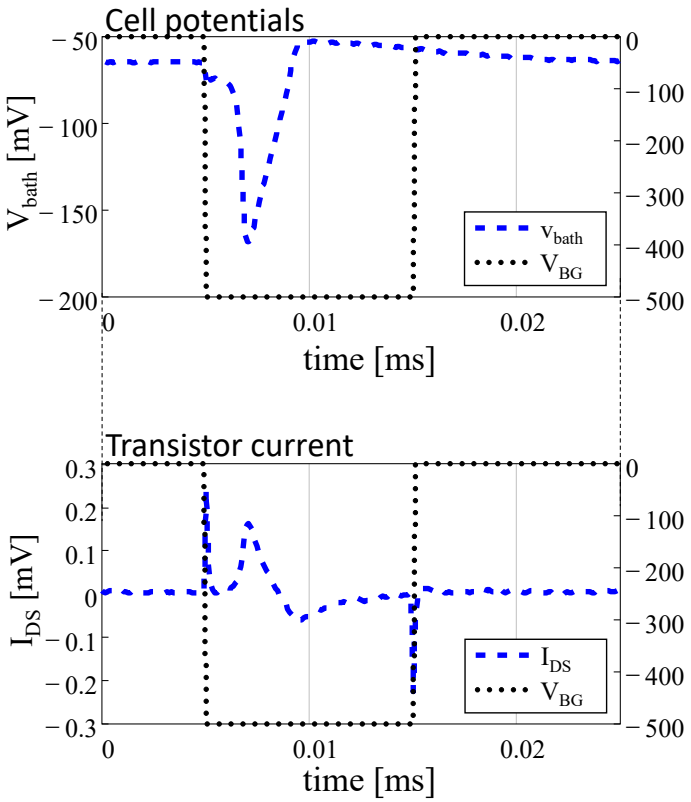

Figure 4.20 – RL-EGOFET cell emulation.
Emulation of the RL-EGOFET neural interface. The Back-Gate voltage induces a perturbation in the solution potential that is measured by a voltage probe and, in response to this perturbation, an AP is emulated (V_{bath}) and it is sensed by the I_{DS} current. The spikes corresponding to the rising and falling edges of the BG pulse are due to the capacitive coupling between the BG and the source and drain electrodes. Notice that, if the cell is removed, $V_{out}=V_{ext}$ is always true. To avoid any missinterpratation, we define V_{bath} as the solution potential.

In response to a Back-Gate voltage stimulation with an RL-EGOFET, a perturbation in the solution potential is induced, thus an AP is emulated. Remarkably, our RL-EGOFET can detect the emulated AP, as shown by the I_{DS} current in ***Figure 4.20***. Hence, simultaneous stimulation and sensing is feasible with a single RL-EGOFET.

4.5. Summary

We presented a model that describes the interaction between a transistor-based sensor and a neuronal cell. Although the model aims to simulate organic neural interfaces made using the EGOFET technology, it can be successfully applied to understand the behavior of a more general class of transistors such as inorganic transistors and OECTs. Using our model, we can simulate the behavior of a neural interface with and without the presence of an external reference electrode in direct contact with the physiological solution. We introduced the concept of the RL-EGOFET and showed that simultaneous stimulation and recordings should be feasible with such a sensor, which was further supported by proof-of-principle experiments. Hence, RL-EGOFETs could be successfully implemented to fabricate a low cost and flexible neural interface for extracellular recording *in vivo* without the need of any reference electrode, making the implant less invasive and easier to use. We believe that our model can play an important role as a tool for designing both EGOFETs and RL-EGOFETs and for optimizing neural interfaces before testing the device with living cells.

References

[Cramer12] T. Cramer, A. Kyndiah, M. Murgia, F. Leonardi, S. Casalini, and F. Biscarini, *Double layer capacitance measured by organic field effect transistor operated in water*, **Appl. Phys. Lett.**, vol. 100, issue 14, pp. 143302, Apr. 2012.

[Cramer13] T. Cramer, B. Chelli, M. Murgia, M. Barbalinardo, E. Bystrenova, D. M. de Leeuw, and F. Biscarini, *Organic ultra-thin film transistors with a liquid gate for extracellular stimulation and recording of electric activity of stem cell-derived neuronal networks*, **Phys. Chem. Chem. Phys.**, vol. 15, issue 11, pp. 3897-3905, Mar. 2013.

[Bernards07] D. A. Bernards, and G. G. Malliaras, *Steady-State and Transient Behavior of Organic Electrochemical Transistors*, **Adv. Funct. Mater.**, vol. 17, issue 17, pp. 3538-3544, Nov. 2007.

[Bove95] M. Bove, M. Grattarola, S. Martinoia, and G. Verreschi, *Interfacing cultured neurons to planar substrate microelectrodes: characterization of the neuron-to-microelectrode junction*; **Bioelectrochem. Bioenerg.**, vol. 38, issue 2, pp. 255-265, Oct. 1995.

[Braun98] D. Braun, and Fromherz, *Fluorescence Interferometry of Neural Cell Adhesion on Microstructured Silicon*, **Phys. Rev. Lett.**, vol. 81, issue 23, pp. 5242-5244, Jul. 1998.

[Braun04] D. Braun, and Fromherz, *Imaging Neural Seal Resistance on Silicon Chip using Fluorescent Voltage-Sensitive Dye*, **Biophys. J.**, vol. 87, issue 2, pp. 1351-1359, Aug. 2004.

[Colinge] J.-P. Colinge, *Silicon-on-Insulator Technology: Materials to VLSI,* **Springer**, 3rd ed., 2004.

[Duan12] X. Duan, R. Gao, P. Xie, T. C.-Karni, Q. Qing, H. S. Choe, B. Tian, X. Jiang, and C. M. Lieber, *Intracellular recordings of action potentials by an extracellular nanoscale field-effect transistor*, **Nat. Nanotech.**, vol. 7, issue 3, pp. 174-179, Mar. 2012.

[Fall02] C. P. Fall, E. S. Marland, J. M. Wagner, and J. J. Tyson, *Computational Cell Biology*, **Springer**, 1st ed., 2002.

[Fang15] Y. Fang, X. Li, Y. Fang, *Organic bioelectronics for neural interfaces*, **J. Mater. Chem. C**, vol. 3, issue 25, pp. 6424-6430, Jun. 2015.

[Fattahi14] P. Fattahi, G. Yang, G. Kim, and M. R. Abidian, *A Review of Organic and Inorganic Biomaterials for Neural Interfaces*, **Adv. Mat.**, vol. 26, issue 12, pp. 1864-1885, March 2014.

[Franks05] W. Franks, I. Schenker, P. Schmutz, and A. Hierlemann, *Impedance Characterization and Modeling of Electrodes for Biomedical Applications*, **IEEE Trans. Biomed. Eng.**, vol. 52, issue 7, pp. 1295-1302, Jun. 2005.

[Frega12] M. Frega, V. Pasquale, M. Tedesco, M. Marcoli, A. Contestabile, M. Nanni, L. Bonzano, G. Maura, and M. Chiappalone, *Cortical cultures coupled to Micro-Electrode Arrays: A novel approach to perform in vitro excitotoxicity testing*, **Neurotoxicol. Teratol.**, vol 34, issue 1, pp. 116-127, Jan. 2012.

[Fromherz91] P. Fromherz, A. Offenhausser, T. Vetter, and J. Weis, A Neuron-Silicon Junction: A Retzius Cell of the Leech on an Insulated-Gate Field-Effect Transistor. **Science**, vol. 252, issue 5010, pp. 1290-1293, May 1991.

[Fromherz99] P. Fromherz, *Extracellular recording with transistors and the distribution of ionic conductances in a cell membrane*, **Eur. Biophys. J.**, vol. 28, issue 3, pp. 254-258, Mar. 1999.

[Hodgkin52] A. L. Hodgkin, and A. F. Huxley, *A quantitative description of membrane current and its application to conduction and excitation in nerve*, **J. Physiol.**, vol. 117, issue 4, pp. 500-544, Aug. 1952.

[Karni09] T. C.-Karni, B. P. Timko, L. E. Weiss, and C. M. Lieber, *Flexible electrical recording from cells using nanowire transistor array*, ***Proc. Nat. Acad. Sci.***, vol. 106, issue 18, 7309-7313, Mar. 2009.

[Keener09] J. Keener, and A. J. R. Sneyd, *Mathematical Physiology*, **Springer**, 1st ed., 2009.

[Kergoat10] L. Kergoat, L. Herlogsson, D. Braga, B. Piro, M.-C. Pham, X. Crispin, M. Berggren, and G. Horowitz, *A Water-Gate Organic Field-Effect Transistor*, **Adv. Mater.**, vol. 22, issue 23, pp. 2565-2569, Jun. 2010.

[Kergoat11] L. Kergoat, N. Battaglini, L. Miozzo, B. Piro, M.-C. Pham, A. Yassar, and G. Horowitz, *Use of poly(3-hexylthiophene)poly(methyl methacrylate) (P3HT:PMMA) blends to improve the performance of water-gated organic field-effect transistors*, **Org. Electron.**, vol. 12, issue 7, pp. 1253-1257, Jul. 2011.

[Kergoat12] L. Kergoat, B. Piro, M. Berggren, G. Horowitz, and M.-C. Pham, *Advances in organic transistor-based biosensors: From organic electrochemical transistors to electrolyte-gated organic field-effect transistors*, **Anal. Bioanal. Chem.**, vol. 402, issue 5, pp. 1813-1826, Feb. 2012.

[Khodagholy13a] D. Khodagholy, T. Doublet, P. Quilichini, M. Gurfinkel, P. Leleux, A. Ghestem, E. Ismailova, T. Hervé, S. Sanaur, C. Bernard, and G. G. Malliaras, *In vivo recordings of brain activity using organic transistors*, **Nat. Commun.**, vol. 4, no. 1575, Mar. 2013.

[Khodagholy13b] D. Khodagholy, J. Rivnay, M. Sessolo, M. Gurfinkel, P. Leleux, L. H. Jimison, E. Stavrinidou, T. Herve, S. Sanaur, R. M. Owens, and G. G. Malliaras, *High transconductance organic electrochemical transistors*. **Nat. Commun.**, vol. 4, no. 2133, Jul. 2013.

[Kim10] D.-H. Kim, J. Viventi, J. J. Amsden, J. Xiao, L. Vigeland, Y.-S. Kim, J. A. Blanco, B. Panilaitis, E. S. Frechette, D. Contreras, D. L. Kaplan, F. G. Omenetto, Y. Huang, K.-C. Hwang, M. R. Zakin, B. Litt, and J. A. Rogers, *Dissolvable films of silk fibroin for ultrathin conformal bio-integrated electronics*, **Nat. Mater.**, vol. 9, issue 6, pp. 511-517, Jun. 2010.

[Larsson11] O. Larsson, A. Laiho, W. Schmickler, M. Berggren, and X. Crispin, *Controlling the Dimensionality of Charge Transport in an Organic Electrochemical Transistor by Capacitive Coupling*, **Adv. Mater.**, vol. 23, issue 41, pp. 4764-4769, Nov. 2011.

[Lempka09] S. F. Lempka, S. Miocinovic, M. D. Johnson, J. L. Vitek, and & C. C. McIntyre, *In vivo impedance spectroscopy of deep brain stimulation electrodes*. **J. Neural Eng.**, vol. 6, issue 4, no. 046001, Jun. 2009.

[Lucas12] B. Lucas, A. El Amrani, A. Moliton, A. Skaiky, A. El Hajj, and M. Aldissi, *Charge transport properties in pentacene films: Evaluation of carrier mobility by different techniques*, **Solid-State Electron.**, vol. 69, pp. 99-103, Mar. 2012.

[Maccione13] A. Maccione, A. Simi, T. Nieus, M. Gandolfo, K. Imfeld, E. Ferrea, E. Sernagor, and L. Berdondini, *Sensing and Actuating electrophysiological activity on brain tissue and neural cultures with a high-density CMOS-MEA*, **2013 Transducers & Eurosensors XXVII: The 17th International Conference on Solid-State Sensors, Actuators and Microsystems**, Barcelona, pp. 752-755, 2013.

[Marinov09] O. Marinov, M. J. Deen, U. Zschieschang, and H. Klauk, *Organic Thin-Film Transistors: Part I–Compact DC Modeling*, **IEEE Trans. Electron Devices**, vol. 56, issue 12, pp. 2952-2961, Dec. 2009.

[Massobrio16] P. Massobrio, G. Massobrio, S. Martinoia, *Interfacing Cultured Neurons to Microtransducers Arrays: A Review of the Neuro-Electronic Junction Models*, **Front. Neurosci.**, vol. 10, pp. 282, Jun. 2016.

[Patolsky06] F. Patolsky, B. P. Timko, G. Yu, Y. Fang, A. B. Greytak, G. Zheng, and C. M. Lieber, *Detection, Stimulation, and Inhibition of Neuronal Signals with High-Density Nanowire Transistor Arrays*, **Science**, vol. 313, issue 5790, pp. 1100-1104, Aug. 2006.

[Petersen17] C. C. H. Petersen, *Whole-Cell Recording of Neuronal Membrane Potential during Behavior*, **Neuron**, vol. 95, issue 6, pp. 1266-1281, Sep. 2017.

[Popescu15] D. Popescu, B. Popescu, M. Brandlein, K. Melzer, and P. Lugli, *Modeling of Electrolyte-Gated Organic Thin-Film Transistors for Sensing Applications*, **IEEE Tran. Electr. Dev.**, vol. 62, issue 12, pp. 4206-4212, Dec. 2015.

[Poghossian09] A. Poghossian, S. Ingebrandt, A. Offenhäusser, and M. J. Schöning, *Field-effect devices for detecting cellular signals*, **Semin. Cell Dev. Biol.**, vol. 20, issue 1, pp. 41-48, Feb. 2009.

[Porrazzo14] R. Porrazzo, S. Bellani, A. Luzio, E. Lanzarini, M. Caironi, and M. R. Antognazza, *Improving mobility and electrochemical stability of a water-gated polymer field-effect transistor*, **Org. Electron.**, vol. 15, issue 9, pp. 2126-2134, Sep. 2014.

[Schoen07] I. Schoen, and P. Fromherz, *The Mechanism of Extracellular Stimulation of Nerve Cells on an Electrolyte-Oxide-Semiconductor Capacitor*, **Biophys. J.**, vol. 92, issue. 3, pp. 1096-1111, Feb. 2007.

[Sharma10] P. Sharma, and T. S. Bhatti, *A review on electrochemical double-layer capacitors*, **Energy Convers. Manage.**, vol. 51, issue 12, pp. 2901-2912, Dec. 2010.

[Spanu15] A. Spanu, S. Lai, P. Cosseddu, M. Tedesco, S. Martinoia, and A. Bonfiglio, *An organic transistor-based system for reference-less electrophysiological monitoring of excitable cells*, **Sci. Rep.**, vol. 5, no. 8807, Mar. 2015.

[Stein04] D. Stein, M. Kruithof, and C. Dekker, *Surface-Charge-Governed Ion Transport in Nanofluidic Channels*, **Phys. Rev. Lett.**, vol. 93, issue 3, no. 035901, Jul. 2004.

[Timko10] B. P. Timko, T. Cohen-Karni, Q. Qing, B. Tian and C. M. Lieber, *Design and Implementation of Functional Nanoelectronic Interfaces With Biomolecules, Cells, and Tissue Using Nanowire Device Arrays*, **IEEE Transactions on Nanotechnology**, vol. 9, issue 3, pp. 269-280, May 2010.

[Wang16] D. Wang, V. Noël, and B. Piro, *Electrolytic Gated Organic Field-Effect Transistors for Application in Biosensors–A Review*, **Electronics**, vol. 5, issue 1, no. 9, Feb. 2016.

[Weis97] R. Weis, and P. Fromherz, *Frequency dependent signal transfer in neuron transistors*, **Phys. Rev. E**, vol. 55, issue 1, pp. 877-889, Jan. 1997.

[Wiegert17] J. S. Wiegert, C. E. Gee, and T. G. Oertner, *Stimulating Neurons with Heterologously Expressed Light-Gated Ion Channels*, **Cold Spring Harbor Protocols**, vol. 2017, issue 2, pp. 85-91, Feb. 2017.

[Yao15] C. Yao, Q. Li, J. Guo, F. Yan, and I.-M. Hsing, *Rigid and Flexible Organic Electrochemical Transistor Arrays for Monitoring Action Potentials from Electrogenic Cells*, **Adv. Healthcare Mater.**, vol. 4, issue 4, pp. 528-533, Mar. 2015.

[Zeng17] R. Zeng, J. Zhang, C. Sun, M. Xu, S.-L. Zhang, and D. Wu, *A reference-less semiconductor ion sensor*, **Sens. Actuators B**, vol. 254, pp. 102-109, Jun 2017.

5. Conclusion

Organic bio-electronics is a valid alternative to conventional technologies, allowing the realizations of more flexible and conformable neural interfaces that can be intrinsically biocompatible due to the nature of the organic semiconductors that is close to that of the living tissues. Moreover, organic materials can be tuned to enhance the device sensitivity to a particular analyte, and organic neural interfaces can be fabricated onto transparent substrate promoting the combination of optical and electrical analysis.

The most attractive technology is that based on organic field-effect transistors (both OECTs and EGOFETs) that allow the integration of sensing and amplification in a single device. Such neural interfaces have proven higher SNR as respect with the inorganic-based sensors, paving the way to new all-organic biosensors for in vivo recording of brain activity with minimum risk of tissues damaging.

Despite all these achievements, the comprehension of the transduction mechanism between cells and transistor-based sensors did no progressed as fast as the development of new technologies. Moreover, organic transistors and organic transistor based sensors are a relative novel technology that differs in many aspects from the standard silicon transistor. In order to master the transduction mechanism behind an organic neural interface working principle, it is therefore important the development of new tools and techniques to characterize and describe the physic of transport in organic transistors, as well to fully understand and model the interaction between ionic solution and organic semiconductor.

In addition, organic neural interfaces still suffer from a low selectivity due to a reduced integration capacity as respect with the CMOS technology. Hence, to achieve in vivo single-cell bidirectional communication, new technologies and fabrication processes must be developed.

To pursuit this goal, our research activity was subdivided into two main research lines: *i)* Study and characterization of OTFTs featuring different organic semiconductor materials; *ii)* Characterization and modeling of the organic semiconductor/solution interface.

In this work, we have shown that pulsed and transient characterizations are useful tools to analyze the dynamic channel response. The current transient duration is related to the tail-states of HOMO and LUMO that limit the speed of the channel formation and depletion, which is not only a fundamental issue for device and material characterization, but also it might severely impact some applications. In fact, characterization procedure must be carefully set up to eliminate any transient phenomena, which affect the extrapolation of mobility, trapped charge density, etc.

We also applied the DLTS technique where both p-type and n-type OFETs were analyzed and they show a similar transient behavior. We correlated the DLTS technique with electrical I_{DS}-V_{GS} characterizations and we extrapolated the activation energies $E\mu$ and $E\tau$ as well as the widths σ of the HOMO and LUMO distribution using the Gaussian approximation.

Our analysis clearly validates the use of pure electrical techniques to give a qualitative and quantitative description of the energy levels as well the Fermi level in polymer and molecular semiconductors. Moreover, we showed that the transient response is strongly limited by the time needed to fully populate the electronic channel. The channel formation requires to move the quasi Fermi energy close to the corresponding transport level by populating all the tale states starting from the deepest states to the shallower levels.

This phenomenon has a strong impact to the dynamic performances of the OFET devices since it can take a very long time to completely form the conductive channel and it directly impacts the mobility of the transistors. Then, even though this phenomenon moderately impacts on the digital applications, particular care must be taken in designing analog circuits, including bio-sensor devices. In fact, in recording neuronal signals it is necessary to proper chose the transistor operative point. In particular, the phenomenon of channel formation and depletion must be carefully considered during the interpretation of the recorded signals.

To investigate the electrochemical transduction mechanisms between living cell and organic biosensor, we presented and validated a comprehensive model that considers and rationalizes all the processes taking place at the interface or in the bulk of the different layers comprising a metal-organic-electrolyte stack.

In order to identify all the possible mechanisms, we performed EIS measurements both at low and at high operating bias voltages applied between the gold layer and the platinum electrode, thus avoiding the use of any constant phase element in the equivalent circuit. This measurement protocol allowed us to separate in the frequency domain the different contributions and, in particular, to demonstrate the occurrence of ion percolation through the organic layer by using a de Levie circuital element. The presence of percolation is demonstrated by ESEM analysis and optical profilometry. Although percolation is much faster and more intense at high negative bias, it is still present at low bias conditions (close to the real operating conditions), even if with different rate.

We further extended our findings presenting a more general model for the metal/organic semiconductor/solution/metal structure, where the solution can be an electrolyte as well as poor water. We considered two case studies, by introducing some simplifications, which are often meaningful in many device architectures. In particular, we studied the use of two different solutions and we showed that they can be described using two different models. On the one hand, the devices featuring deionized water are characterized by the absence of the diffusion impedance, and by an impedance lobe, associated to the solution capacitance, which hides, at least partially, the contribution of the counter electrode and the organic semiconductor capacitance. On the other hand, the devices measured with saline solutions are characterized by the absence of the solution capacitance, whereas the organic semiconductor geometry capacitance is perfectly observable, especially at high biases, and it can be easily estimated using our model. Noticeably, it can be easily shown that both models are a particular case of the general equivalent circuit model presented in this work, that can be successfully applied to a plethora of other architectures characterized by different electrical and chemical properties. In particular, we showed that, changing the nature of the OSC or of the OSC/solution interface, our model, with the proper parameters sets, is able to correctly describe the whole impedance spectra. We demonstrated a very good accordance between model and the experimental data, proving that this model is a valid tool for studying the interaction between bio-sensing devices and physiological environment, such as OECTs, EGOFET, and many other electrochemical systems, where electrodes are coated with organics or porous material, with particular emphasis to organic neural interfaces.

Finally, we integrated the metal/OSC/solution model with the Hodgkin-Huxley model, hence presenting a model that describes the interaction between a transistor-based sensor and a neuronal cell. Although the model aims to simulate organic neural interfaces made using the EGOFET technology, it can be successfully applied to understand the behavior of a more general class of transistors such as inorganic transistors and OECTs. Using our model, we can simulate the behavior of a neural interface with and without the presence of an external reference electrode in direct contact with the physiological solution. We introduced the concept of the RL-EGOFET and showed that simultaneous stimulation and recordings should be feasible with such a sensor, which was further supported by proof-of-principle experiments. Hence, RL-EGOFETs could be successfully implemented to fabricate a low cost and flexible neural interface for extracellular recording *in vivo* without the need of any reference electrode, making the implant less invasive and easier to use.

We believe that this work can pave the way to the development of new organic ECoG arrays made by reference-less sensors for simultaneous stimulation and recording.

Publications

List of publications on international journals:

J1. N. Wrachien, A. Cester, N. Lago, G. Meneghesso, R. D'Alpaos, A. Stefani, G. Turatti, M. Muccini, *Stress-induced degradation of p- and n-type organic thin-film-transistors in the ON and OFF states*, **Microelectronics Reliability**, vol. 54, issues. 9-10, pp. 1638-1642, September-October. 2014.

J2. N. Wrachien, A. Cester, N. Lago, A. Rizzo, R. D'Alpaos, A. Stefani, G. Turatti, M. Muccini, and G. Meneghesso, *Reliability study of organic complementary logic inverters using constant voltage stress*, **Solid-State Electronics**, vol. 113, issue 11, pp. 151-156, November 2015.

J3. N. Wrachien, N. Lago, A. Rizzo, R. D'Alpaos, A. Stefani, G. Turatti, M. Muccini, G. Meneghesso, and A. Cester, *Effects of thermal and electrical stress on DH4T-based organic thin-film-transistors with PMMA gate dielectrics*, **Microelectronics Reliability**, vol. 55, issues 9-10, pp. 1790-1794, August-September 2015.

J4. A. Cester, A. Rizzo, A. Bazzega, N. Lago, J. Favaro, M. Barbato, N. Wrachien, S.A. Gevorgyan, M. Corazza, and F.C. Krebs. *Effects of constant voltage and constant current stress in PCBM: P3HT solar cells*, **Microelectronics Reliability**, vol. 55, issues 9-10, pp. 1795-1799, August-September 2015.

J5. N. Lago, A. Cester, N. Wrachien, I. Tomasino, S. Toffanin, S. D. Quiroga, E. Benvenuti, M. Natali, M. Muccini, and G. Meneghesso *On the Pulsed and Transient Characterization of Organic Field-Effect Transistors*, **IEEE Electron Device Letters**, vol. 36, issue 12, pp. 1359-1362, December. 2015.

J6. N. Lago, A. Cester, N. Wrachien, M. Natali, S. D. Quiroga, S. Bonetti, M. Barbato, A. Rizzo, E. Benvenuti, V. Benfenati, M. Muccini, S. Toffanin, and G. Meneghesso, *A physical-based equivalent circuit model for an organic/electrolyte interface*, **Organic Electronics**, vol. 35, pp. 176–185, August 2016.

J7. N. Lago, A. Cester, N. Wrachien, E. Benvenuti, S. D. Quiroga, M. Natali, S. Toffanin, M. Muccini, and G. Meneghesso, *Investigation of Mobility Transient on Organic Transistor by Means of DLTS Technique*, **IEEE Transactions on Electron Devices**, vol. 63, issue 11, pp. 4432-4439, November 2016.

J8. A. Rizzo, A. Cester, N. Wrachien, N. Lago, L. Torto, M. Barbato, J. Favaro, S. A. Gevorgyan, M. Corazza, and F. C. Krebs, *Characterization and modeling of organic (P3HT:PCBM) solar cells as a function of bias and illumination,* **Solar Energy Materials and Solar Cells**, vol. 157, pp. 337–345, December 2016.

J9. N. Lago, A. Cester, *Flexible and Organic Neural Interfaces: A Review*, **Applied Sciences**, vol. 7, issue 12, no. 1292, December 2017.

List of publications on conference proceedings

C1. N. Wrachien, A. Cester, N. Lago, G. Meneghesso, R. D'Alpaos, A. Stefani, G. Turatti, and M. Muccini, *Effects of constant voltage stress on organic complementary logic inverter*, **2014 44th European Solid State Device Research Conference**, pp. 298-301, 2014.

C2. M. Natali, N. Lago, M. Brucale, S. D. Quiroga, S. Bonetti, E. Benvenuti, E. Bonaretti, N. Wrachien, M. Muccini, A. Cester, V. Benfenati, and S. Toffanin, *Investigation on the Mechanism of Bioelectrical Transduction at the Organic/Electrolyte Interface in Perylene-Based O-CST*, **MRS – Fall Meeting**, 2015.

C3. A. Rizzo, A. Cester, L. Torto, M. Barbato, N. Wrachien, N. Lago, M. Corazza, F. C. Krebs, and S. A. Gevorgyan, *Effects of Current Stress and Thermal Storage on polymeric heterojunction P3HT:PCBM solar cell*, **2016 IEEE International Reliability Physics Symposium**, 2016.

C4. N. Wrachien, L. Torto, N. Lago, A. Rizzo, G. Meneghesso, R. D'Alpaos, G. Generali, G. Turatti, M. Muccini, and A. Cester, *Thermal Stress Effects on Organic-Thin-Film-Transistors*, **12th Internation Conference of Organic Electronics**, *2016*.

List of publications under submission

S1. N. Lago, M. Buonomo, N. Wrachien, F. Prescimone, M. Natali, M. Muccini, S. Toffanin, and A. Cester, *A general equivalent circuit model for an organic/solution interface*, 2018.

S2. N. Lago, N. Wrachien, M. G. Pedersen, A. Cester, *Simultaneous stimulation and recording of cell activity with reference-less sensors: is it feasible?*, 2018.